Multi-Scale Investigation of Nucleate Boiling Phenomena in Microgravity

Nils Schweizer
Institute of Technical Thermodynamics

TECHNISCHE
UNIVERSITÄT
DARMSTADT

Multi-Scale Investigation of Nucleate Boiling Phenomena in Microgravity

Vom Fachbereich Maschinenbau
an der Technischen Universität Darmstadt
zur
Erlangung des akademischen Grades eines Doktor-Ingenieurs (Dr.-Ing.)
genehmigte

D I S S E R T A T I O N

vorgelegt von

Dipl.-Ing. Nils Schweizer
aus Erbach/Odw.

Berichterstatter:	Prof. Dr.-Ing. Peter Stephan
Mitberichterstatter:	Prof. Paolo Di Marco
Tag der Einreichung:	04.10.2010
Tag der mündlichen Prüfung:	08.12.2010

Darmstadt 2010

D 17

Vorwort

Die vorliegende Arbeit entstand während meiner Tätigkeit am Fachgebiet Technische Thermodynamik der Technischen Universität Darmstadt. Dem Leiter des Fachgebiets, Herrn Prof. Dr.-Ing. Peter Stephan danke ich besonders herzlich. Er hat mir als Mitarbeiter nicht nur die technischen und finanziellen Rahmenbedingungen bereitgestellt, sondern auch die Möglichkeit gegeben, eigene Ideen zu verwirklichen. Obwohl er mir die sehr geschätzten Freiräume und Eigenverantwortlichkeiten einräumte, stand er trotzdem stets durch hilfreiche Ratschläge und fruchtbare fachliche Diskussionen zur Seite. Schon während meiner studentischen Tätigkeit am Fachgebiet ermöglichte er mir die Übernahme der Verantwortung für das Parabelflug-Experiment. Im Rahmen meiner Arbeit als Assistent durfte ich dann meine Weltraumbegeisterung durch die Mitarbeit in den ESA Projekten des Fachgebiets ausleben. Dazu gehörte die fachgebietsseitige Vorbereitung der ISS Experimente EMERALD und vor allem RUBI, dessen Zielsetzung und Messmethodik sehr stark mit meinen Parabelflug-Experimenten verwandt ist. Des Weiteren konnte ich das ESA ITI (Innovation Triangle Initiative) Projekt “Miniature, mechanically pumped two-phase loop” durchführen, das die konzeptionelle Entwicklung, sowie Aufbau und Test eines experimentellen Kreislaufs umfasste. Ich hatte im Rahmen dieser Projekte die Chance wertvolle Erfahrungen im Bereich “Space Business” zu sammeln und eine Reihe herausragender Persönlichkeiten kennen zu lernen.
Herrn Prof. Paolo Di Marco danke ich für die freundliche Übernahme des Ko-Referats und die Zusammenarbeit bei der Untersuchung der Wirkung eines elektrischen Feldes auf den Siedevorgang.
Ein ganz herzlicher Dank gilt dem Team der Fachgebiets-Werkstatt für die hoch genaue und immer zeitnahe Fertigung der Komponenten meiner Versuchsanlagen. Besonders Roland Berntheisel stand mir nicht nur bezüglich der Lösung fertigungsrelevanter, sondern auch technischer oder gar wissenschaftlicher Probleme mit Rat und Tat zur Seite.
Von ganzem Herzen danke ich auch der Sekretärin des Fachgebiets, Frau Gabi Gunkel für die freundschaftliche Unterstützung nicht nur in administrativen Belangen.
Zum Gelingen der Arbeit haben meine Kollegen am Fachgebiet durch das außerordentlich gute Arbeitsklima und die stets offenen Türen zu einem bedeutenden Teil beigetragen. Vor allem mit Christof Sodtke, Tobias Schulze und Christian Kunkelmann konnte ich während unserer Zeit im gemeinsamen Büro einige interessante Diskussionen rund um Verdampfungsphänomene und ganz besonders die Mikrozone führen. Auch die enge Zusammenarbeit mit Enno Wagner, dessen Bodenexperimente stark mit meinen Parabelflugexperimenten verwandt sind, trug erheblich zum Gelingen der Arbeit bei und dafür danke ich ihm sehr herzlich.
Besondere Erwähnung verdient auch die Arbeit meines Studenten Sebastian Fischer für seine herausragenden Leistungen bei der Vorbereitung des Versuchstandes und während der Experiment-Durchführung im Flug.
Des Weiteren danke ich Felix Brinckmann ganz herzlich für seine Unterstützung im Bereich Rechner-Administration und Messtechnik, sowie ihm, Christian Kunkelmann und Heike Sattler für das Korrekturlesen der Arbeit.

Ich bedanke mich bei allen Mitgliedern der TTD-Parabelflug-Teams für die tolle Zusammenarbeit und den außerordentlichen Team-Spirit.
Ich danke weiterhin der ESA für die finanzielle Unterstützung der Projekte und zusammen mit dem DLR für den Zugang zu den Parabelflugkampagnen.
Nicht zuletzt danke ich von ganzem Herzen meiner lieben Frau Kim, die während der ganzen Zeit stets hinter mir gestanden und meinen Rücken gestärkt hat. An dieser Stelle geht auch ein großes Dankeschön an unsere große Familie, ohne deren Rückhalt die Anfertigung dieser Arbeit nicht möglich gewesen ware und ganz besonders an meine Eltern, Heidrun und Friedrich Schweizer, die mich mit meiner Weltraumbegeisterung immer vorbehaltlos unterstützt haben.

Ich versichere an Eides statt, dass ich die vorliegende Arbeit, abgesehen von den genannten Hilfsmitteln, selbständig angefertigt habe.

Nils Schweizer

Markdorf, im August 2010

Kim

Kurzfassung

Das Thema der vorliegenden Arbeit ist die experimentelle Untersuchung von Blasensiede-Phänomenen in Mikrogravitation auf verschiedenen Längenskalen. Blasensieden ist ein hocheffizienter Wärmeübertragungsmechanismus und wird in vielfältigen industriellen Anwendungen eingesetzt. Beispiele hierfür sind Dampferzeuger in Kraftwerken, Klima-Anlagen, Kühlaggregate, Kühlsysteme für Elektronik und Prozesse in der Verfahrenstechnik und chemischen Industrie. Zur Auslegung von Prozessen, in denen Blasensieden vorkommt, ist es unerlässlich, zuverlässige und präzise Berechnungswerkzeuge zur Verfügung zu haben, um die Leistung des Prozesses vorherzusagen. Auch eine präzise Vorhersage der Grenzen des Prozesses, wie beispielsweise des kritischen Wärmestroms, sind unter sicherheitstechnischen Aspekten wichtig, da die Überschreitung dieser Grenzen zur Zerstörung des entsprechenden Bauteils führen kann. Aufgrund der hochdynamischen Natur von Siedeprozessen und der zahlreichen involvierten Phänomene, die in komplexer Weise miteinander interagieren, steht eine geschlossene theoretische Beschreibung noch aus. Ein grundlegendes Verständnis für die Phänomene und deren Zusammenhänge ist noch nicht gegeben. Ziel der vorliegenden Arbeit ist es, zum grundlegenden Verständnis des Blasensiedens beizutragen.

Kernstück des Versuchsaufbaus ist eine Edelstahl-Heizfolie mit einer Dicke von 20 μm. In der Oberseite der Heizfolie ist zentrisch eine einzelne, künstliche Keimstelle elektrolytisch erzeugt worden. Die Heizfolie umschließt eine kubische Siedezelle, gefüllt mit dem Arbeitsmedium n-Perfluorohexan. Die Sättigungsbedingungen (Druck und Temperatur) in der Siedezelle können mithilfe einer Vakuumpumpe und der Temperierung der Zellwände eingestellt, sowie mit Thermoelementen und einem Drucksensor gemessen werden. Die Temperaturverteilung der Heizfolie im Bereich der Keimstelle wurde mittels Infrarot-Thermographie von der Unterseite aus gemessen. Die räumliche Auflösung der Infrarotkamera betrug dabei 30 μm/Pixel bei einer Bildfrequenz von 1000 Hz. Die Größe und das Verhalten der Dampfblasen wurden mit einer zur Infrarotkamera synchronisierten Hochgeschwindigkeitskamera erfasst.

Als zusätzlicher Stimulus wurde bei einigen Experimenten eine Hochspannungselektrode in Form einer Unterlegscheibe im Abstand von 5 mm über der Heizfolie platziert und mit maximal 10 kV aufgeladen. Ziel der Versuche mit dem elektrischen Feld war die Untersuchung von dessen Wirkung auf die Dampfblasen, unter anderem im Hinblick auf den Ersatz des Auftriebs als ablösende Kraft in Schwerelosigkeit.

Die Experimente wurden während Parabelflügen durchgeführt. Grund dafür war zum einen die Verbesserung der zeitlichen und räumlichen Auflösung, da die Blasen unter reduzierter Schwerkraft später und größer ablösen. Zum anderen können Effekte sichtbar werden, die normalerweise durch natürliche Konvektion, welche in Schwerelosigkeit nicht-existent ist, überlagert werden. Weiterhin wurde die Einbindung der Gravitation in einigen empirischen Korrelationen überprüft, indem das gesamte Gravitationsspektrum eines Parabelfluges von 1.6g bis 0g zur Messung genutzt wurde. Für die Raumfahrt sind Siedeversuche in Schwerelosigkeit insofern interessant, da die Untersuchung des Siedeverhaltens in Schwerelosigkeit eine Voraussetzung für dessen Vorhersage bei Vorkommen oder Nutzung in Raumfahrtsystemen ist.

Zur Versuchsdurchführung wurde zunächst in Phasen mit normaler oder erhöhter Gravitation meist ein kontinuierlicher Siedeprozess an der einzelnen, künstlichen Keimstelle, oder alternativ, ausgeprägtes Blasensieden auf der ganzen Heizfolie etabliert. Die Messsequenz mit einer Dauer von 4 s wurde während des Übergangs von der Hypergravitation (1.6g) in die Mikrogravitation oder erst in der Mikrogravitationsphase selbst ausgelöst.
Der Einfluss der Gravitation auf Blasenfrequenz und Abreißdurchmesser wurde untersucht und mit gängigen empirischen Korrelationen verglichen. Obwohl einige Korrelationen den Schwerkraft-Einfluss für den gegebenen Siedeprozess korrekt abbilden, zeigten sich bei diesen Korrelationen erhebliche Abweichungen zu den Messwerten. Für den Abreißdurchmesser wurde eine neue Korrelation entwickelt, die, wie die wohlbekannte Fritz' Korrelation, auf dem Kräftegleichgewicht zwischen ablösend wirkendem Auftrieb und anhaftend wirkender Oberflächenspannung beruht. Die neue Korrelation basiert rein auf theoretischen Überlegungen, ohne die Einbeziehung eines empirischen Faktors. Trotzdem zeigte sich eine außerordentlich gute quantitative Übereinstimmung mit den Messwerten. Weiterhin wurde eine neue Blasenfrequenz-Korrelation, basierend auf der Korrelation von Mikic und Rohsenow, vorgeschlagen.
Die transiente Verteilung der Heizfolien-Temperatur und der Wärmestromdichte in das Fluid wurde untersucht. Die Verteilung der Wärmestromdichte wurde mithilfe einer Energiebilanz für jedes Pixelelement der Heizfolie berechnet. Dabei wurde die Wärmespeicherung im Pixelelement durch die Temperaturänderung über die Zeit, die Wärmeleitung zu benachbarten Pixelelementen und die volumetrische Wärmequelle durch den Stromdurchfluss miteinbezogen. Bei der Betrachtung der Wärmestromdichtenverteilung zeigte sich ein charakteristisches ringförmiges Maximum, dessen Ursache die hohen Verdampfungsraten in der Nähe der Drei-Phasen-Kontaktlinie am Blasenfuß sind. Der Ring umschließt ein Gebiet, innerhalb dessen praktisch keine Wärme an das Fluid übertragen wird. In dieser Region des adsorbierten, nicht verdampfenden Flüssigkeitsfilms wird Wärme nur konvektiv an den Dampf innerhalb der Blase übertragen, was die geringe Wärmestromdichte hier erklärt. Die Wärmestromdichte in der Region außerhalb des Maximum-Rings wird durch Konvektion und Wärmeleitung an die Flüssigkeit bestimmt und vom beobachteten Siedeprozess praktisch nicht beeinflusst. Sie liegt im Bereich der, durch die elektrische Heizleistung erzeugten, Wärmestromdichte. Die Wärmeströme in den drei Regionen des charakteristischen Wärmestromdichten-Fußabdrucks einer Blase (innerhalb und außerhalb des Rings, sowie das ringförmige Maximum selbst) wurden zusammen mit dem latenten Wärmestrom herangezogen, um die Gewichtung verschiedener Wärmestrompfade während eines Blasenzyklus zu evaluieren. Die Ergebnisse der Evaluierung wurden mit den Ergebnissen von numerischen Simulationen verglichen und sehr gute qualitative, aber auch gute quantitative Übereinstimmung gefunden.
Die Wirkung des elektrischen Feldes auf den Siedeprozess wurde untersucht. Nach Aktivierung des Feldes in der Schwerelosigkeit wurde die an der Heizfolie haftende Dampfblase durch das Zentrum der Elektrode gezogen und dadurch abgelöst. Die dielektrophoretische Kraft auf die anhaftenden Blasen wird durch die Elongation der sonst sphärischen Blasenform ausgedrückt. Bei aktiviertem Feld konnte ein zuverlässiger Siedeprozess auch in Schwerelosigkeit etabliert werden.
Ein Ausblick auf weiterführende Forschung beinhaltet die Vorstellung des Siedeexperiments RUBI (Reference mUltiscale Boiling Investigation), das im Fluid Science Laboratory an Bord der Internationalen Raumstation durchgeführt werden soll. RUBI vereint die Forschungsinteressen des ESA Topical Teams „Boiling and Multiphase Flow". Die Messmethodik des RUBI Experiments, das sich in der Entwicklung bei Astrium befindet, ist mit der Edelstahl-Heizfolie, Infrarot-Thermographie, Hochgeschwindigkeits-Blasenobservation und dem elektrischen Feld sehr stark an das vorgestellte Parabelflugexperiment angelehnt. Allerdings sollen bei RUBI zusätzlich ein Mikro-

Thermoelement-Rack und ein Flüssigkeitskreislauf zur Erzeugung einer Scherströmung zum Einsatz kommen.
Weiterhin wurde die Messmethodik (Edelstahl-Heizfolie, hoch auflösende Infrarot-Thermographie und Hochgeschwindigkeits-Fotographie) zur Untersuchung von Strömungssieden in Minikanälen herangezogen. Dazu wurde ein Versuchsaufbau entwickelt und in Betrieb genommen, und vielversprechende erste Messergebnisse vorgestellt. Je nach Durchfluss-Rate konnten verschiedene Verdampfungsphänomene, unter anderem auch Kontaktlinienverdampfung identifiziert werden.

Abstract

The subject of the present thesis is the investigation of nucleate boiling in microgravity by measuring the heating wall temperature distribution with high spatial and temporal resolution in conjunction with high speed imaging of the bubble shapes. The measurements were performed not only during the microgravity but also during the hypergravity phase of the parabolic flight manoeuvre and during the transition between these phases. A continual nucleate boiling process of the working fluid n-Perfluorohexane (nPFH) was established at a single artificial nucleation site manufactured in the upper surface of a 20 μm stainless steel foil that was used as a resistance heater. The temperature distribution of the foil was measured via infrared thermography at a frame rate of 1000 Hz and a spatial resolution of 30 μm/pixel. Synchronized to the infrared camera a black and white high speed camera was used for bubble shape imaging.

The dependency of departure diameter and bubble frequency on gravity was evaluated and new correlations for both the departure diameter and the bubble frequency were proposed.

From an unsteady energy balance applied at each pixel of the successive temperature images the local heat flux to the fluid was calculated. The evaluation of the local heat flux distribution revealed a characteristic ring-shaped peak. This characteristic heat flux imprint was used to quantitatively investigate the heat flows through the various paths of the single bubble subsystem. Additionally, the evolution of the global temperature and heat flux values obtained by spatial averaging over the field of view was studied.

As an additional stimulus a washer-shaped electrode was placed above the heating foil charged with up to 10 kV. The effect of the electric field on the boiling process was investigated in order to evaluate the possible replacement of buoyancy and ensure a reliable bubble detachment mechanism in microgravity.

Table of Contents

Nomenclature

Roman Letters

A	Surface area	m^2
a	Thermal diffusivity	m^2/s
B,b	Width	m
Bo	Bond number	
c,c_p	Specific heat capacity	$J/(kg \cdot K)$
d	Diameter	m
F	Force	N
f	Frequency	s^{-1}
f_k	Condensation coefficient	
g	Gravitational acceleration (z-axis)	m/s^2
g_e	Earth gravity	$9.81\,m/s^2$
H	Dispersion/Hamaker constant	J
h	Height	m
h_g	Gaussian filter weighting	
I	Current	A
Ja	Jacob number	
K	Curvature	m^{-1}
L	Length	m
M	Mass	kg
$\overline{M}$	Molar mass	kg/kmol
$\dot{M}$	Mass flow	kg/s
m	Exponent	
P	Power	W
p	Pressure	Pa
Q	Heat	J
$\dot{Q}$	Heat flow	W
$\dot{q}$	Heat flux	W/m^2
R_g	Gas constant	$J/(kg \cdot K)$
R_{int}	Interfacial thermal resistance	$(m^2 \cdot K)/W$
r	Radius	m
T	Temperature	K
t	Temperature	°C
U	Voltage	V
V	Volume	m^3

v	Specific volume	m^3/kg
w	Velocity	m/s
x	Coordinate x-axis	m , pixel
y	Coordinate y-axis	m , pixel
z	Coordinate z-axis	m

Greek Letters

α	Heat transfer coefficient	$W/(m^2 \cdot K)$
α_t	Temperature coefficient of resistivity	K^{-1}
Δh_v	Vaporization enthalpy	J/kg
δ	Thickness	m
ε	Emissivity	
ε	Dielectric constant	$C^2/(Nm^2)$
η	Dynamic viscosity	$kg/(m \cdot s)$
θ	Contact angle	
λ	Thermal conductivity	$W/(m \cdot K)$
ν	Kinematic viscosity	m^2/s
ξ	Radial coordinate	m
ρ	Density	kg/m^3
ρ_{20}	Electrical resistivity at 20 °C	$\Omega \cdot mm^2/m$
σ	Surface tension	N/m
σ_S	Stefan-Boltzmann-Constant	$5.6704e^{-8}\ W \cdot m^{-2} \cdot K^{-4}$
σ_{std}	Standard deviation	
τ	Time	s

Subscripts

a	Outer
b, bub	Bubble
bubfoot	Bubble foot
B	Buoyancy
c	Critical
CL	Contact line
cap	Capillary
cav	Cavity
cond	Conduction
cross	Cross section
D	Bubble departure
DEP	Dielectrophoretic
ef	Electric field
el	Electrical

eq	Equilibrium
fc	Free charge
fluid	Fluid
growth	Growth time
hf	Heating foil
hs	High-speed greyscale
i	Index
i	Inner
int	Interface
ir	Infrared
l	Liquid
loc	Local
m_av	Mean averaged
max	Maximum
mic	Micro region
min	Minimum
pix	Pixel
sat	Saturation
sp_av	Spatial averaged
store	Storage
t	Thermal layer
τ_av	Temporal averaged
v	Vapour
vol	Volumetric
w	Wall
wait	Waiting time
x,y	Coordinates
σ	Surface tension
∞	Far field

Abbreviations

CCD	Charged-coupled Device
CEV	Centre d'Essais en Vol (French Flight Test Centre)
CHF	Critical Heat Flux
CNES	Centre National d'Études Spatiales (French Space Agency)
DLR	Deutsches Zentrum für Luft- und Raumfahrt (German Space Agency)
ESA	European Space Agency
FIB	Focused Ion Beam
FOV	Field of View
IR	Infrared
ISS	International Space Station

IUSTI	Institute Universitaire des Systèmes Thermiques Industriels, Marseille
LWIR	Long Wavelength Infrared
MTC	Micro Thermocouple
NETD	Noise Equivalent Temperature Difference
ONB	Onset of Nucleate Boiling
PFC	Parabolic Flight Campaign
RUBI	Reference mUltiscale Boiling Investigation
TC	Thermocouple
TLC	Thermochromic Liquid Crystal
TTD	Institute of Technical Thermodynamics, Technische Universität Darmstadt

1. Introduction

Whenever people asked me what I am doing at University I always give the question back and counter if they have ever watched the little vapour bubbles forming at the bottom of the cooking pot before inserting the pasta. Surely they have because everybody has. The use of boiling processes is almost as old as mankind and since its “discovery” it has touched the daily life of nearly every human being.
Anyway, it is doubtful if cooking pasta will ever benefit from the development of numerical models and enhanced surface structures. Nevertheless, the reason for the strong efforts in boiling research is the tremendous significance of boiling in industry. Some examples for application are steam generation in power plants and nuclear reactors, steam engines widely used in the beginning of the last century, air conditioners and refrigerators, electronic cooling and the chemical industry. However, due to the dynamic nature of a boiling process and the numerous influencing parameters the fundamental understanding and a closed theoretical description of nucleate boiling is still to be accomplished.

1.1. A Brief Introduction to Nucleate Boiling

Nucleate boiling is a two-phase heat transfer process. Small imperfections and cavities existing in every technical surface act as nucleation sites. Gas or vapour is trapped inside the cavities forming a bubble embryo generally with a highly curved interface. Evaporation occurs at the embryo’s interface as the local temperature exceeds the saturation temperature corresponding to the pressure inside the embryo. Due to its interfacial curvature, the internal pressure is higher than the pressure of the surrounding liquid. Hence, a superheat over the liquid saturation temperature is needed to cause evaporation at the embryo’s interface, i.e. to activate the nucleation site. The required activation superheat is dependent on the interfacial curvature that is among others a function of the cavity geometry and size. Due to the statistical distribution of cavity sizes the number of active nucleation sites is a function of the wall superheat.
As soon as a nucleation site becomes active the periodic nucleation, growth and detachment of vapour bubbles can be observed at this spot. With the wall superheat the active nucleation site density increases and neighbouring sites begin to influence each other, bubble coalescences become visible.
However, large heat fluxes can be transferred during nucleate boiling at comparatively small wall superheats. This fact makes the process so interesting for industrial applications. Although a significant part of the heat is transferred by evaporation, the enhancement of the heat transfer coefficient is also induced by strong liquid motion caused by the bubbles and further small scale effects like transient conduction. At a certain heat flux the evaporation rate is so high that a vapour film is formed at the wall preventing its re-wetting, the wall is dried-out. The insulating nature of the vapour film leads to a severe and sudden increase in the wall temperature that often causes damage to or even destruction of the device. The corresponding heat flux at which this happens is referred to as critical heat flux.

For the design of a boiling heat transfer system not only calculation methods for the heat transfer coefficient are important in order to predict the system performance but also the determination of the critical heat flux that defines the heat transfer limit for safety reasons. The available mathematical tools are still based on empirical correlations and large uncertainties have to be taken into account.

1.2. Nucleate Boiling Research in Microgravity

Generally, boiling investigations in reduced gravitational conditions are triggered by two reasons:

1. Buoyancy is a dominant mechanism in nucleate boiling. It appears in most empirical correlations, for instance in the bubble departure diameter equations. Furthermore, vapour buoyancy and natural convection often superpose or even mask effects and phenomena that are therefore hardly observable in normal earth gravity. Bubble departure for example could be caused by buoyancy but also by inertial forces dependent on boundary conditions like wall superheat. Thermocapillary convection due to a surface tension gradient is commonly less pronounced than natural convection and restricted to a small influencing area in the vicinity of the interface. Nevertheless, it could also have a significant effect on the boiling mechanism in earth gravity. These are only two examples of a number of superposed and masked phenomena. In order to investigate these phenomena microgravity and also variable gravity are experimental tools that allow the separation and quantification of gravity-dependent and gravity-independent effects. Furthermore, reduced gravity leads to a decrease of the bubble frequency and an increase of the bubble departure diameter. The slower boiling behaviour at a larger length scale leads to a resolution enhancement of the measurement techniques allowing a detailed insight in the otherwise highly dynamic process. Hence, microgravity is used to gain a better understanding for the fundamentals of nucleate boiling like it is done in the present thesis.

2. Nucleate boiling is a high performance heat transfer process. It is therefore very interesting for space applications where every heat source (i.e. all electronics) has to be cooled separately due to the lack of natural convection. Additionally, high demands concerning mass and volume are existing. Since buoyancy is such a dominant mechanism its absence leads to a significant alteration in the behaviour of boiling but the knowledge about and predictability of boiling processes in weightlessness is a precondition for its application in spacecraft thermal control. Furthermore, knowing how boiling behaves in weightlessness is also a safety issue. It may occur at a hot spot at the inner wall of a liquid vessel that is created by e.g. solar radiation or a system failure. Dry-out at this hot spot or a pressure increase due to evaporation could lead to the damage of the system. Hence, additional to the contribution of microgravity experimentation to fundamental research it has a practical and application orientated objective for spacecraft engineering.

Investigations of nucleate boiling processes in reduced gravity were already performed in the 1950s and 1960s [106]. In this era drop towers have mainly being used to achieve microgravity conditions. Up to now scientists from all over the world have used almost all available microgravity platforms like drop towers, parabolic flights, sounding rockets, satellites, and the space shuttle to perform boiling experiments. Two experiments for the International Space Station (RUBI and BXF) are currently in preparation in Europe and in the USA.

1.3. Problem Definition and Objectives

Since boiling is such a complex and dynamic process, its fundamental understanding is hardly achievable by looking at the fully developed boiling process as a whole. In contrary, several effects may only be revealed by focusing the investigation on the elementary event, which is the bubble ebullition cycle or even more basic, the single stationary vapour bubble. The aim of the present work is to contribute to the fundamental understanding of the various thermodynamic phenomena that are involved in nucleate boiling and their interactions.

It is focused on the experimental measurement of the heat flux and temperature distribution of the heated wall with high spatial and temporal resolution. This allows investigating the mechanisms of heat transfer to the fluid and the influence of bubble nucleation, growth, detachment and rising processes on the local heat flux. A key question is how evaporation, natural convection, bubble induced convection and transient conduction contribute to the overall heat transfer. Especially the role of evaporation at the three phase contact line is of great interest since numerical and theoretical models predict a significant portion of the latent heat transferred through this tiny part of the bubble. The reduction of gravity is a method to strongly enhance the resolution of the measurement techniques by slowing down the boiling process.

A second focus is the investigation of the gravity influence on the boiling process. Empirical correlations for nucleate boiling bubble dynamics generally contain the earth gravity as a constant value mostly to include the dimensionless Bond number Bo. Since gravity is not a variable parameter in ground experiments not much care has been taken to properly implement it into the correlations. Boiling investigations in variable or absent gravity enhances the understanding of the role of buoyancy forces, inertial forces and the bubble detachment mechanisms.

2. State of the Art

The purpose of this chapter is to address the phenomena and their current research status that are relevant for this thesis. It is not intended to provide an extensive overview on every aspect of nucleate boiling.
The chapter is divided in five sections. The first part deals with fundamental aspects at the liquid vapour interface, near the contact line and with investigations of local heat flux and temperature distributions at single vapour bubbles. The second part is devoted to boiling in microgravity which is a special aspect in this thesis. In the third section some of the most common empirical correlations for departure diameter and bubble frequency are presented and the role of gravity in these correlations is evaluated. Boiling in the presence of an electric field is the topic of the fourth section. Here, theoretical aspects are briefly introduced and already conducted experiments are described. In the last section of this chapter two numerical models are presented that are currently in development at the Institute of Technical Thermodynamics (TTD).

2.1. Fundamental Aspects

2.1.1. Nucleate Boiling Heat Transfer

The fundamental characteristics of a boiling process can be most clearly explained when looking at a typical boiling curve (see Figure 2.1) as it was first measured and published by Nukiyama [88]. Increasing the heat flux at the bottom surface of a vessel, filled with a liquid, leads at first to an increase in the wall superheat while the heat is still transferred by natural convection. At a certain wall superheat the onset of nucleate boiling (ONB) occurs and the wall temperature suddenly decreases. This overshoot at ONB is due to the initial activation of nucleation sites. Depending on various system properties it is more or less pronounced. In the following regime of nucleate boiling the wall temperature increases only slightly with the heat flux indicating the efficiency of boiling heat transfer. At the critical heat flux (CHF) vapour is insulating the heating surface causing a sudden, steep increase in the wall temperature to point B. In industrial applications the CHF is of immense importance since it can cause severe damage to the system. If the system is controlled by the heat flux which is the case in most applications the Leidenfrost-Point can only be reached by decreasing the heat flux starting from point B. A further decrease of the heat flux from the Leidenfrost Point leads to a transition to the nucleate boiling regime. If the temperature of the heating surface can be controlled (or its heat capacity and thermal conductivity is large enough that a constant temperature could be assumed) the whole curve can be characterized by increasing the wall superheat. The Leidenfrost-Point indicates the beginning of stable film boiling where a vapour cushion prevents re-wetting of the surface. This work only deals with nucleate boiling well below the CHF, near point A.
In almost a century of nucleate boiling research numerous correlations for the heat transfer were proposed. These correlations were only valid for a very limited range of parameters they were developed for. Currently, no correlation includes the governing physical phenomena in a

comprehensive way [117]. Nevertheless, due to the lack of practically applicable numerical models industry has to rely on these correlations. Still, expensive experimental validations of the heat transfer performance of the engineered devices are necessary. A good overview on nucleate boiling heat transfer correlations can be found for example in [9], [33] and [56].

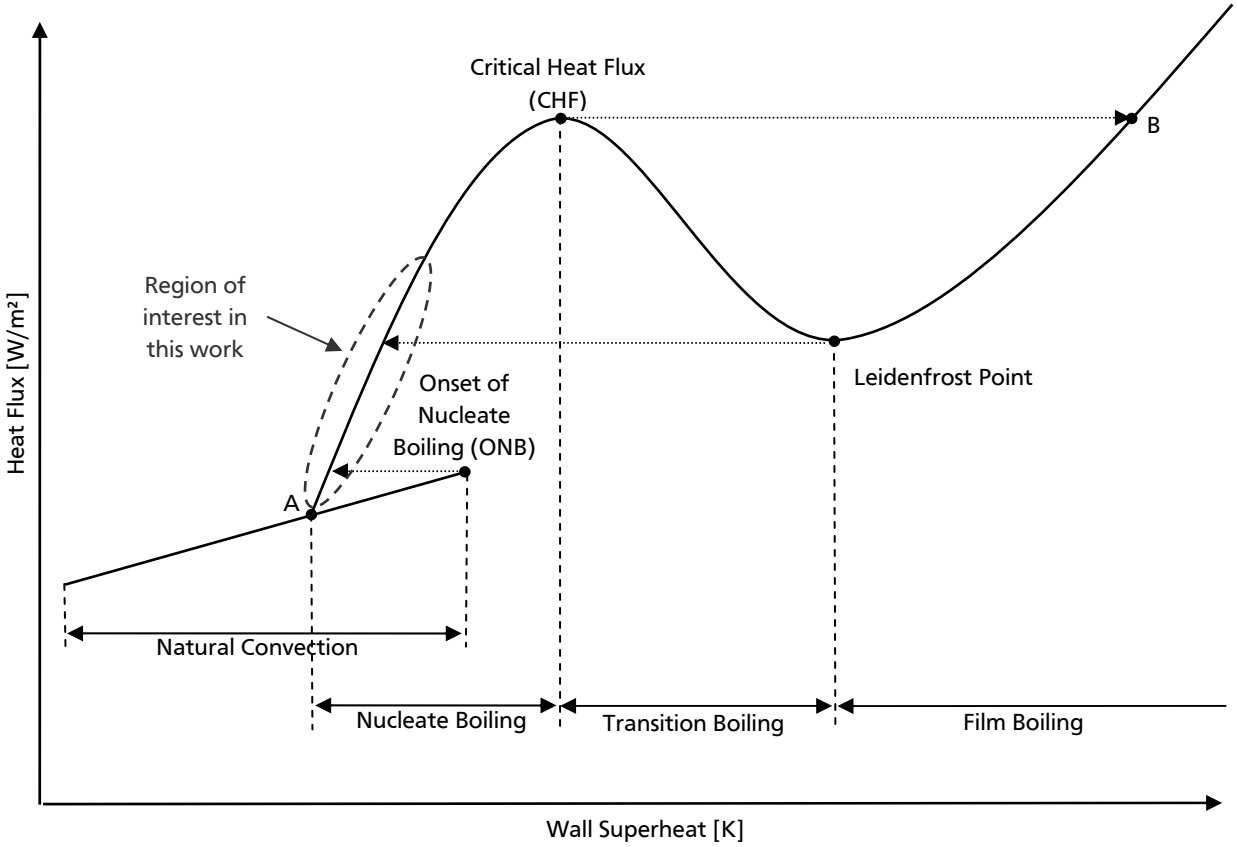

Figure 2.1: Typical boiling curve as published by Nukiyama

2.1.2. Heat Transfer Mechanisms

Generally, in nucleate boiling heat is transferred from the heated surface to the fluid by three mechanisms [117]:

1. Convective heat transfer including natural convection induced by gravity, forced convection induced by bubble motion and thermocapillary convection.
2. Transient heat conduction: The term “transient conduction” in pool boiling was firstly introduced by Mikic and Rohsenow [78] and related to the re-establishment of the thermal boundary layer after bubble detachment. Heat is transferred to the bulk liquid that replaces the hot liquid at the surface which was pumped away by the bubble. This mechanism was also described by other authors (e.g. Forster and Greif [28], Han and Griffith [41], Haider and Webb [38]) but no clear distinction between forced convection induced by bubble motion and transient conduction was made. Defining a single bubble subsystem, Forster and Greif [28] considered the area influenced by transient conduction to be twice the bubble diameter.
3. Latent heat transfer composed of contact line evaporation and evaporation/condensation at the bubble hull.

Unlike to the film boiling regime, radiation heat transfer can be neglected in nucleate boiling. Some early boiling models (e.g. Jakob and Linke [51], Gunther and Kreith [37], Rhosenow [98], Levy [73], Forster and Zuber [29], a summary and brief description is provided by Zell [134]) considered only forced convective heat transfer from the heated surface to the bulk liquid induced by bubble motion as the dominant heat transfer mechanism. Latent heat transfer is neglected in these models and the transient conduction concept is included in the forced convection modelling.
An attempt to quantify the heat transfer mechanisms was performed by Judd and Hwang [53] in the 1970s based on their interferometry and high-speed imaging experiments. They distinguished three mechanisms: microlayer evaporation, natural convection and boiling induced convection. Microlayer evaporation is a substantial feature of their model. They attributed up to one third of the overall heat flux in their experiments to microlayer evaporation.
Ammermann et al. [1] investigated experimentally the contribution of each mechanism to the overall heat transfer for boiling at a heated wire. They found that evaporation is the dominant mechanism throughout the boiling curve. Only at low heat fluxes natural convection dominates.
A similar study was performed numerically by Mann and Stephan [76] for boiling at horizontal tubes. The outcome of that study was that convective effects play a significant role in the heat transfer due to bubbles sliding on the tube surface.
Yaddanpudi and Kim [133], Demiray and Kim [16] as well as Myers et al. [86] used a microheater array with 100 μm resolution to study heat transfer mechanisms during nucleate boiling of FC-72 at atmospheric pressure. They concluded transient conduction/microconvection is the dominant heat transfer mechanism. Most of the latent heat of the bubble was transferred through the superheated liquid thermal layer, only 23% was transferred by contact line/microlayer evaporation.
From their local measurement of heating wall temperatures and the corresponding numerical evaluation of the local heat flux to the fluid Moghaddam and Kiger [80],[81] made an attempt to quantify the contributions of the mechanism. They found that microlayer evaporation contributes from 16.3% to 28.8%, transient conduction from 32.1% to 45.3% and convection from 25.8% to 51.6% to the overall heat flux. However, their definition of the transient conduction heat transfer also includes evaporation at the receding contact line (growing bubble) while the microlayer evaporation is attributed to the advancing contact line (detaching bubble). It seems their experimental technique does not allow a distinction between the latent heat transfer at the contact line and the heat transferred to colder liquid that is sucked to the wall by the advancing interface.
Dhir et al. [18] used their comprehensive numerical model to calculate bubble dynamics and analyze the heat transfer mechanisms. The model includes evaporation at the contact line based on the concept of Wayner [130], [131]. Their numerical results are in good agreement with experimental results performed on ground and in microgravity when fitting the dynamic contact angle to the experimental observation. Furthermore, they presented the evolution of the total latent heat flow as well as the heat flows due to evaporation at the bubble hull, microlayer evaporation and condensation for a complete bubble ebullition cycle with water as test fluid (see Figure 6.41).
However, the identification and quantification of the heat transfer mechanisms is only possible with high resolution measurement techniques in conjunction with numerical studies and still subject of ongoing investigations. Nevertheless, the outcome of most studies was a contribution of contact line evaporation in the range of 16%-33% of the overall heat transfer. The judgment if this value is significant is often a subjective decision of the corresponding author.

2.1.3. Equilibrium at Liquid-Vapour Interface

Two preconditions have to be fulfilled for a vapour bubble at thermodynamic equilibrium:

1. Thermal equilibrium of the liquid and vapour phases: $T_l = T_v$
2. Mechanical equilibrium across the interface. The Young-Laplace-Equation applied on a spherical bubble yields to:

$$p_v = p_l + \sigma K \tag{1}$$

Incorporating the Gibbs-Thomson- and Clausius-Clapeyron-Equation the curvature K of the bubble interface at thermodynamic equilibrium for a given liquid superheat can be derived:

$$K = \frac{\rho_v \Delta h_v \left(T_{l,eq} - T_{sat}\right)}{\sigma T_{sat}} \tag{2}$$

A detailed derivation can be found in [2] and [9].
Evaporation takes place at the part of the liquid vapour interface of a bubble where the liquid temperature T_l is superheated with respect to the thermodynamic equilibrium temperature $T_{l,eq}$. While in superheated or even saturated boiling evaporation may take place at the whole interface during the bubble growth time, for subcooled boiling condensation occurs at the bubble cap when it leaves the superheated thermal layer and enters subcooled regions.

2.1.4. Heat Transfer at the Three-Phase Contact Line

The part of the vapour bubble where the liquid vapour interface approaches the heating wall near the three phase contact line is of great interest for the research community. Due to the thin liquid film in this area a high amount of the overall latent heat of the bubble passes through that region. The corresponding temperature fluctuations of the heated wall were firstly measured by Moore and Mesler [83] and attributed to the evaporation of a microlayer at the contact line of a bubble.
Evaporation at the three-phase contact line is not only important for nucleate boiling but also for all two-phase heat transfer systems. Brandt [7] investigated heat and mass transfer in high performance capillary structures for heat pipes in space applications. He found that the heat transfer coefficient in the evaporator is directly linked to the length of the three-phase contact line. His findings were supported by experimentally comparing two evaporator structures that differ only in the length of the contact line in a flat heat pipe in space[1] [101]. The role of evaporation at the three-phase contact line in spray cooling was investigated by Sodtke [114]. He experimentally showed the enhancement of the heat transfer coefficient at the rupture of the liquid film on the target due to the occurrence of three-phase contact lines. The thermal performance increases with the length of the contact line as already observed in the heat pipe experiment. The performance could further be significantly enlarged by applying a micro structure on the spray target surface which main function is to enhance the contact line length [110]. In order to locally investigate heat and mass transfer at the contact line, Höhmann [45], [46] developed a high resolution measurement technique based on TLCs and applied it at a single evaporating meniscus. He evidenced a local temperature drop due to the high cooling rate induced by contact line evaporation. His work is supported by the experiments of Buffone and Sefiane [8] and by the recently published study of Garimella et al. [17]. In their experiments nearly 70% of the overall heat flux passes through a region next to the contact line with a width of 50 μm. Panchamgam et al. [92] studied heat and mass transfer in an evaporating moving extended meniscus supporting the concept of thin film evaporation of Wayner [130],[131].

[1] FOTON M2, experiment DAGOBERT

The baseline of this concept is the transition of the interface into an adsorbed layer in the vicinity of the wall. Intermolecular forces are so strong within that layer that they prevent its evaporation. Based on this concept a mathematical model was developed by Stephan [120] for the heat transfer in the microregion. The microregion is defined as the part of the interface where its slope changes from zero at the adsorbed film to the macroscopic contact angle θ. Here, the curvature of the interface has a strong local maximum and the adhesion pressure is not yet negligible. Therefore, it is very important to exactly implement the physical phenomena.
The microregion model is illustrated in Figure 2.2. From a non-evaporating adsorbed layer underneath the bubble the interface slope changes steadily to the macroscopic contact angle with the curvature of the bubble hull. This change happens at a length scale of about 1 μm.
Although the model was initially developed for the computation of the heat transfer in capillary grooves of heat pipes it could also be applied in boiling ([39], [116]). Furthermore, it was modified by Kern and Stephan [61] for boiling of binary mixtures.

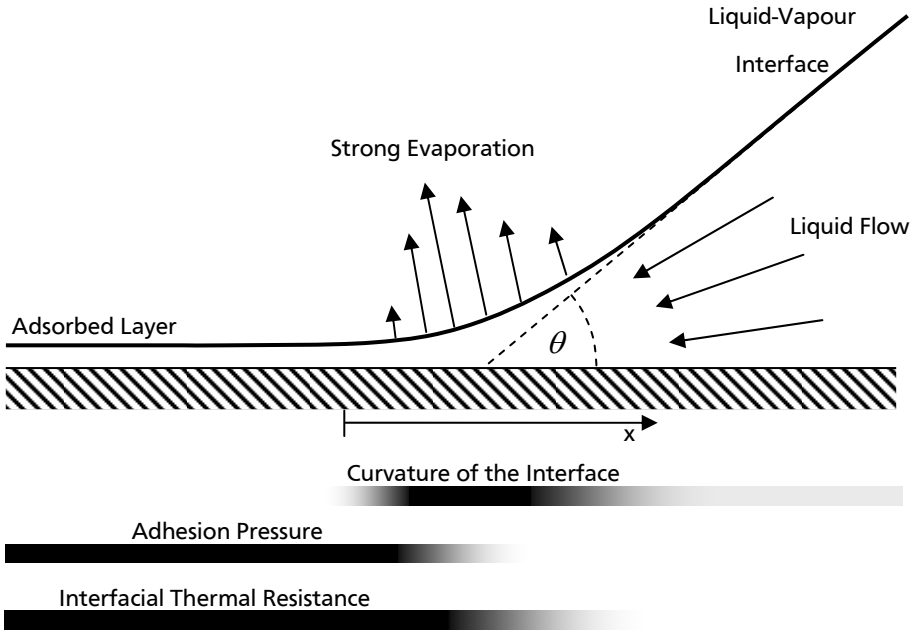

Figure 2.2: Influence of interfacial curvature, adhesion pressure and interfacial thermal resistance in the microregion

The microregion model is, moreover, based on the following assumptions and simplifications as e.g. summarized in [114]:

- Heat is transferred through the liquid film only by heat conduction perpendicular to the heating wall. Convection is negligible.
- The wall temperature $T_{w,mic}$ is constant within the micro region.
- The condensation coefficient is determined assuming ideal conditions, i.e. $f_k = 1$.
- The simplifications of a Stokes flow are applied. The influence of gravity is neglected.
- Fluid properties are constant. Marangoni convection does not occur. The liquid is incompressible and viscosity is equivalent to that of macroscopic flows.
- Thermodynamic equilibrium is assumed at the interface. Pressure differences in the vapour phase and due to vapour inertia are neglected.

Hence, the equation of the heat flux through the liquid layer yields to:

$$\dot{q} = \frac{\lambda_l}{\delta_l}\left(T_{w,mic} - T_{\mathrm{int}}\right) \tag{3}$$

Additionally, the heat flux has to overcome the thermal resistance of the interface:

$$\dot{q} = \frac{1}{R_{\mathrm{int}}}\left(T_{\mathrm{int}} - T_{\mathrm{int},eq}\right) \tag{4}$$

where $T_{\mathrm{int},eq}$ is the interface temperature at thermodynamic equilibrium:

$$T_{\mathrm{int},eq} = T_{sat}\left(1 + \frac{p_{cap}}{\rho_l \Delta h_v}\right) \tag{5}$$

Adhesion pressure can not be neglected at the given liquid film thickness. It modifies the capillary pressure p_{cap}:

$$p_{cap} = \sigma K + \frac{H}{\delta_l^{\,3}} \tag{6}$$

where H is the dispersion constant, also known as Hamaker constant. Theoretical and experimental approaches for the determination of H can be found in e.g. [14] and [15].
Stephan [120] expressed the interfacial thermal resistance:

$$R_{\mathrm{int}} = \frac{T_{sat}\sqrt{2\pi R_g T_{sat}}}{\rho_v \Delta h_v^{\,2}}\left(\frac{2 - f_k}{2 f_k}\right) \tag{7}$$

From geometrical examinations the curvature K of the interface can be expressed by the differential equation:

$$K = \frac{\delta_l''}{\left(1 + \delta_l'^{\,2}\right)^{3/2}} + \frac{1}{\xi} \cdot \frac{\delta_l'}{\left(1 + \delta_l'^{\,2}\right)^{1/2}} \tag{8}$$

where δ' is the first, δ'' the second derivative of the liquid film thickness δ and ξ the radial coordinate of the axis symmetric system of the bubble computational domain.
The incorporation of the conservation equations for mass, momentum and energy leads to a system of first order differential equations that are commonly solved using a Runge-Kutta method [67].
The development of the heat flux $\dot{q}$ and the liquid film thickness δ is shown in Figure 2.3. The calculation was performed by the author of the present work using MALAB scripts provided by Kunkelmann [68]. In the computed case the working fluid was FC-72 which has the same properties as pure n-Perfluorohexane (nPFH) at $T_{sat} = 42.4\,°\mathrm{C}$ and $T_{w,mic} - T_{sat} = 30\,\mathrm{K}$. Additionally, the apparent macroscopic contact angle for the static case could be derived from the calculation to $\theta = 46.8°$ for the computed case. This contact angle is not equal to the contact angle of an

isothermal fluid system which can be determined from the surface energies of the vapour, liquid and solid phase. Instead, beside the fluid properties, it is only dependent on the wall superheat.

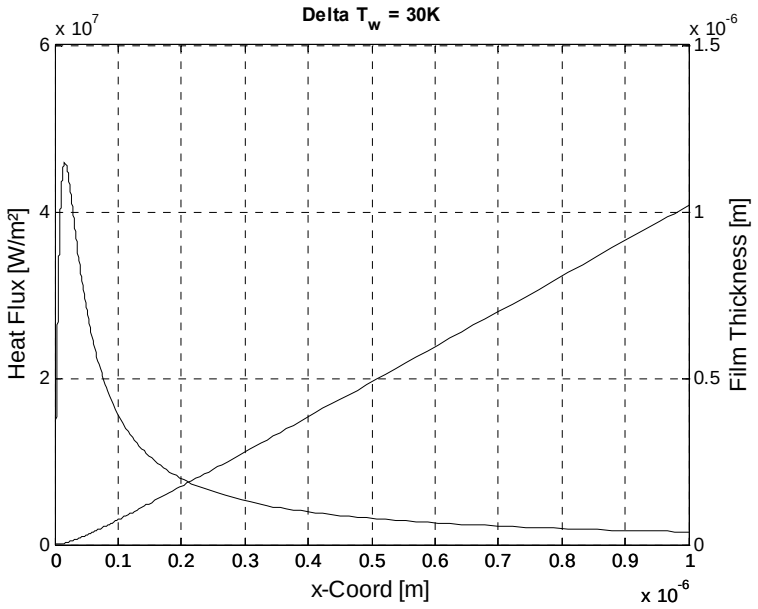

Figure 2.3: Heat flux and film thickness versus the radial coordinate x in the micro region for FC-72/nPFH at 42.4 °C saturation temperature and 30 K wall superheat

2.1.5. Bubble Nucleation

The thermodynamic equilibrium is of high significance when evaluating bubble nucleation on a heating surface. Typically, in boiling processes the bubbles are formed at small cavities in the heating surface, so called nucleation sites. On the one hand these cavities could be the result of normal machining procedures of the surface and are described by the surface roughness properties. A detailed analysis of the influence of the surface roughness was performed by Luke [74]. On the other hand a systematic structuring of the surface e.g. by micro machining techniques could create artificial cavities and thereby significantly enhance the heat transfer performance of the boiling process. The boiling on micro pin finned tubes was investigated by Wondra and Stephan [132]. They found that the superheat necessary for boiling incipience could be significantly reduced and the heat transfer coefficients could be improved by a factor of 7.1 compared to a smooth surface. Nevertheless, the mechanisms on which bubble nucleation is based on are the same for both “natural” surfaces and structured surfaces. However, nucleation site density is a crucial parameter for both characterization and enhancement of the boiling process but its determination is challenging in most cases.

Before a bubble grows at a nucleation site a small gas or vapour embryo is entrapped inside the cavity. To activate a nucleation site the superheat at the liquid-vapour interface of the embryo has to exceed the value for the thermodynamic equilibrium. As Equation (2) shows the equilibrium temperature is dependent on the radius of the embryo’s interface which, moreover, depends on the geometrical properties of the cavity, the contact angle and the filling state of the cavity. A theoretical model of gas entrapment during the filling process was published by Bankoff [3]. In the model a three phase contact line (the liquid filling front) moves over a cone-shaped cavity. The conditions of gas entrapment depend on the cone angle and the advancing contact angle. The gas

entrapment theory predicts the superheat needed for the initial activation of the nucleation site during the onset of nucleate boiling (ONB).
However, after initial activation the interfacial curvature of the vapour rest remaining in the cavity after bubble departure determines the superheat needed for the next bubble growth which is generally much lower than the initial superheat. This explains the hysteresis effect at ONB. The interaction between the detaching bubble and the nucleation site thereby influences the waiting time between bubble detachment and successive nucleation [126]. Hence, the performance of the boiling process is not only influenced by the nucleation site density but it also depends on the cavities geometrical properties.
In order to predict the size of active cavities at a certain wall superheat the approach of Hsu [47] could be applied as it is also described in [9]. The approach estimates the range of active cavity mouth radii at a certain wall superheat assuming conical cavity geometry. At the minimum mouth radius the bubble embryo is so small that the required equilibrium superheat is just sufficient to cause the bubble grow. At the maximum mouth radius the superheat at a part of the embryo's interface is negative. Condensation counteracts the evaporation. Therefore, the cavity is not regarded as active. The equation for the calculation of the minimum mouth radius $r_{cav,\min}$ and the maximum mouth radius $r_{c,\max}$ is:

$$\begin{Bmatrix} r_{cav,\max} \\ r_{cav,\min} \end{Bmatrix} = \frac{\delta_t}{4}\left[1 - \frac{T_{sat}-T_\infty}{T_w-T_\infty}\begin{Bmatrix}+\\-\end{Bmatrix}\sqrt{\left(1-\frac{T_{sat}-T_\infty}{T_w-T_\infty}\right)^2 - \frac{12.8\sigma T_{sat}}{\rho_v \Delta h_v \delta_t (T_w-T_\infty)}}\right] \tag{9}$$

where δ_t is the thermal layer thickness. It is approximated according to [9]:

$$\delta_t = \frac{\lambda_l (T_w - T_\infty)}{\dot{q}} \tag{10}$$

2.2. Measurement of local heat transfer phenomena

Fully developed pool boiling is a highly complex and dynamic process in which numerous physical phenomena on length scales ranging from sub-micro (e.g. adsorbed layer thickness $\sim 10^{-9}$ m) to macro (heater sizes $\sim 10^{-1}$ m) are involved in. In order to fundamentally understand these phenomena and their interaction the core of nucleate boiling which is the ebullition cycle is often investigated separately. The ebullition cycle is the steady cyclic growth and release of vapour bubbles at a single nucleation site [9]. This approach is nearly as old as the boiling research itself. Fritz [30] already studied the detachment of single bubbles in 1935, proposing his well known and still often used correlation for the departure volume.
The dynamic nature of boiling induces the need of high performance measurement techniques. High-speed imaging of the bubbles in a boiling process is today a common and mature technique. It is available in most laboratories and will not be reviewed here.
To investigate local temperature and heat flux distributions at the heating wall underneath single vapour bubbles measurement systems are necessary that provide high spatial and temporal resolution and accuracy. In general, these techniques can be split in two categories: micro-sensors arrays and thermography systems. Kenning et al. [58], [59], [60] used thermochromic liquid crystals (TLCs) to study the temperature field at the backside of a 130 μm thick stainless steel plate. Their thermography system worked with a frame rate of 200 Hz. They studied the temperature

imprint caused by the growth and detachment of a single vapour bubble by focusing on a single nucleation site during fully developed pool boiling. The local temperature drop due to high evaporation rates at the contact line could not be resolved but large temperature fluctuations at the nucleation sites were reported. They concluded that constant wall temperature boundary conditions are not applicable in nucleate boiling simulations. Furthermore, they expressed their concerns about the influence of the thin heating wall on the boiling process. The thin wall minimizes lateral heat conduction and, therefore, maximizes the local temperature variation what may be atypical in real boiling situations.

An enhanced thermography technique based on the system of Kenning et al. was developed by Höhmann [46] using un-encapsulated TLCs. This technique was implemented in an experiment by the author of this work to investigate the local temperature distribution at stationary vapour bubbles in microgravity, see Chapter 3.3.1. The temperature drop at the contact line was measured and compared to numerical simulations [62]. Good qualitative agreement between the experimental and numerical results has been found.

In a further study the author measured the temperature field during the whole ebullition cycle at continual boiling at a single artificial cavity in variable gravity conditions [127], see also Chapter 3.3.2. In that study a high speed thermography technique still including un-encapsulated TLCs was used in conjunction with high speed imaging of the bubble shapes.

In a subsequent study the author improved the temperature measurement system by replacing the TLCs with high speed infrared thermography [102], see Chapter 3.3.3. The same experimental technique was used by Wagner [128]. He investigated local temperature and heat flux distributions at a single nucleation site for boiling with pure fluids and binary mixtures under normal gravitational conditions. The results were qualitatively compared to the numerical model of Fuchs [32] and good agreement was found.

The evaluation of the local heat flux distribution in both experimental studies revealed interesting phenomena which are explicitly described in Chapters 0 and 6. From a cold spot at bubble nucleation a cold ring is formed due to high evaporation rates at the contact line. The temperature of the heated wall inside the bubble foot rises as the wall is insulated by a non-evaporating adsorbed layer and the vapour. This phenomenon could be clearly observed at non-departing bubbles in microgravity. High heat fluxes are observed near the contact line while the heat flux inside the bubble foot is nearly zero.

This observation is a contradiction to the observations of Golobic et al. [34], [35]. They also used high speed IR thermography to measure the temperature field at the backside of a 6 μm platinum foil. They observed the temperature drop caused by strong evaporation near the contact line. By evaluating the local heat flux they found that it is not negligible in the adsorbed layer region. However, it is doubtful if the accuracy of their local heat flux measurement could justify this conclusion.

Theofanous et al. [123], [124] also applied high speed IR thermography to study high dynamic effects near the CHF and during burn-out. They used an LWIR camera (8-12 μm) focused on layer of titanium (140 nm thickness) through a borosilicate glass substrate with a thickness of 130 μm. However, although they used a sapphire substrate for some of their experiments they did not mention how they overcame the very low transmissivity of borosilicate in the LWIR spectrum. Nevertheless, the characteristic ring-shaped temperature imprints are visible in their thermography images.

The group around Kim at University of Maryland studied the local heat flux using a micro heater array with 96 heaters, each 100 μm by 100 μm in size. In their setup each heater is capable of maintaining a constant mean surface temperature. They observed the influence of gravity,

subcooling and heater size on boiling of FC-72 [65], [16]. Furthermore they investigated the heat transfer mechanisms at boiling at single nucleation sites and during bubble coalescence [133], [86]. In a recent study they reported a non-smooth but step-like transition between the boiling regimes in high and low gravity [97].
Moghaddam and Kiger [80], [81] used a micro temperature sensor array around a single nucleation site. They studied the temperature as well as the local heat flux at the distinctive sensors in time. They clearly showed the temperature drop and the heat flux peak when the three phase contact line moves over the sensors. They evaluated the contribution of the microlayer evaporation at the contact line, the transient conduction and micro convection in the vicinity of the bubble to the overall heat transfer. They compared their experimental results to correlations for bubble dynamics and heat transfer coefficients [82].
Moreover, many theoretical, numerical and experimental investigations of single bubble dynamics not regarding the local distributions of temperature and heat flux but regarding global heat and mass transfer to a vapour bubble were performed.

2.3. Boiling in Microgravity

Siegel [106] summarized the first boiling experiments conducted in microgravity in the 1950s and 1960s. Furthermore, he theoretically evaluated the attaching and detaching forces on a vapour bubble regarding their dependency on gravity. The surface tension force and the drag force were included as attaching forces, whereas the buoyancy force, the pressure force and the inertial force as detaching forces. The drag force was found to be negligible. He evaluated the development of the forces in time for a bubble in earth gravity and in low gravity. He stated that if the inertial force that reaches its maximum in an early stage of the bubble growth did not detach the bubble, it plays a minor role in the later detachment process. In that case, the detachment process in mainly governed by buoyancy and surface tension. Hence, the departure diameter depends on $g^{-1/2}$ as it can be derived from the force balance (see Fritz' evaluation [30]). That implies a change of dependency when the detachment is driven by inertial forces as it occurs at higher heat fluxes and wall superheats.
Already in this early work several conclusions were drawn from these short duration experiments. Siegel proposed to support these conclusions by further experiments:

1. *Vapour accumulations tend to linger near the surface and collect new bubbles being formed thereby helping to remove them from the surface.* This point was supported by a number of authors [25], [65], [71], [90], [91], [122].
2. *The dependency of bubble diameter on time during bubble growth is insensitive to gravity as shown by both theory and experiment.*
3. *The diameter of single bubbles at departure depends on* $g^{-1/2}$ *for bubbles that grow slowly. For these bubbles, buoyancy is the force causing bubble departure.* This statement has also been supported by many authors [25]. A similar conclusion was drawn by Ivey [48] concerning bubble frequency in the thermodynamic region. Here the bubble frequency is proportional to the gravity.
4. *For rapidly growing bubbles, departure is governed by inertial forces and the departure size becomes insensitive to gravity.* Referring again to Ivey [48] the bubble frequency is also governed by inertial forces at higher heat fluxes. Together with point (1) this could help to establish a reliable boiling process in weightlessness [122].

5. *The velocity at which detached bubbles rise through the liquid appears from limited data to decrease with gravity as predicted by theory.*

Concerning bubble dynamics in microgravity the contribution of Prof. Straub has to be outlined. He and his co-workers performed a large number of boiling experiments on many available microgravity platforms. Straub summarized the results of his long term research in [122]. He analyzed the detachment process e.g. of a single bubble by surface tension forces when the heat flux is turned off as well as vertical and lateral coalescence phenomena. Also, Marangoni convection around bubbles in subcooled boiling conditions was studied. He concluded that in microgravity bubble detachment is caused by surface tension force and bubble reformation as soon as the superheat energy around the bubble is absorbed. At saturated boiling bubble dynamics are further dominated by vertical and lateral coalescence. Finally, he stated that pool boiling can be maintained in weightlessness and therefore be used in spacecraft thermal control.

Prof. Merte and his co-workers investigated boiling in various gravity environments. They studied the effect of natural convection absence on the onset of boiling of R-113 [27] and described several bubble behaviours. Rapid bubble growth with turbulent interface observed in microgravity was attributed to the energy stored in the larger thermal layer. In conjunction with the thermal layer superheat the enhancement of the interfacial surface area caused by the small scale protuberances resulted in high evaporation rates. Furthermore, they measured boiling curves of R-113 in microgravity during several space shuttle missions [71], [72]. In agreement with the findings of Straub they concluded that stable boiling in microgravity is possible. They achieved to establish a stable process with a large bubble taking in smaller bubbles from the surface similar to the mechanism firstly described by Siegel. The heat transfer coefficient was significantly enhanced in microgravity but CHF is considerably lower in their experiments. They emphasized the role of surface tension in the wetting behaviour of the process and in the detachment of the initial large bubble.

Qiu and Dhir [95] studied single bubble dynamics in microgravity. They defined the equivalent bubble diameter of a bubble as the diameter of a sphere with the same volume. The development of the equivalent diameter as well as the bubble foot diameter versus time is shown for different subcooling levels. In agreement with Siegel [106] and Fritz [30] they found that the departure diameter is dependent on $g^{-1/2}$ for their slow growing bubbles. They concluded that at low gravity, but where g still dominates, buoyancy and surface tension are the forces that govern the detachment process. Acceleration in lateral direction along the heating surface causes smaller detachment diameters than predicted. This is contributed to shear forces at the bubble foot. Although subcooling had a strong impact on the growth rate they found that its influence is negligible on the detachment diameter.

The group around Prof. Kim conducted a large number of boiling experiments mainly on parabolic flights using FC-72 as working fluid. In most of their experiments they used a microheater array to study local temperature and heat flux phenomena (see also Chapter 2.2). They also observed stable boiling in microgravity. In contrast to Merte they could not see any enhancement of the heat transfer coefficient compared to boiling in normal gravity [63]. They observed an enhancement of CHF at higher subcooling and attributed it to the onset of strong thermocapillary convection. The thermocapillary convection decreased the size of the primary large bubble. However, in their experiments the primary bubble did often not detach and was therefore insulating a part of the heater [65]. A contrary effect of thermocapillary convection on CHF was reported by Shatto and Peterson [103]. A reduction of CHF below the prediction was attributed to thermocapillary convection that tends to inhibit the vapour flow away from the surface.

From a recent study the team of Kim [97] derived a gravity threshold at 0.1…0.2g defining a “low-g” and a “high-g” regime. While in the “high-g” regime the bubble dynamics are governed by buoyancy and surface tension in the “low-g” regime bubble departure is not observed. They did not observe the hovering primary bubble fed by smaller secondary bubbles. This absence of the primary bubble, they called it third regime was attributed to the heater size.

2.4. Empirical Correlations

Despite the fact that the development of numerical methods for boiling processes is preceding quickly these methods are not yet applicable in the engineering work. Still, the design of systems incorporating boiling processes relies on available empirical correlations and verification by testing. A large repertory of correlations especially for the heat transfer coefficient and CHF can be found in literature. However, those are only valid in their narrow bandwidth of verified parameters. A good overview is provided by [9] and [33]. For the present work the correlations of the bubble departure diameter and the bubble frequency and the influence of gravity in these correlations, respectively, are interesting.

2.4.1. Departure Diameter Correlations

Numerous correlations for the departure diameter have been published by a number of authors. A good overview on the correlations is given by Carey [9]. Many of these correlations include the Bond number Bo (see eq. (11)). This dimensionless group relates the gravitational forces to the surface tension forces. Sometimes instead of gravity other body forces are used.

$$\mathrm{Bo} = \frac{g(\rho_l - \rho_v)d_D^2}{\sigma} \tag{11}$$

In 1935 Fritz [30] derived the maximum volume of vapour bubbles by balancing the surface tension as the attaching force with the buoyancy as the detaching force, empirically including the contact angle. The well-know Fritz’ correlation, equation (13a) for the departure diameter is a result of his derivation.
Zuber [135] proposed equation (14a) taking into account the superheated thermal layer above the heating surface. Additionally to surface tension and buoyancy forces, Ruckenstein [99] also considered drag forces and proposed equation (15a). Based on Fritz’ correlation Borishanky and Fokin [6] tried also to include dynamic influences of the surrounding liquid, see eq. (17).
A very simple correlation (19a) was developed by Cole and Shulman [11]. Here, the term $0.0208 \cdot \theta$ from Fritz’ correlation is replaced by the term $1000/p$ which is a rough approximation of the physical properties that are included in other correlations. Cole [13] further proposed another simple equation (20a) including the Jakob number Ja. This equation was again improved by Cole and Rohsenow [12] replacing the wall superheat by the critical temperature T_c. Golorin et al. [36] published equation (23) taking into account the dynamic interaction between bubble, liquid and wall as well as the roughness of the heating surface. By correlating a large number of available data Kutateladze and Gogonin [69] developed equation (26a). Jensen and Memmel [52] slightly enhanced the empirical factors after comparing to an enlarged data pool, see eq. (28a).

However, all of the mentioned correlations include gravity but not in the same way. During the development of these correlations gravity had never been a varied parameter and appeared more or less as a constant for all experiments on ground.
Di Marco [23] further summarized the dependencies of gravity on the detachment diameter found by other authors. It can be expressed as (12) as proposed by Straub et al. [121].

$$\frac{d_D}{d_{D,g_e}} = \left(\frac{g}{g_e}\right)^{-m} \tag{12}$$

Including the works of Straub, Qiu et al. [95], Singh and Dhir [107] and Siegel and Keshock [105] the exponent m was determined in the range of 0.25…0.5. Most commonly it was found that $m = 1/2$, which is in agreement with several theoretical models [106], [107].
The relation (12) was used to derive m from the correlations. Here m ranges from $1/6$ to $1/2$. Again, $m = 1/2$ is often found. The reason is the balance between buoyancy and surface tension forces that is often used as a baseline for the correlation development.

Fritz:

$$\mathrm{Bo}^{1/2} = 0.0208 \cdot \theta \qquad m = \frac{1}{2} \tag{13a}$$

$$\text{or } d_D = 0.0208 \cdot \theta \cdot \sqrt{\frac{\sigma}{g(\rho_l - \rho_v)}} \tag{13b}$$

Zuber:

$$\mathrm{Bo}^{1/2} = \left[\frac{\sigma}{g(\rho_l - \rho_v)}\right]^{-1/6} \left[\frac{6\lambda_l (T_w - T_{sat})}{\dot{q}}\right]^{1/3} \qquad m = \frac{1}{3} \tag{14a}$$

$$\text{or } d_D = \left[\frac{\sigma}{g(\rho_l - \rho_v)}\right]^{1/3} \left[\frac{6\lambda_l (T_w - T_{sat})}{\dot{q}}\right]^{1/3} \tag{14b}$$

Ruckenstein:

$$\mathrm{Bo}^{1/2} = \left[\frac{3\pi^2 \rho_l a_l^2 g^{1/2} (\rho_l - \rho_v)^{1/2}}{\sigma^{3/2}}\right]^{1/3} \cdot \mathrm{Ja}^{4/3} \qquad m = \frac{1}{3} \tag{15a}$$

$$\text{or } d_D = \left[\frac{3\pi^2 \rho_l a_l^2}{g^{1/3} (\rho_l - \rho_v)^{1/3}}\right]^{1/3} \cdot \mathrm{Ja}^{4/3} \tag{15b}$$

$$\text{where } \mathrm{Ja} = \frac{\rho_l c_{pl} [T_w - T_{sat}(P_\infty)]}{\rho_v \Delta h_v} \tag{16}$$

Borishanky & Fokin:

$$d_D = -C + d_F \sqrt{\frac{C^2}{d_F^2} + 1} \tag{17}$$

$$\text{where } C = \left(\frac{6}{g}\right)\left(\frac{\rho_l}{\rho_l - \rho_v}\right)\left(\frac{\rho_v}{\rho_l}\right)^{0.4}\left(\frac{\dot{q}}{\Delta h_v \rho_v}\right) \tag{18}$$

and d_F is the diameter obtained from Fritz' correlation (13a)

Cole & Shulman

$$\mathrm{Bo}^{1/2} = \frac{1000}{p} \; (p \text{ in mm} \cdot \mathrm{Hg}) \qquad m = \frac{1}{2} \tag{19a}$$

$$\text{or } d_D = \frac{1000}{p} \sqrt{\frac{\sigma}{g(\rho_l - \rho_v)}} \; (p \text{ in mm} \cdot \mathrm{Hg}) \tag{19b}$$

Cole

$$\mathrm{Bo}^{1/2} = 0.04 \cdot \mathrm{Ja} \quad \text{with Ja from eq. (16)} \qquad m = \frac{1}{2} \tag{20a}$$

$$\text{or } d_D = 0.04 \cdot \mathrm{Ja} \sqrt{\frac{\sigma}{g(\rho_l - \rho_v)}} \quad \text{with Ja from eq. (16)} \tag{20b}$$

Cole & Rohsenow

$$\mathrm{Bo}^{1/2} = C\left(\mathrm{Ja}^*\right)^{5/4} \qquad m = \frac{1}{2} \tag{21a}$$

$$\text{or } d_D = C\left(\mathrm{Ja}^*\right)^{5/4} \sqrt{\frac{\sigma}{g(\rho_l - \rho_v)}} \tag{21b}$$

$$\text{where } \mathrm{Ja}^* = \frac{T_c c_{pl} \rho_l}{\rho_v \Delta h_v} \tag{22}$$

$$C = 1.5 \times 10^{-4} \qquad \text{for water}$$
$$C = 4.65 \times 10^{-4} \qquad \text{for fluids other than water}$$

Golorin et al.

$$d_D = d_1 + d_2 \qquad m > \frac{1}{3} \tag{23}$$

$$d_1 = \frac{1.65 d^* \sigma}{g\left(\rho_l - \rho_v\right)} \text{ with } d^* = 6.0 \times 10^{-3} \text{ mm} \tag{24}$$

$$d_2 = \left[\frac{15.6 \rho_l}{g\left(\rho_l - \rho_v\right)}\right]^{1/3} \left[\frac{\beta_d \lambda_l \left(T_w - T_{sat}\right)}{\Delta h_v \rho_v}\right]^{2/3} \tag{25}$$

$$\beta_d = 6.0 \qquad \text{for water, alcohol and benzene}$$

Kutateladze & Gogonin

$$Bo^{1/2} = 0.25\left(1 + 10^5 K_1\right)^{1/2} \quad \text{for } K_1 < 0.06 \qquad 0.25 < m < 0.5 \tag{26a}$$

$$\text{or } d_D = 0.25 \left[\left(1 + 10^5 K_1\right) \frac{\sigma}{g(\rho_l - \rho_v)}\right]^{1/2} \quad \text{for } K_1 < 0.06 \tag{26b}$$

$$K_1 = \left(\frac{Ja}{\mathrm{Pr}_l}\right) \left\{\left[\frac{g \rho_l \left(\rho_l - \rho_v\right)}{\eta_l^2}\right] \left[\frac{\sigma}{g\left(\rho_l - \rho_v\right)}\right]^{3/2}\right\}^{-1} \tag{27}$$

Jensen & Memmel

$$Bo^{1/2} = 0.19\left(1.8 + 10^5 K_1\right)^{2/3} \text{ with } K_1 \text{ from eq. (28a)} \qquad \frac{1}{6} < m < \frac{1}{2} \tag{28a}$$

$$\text{or } d_D = 0.19\left(1.8 + 10^5 K_1\right)^{2/3}\sqrt{\frac{\sigma}{g(\rho_l - \rho_v)}} \tag{28b}$$

2.4.2. Bubble Frequency Correlations

Carey [9] summarizes some of the most significant correlations for the bubble frequency f_b. The first attempt to predict the mean frequency of vapour bubbles departing from a heating surface was proposed by Jakob and Fritz [50] in 1931, see eq. (32). Peebles and Garber [93] suggested equation (33) including the growth time τ_g and the waiting time τ_w. Zuber [136] accounted also for natural convection included in an analogy to the bubble detachment process in his equation (34).
Ivey [48] divided the f_b, d_D – relation into three regions:

Hydrodynamic:	$f_b^{\,2} d_D = const.$	for inertia controlled bubble growth	(29)
Thermodynamic:	$f_b^{\,1/2} d_D = const.$	for heat-transfer controlled bubble growth	(30)
Transition:	$f_b^{\,m} d_D = const.$	both mechanism are involved in the detachment process, $1/2 < m < 2$	(31)

Mikic and Rohsenow [79] derived equation (35) from their theoretical model of bubble growth. Since waiting time and growth time are normally not known the correlation may be simplified to eq. (36) for $0.15 < t_w/\left(t_w + t_g\right) < 0.8$.
One of the most comprehensive correlations (37) of the bubble frequency was developed by Malenkov [75]. Di Marco [23] evaluated the weighting of the different terms in equations (37) and (38) and found that the f_b, d_D – relation becomes $f_b^{\,1/2} d_D = const.$ for small heat fluxes and large departure diameter while at intermediate diameter the relation is $f_b d_D = const$. The relation changes to $f_b^{\,2/3} d_D = const.$ at small diameters and low gravity. This indicates that in Malenkov's correlation the change of the f_b, d_D – relation from the thermodynamic to the hydrodynamic region was implemented, although not exact in the way as it had been proposed by Ivey.

Jakob & Fritz:
$$f_b \cdot d_D = 0.078 \tag{32}$$

Peebles & Garber:
$$f_b \cdot d_D = 1.18\left(\frac{\tau_g}{\tau_g + \tau_w}\right)\left[\frac{\sigma g\left(\rho_l - \rho_v\right)}{\rho_l^2}\right]^{1/4} \tag{33}$$

Zuber:
$$f_b \cdot d_D = 0.59\left[\frac{\sigma g\left(\rho_l - \rho_v\right)}{\rho_l^2}\right]^{1/4} \tag{34}$$

Mikic & Rohsenow:
$$f_b^{\,1/2} d_D = \left(\frac{4}{\pi}\right)\mathrm{Ja}\sqrt{3\pi a_l}\left[\left(\frac{\tau_g}{\tau_w + \tau_g}\right)^{1/2} + \left(1 + \frac{\tau_g}{\tau_w + \tau_g}\right)^{1/2} - 1\right] \tag{35}$$

$$f_b^{\,1/2} d_D = 0.83\,\mathrm{Ja}\sqrt{\pi a_l} \text{ for } 0.15 < t_w/\left(t_w + t_g\right) < 0.8 \tag{36}$$

Malenkov:
$$f_b = \frac{V_A}{d_D \pi\left(1 - \frac{1}{1 + V_A \rho_v \Delta h_v / \dot{q}}\right)} \tag{37}$$

where $V_A = \sqrt{\frac{d_D g(\rho_l - \rho_v)}{2(\rho_l + \rho_v)} + \frac{2\sigma}{d_D(\rho_l + \rho_v)}}$ (38)

2.5. Boiling in the Presence of an Electric Field

2.5.1. Theoretical Aspects

Di Marco et al. [24] studied the influence of an electric field on a single gas bubble in microgravity. According to the derivation of Landau and Lifshitz [70] the volumetric electric force F_{ef} on a fluid is expressed as

$$F_{ef} = \rho_{fc} E - \frac{1}{2} E^2 \nabla \varepsilon + \frac{1}{2} \nabla \left[E^2 \rho \left(\frac{\partial \varepsilon}{\partial \rho} \right)_T \right] \tag{39}$$

where E is the electric field, ε the electric permittivity and ρ_{fc} the free charge density. The subscript T stands for constant temperature conditions.
The first term generally predominates if free charge is built up, which is not the case in the present study. In contrast to the first term the other two terms are not dependent on the polarity of the electric field. They depend on the magnitude of E^2 and on the gradient of the field and of the permittivity. The second term expresses the volumetric force due to gradients in the permittivity. The general equation of this dielectrophoretic force acting on a spherical bubble as well as on a spherical droplet can be applied since the permittivity is not differentiable at the liquid vapour interface [108] and can be expresses as [70]:

$$F_{DEP} = \frac{\pi}{6} d_{eq}^3 \frac{\varepsilon_v - \varepsilon_l}{n_1 \varepsilon_v + (1 - n_1)\varepsilon_l} \varepsilon_l \nabla E^2 \tag{40}$$

The constant n_1 is related to the bubble shape. For a spherical bubble $n_1 = 1/3$ while it becomes $n_1 > 1/3$ for a flattened, ellipsoid bubble [70]. The derivation of F_{DEP} is based on several assumptions and simplifications [24]:

- The dielectric fluid must be isotropically, linearly and homogenously polarizable.
- It must not be electric conductive.
- The bubble must be small enough to obtain the amount of polarization by approximating the field as locally uniform.

A more general equation was published by Karayannis and Xu [57] in the form of a surface or a volume integral of the Maxwell Stress Tensor $\vec{T}$:

$$F_{EF,S} = \iint_S \vec{T} \cdot \vec{n} \, dS \tag{41}$$

$$F_{EF,V} = \iiint_V \operatorname{div} \vec{T} \, dV \tag{42}$$

The components of the Maxwell Stress Tensor depend same properties as equation (39) which are the electric field E, the electric permittivity ε and the eventually existing free charge [77].

It can be shown that a net force on a fluid volume arises only in the presence of non-uniformities in the electric field. These non-uniformities may be caused by the difference in the electric permitivitty between vapour and liquid or by the temperature dependency of the permitivitty.
Generally, the dielectrophoretic effect on a two-phase system can be concluded as [22]:

- The phase with the lower electric permittivity is driven towards the zone of weaker electric field.
- The surface electric force destabilizes the interface.

The electrostrictive effect is expressed in the third term of Equation (39). Its physical significance is not well evaluated yet. It may act in such a way that it creates an extra pressure difference across the interface, modifying the interface shape and increasing the internal pressure, thus, providing an additional contribution to the detachment force.

2.5.2. Experimental Investigations

Di Marco investigated boiling at a horizontal platinum wire of 0.2 mm diameter in the presence of an electric field that is created by applying high voltage at a coaxial 8-rod cylindrical “squirrel cage”. The cage had a diameter of 60 mm and a length of 200 mm ensuring that side effects are negligible. The experiments were conducted on ground and on parabolic flights. FC-72 [22] and R113 [19] were used as working fluids. The electrode rods were charged to up to 10 kV. Pool boiling as well as film boiling was investigated.
The results of the microgravity pool boiling experiment showed a significant improvement in the CHF due to the electric field but only a weak dependence of the heat transfer coefficient on the field intensity. The electric field prevented vapour accumulations near the heating surface in microgravity. A correlation for the CHF enhancement was developed.
The conclusions of the film boiling experiment were a strong improvement of the heat transfer coefficient both in microgravity and on ground. Three wave patterns were identified showing different dimensional behaviour and bubble shapes. The influence of the electric field on the patterns was evaluated. Di Marco et al. [20], [21] also investigated pool boiling on a flat square heater of 20 x 20 mm² on board a scientific satellite[2]. They studied the influence of an electric field created by 5 parallel stainless steel rods with 1 mm diameter that were placed 5 mm above the heater with 5 mm spacing in between them. Again, FC-72 was used as experiment fluid. The results agree with the results of the previous experiments. The accumulation of vapour above the heater was prevented. Thus, the heat transfer in microgravity was enhanced as well as the CHF.
Siedel et al. [104] studied the growth, departure and rise of single bubbles in normal gravity under the influence of an electric field. A plane grid placed above the heating surface was used as electrode that could be charged to up to 30 kV. N-pentane was used as working fluid. The bubble shapes were recorded by high speed imaging. They observed the elongation of the bubbles due to the electric field.
Snyder et al. [109] compared different electrode geometries during pool boiling of FC-72 on a thin wire in microgravity. The dielectrophoretic force acting on the bubbles was compared to the buoyancy force in the form proposed by Di Marco. The heat transfer coefficient of boiling in an electric field with a diverging plate electrode in microgravity exceeded even the heat transfer coefficient on ground without electric field at low to medium heat fluxes. The enhancement of the heat transfer coefficient due to the electric field decreased with increasing heat flux.

[2] FOTON M2 (2005) Experiment ARIEL

2.6. Numerical Models for Nucleate Boiling at TTD

The two numerical models to which the experimental results are partly compared to are briefly introduced in this section. These models of continual boiling at a single cavity i.e. in a single bubble sub-system are currently under development at the Institute of Technical Thermodynamics in Darmstadt.
Fuchs [32] developed a model for repeated ebullition cycles on a single cavity using an arbitrary Lagrangian-Eulerian (ALE) kinematic description. Kunkelmann [67] applied a combined Volume-Of-Fluid (VOF) / Level-Set approach on the simulation of the growth and detachment of a single bubble. In both models the microregion model of Stephan [120] is implemented but in completely different ways. While Fuchs directly applies the model using a very high grid resolution at the contact line Kunkelmann parameterizes it and applies the integrated heat flux at one cell next to the contact line.

2.6.1. ALE Model

Based on a model for quasi-stationary heat transfer to single bubbles developed by Hammer [40] for pure fluids and Kern [64] for mixtures, Fuchs developed a model for fully transient heat and fluid flow computation during boiling of pure fluids or mixtures. It is capable of simulating periodic bubble ebullition cycles at single nucleation sites and rising bubbles with a free surface. Beside the fluid and wall properties and the outer wall heat flux or temperature the model only requires the waiting time between successive bubbles. The waiting time accounts for the nucleation site properties.
Fuchs fully implemented the micro region model of Stephan [120] in his FEM code. Therefore, a high grid resolution is mandatory in the micro region. In order to move the high grid resolution with the contact line an arbitrary Lagrangian-Eulerian kinematic description was implemented into the SEPRAN source code. Fuchs also used his numerical model to study boiling phenomena of a binary mixture. The model allows to analyze the heat transfer through the specific interfaces of the computational domain that is shown in Figure 2.4a in order to evaluate the influence of transient conduction, heat storage, convection in the liquid and heat transfer at the wall.
The model is based on the following assumptions and simplifications [31]:

- Incompressible fluid
- Axis symmetry
- Laminar flow without vortices around the normal-to-surface coordinate
- Gravity as the only volume force
- Dissipation can be neglected in the energy equation
- No nucleation site and neighbouring bubble interaction
- Spherical bubble shape for attached bubbles
- Vapour phase is not included in the simulation
- Vapour/wall interface (adsorbed film) is adiabatic

The computations were performed with a binary mixture of propane/n-butane. The departure diameter is around 0.2 mm. The diameter of the computational domain is 0.4 mm.
The results of a computation are shown in Figure 2.4b-c. Fuchs found that the heat flow through the micro region (interface 3) is roughly proportional to the length of the circumferential contact

line at the bubble foot. The heat flow through the bubble hull (interface 5) increases as the bubble and the interfacial surface grow. A decreasing but still positive heat flow after detachment indicates evaporation until the bubble leaves the superheated thermal layer.

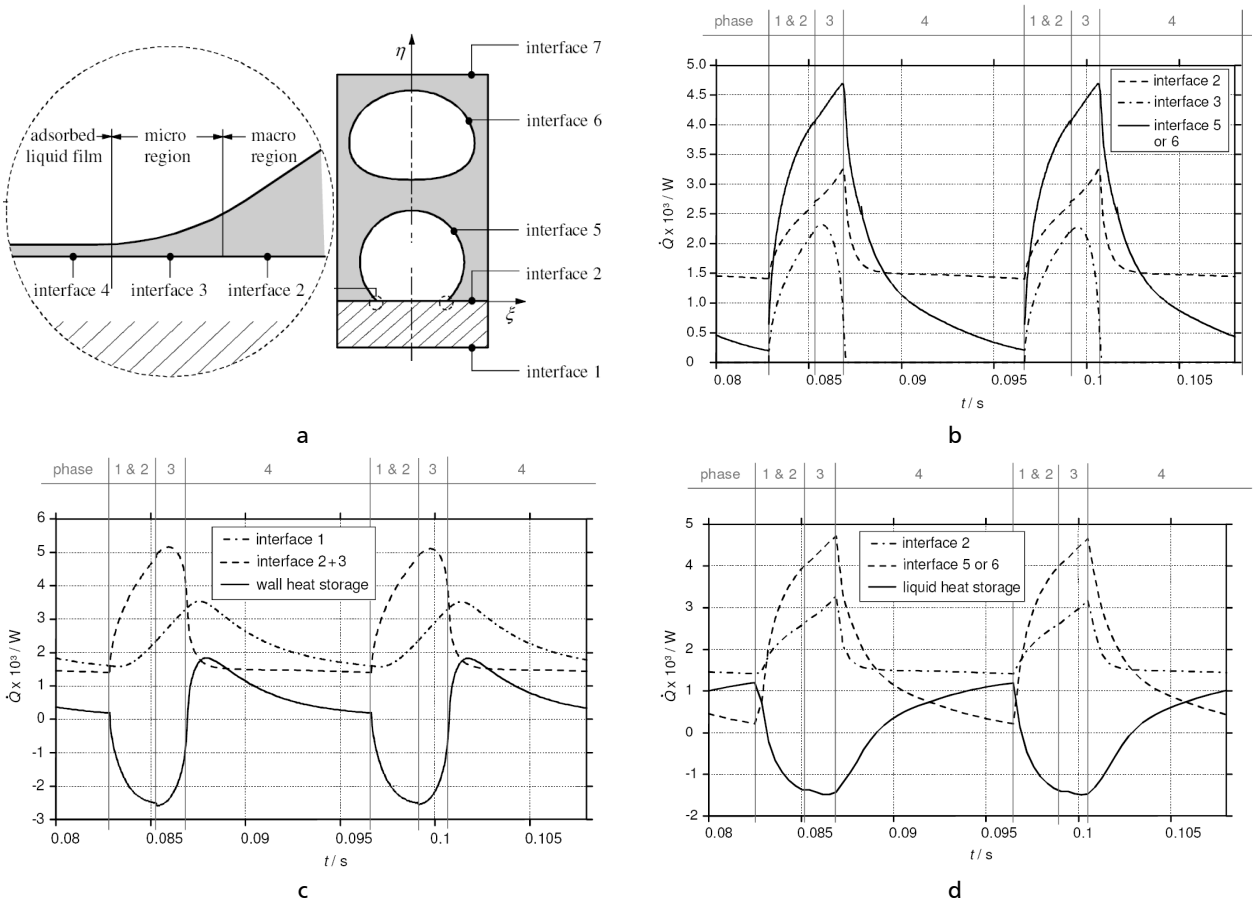

Figure 2.4: Results of numerical simulation from [31]: a) computational domain and interfaces; b-d) heat flows through specific interfaces for the same computed case

2.6.2. Combined VOF/Level-Set Model

Recently, Kunkelmann and Stephan [67] published the first results of a combined volume of fluid (VOF) / Level-Set simulation of a bubble ebullition cycle. The Level-Set method was applied for sharp liquid-vapour interface tracking and accurate computation of the temperature gradient near the liquid-vapour interface. To avoid the need of high grid resolution in the microregion Kunkelmann parameterized the integrated heat flux $\dot{Q}_{mic}$ in the micro region model of Stephan in dependence on the wall superheat $T_{w,mic} - T_{sat}$. The parameterized heat flow of the microregion $\dot{Q}_{mic}$ was numerically applied at the first liquid cell next to the contact line. Evaporation was implemented using the model proposed by Hardt and Wondra [42]. The mass flux at the liquid-vapour interface is calculated using the interfacial thermal resistance (7).

The simulation was performed with working fluid HFE-7100 at 500 mbar and a 50 μm thick stainless steel heating foil with a volumetric heat source. The conditions were chosen according to experimental investigations by Wagner [128]. The wall superheat was 5 K. The computational domain and the initial thermal layer are shown in Figure 2.5. The shape of the thermal layer is an arbitrary assumption since the results are of preliminary nature. The real thermal layer will be obtained after several bubble ebullition cycles (for the onset of boiling in microgravity it may also

be computed using the one-dimensional transient heat conduction equation with imposed heat flux (43) as proposed in [27], note from the author).

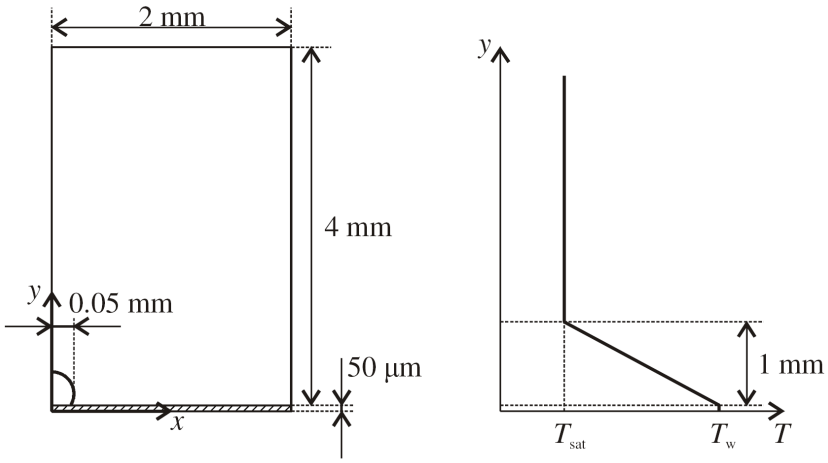

Figure 2.5: Computational domain (left) and initial thermal layer (right) of the VOF simulation [67]

The results of the simulation are presented in Figure 2.6. The liquid-vapour interface is nearly at saturation temperature even though this is not a boundary condition like in other models. Although the results are preliminary information concerning the heat transfer mechanisms could be obtained from the deformation of the thermal layer (see Chapter 6.6). In agreement with micro thermocouple measurements of the vapour temperature inside a bubble, performed by Wagner [128] a significant superheat of the vapour inside the simulated bubble is visible. This can be explained by a higher thermal diffusivity of the vapour than the liquid. However, the heat transferred to the vapour phase is negligible as it can also bee seen in Figure 2.7 and the vapour superheat diffuses very fast. Nevertheless, the influence of the vapour superheat on the boiling process is not yet evaluated.

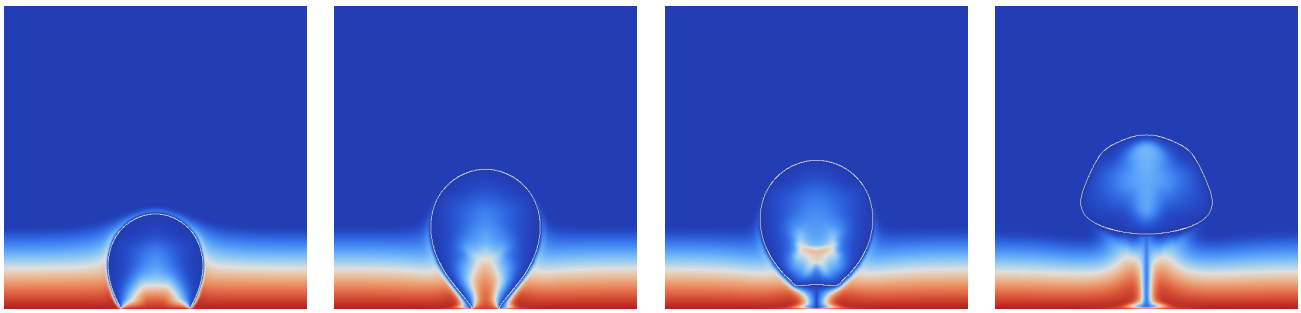

Figure 2.6: Numerical simulation of a growing and detaching vapour bubble (HFE-7100, 5K wall superheat) at 13, 24, 26 and 31 ms, performed by Kunkelmann and Stephan [67].

The heat flows during the bubble ebullition cycle are plotted in Figure 2.7. As already stated above the heat flow to the vapour through the adsorbed film $\dot{Q}_v$ is very small and can be neglected. The overall latent heat flow of the bubble increases steeply to a maximum and then decreases until bubble detachment. Some net evaporation still takes place after detachment as the bubble is in contact with the thermal layer at the bottom while the liquid is not subcooled at the bubble cap. The heat transferred through the microregion at the contact line $\dot{Q}_{cl}$ is significant since the dimension of this region is very small compared to the interfacial surface of the bubble hull. The

heat flow through the microregion is roughly proportional to the contact line length supporting the observations of Fuchs [32]. However, since the liquid film adjacent to the microregion is still thin, the evaporative heat flux at the contact line is not equal to the microregion heat flux but equal to the microregion heat flux plus the heat flux through this thin film region (see evaluation in Chapter 6.6). The heat flow to the liquid $\dot{Q}_\mathrm{l}$ is in the same order of the microregion heat flow. In order to anticipate with the evaluation of the heat flow distribution at single vapour bubbles in Chapter 6.6 the author calls attention to the slight increase of the liquid heat flow during bubble detachment with a maximum at departure. This could be attributed to transient conduction in the liquid (note from the author).

The temperature profiles at the fluid side and at the back side of the stainless steel foil are presented in Figure 2.8. The temperature profiles at the back side of the foil can be compared with the thermography measurements of the present work. The difference between the fluid side and the back side illustrates the blurring effect of the 50 μm foil.

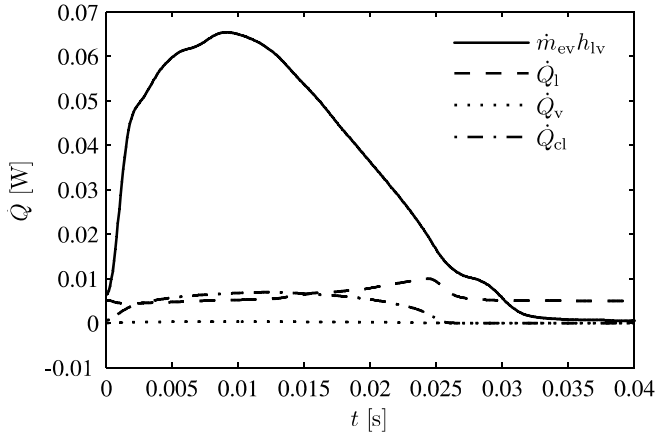

Figure 2.7: Heat flows during growth and detachment [67]

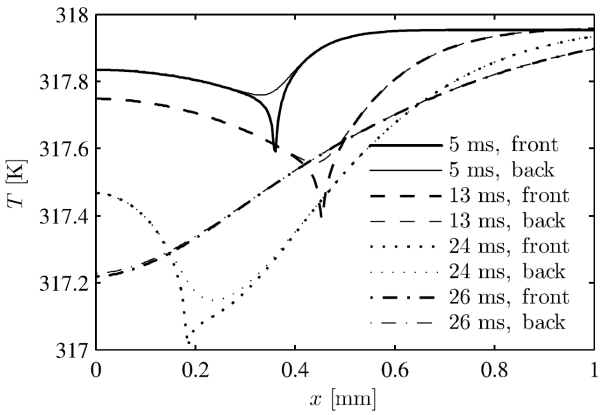

Figure 2.8: Temperature profiles on front (solid-fluid interface) and back (adiabatic) of the steel foil [67]

3. Basic Measurement Principle and History of Microgravity Boiling Experiments at TTD

Since 2004 several microgravity boiling experiments have successfully been conducted at TTD. All experiments are based on the same experimental idea. The basic measurement principle is explained in this chapter. Before, special aspects of experimentation in microgravity are explained. Furthermore, the experiments of the campaign 2004 to 2008 and their results are briefly presented.

3.1. Experimentation in Microgravity

The term weightlessness expresses the condition of a body being in free-fall. In that condition a body is only subjected to uniformly distributed volume forces and no forces are acting on the surface of the body. However, the term microgravity is also used if the weightlessness is disturbed by small acceleration phases or vibrations which results in reaction forces on the body's surface.

Conducting scientific experiments in microgravity is generally motivated by two reasons:

1. For space flight it is mandatory to know how physical, chemical and biological systems behave in weightlessness, how they are affected by the change of gravitational acceleration and if they are generally deployable in space applications. In the field of thermodynamics and fluid physics two phase systems are very effective for heat transfer and, therefore, highly interesting for spacecraft thermal control. However, they are strongly influenced by buoyancy due to the large density difference between vapour and liquid. The absence of buoyancy imposes a completely different behaviour of two phase systems (for Bond numbers $\mathrm{Bo} > 1$).
2. A more scientific reason for the experimentation in microgravity is the fact that weightlessness often reveals effects that are hardly observable and measurable under normal gravity conditions. This leads to a better understanding of the phenomena and their interaction and contributes primary to fundamental research.

The European Space Agency (ESA) offers access to several facilities for experimentation in microgravity conditions. An overview is provided by Ryuters and Preu [100] and summarized in Table 3.1.

	Droptower at ZARM in Bremen	Parabolic flight (A300 zero-g)	Sounding rockets (TEXUS, MAXUS)	Satellite (FOTON, BION)	International Space Station ISS
Microgravity duration	5/9 sec	22 sec repeatable (31/day)	6 to 12 min	~20 days	Continuous
Microgravity quality	10^{-5}g	10^{-2}g	10^{-4}g	10^{-6}g	10^{-4}g
Manufacturer of experiment hardware	Experimenter	Experimenter	Industry	Industry	Industry
Execution	Automatically	Experimenter	Automatically / Experimenter via telemetry	Automatically / Experimenter via telemetry	Automatically / Astronaut / Experimenter via telemetry
Last access before start	30 min	10 min	90 min	5 days	17 h
Earliest access after landing	30 min	1 min	30 min	Several hour up to one day	3 h if download capability present
Laboratory available at launch/start site	yes	yes	yes	In preparation	yes

Table 3.1: Overview on microgravity facilities offered by the European Space Agency [100].

For the present work nucleate boiling experiments were conducted during parabolic flights. In order to establish microgravity inside the aircraft the trajectory of the aircraft matches that of a thrown object which is not subjected to any drag. That means the horizontal velocity is constant. The engines are only counteracting the drag. The vertical acceleration is equal to the gravitational acceleration. The resulting flight path is a parabolic trajectory during the microgravity phase. The whole parabolic manoeuvre also includes a pull-up phase prior to the microgravity phase during which the aircraft speed and inclination angle is adjusted for entering the parabola and a recovery phase during which the aircraft returns to horizontal flight. Gravity and aircraft trajectory are illustrated in Figure 3.1. The pull-up phase for the Airbus A300 ZERO-G is 20 seconds; the gravity inside the aircraft is 1.8g (1.8-times nominal earth gravity). The transition into the microgravity phase lasts 1-2 seconds. After the microgravity phase the aircraft has to be recovered to horizontal flight. The gravity during the recovery-phase is between 1.5g and 1.8g and it lasts also 20 seconds. The duration of the microgravity-phase of the Airbus A300 ZERO-G is 22 seconds. The microgravity quality is influenced by atmospheric turbulences and piloting skills. The residual acceleration fluctuates around +0.05g and -0.05g. The fluctuation is called g-jitter and has to be considered when designing a parabolic flight experiment.

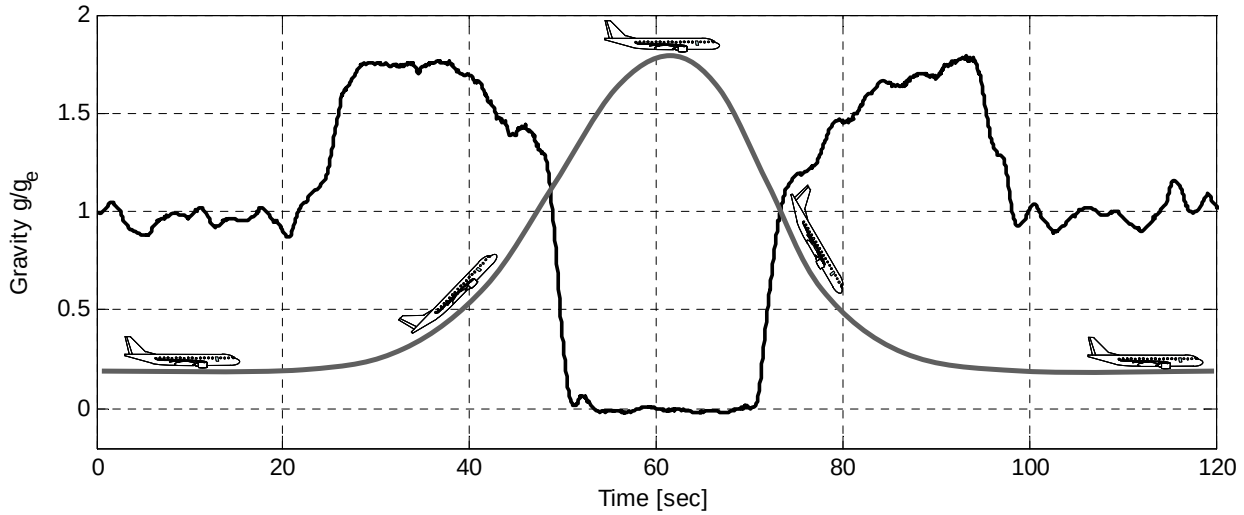

Figure 3.1: Aircraft trajectory and gravity during parabolic manoeuvre

For the design of a parabolic flight experiment the safety rules and guidelines of the aircraft operating company NOVESPACE[3] have to be fulfilled. That makes a parabolic flight experiment much more complex compared to a similar ground experiment. Additionally, special precautions regarding the reliability of the experiment have to be taken since it is not possible to perform any reparations during the flight. Only small modifications can be carried out in between the flights which take place on successive days.

The parabolic flight campaigns of ESA, DLR and CNES take place at Bordeaux Merignac airport where the Airbus A300 zero-g is sited. Roughly 14 to 16 experiments take part in one campaign. The campaign lasts 10 to 11 days. The first week is used for experiment preparation. The experiments are set up from transport to flight configuration. All experiments have to pass a preliminary safety review performed by a NOVESPACE engineer before they are allowed to be loaded into the aircraft. The second week is the flight week. An official safety review is performed by the French test flight centre CEV and a flight briefing takes place on Monday. On Tuesday, Wednesday and Thursday the parabolic flights with 31 parabolas in each flight are performed. The parabolas are flown in intervals of 3 min with some minutes break after sets of 5 parabolas. This has also to be taken into account during the experiment planning. Experimental data has to be stored and the next run has to be prepared within these 2 min. In the present case this time was the limiting factor for the number of high speed camera images. The images had to be transferred from the camera memory to the computer and stored onto hard disc. The average flight duration is 3 hours. Immediately after the last flight the experiments are unloaded and all equipment is packed for departure.

[3] www.novespace.fr

3.2. Measurement Principle

From 2004 to 2009 the author has successfully performed boiling experiments on parabolic flights, one campaign per year. The basic experimental idea was common during all campaigns and is illustrated in Figure 3.2.
A thin metallic foil was used as a resistance heater for a boiling process with FC-72 or pure n-Perfluorohexane (nPFH) which is the primary component of FC-72 as working fluid. The temperature of the foil was measured at the back side via high resolution thermography. At the same time bubble shape and motion were recorded by a digital camera.

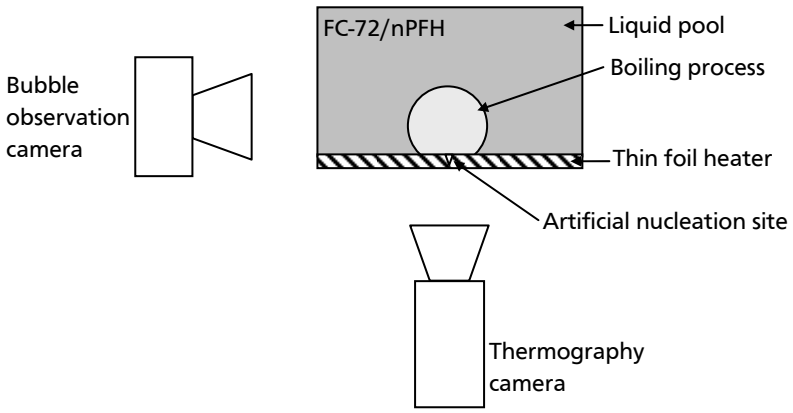

Figure 3.2: Basic measurement principle

The objective of the experiment in the 37th ESA campaign in 2004 was the measurement of the temperature distribution at the contact line of a single, stationary FC-72 vapour bubble. A stainless steel (1.4301) foil with a thickness of 10 μm was heated by electrical current. The thermography system incorporated unencapsulated thermochromic liquid crystals (TLCs). The TLC colour field was recorded by a 3-chip CCD camera. The temperature drop caused by high local heat fluxes in the vicinity of the micro region of a vapour bubble was measured (see Chapter 3.3.1).
For the 41st ESA campaign in 2005 the objective changed from a stationary bubble to continual boiling of FC-72 at a single artificial cavity. Since the boiling process is highly dynamic, temperature images and bubble shapes were recorded at 250 fps, synchronously. Still, unencapsulated TLCS were applied at the back side of the heating foil (Chapter 3.3.2).
High speed IR thermography was used in the 42nd ESA campaign in 2006. Thus, the problem regarding the sensitivity of the TLCs to superheating has been solved. The microgravity quality was enhanced due to the use of a free floating test cell. That prevented problems with small negative g at the beginning of the microgravity phase (Chapter 3.3.3).
For the 11th DLR campaign in 2007 a new test cell was designed. The new design was based on a concept study for the RUBI ISS experiment. To activate the artificial cavity and to initiate the bubble growth the heating foil could be locally heated by a focused laser beam at the nucleation site. The objective was to initiate bubble growth in microgravity under clearly predefined conditions. The temperature adjustment of the working fluid was also enhanced to control the saturation state. Furthermore, the working fluid was changed from FC-72 (3M) to pure n-Perfluorohexane. Since nPFH has the same fluid properties because it is the primary component of FC-72 but is a pure fluid any mixture effects can be excluded.

In 2008 (48th ESA PFC) an additional heater incorporating a heat flux meter was implemented into the test cell. The heater was developed at IUSTI in Marseille and is part of the preparation of the RUBI experiment (Chapter 3.3.4).
During the 50th ESA campaign in 2009 a micro thermocouple and an electric field electrode have been placed above the heating foil.

3.3. A History of Microgravity Boiling Experiments of the Institute of Technical Thermodynamics

3.3.1. 37th ESA PFC 2004

The experimental objective for the 37th ESA Parabolic Flight Campaign was the measurement of the temperature drop at the contact line of a stationary spherical single vapour bubble. The results of the investigations already presented in [111] are summarized in this chapter.
A quasi stationary boiling model was developed by Stephan and Hammer [116] implementing the micro region model of Stephan [120] (see Chapter 2.1.4). A detailed description can also be found in [61] presenting the implementation of binary mixture effects in the model by Kern and Stephan. The model predicts a temperature drop of ~8 °C caused by strong evaporation in the micro region at the contact line at length scales of a few micrometers on the heating wall.
A drawing of the boiling cell is shown in Figure 3.3a. A stainless steel foil with a thickness of 10 μm was used as a resistance heater. A Plexiglas cylinder with an inner diameter of 15 mm and a height of 20 mm was attached to the bottom side of the heating foil. The cylinder contained the working fluid FC-72 and was closed at the bottom by an aluminium plate with a connection to the compressible fluid reservoir. The cell was equipped with a coil heater and a connection to a vacuum chamber allowing the exhaust of vapour and non-condensable gas. The heating foil was strained onto a copper support that served as a heat sink for the foil surface area not in contact with the fluid. For electrical insulation the copper support was coated by a thin layer of paint. The copper support featured a cut-out for the optical access of the thermography camera. A thermochromic liquid crystal (TLC) layer composition was applied on the top side of the foil within the cut-out. The TLC layer composition was developed by Höhmann [46] for the measurement of the temperature drop at a stationary evaporating meniscus. In the first step, the foil was coated by a black layer[4] of 5 μm thickness. The un-encapsulated thermochromic liquid crystals were applied at the black coating with a thickness of approximately 10 μm. The TLCs featured a working range of 50 °C to 60 °C (red to blue colour).

[4] Alfac GmbH, Al 109

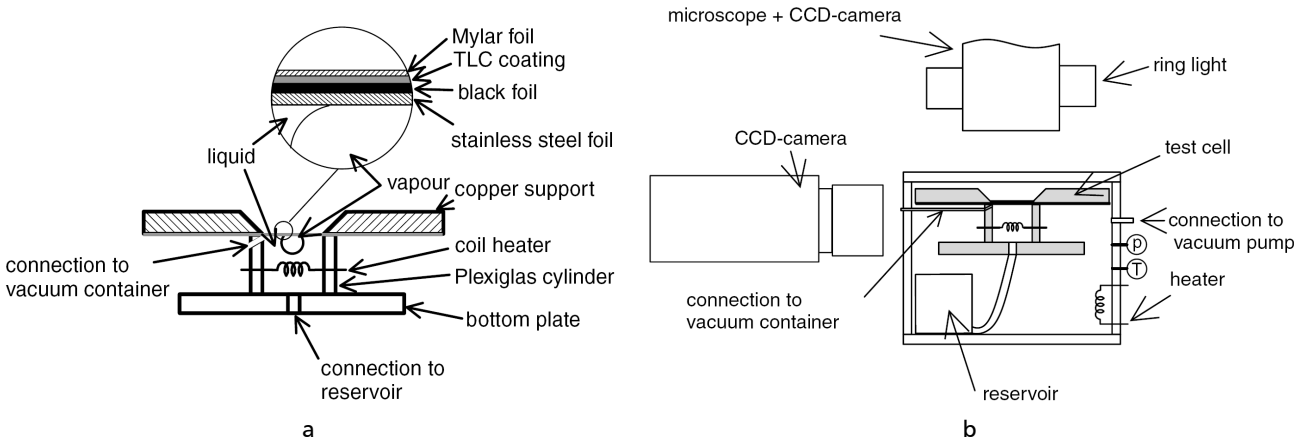

Figure 3.3: Boiling cell (a) and measurement setup (b) of the 37th ESA PFC

In order to adjust the saturation temperature according to the working range of the TLCs the pressure inside the test cell had to be controlled. This was accomplished by locating both the cell and the compressible reservoir inside a Plexiglas container (see Figure 3.3b). The Plexiglas container was equipped with a heating system for preheating and heat loss reduction. In order to enhance the reliability of the experiment four test cells were integrated into the Plexiglas container. This was strongly recommended due to the sensitivity of the TLCs regarding overheating.

A three-chip CCD camera in conjunction with a long distance microscope was used to record the colourplay of the TLCs. Coaxial illumination was arranged using a fibre-optic ring light connected to a cold light source. The FOV of the camera was 800 μm x 600 μm. The resolution was 1.04 μm/pixel. A temperature-hue-calibration was been performed after each parabolic flight. Therefore, the RGB matrices (bmp-images) of the frame grabber were converted into HSV (hue, saturation, value) matrices using a MATLAB algorithm. The hue value was averaged over the entire FOV at distinctive spatial-homogenous temperature levels. The temperature-hue-data points were interpolated by a 6-order polynomial fit.

Prior to each experiment the FC-72 was carefully degassed. In order to prevent any fluid motion during the measurements in microgravity it was ensured that neither any gas nor any vapour were present inside the test cell during the transition from hypergravity to microgravity. A bubble was created in microgravity at the artificial cavity or by re-injection of vapour from the exhaust line into the test cell that served as a bubble embryo.

The growth rate and movement of the bubble sliding on the surface was low compared to a dynamic boiling process. The assumption of a stationary bubble was therefore justified.

The result of a measurement run is shown in Figure 3.4. A temperature drop in the TLCs image (Figure 3.4a) indicates the route of the contact line. The temperature profile along the white arrow in Figure 3.4a is shown in Figure 3.4b. To reduce the signal noise the temperature was averaged over 10 pixels orthogonal to the arrow. The temperature drop caused by strong evaporation at the contact line of a vapour bubble in a boiling process was measured. The temperature of the heating foil underneath the bulk liquid is 56.1 °C, the minimum temperature at the contact line is 51.7 °C and in the adsorbed film region above 56.7 °C. An image of the corresponding vapour bubble is presented in Figure 3.4c.

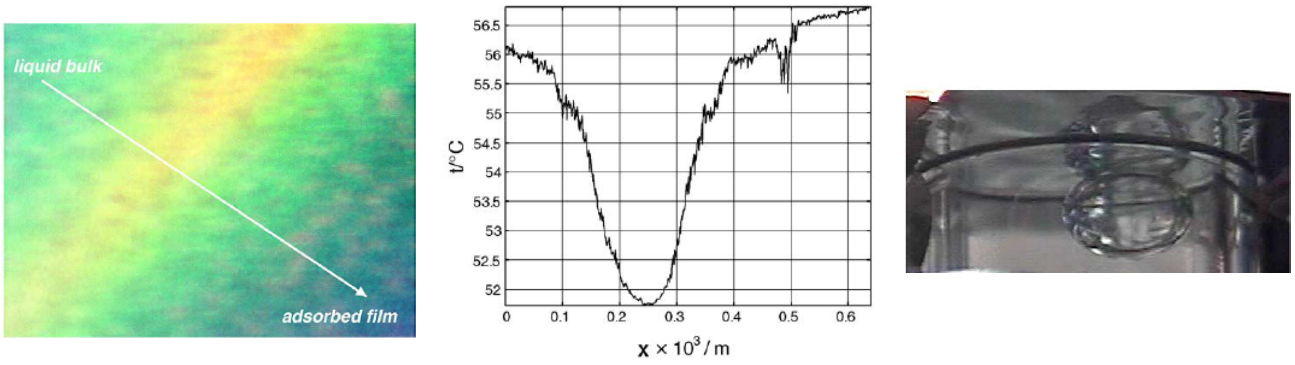

Figure 3.4: Results from the temperature measurements at a single, stationary vapour bubble during the 37th ESA PFC 2004: a) TLC colourplay; b) temperature development along white arrow; c) image of the bubble

The temperature profiles were compared to the numerical results of the quasi stationary model (see Figure 3.5). Good qualitative agreement was found. Quantitatively, the computed temperatures are roughly 2 °C below the measured values which is within the measurement and computation accuracy.

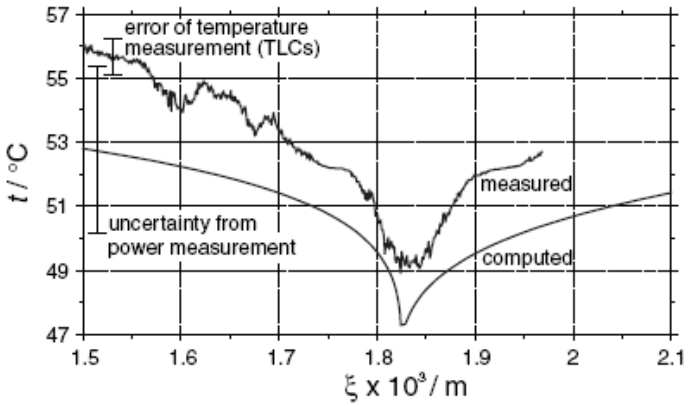

Figure 3.5: Comparison of computed and measured wall temperature distribution close to the microregion

3.3.2. 41st ESA PFC 2005

The objective for the 41st ESA PFC was the measurement of the wall temperature distribution at a continually boiling single nucleation site during the transition from hypergravity into microgravity with high spatial and temporal resolution. The results have been published in [112], [113] and [127]. In the following chapter these results are summarized from the publications.

A new boiling test cell was developed based on the experience gained from the 37th ESA PFC and is shown in Figure 3.6. It consisted of a heating foil carrier and a Plexiglas box in the lower part and a vapour reservoir, an exhaust system and a pressure equalisation module in the upper part. In contrast to the previous cell the boiling process took place at the top side of the heating foil. The bubbles detached and rose in the test cell due to buoyancy while not being in microgravity. An artificial cavity was created in the centre of the upper surface of a thin stainless steel heating foil (26 mm x 18 mm x 10 μm) by creating a small frayed hole. The heating foil was used as a resistance heater, powered by DC current. It was fixed on a copper-made heating foil carrier with heat conductive adhesive tape[5] which positioned the heating foil in the centre of the test cell bottom.

[5] 3M, 8940

Additionally, the foil carrier provided the connection to the power supply and prevented boiling at undesired places (e.g. edges of the foil, electrical clamping jars) by conducting heat away from these parts. A hole with a diameter of 10 mm in the middle of the foil carrier allowed optical access to the lower surface of the heating foil where a TLC measurement system was attached. The TLC measurement system consisted of a layer composition of a 5 μm thin black tape[6], a layer of un-encapsulated TLCs and a transparent Mylar-sheet[7]. The thin black tape coated the lower surface of the heating foil in the area that could optically be accessed, providing a light absorbing background to improve the colourplay of the TLCs. The TLC layer was applied onto the black tape with a brush and had a thickness of ~ 20 μm. It was protected from adverse environmental effects by the Mylar sheet, which also homogenised the thickness of the TLC layer.

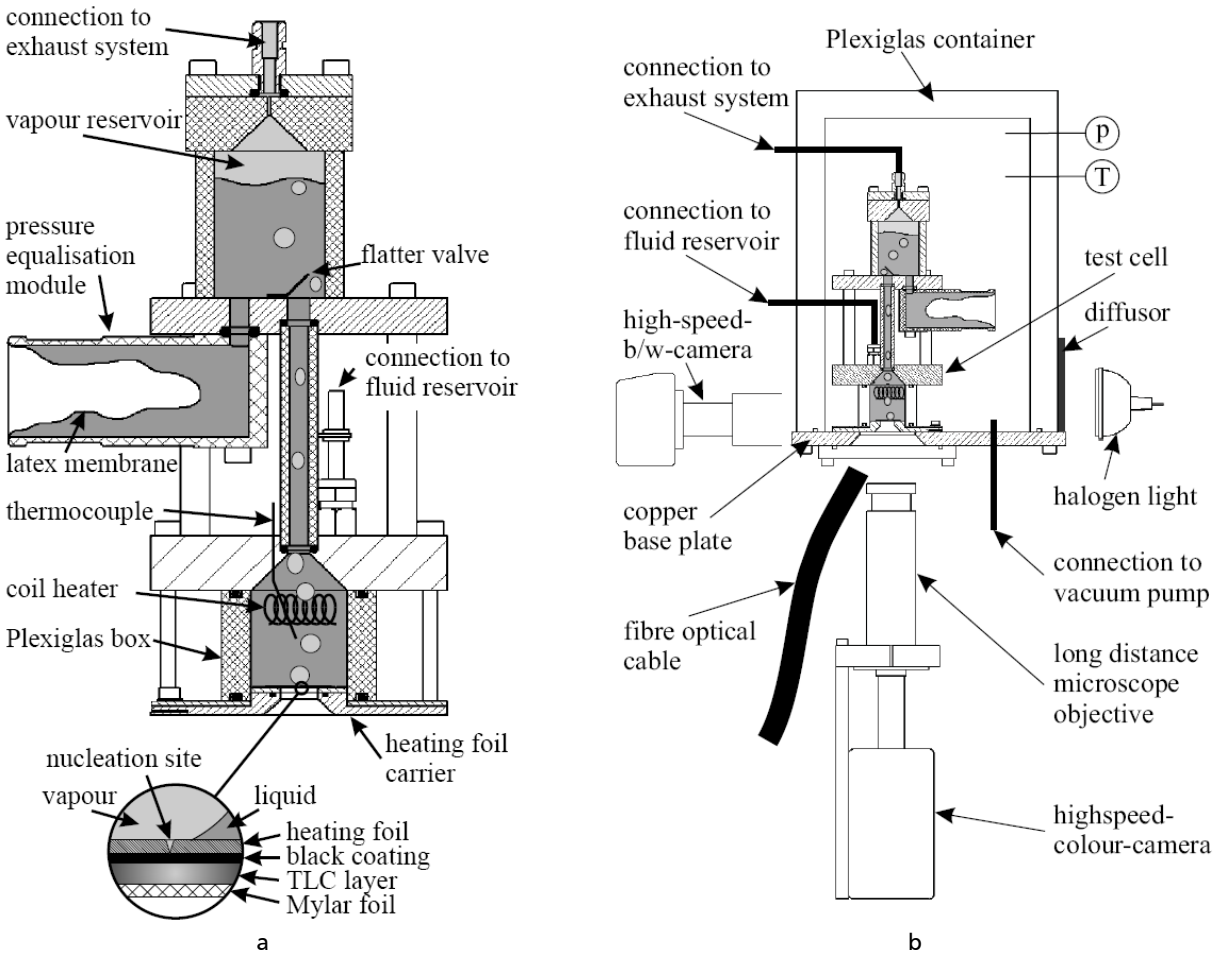

Figure 3.6: Boiling cell (a) and measurement setup (b) of the 41st ESA PFC

For the optical observation of the vapour bubbles a transparent Plexiglas box enclosed the working fluid on the carrier. To control the subcooling of the liquid the lower part of the test cell was equipped with a coil heater. The fluid temperature was measured with a K-type thermocouple. For filling and draining the test cell an inlet tube was used. Due to gravity, vapour bubbles created on the heating foil rose through the connection tube into the vapour reservoir. Before entering the vapour reservoir, the bubbles had to pass a flatter valve, that prevented the vapour from flowing back into the lower part of the test cell under microgravity conditions. The vapour reservoir could

[6] Alfac GmbH, GS116

[7] Puetz GmbH + Co. Folien KG

be drained using an exhaust tube. To minimise any pressure on TLCs and heater, a pressure equalisation system basically consisting of a latex membrane was used for pressurisation between inside and outside of the test cell. The test cell was mounted on a copper base plate which formed the bottom of a second, larger transparent Plexiglas container. This base plate acted as a heat sink for the heating foil carrier. Inside the container the pressure could be varied using a vacuum pump. In that way, the saturation temperature of the working fluid could be adjusted to fit the working range of the TLCs. Temperatures of the base plate, the heating foil carrier, the working fluid and the air inside the container as well as the pressure inside the container and the heating power were measured and recorded by a data acquisition system[8]. To capture the wall temperature distribution, the colour play of the TLCs were observed through the wall of the Plexiglas container using a high speed colour camera[9] in connection with an adjustable long-distance-microscope, resulting in a spatial resolution of 7.8 μm/pixel. The TLCs were illuminated by a cold light source in conjunction with a fibre optic cable. Despite the use of a cold light source and a fibre optic for illumination, up to 20 % of the total heat supplied to the heating foil was provided by the light. A high speed black/white camera[10] recorded the shape of the vapour bubbles via the shadow method. The bubbles were illuminated from the backside using a halogen light source behind a diffuser. The camera was positioned in a way that its image plane is normal to the heating foil. The spatial resolution of the images is 20 μm/pixel. Both high speed cameras were synchronized using a trigger and recorded at 250 fps. Before each experiment the working fluid was carefully degassed by reducing the pressure inside the Plexiglas container and heating the FC-72 up to saturation temperature. Any vapour formed in the reservoir and test cell was removed. Prior to each measurement, the fluid in the test cell was heated close to saturation temperature. After a set of 31 parabolas, i.e. after each flight the TLCs were calibrated. This was accomplished by attaching a tempered copper block to the fluid side of the heating foil. A TLC thermography image was taken at several temperature levels. Mean colour (hue) values at each level of the TLCs were attributed to the block temperature and a polynomial fit was applied.

The measurement sequences were triggered during the transition between hypergravity and microgravity. Above a certain gravity level only a pulsating cold spot is visible at the nucleation site. The bubble foot expands and constricts with a frequency that is too high to form the temperature drop at the back side due to the heat capacity of the heating foil. At low residual gravity the bubbles grow larger and the bubble frequency decreases. The temperature drop at the contact line becomes measurable as it is shown in Figure 3.7. The presented bubble was recorded at a residual gravity of $g/g_e < 0.03$. The saturation temperature was $t_{sat} = 30.7\,°C$ and the measured fluid temperature was $t_{fluid} = 30.8\,°C$. In Figure 3.7c the image of the bubble camera is shown. The observed bubble is marked by a white ring. The colourplay of the TLCs is shown in Figure 3.7a. The temperature along the white arrow is plotted in Figure 3.7b. At $\tau = 64$ ms counted from bubble nucleation the characteristic circular imprint of low temperature (red colour) can be seen. The wall temperature underneath the bulk liquid is 55 °C, at the drop caused by the contact line evaporation 45 °C and in the adsorbed film region 50 °C. The development of this temperature imprint from $\tau = 0$ ms to $\tau = 64$ ms is presented in [127] and [113]. The obtained results agree with the numerically predicted effects and confirm the existence of the micro region.

[8] National Instruments 4350

[9] X-Stream XS-3

[10] Photron Fastcam-Ultima512 32K

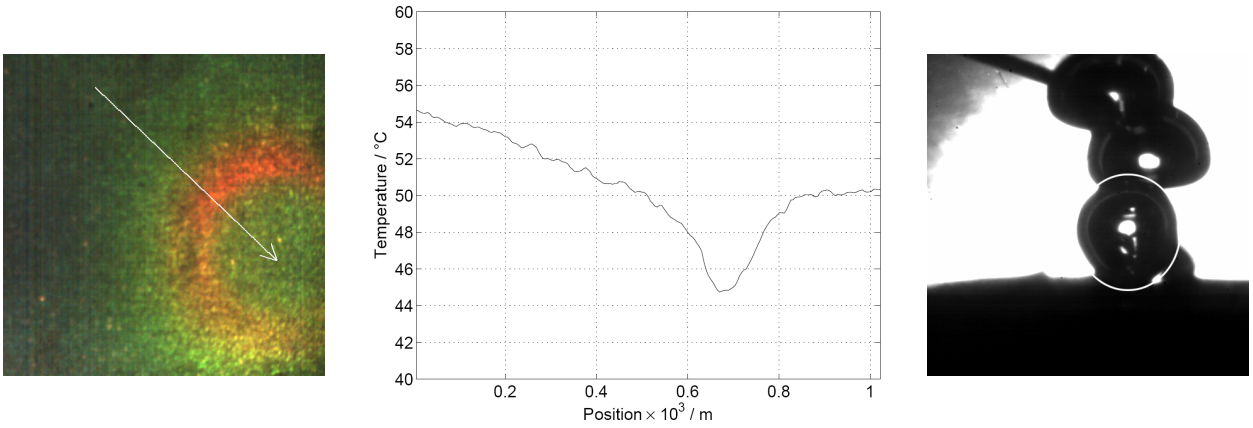

Figure 3.7: Results from the temperature measurements at a continually boiling cavity during the 41st ESA PFC: a) TLC colourplay; b) temperature development along white arrow; c) image of the bubbles

3.3.3. 42nd ESA PFC 2006

From the experience gained in the two previous campaigns in 2004 and 2005 two main issues were identified whose improvement would lead to a strong enhancement of the quality of the experimental results:

A. The overshoot into negative gravity values at the beginning of the microgravity phase causes vapour that is present in the test cell to come back to the heating surface. The consequence is a shortened measurement time for the sequences that are recorded during the transition until the vapour disturbs the measurement. The overshoot is a transient effect caused by the manual piloting and controlling of the microgravity. Generally, three improvement approaches are possible on this issue:

1. Prevention of the overshoot by the responsible pilot. To avoid the transient effect a smoother and longer transition phase is necessary. This would result in the reduction of the microgravity time. The reduction would have no negative effect on the present boiling experiment since the measurement time was only 4 s at 250 fps restricted by the memory and interface of the high speed camera. Nevertheless, this is not an option because the teams of the other scientific experiments on board the aircraft are interested in a long microgravity phase. However, it is fact that the overshoot is dependent on the piloting skills and was varying strongly between the flights and campaigns. Especially two phase fluid science experiments are often very sensitive to negative gravity or g-jitter.
2. Vapour handling inside the test cell. Enhancement of the time until the vapour reaches the bottom of the cell by changing the geometry of the cell could be performed as well as preventing the vapour from coming back at all. When starting the measurement sequence in the microgravity phase it could be made sure that neither vapour nor gas is present inside the cell. This approach was chosen for the campaigns 2007-2009 for which a new test cell was designed and built.
3. Avoiding the overshoot to be transferred to the test cell by decoupling the measurement system from the aircraft. The whole measurement system (test cells, second containment, thermography and high speed camera) could be included into a free floating unit that is only loosely fixed at the rack. It may move within some centimetres at the beginning of the microgravity phase. This leads not only to a prevention of the overshoot but also to an

improvement of the microgravity quality in the first 2 or 3 seconds of the microgravity. After that time the free floating unit would very likely have approached the limitation of the fixation straps what would result in a sharp disturbance of the microgravity. Nevertheless, this time is long enough to record a measurement sequence during the transition phase. Therefore, this approach was chosen for the 42nd ESA PFC 2006.

B. The sensitivity of the un-encapsulated thermochromic liquid crystals regarding ageing and overheating limited the usability of the thermography system. The TLCs are working only in a narrow temperature range of 50 °C to 60 °C. The surface temperature of the boiling process had to be limited to 65 °C. Above this temperature the danger of damaging the TLCs significantly increases. That fact triggered large difficulties in the activation of the nucleation site where initially large superheating is necessary. Additionally, the TLC layer composition on the heating foil was only usable for one flight. Therefore, the heating foil with the nucleation site had also to be exchanged. This reduced the comparability of the experimental data among the different flights due to the different behaviour of the nucleation sites.

By switching to high speed infrared thermography instead of using TLCs these problems vanished. A newly available high speed IR camera[11] in conjunction with microscope lenses was implemented. Additionally, the problem of transferring heat from the light source to the heating foil as described in Chapter 3.3.2 was overcome. With the IR thermography system a wider variation of heat flux and temperatures is possible. However, the improvements were accompanied by mainly two disadvantages. The maximum resolution of the IR camera is 14.8 μm/pixel and the IR chip has only 320 x 256 pixels instead of 800 x 600.

The test cell already used in the 41st ESA PFC 2005 (see Chapter 3.3.2) was slightly modified for the 42nd ESA PFC 2006 (Figure 3.8).

The back side of a thin metal foil (stainless steel/titanium) was coated with 10 μm thin black tape[6]. The purpose of this coating was to provide a surface emission coefficient near 1.0 to minimize any reflection for the infrared thermography. A high speed infrared camera[11] (320 x 256 pixel) was used in conjunction with long distance microscope lenses. The spatial resolution was 14.8 μm/pixel and the frame rate was 250 Hz. To relate the measured intensity to a corresponding temperature, a calibration procedure was performed after each experimental run. Homogeneous temperature levels were maintained at the top side of the heating foil using a copper block and a bath thermostat. The temperature levels were set between 25 °C and 70 °C in steps of 5 °C. For each level, an infrared image was taken. With the help of MATLAB image processing tools, a polynomial fit was applied at each pixel of the images.

The test cell is divided into three main parts: the boiling cell in the lower part, the vapour reservoir above, and the pressure equalization module.

At the bottom of the boiling cell, the thin metal foil (26 mm x 18 mm) is used as an electrical resistance heater. The material chosen for the foil was stainless steel (1.4301, thickness: 25 μm) for all experiments except for the investigations of explosive bubble growth. The investigations of explosive bubble growth were conducted with a 6 μm titanium foil. A cylindrical artificial cavity with a diameter of 20 μm and a depth of 20 μm was created in the centre of the heating foil by ion beam milling. The foil was glued on a copper carrier with a central opening by heat conductive tape[5]. The boiling cell itself was made of a rectangular Plexiglas box and was equipped with a coil heater and a K-type thermocouple. At positive gravity levels the vapour bubbles which are created at the heating foil rise through the boiling cell and the connection tube into the reservoir where

[11] Indigo-Systems, Phoenix DAS

they are either re-condensed or exhausted. A flatter valve at the end of the tube hindered vapour re-entering the boiling cell in microgravity due to g-jitter. The pressure equalization module maintains the same pressure at both sides of the heating foil. The test cell is mounted on a copper base plate inside a Plexiglas container. The pressure inside the container is controlled by a vacuum pump and measured by a pressure transducer. Temperatures are recorded at different locations of the system using K-type thermocouples. The experimental system consisting of Plexiglas container, infrared camera, b/w camera and light source (which are fixed on a strut profile assembly) was designed as a free-floating unit that is loosely fixed by ropes inside the experimental rack. Thus, the experimental system could move approximately 100 mm in all directions. During the microgravity phase, the unit was free-floating within its cage, carefully controlled by the experimenters. With that measure, g-jitter effects were reduced and the quality of microgravity was significantly enhanced. The acceleration in all axes was measured by accelerometers at the free-floating unit. All sensors were connected to a data acquisition device[12] and read out with a frequency of 1000 Hz during the measurement sequences.

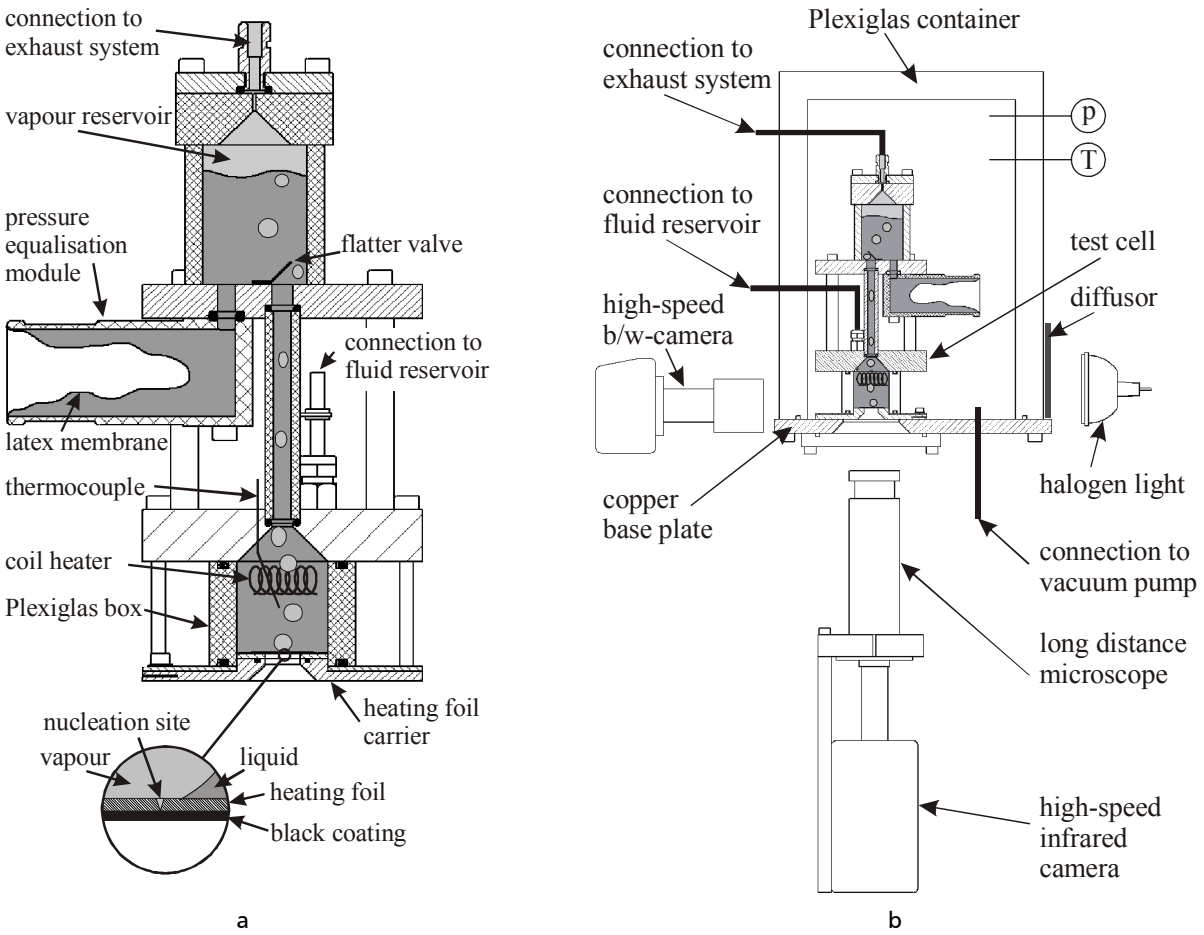

Figure 3.8: Boiling cell (a) and measurement setup (b) of the 42nd ESA PFC

Prior to the parabolas the pressure was adjusted at 500 mbar and the working fluid FC-72 was heated close to saturation temperature. The power to the heating foil was turned on and the single artificial cavity was activated just before the parabola. Any vapour or gas accumulation in the

[12] National Instruments PCI-6289 + SCXI system

reservoir was exhausted. Most of the data and picture sequences were triggered at the injection into the parabolic trajectory, i.e. during the transition between hypergravity and microgravity.
The results of this campaign were published in [102]. In Figure 3.9 the pictures of the b/w camera at different gravity levels are shown. The pictures belong to a single sequence that was recorded during the transition between hypergravity and microgravity at the beginning of a parabola. Pool boiling at a single nucleation site was established. The heat source of the foil was 7000 W/m². The temperature of the bulk liquid was maintained closed to saturation temperature at 37 °C.
It was possible to trace the trajectory of every bubble and to evaluate its volume using MATLAB Image Processing Toolbox (see Chapter 5.2). While the shape of the bubbles does not change, their size increases strongly with decreasing gravity. During the microgravity phase bubble detachment was only observed when g-jitter disturbed the weightlessness.

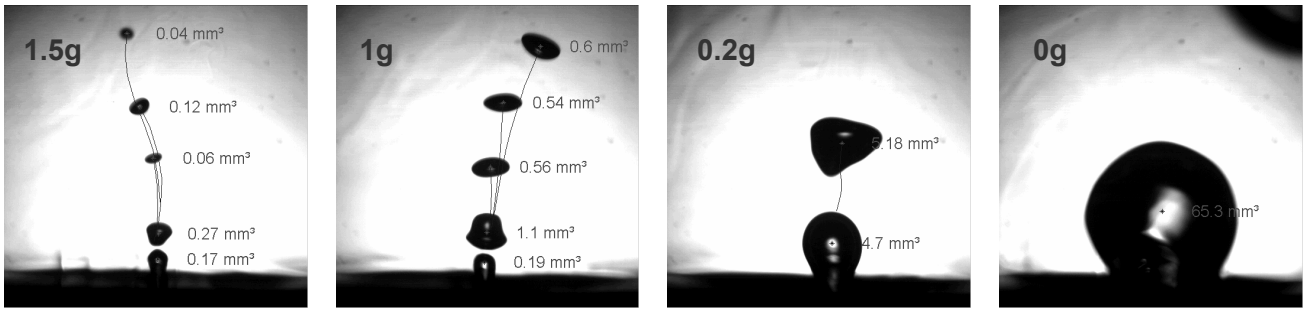

Figure 3.9: Bubble shapes at various gravity levels: a) 1.5g; b) 1g; c) 0.2g; d) 0g

The development of bubble frequency and departure diameter were evaluated for the sequences recorded during the hypergravity-microgravity-transition. The plot of bubble frequency and gravity versus time is shown in Figure 3.10 and departure diameter as well as gravity versus time in Figure 3.11. The curves indicate a close relationship among these parameters. A more detailed investigation is presented in Chapter 6.2 and Chapter 6.3.

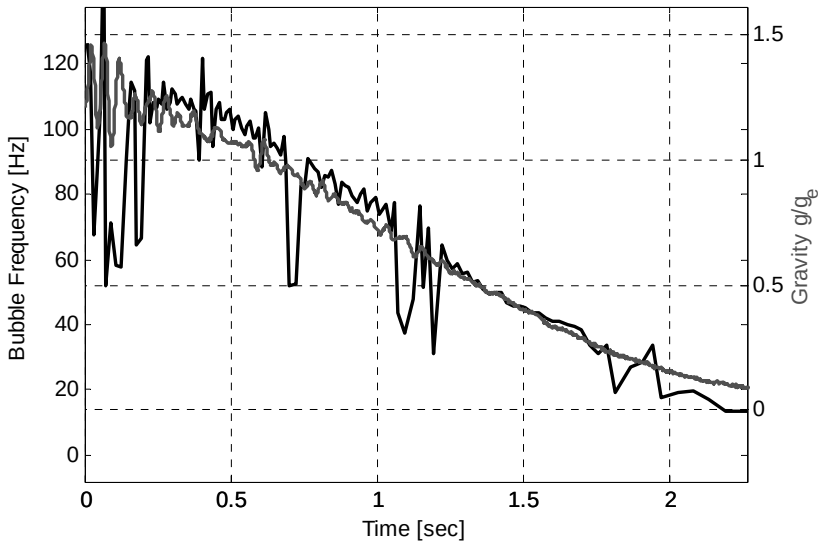

Figure 3.10: Bubble frequency and gravity versus time

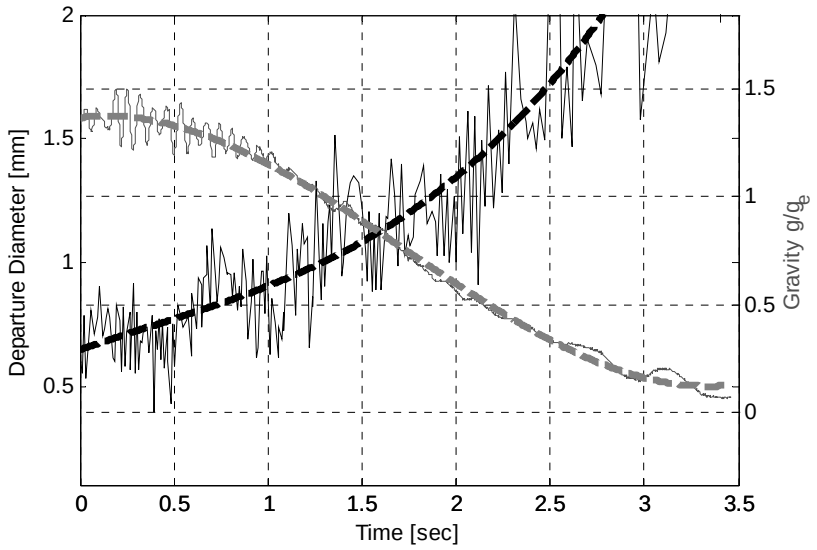

Figure 3.11: Departure diameter and gravity versus time

Bubble shapes, temperature field and local heat flux distribution for a complete bubble cycle is shown in Figure 3.12. The computation of the heat flux distribution is based on an unsteady energy balance at each pixel element of the IR image similar to the procedure described in Chapter 5.1.1. The presented bubble cycle is part of a sequence recorded during the transition. The gravity at the time of nucleation of the actual bubble is $g/g_e = 0.5$. Bulk liquid temperature was 38.4 °C and the heating power $\dot{q}_{el} = 6700\ \mathrm{W/m^2}$. The regarded bubble is nucleated immediately after the detachment of the previous one. No waiting time was measurable. A fluctuating cold spot can be observed in the temperature field. The pronunciation of a ring-shaped colder area caused by the high local heat transfer rates at the contact line is only slightly visible when the bubble foot is near its maximum diameter. Nevertheless, the imprint in the heat flux image clearly indicates the heat transfer distribution. The characteristic ring-shaped area of high heat flux at the contact line is visible from the early stage of the bubble growth. Any effect of the bubble growth on heat transfer to the bulk liquid is not observable. The heat flux in the adsorbed film region is nearly zero.
The investigation of the heat flux distribution using the described measurement technique in conjunction with the developed calculation algorithm was performed by the author at TTD in close cooperation with E. Wagner. It led to the revelation of the characteristic heat flux imprint at the bubble foot which is a significant contribution in fundamental boiling research.

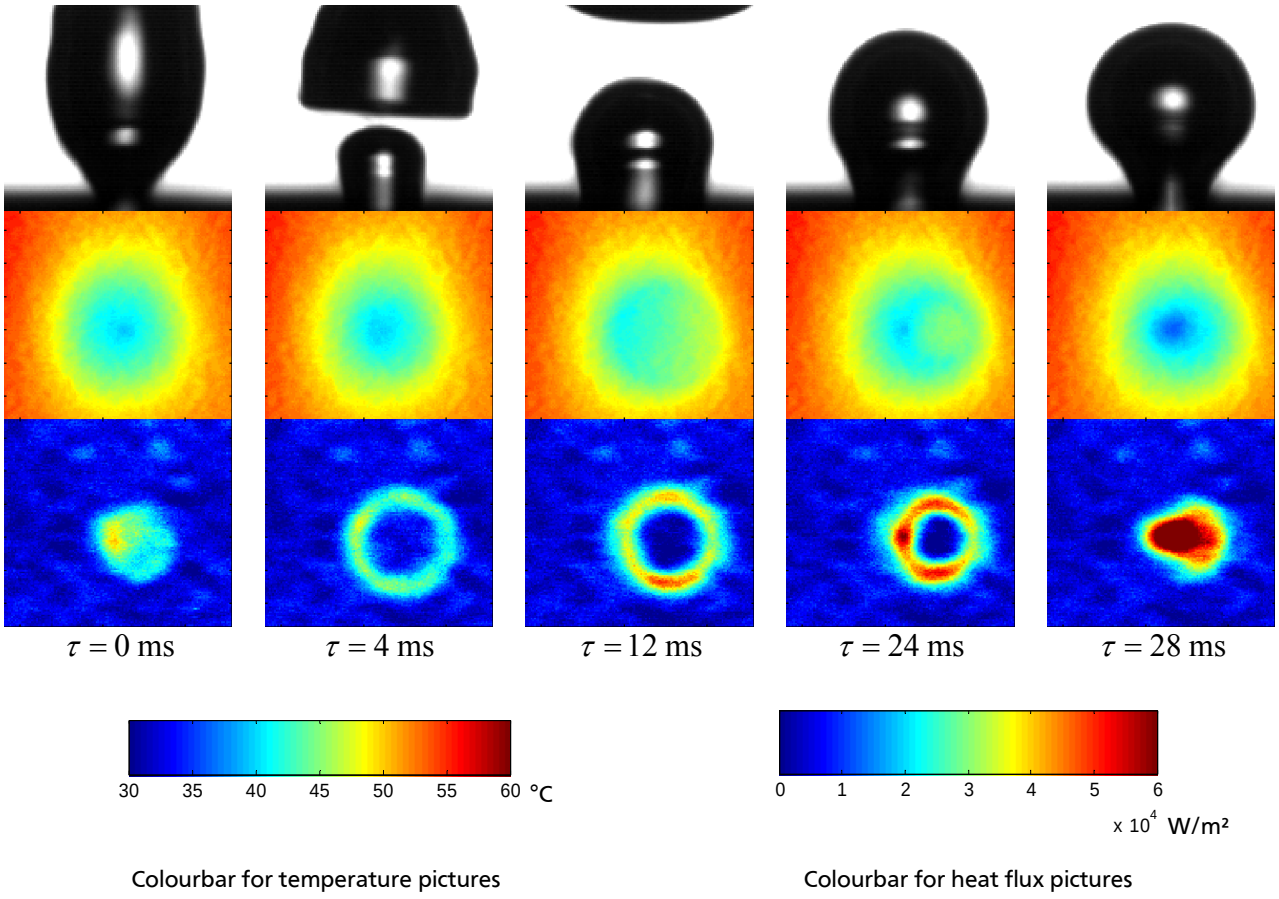

Figure 3.12: Bubble shape (top), temperature field (middle) and calculated local heat flux (bottom) for a bubble cycle

In order to quantify the role of the evaporation near the contact line regarding the overall vapour generation of the bubble a heat flow ratio was proposed as $\gamma_{bubfoot} = \dot{Q}_{bubfoot} / \dot{Q}_{bub}$ where $\dot{Q}_{bub}$ is the latent heat flow calculated from the development of the bubble volume in time. To identify the heat flow at the bubble foot $\dot{Q}_{bubfoot}$ a threshold was empirically defined as 1.3-times the electrical heating power $\dot{q}_{el}$ taking into account patterns and noise of the heat flux distribution in the far field of the bubble influenced area. The pixels with a heat flux above the threshold belong with high certainity to the ring-shaped maximum and their heat flow was summoned. The heat flow ratio of several bubbles is shown in Figure 3.13. Remarkable is a ratio of 0.2 at the early stage of the bubble growth for all investigated bubbles. The maximum ratio occurs close to the detachment of the bubble. The absolute value of the maximum is dependent on subcooling conditions and gravity. If the level of subcooling is high enough and/or the gravity low enough to allow a large portion of the bubble cap entering the subcooled region above the thermal layer the ratio can exceed 1 indicating the evaporation rate at the bubble foot is higher than the overall vapour generation of the bubble. In that case condensation overcomes the evaporation at the interface of the bubble hull. This phenomenon is illustrated in Figure 3.14 where the development of the ratio in time is shown for a bubble in low gravity and almost saturated liquid (Bubble A), medium gravity and highly sub cooled liquid (Bubble B) and medium gravity and almost saturated liquid (Bubble C).

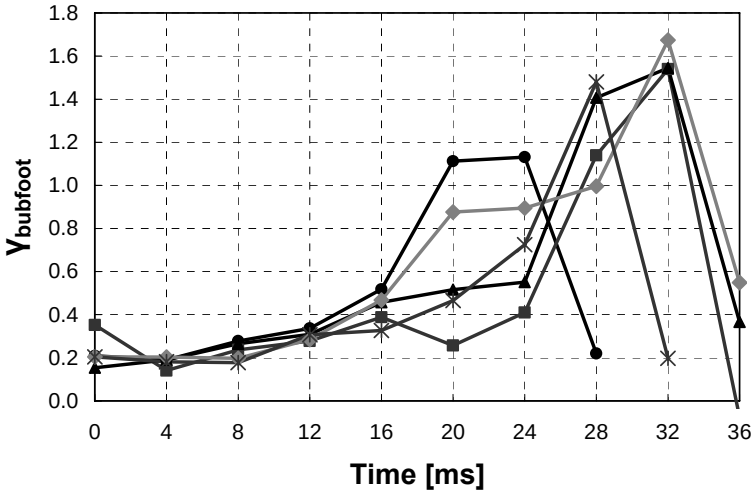

Figure 3.13: Heat flow ratios for several bubbles in low gravity at low sub-cooling

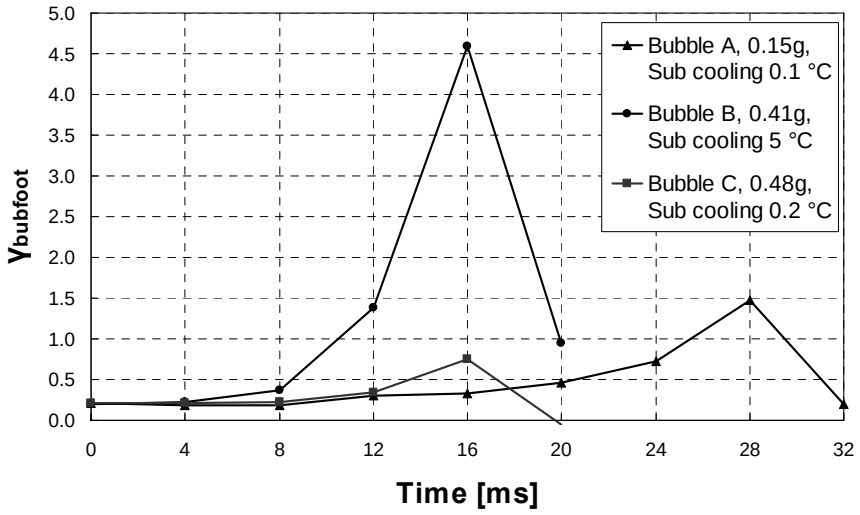

Figure 3.14: Heat flow ratios for bubbles at different gravity and sub-cooling levels

The heat flux imprint during bubble coalescence was also observed in this campaign. The imprint during coalescence of two sliding bubbles in microgravity is presented in Figure 3.15. As the bubbles merge a second ring is formed inside the contact line ring of the big bubble. This ring indicates high heat fluxes at the contact line of a droplet that is trapped inside the merged bubble.
Additionally, the merging of smaller satellite bubbles into a bigger one was observed. This process improves the heat transfer. It is similar to the phenomenon of a vapour cloud hovering above the heating surface in taking bubbles coming from the surface in microgravity as described in Chapter 2.3 with the difference that the big bubble is attached to the heating surface in the regarded case.
Studies of explosive bubble growth on a 6 μm titanium foil were also performed including the impact of the bubble eruption on the free floating system measured by accelerometers.

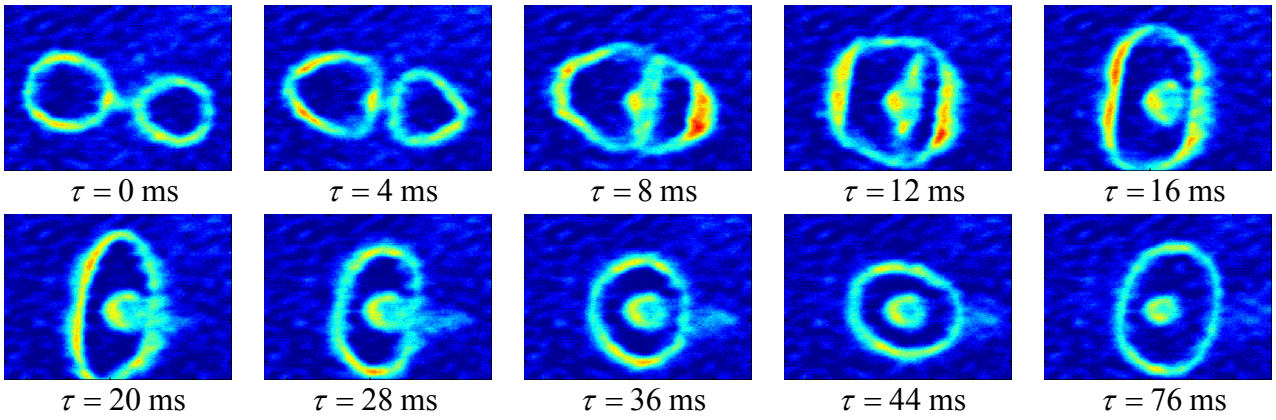

Figure 3.15: Heat flux imprint during bubble coalescence

3.3.4. 11th DLR PFC 2007 and 48th ESA PFC 2008

For the 11th DLR PFC 2007 a new test cell was designed. A photo of the test cell is shown in Figure 3.16. The design is based on a concept study for the RUBI experiment (see Chapter 8.1). Several stimuli and measurement techniques that are foreseen in the RUBI scientific requirements should be tested in the parabolic flight campaigns from 2007 to 2009. The new design was a further development and adaptation to parabolic flight of the test cell Wagner used for his ground experiments [128] which in turn is based on the design of the parabolic flight boiling cell employed in the 42nd ESA PFC 2006 (see Chapter 3.3.3).

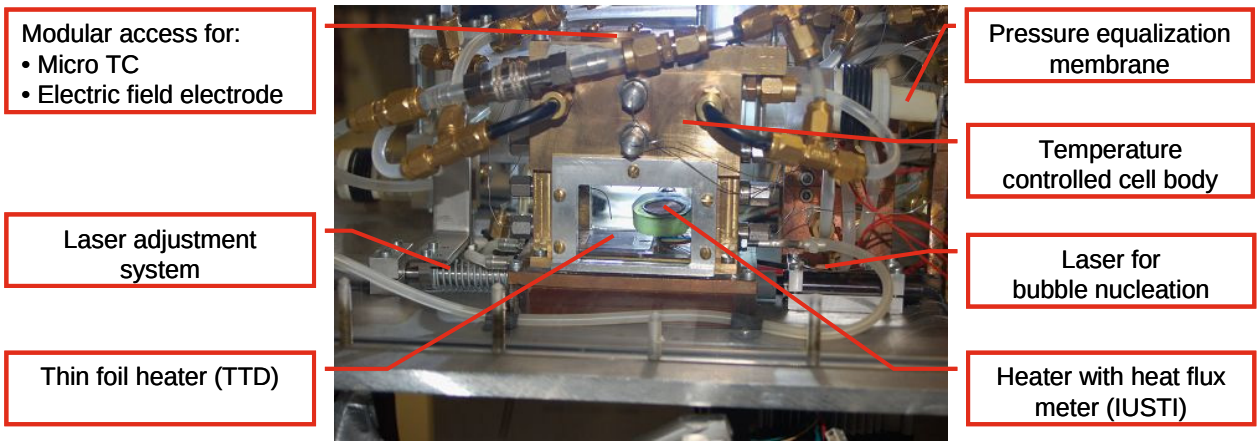

Figure 3.16: Boiling cell for the 48th ESA PFC 2008

The new test cell featured several enhancements like an improved temperature control system, water cooled electrodes at the heating foil, a second heater capability, modular access for additional stimuli (e.g. high voltage electrode or micro thermocouple) but the most significant modification was the integration of a bubble nucleation device.
Additional to the thin foil heater that was developed at TTD in Darmstadt a second heater was integrated into the test cell for the 48th ESA campaign 2008. The second heater was developed by the team of Professor Lounès Tadrist at IUSTI[13] in Marseille. The heater featured a heating foil[14] and a heat flux meter attached to a copper plate that is used as the boiling surface. The assembly

[13] Institute universitaire des systèmes thermique industriels
[14] MINCO, diameter 19.8 mm, resistance 10 Ω

was moulded in an epoxy resin. The temperature of the surface was measured by a built in thermocouple. The test of the heater was part of the preparation of the RUBI experiment. The preliminary results obtained in the 48th ESA campaign were promising. However, further test are mandatory.

In order to initially activate the nucleation site a high wall superheat is necessary as described in Chapter 2.1.5. This is generally accompanied with a large amount of energy stored in the thermal layer and resulting in explosive bubble growth and activation of neighbouring cavities. The challenge of activating a single nucleation site on demand was met by locally heating the back side of the foil at the location of the artificial cavity by a short energy pulse from a focused laser beam. This allows nucleating the bubbles under highly predefined thermal conditions and avoids high superheat except at the nucleation site. In microgravity due the absence of natural convection the thermal layer at the heated wall is created only by heat conduction in the liquid. Therefore, knowing the liquid properties, the heating power of the foil and the heating time before nucleation an exact calculation of the thermal layer is possible by using a one-dimensional conduction prediction for a semi-infinite media with an imposed heat flux [27]:

$$\Delta T_z = T(z) - T_0 = \frac{2\dot{q}}{\lambda_l}\sqrt{\frac{a\tau}{\pi}}\exp\left(\frac{-z^2}{4a\tau}\right) - \frac{\dot{q}z}{\lambda_l}\operatorname{erfc}\left(\frac{z}{2\sqrt{a\tau}}\right) \tag{43}$$

During the campaign the laser nucleation device has successfully been tested. However, the quality of the results was reduced due to the disturbance of the thermography measurements by the high heat flux introduced by the laser. The high heat flux and relatively large laser pulse time of 0.2 s was needed to activate the nucleation site. By integrating an artificial cavity with a lower superheat needed for activation both values, laser power and pulse time would significantly be reduced.

The technical details of the experimental setup are described in Chapter 4.

In order to nucleate a bubble in clearly defined conditions the measurement sequence shown in Figure 3.17 was started during the second half of the microgravity phase. This allowed the fluid motion induced by the transition phase to stop. Additionally it was ensured that no vapour or gas is present inside the test cell during the transition to minimize the fluid motion.

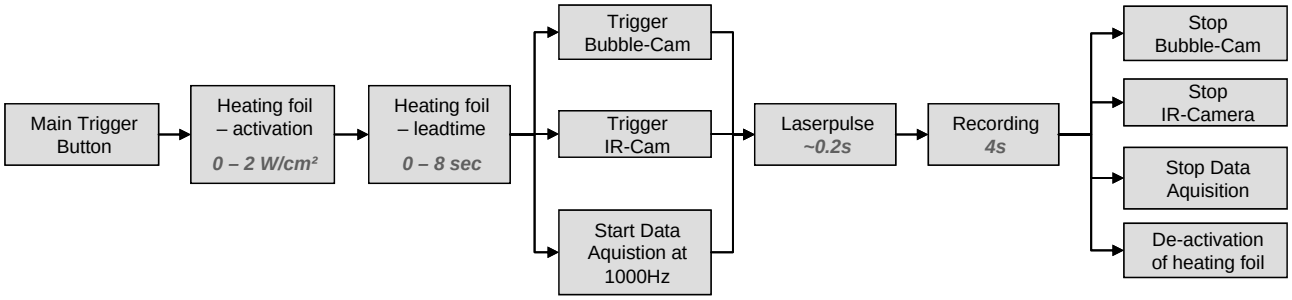

Figure 3.17: Procedure of a measurement sequence

The working fluid was homogenously tempered. Initially, the heating foil was deactivated during the transition to prevent fluid motion induced by natural convection. By manually pushing the trigger button the sequence is started, controlled by the data acquisition system. First, the heating foil is set to a desired heating power value for a defined time. During this lead time the thermal layer is created. Then, the high speed IR and greyscale cameras are started. Simultaneously, the sampling rate of the data acquisition system is set to 1000 Hz according to the camera frame rates.

Directly after the start of the cameras a laser pulse is shot at the back side of the foil activating the nucleation site.
Images of the bubble camera are shown in Figure 3.18. The first bubble detaches due to its own inertia. The rapid bubble growth was caused by the superheat energy stored in the thermal layer and by the laser introduced high heat flux. The following bubble detached very lately because the layer energy was already consumed by the first bubble and the laser pulse duration did not cover the growth of the following bubbles.

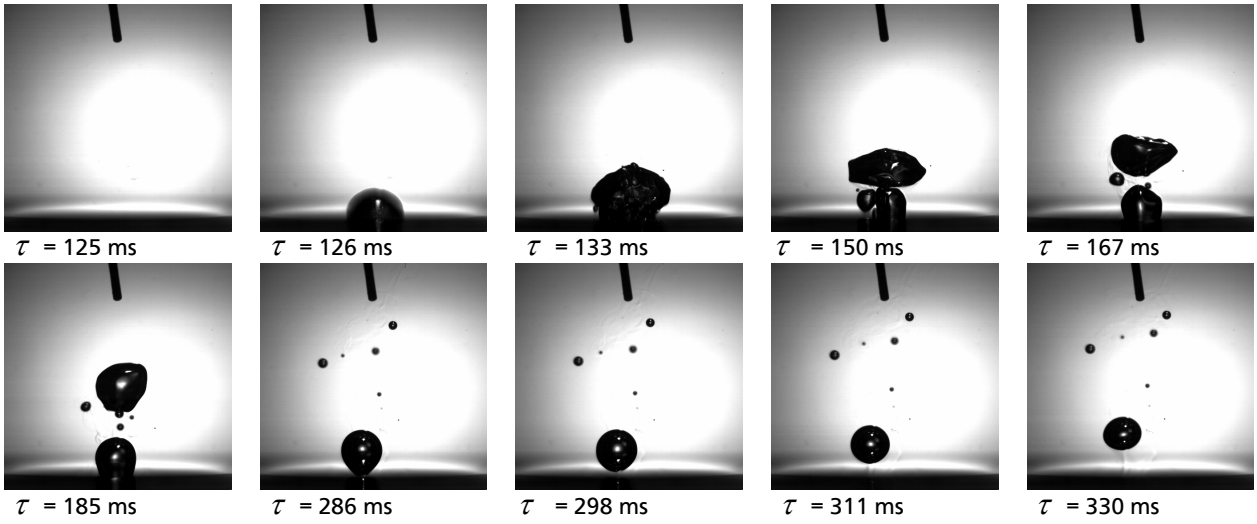

Figure 3.18: Bubble detachment by inertial forces

The growth of the following bubbles is thermodynamically controlled. The difference between inertia and thermodynamic controlled bubble growth is clearly visible in the presented case. The surface of the inertia controlled bubble is not smooth. Interface turbulence occurs due to its high velocity. The shape of the bubble is far from being spherical. It rather looks like the characteristic mushroom shape of an explosion (see Figure 3.19). This implies the assumption that the governed mechanisms are comparable.

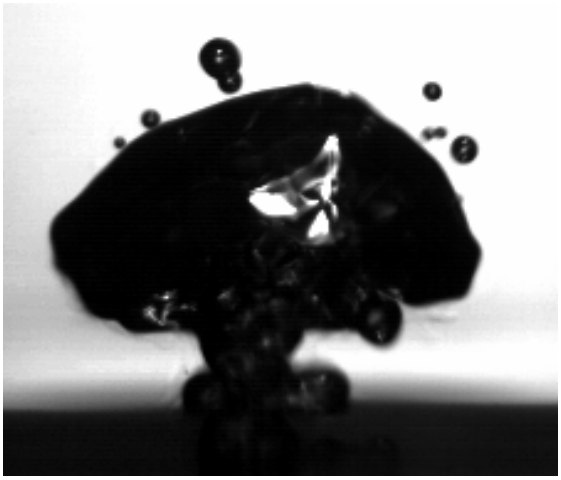

Figure 3.19: Mushroom-shaped vapour explosion

Thermodynamically controlled bubbles have a smooth interface. The bubble shape is nearly spherical as it can bee seen in Figure 3.18, bottom row. An interesting subject of further

investigations would be the transition between the thermodynamic and inertial controlled growth in microgravity.

In Figure 3.20 the development of the heat flux distribution during the laser induced bubble nucleation is presented. At $\tau = 22$ ms, just before the laser activation the heat flux was uniformly distributed. At $\tau = 92$ ms the laser was working but the nucleation site was still not active. An ellipsoid area of dark blue colour in the image indicates a value of the local heat flux below zero. This area of the foil is heated by the laser. At $\tau = 122$ ms, when the laser was still working, nucleation of the first bubble took place. The red ring indicates very high, positive heat flux to the bubble. The image at $\tau = 165$ ms shows already the heat flux imprint of the second bubble. The sharp ring of high heat flux displays the location of the slow moving micro region at the foot of the bubble. From $\tau = 165$ ms to $\tau = 282$ ms the bubble passes through a slow detachment process. The diameter of the bubble foot is decreasing until only a small dot of high heat flux can be seen.

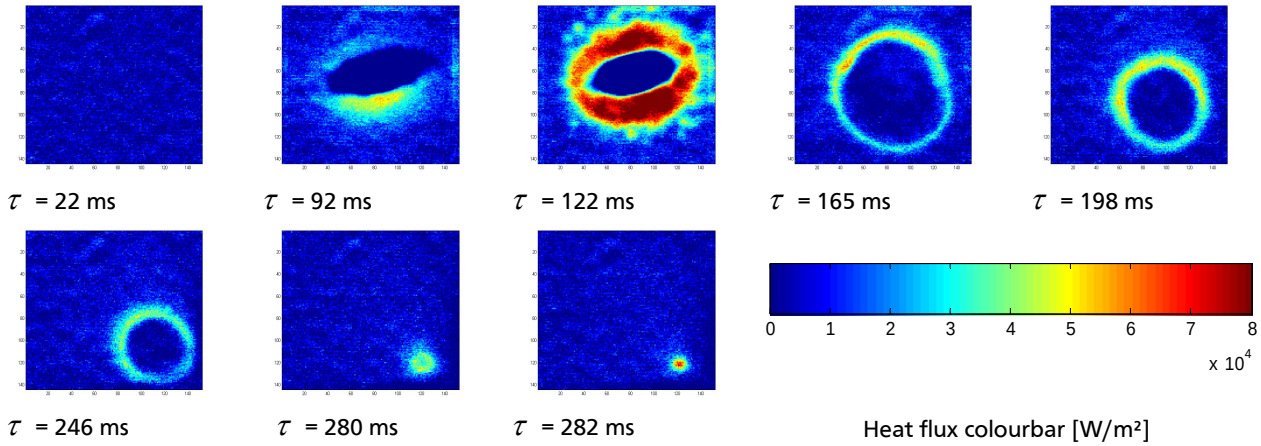

Figure 3.20:Heat flux during laser induced bubble nucleation

4. Experimental Method and Apparatus for the 50th ESA PFC in 2009

In this chapter the latest and most advanced version of the microgravity boiling setup as shown in Figure 4.1 is introduced. This setup was used in the 50th ESA PFC 2009. First, an overview on the setup is given. The basic measurement principle as described in Chapter 3.2 is shown with the modifications implemented for the 50th ESA PFC. Second, the thermography system which is a key element of the setup is explained in detail since much know-how was generated on this topic. Then the test cell is described stepwise from its central core element which is the nucleation site over the thin foil heater to the boiling cell as a whole including its sub-systems.

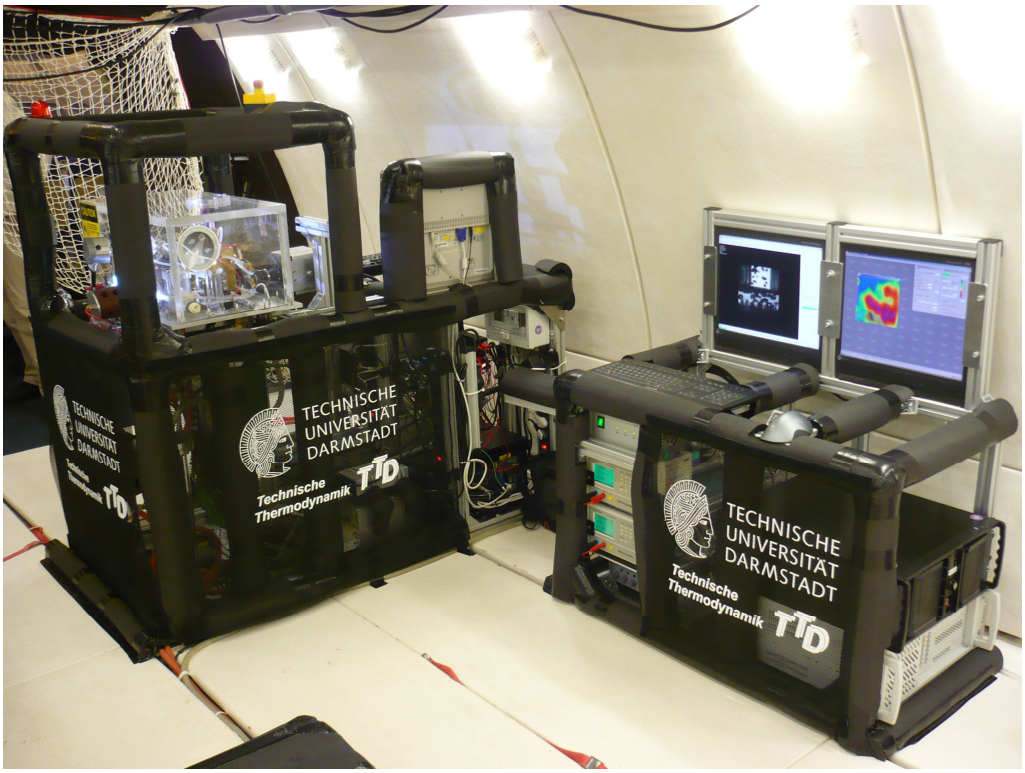

Figure 4.1: Parabolic flight setup 2009 in flight configuration on board the Airbus A300 ZERO-G

4.1. Experimental Setup Overview

The experimental setup used in the 50th ESA PFC 2009 is the latest and most enhanced version of the boiling test facilities for parabolic flights developed at TTD. Beside the scientific objectives it was also used for the preparation of the RUBI experiment for the ISS. The main requirements and functions of the experimental setup are:

- Measurement of heating wall temperature with high spatial and temporal resolution

- High speed imaging of bubble shapes synchronized to the measurement of heating wall temperature
- Synchronized acquisition of fluid and test cell temperatures, pressure, acceleration, voltage, current, etc.
- Activation of a single, artificial nucleation site on demand
- Accurate pressure and fluid temperature control for adjustment of saturation conditions
- Working fluid n-Perfluorohexane (nPFH)
- Second heater capability for the test of the IUSTI heater prototype as part of the RUBI preparation
- Implementation of a micro thermocouple (MTC) in the fluid above the nucleation site
- Integration of an electric field electrode above the nucleation site (alternatively to the MTC)
- Compliant to specific parabolic flight safety requirements (e.g. double containment)
- High reliability
- Exhaust of vapour and non-condensable gas

The measurement principle shown in Figure 4.2 is based on the basic principle already described in Chapter 3.2.

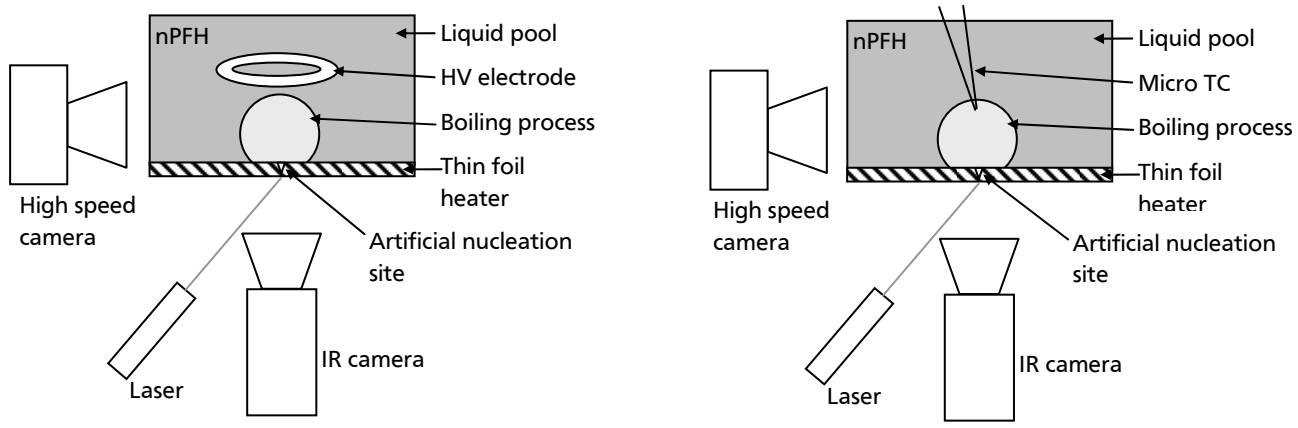

a) Electric field configuration

b) Micro thermocouple configuration

Figure 4.2: Measurement principle of the 50th ESA PFC

The basic principle is modified by the integration of the electric field electrode and the micro thermocouple, respectively. These two systems would disturb each other. Further, they use the same access slot to the test cell. Therefore, they can not be used at the same time and have to be changed between two flights.

In order to activate the nucleation site on demand a laser was integrated that is focused at the back side of the heating foil where the artificial cavity is located on the fluid side. A detailed description of the sub-systems can be found in the following chapters.

A scheme of the experimental system is shown in Figure 4.3. The test cell is located inside a Plexiglas container that is closed by an aluminium base plate. The container is the second containment (safety purposes) in which the pressure for the experiment is adjusted by a vacuum pump with controller[15]. A flexible latex membrane equalizes the pressure between the second containment and the working fluid in order to prevent tension on the heating foil due to a pressure

[15] KNF LABOPORT SD

difference between the fluid and the compartment below the foil. The pressure is measured by a transducer[16] connected to the data acquisition system[17] (DAQ).

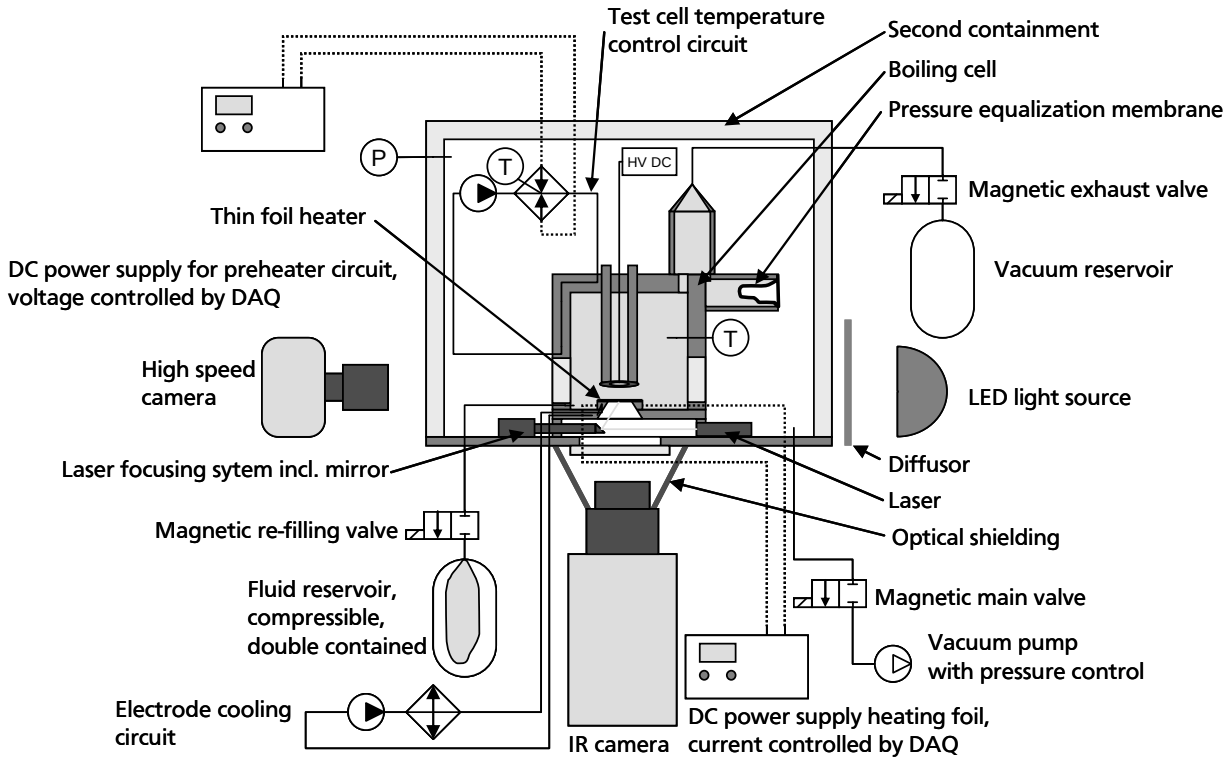

Figure 4.3: Scheme of the experimental system in electric field configuration

The boiling cell is mounted on a socket that contains the laser for bubble nucleation and the corresponding focus adjustment system with a mirror to direct the beam onto the foil. Optical access to the foil is enabled by an infrared transparent window[18] made of CaF_2. In order to prevent any laser radiation exiting to the ambience for safety reasons the compartment below the heating foil including the space between IR window and IR optics is optically shielded.
The heating foil is connected to a power supply[19] capable of delivering high currents (0-40A). The output current is controlled by the DAQ via a 0-10V input.
The walls of the boiling cell which are made of brass are equipped with flow channels. A water cooling circuit is connected to these channels. The water is driven by a pump[20] through cylindrical copper heat exchangers. The temperature of these copper cylinders is controlled by the DAQ via adjustable power supply[21], heater cartridges[22] and thermocouples for feedback. With that system the test cell walls could precisely be tempered and, thereby, the subcooling or superheating conditions of the boiling process are well adjustable.
To prevent boiling at undesired places (e.g. at the foil electrodes, foil edges) the copper support of the heating foil is also equipped with flow channels connected to a second water circuit. The water

[16] JUMO dTrans p30
[17] National Instruments PCI-6289 + SCXI system
[18] Korth Kristalle GmbH
[19] EA-PS 3016-40B (0-16V, 0-40A)
[20] Laing DDC-1T
[21] EA-PS 3032-20B (0-32V, 0-20A)
[22] HS Heizelemente GmbH, S/HS-4.5/50/100/42-A

is pumped by a second pump[23] through a copper block located outside the second containment. The copper block is attached to a peltier element. Heat is transferred from the hot side of the element to the ambient air by forced convection generated by a fan.
An accumulation reservoir is attached to the highest point of the test cell. The vapour produced by the boiling process rises into the reservoir at $g/g_e > 0$ and condenses there. Also, non-condensable gas can be exhausted from the tip of the reservoir during the degassing procedure by opening a magnetic vale to a vacuum vessel. The vacuum vessel provides pressure levels below the test cell pressure to enable the exhaust. Additionally, the exhaust can be used if the vapour generation exceeds the condensation rate.
The electric field electrode is connected to a high voltage power supply[24] that is also located inside the second containment for safety reasons. The voltage of the electrode is controlled by the DAQ.
The bubble shapes are recorded through the Plexiglas container and the Plexiglas windows of the boiling cell by a high speed camera[25] in conjunction with 50 mm lenses[26] and 40 mm distance tubing. The bubbles are illuminated from behind by a high power LED light source[27]. The light spot is homogenised by a diffuser between the source and the second containment.
For filling and re-filling purposes a fluid reservoir is connected to the boiling cell. No gas is present in the compressible reservoir[28] that is double contained. Since the working pressure in the cell is always lower than the ambient pressure in the fluid reservoir re-filling can be accomplished by only open the magnetic valve. The fluid is sucked into the test cell due to the pressure difference.

4.2. Thermography System

One aim of the experiment is to obtain detailed information about the wall temperature distribution at the foot of a vapour bubble in a dynamic boiling process. This causes three main requirements for the measurement system:

1. High spatial and temporal resolution to resolve the expected micro scale temperature drop at the contact line
2. Fast response time for the highly dynamic boiling process
3. Access to the wall temperature by the measurement system with a minimum of disturbance of the boiling process

Up to date only two thermography systems that meet the requirements are known. Un-encapsulated TLCs have been used in previous parabolic flight campaigns (2004, 2005). In conjunction with a high speed colour camera and a long distance microscope this thermography system provides very high spatial resolution ($\sim$1 μm/pixel). A detailed analysis of the frequency response of the TLC system was performed by Wagner and Stephan [129]. They found out that it is possible to quantitatively observe temperature fluctuations up to a frequency of 70 Hz but the temperature signal is significantly attenuated and phase-shifted. Therefore, quantitative measurements with TLCs at a dynamic boiling process were only possible in microgravity at low bubble frequencies (see Chapters 3.3.1 and 3.3.2). Additional drawbacks of the TLCs are the sensitivity regarding superheating and ageing and the narrow temperature range of only 10 K (50 °C – 60 °C).

[23] EHEIM innovatek, PCPS 1104
[24] Brandenburg, Model 590 Series
[25] PHOTRON Fastcam 1024PCI
[26] COSMICAR/PENTAX TV Lens 50 mm 1:1.4
[27] Beautiful Light Technology Corporation, High Power LED Spotlight, 3W, 20°
[28] Fresenius freeflex infusion bag 250 ml

The second measurement system that meets the requirements is high speed infrared thermography. The temperature of a surface is measured by metering the thermal radiation in a certain wavelength band emitted by this surface. The physical basics and measurement principle is explained in the following.

Theory of IR thermography

The theory of IR thermography is explained in this section. The common nomenclature for optical expressions is used and may interfere with the defined nomenclature of the thesis.

Thermal radiation is defined as "*radiant energy emitted by a medium that is due solely to the temperature of the medium*" [115]. The corresponding property is the emittance ε that describes the ability of a body to emit thermal radiation [89]. Furthermore, the radiation coming from a body is also dependent on the "illumination" of the body. A part of the incident radiation is reflected, a part is absorbed by the medium and a part may be transmitted through the body. Therefore, three optical surface properties have to be accounted:

1. The reflectance ρ
2. The absorptance α
3. The transmittance τ

The value of each parameter is in the range of 0 to 1. Energy conversation leads to the following relationship including the dependency of the properties on the wavelength λ:

$$\rho_\lambda + \alpha_\lambda + \tau_\lambda = 1 \tag{44}$$

According to Kirchhoff's law the emittance ε_λ is equal to the absorptance α_λ in a system that is in thermodynamic equilibrium [115]. Hence, Equation (44) can be transformed into

$$\rho_\lambda + \varepsilon_\lambda + \tau_\lambda = 1 \tag{45}$$

As it can be concluded from Equation (45) the emittance ε is the most important surface property for infrared thermography. At low emittance near 0 the radiation coming from a body is less dependent on its temperature but strongly dependent on the environmental radiation. An emittance of $\varepsilon = 1$ indicates that all radiation coming from a body is due to the temperature of the body. Incident radiation from the ambience is only influencing by heating the body, no radiation is reflected or transmitted. Such a body is called "black-body".

The spectral radiation $e_{b\lambda}$ of a black-body is expressed by Planck's law:

$$e_{b\lambda}(T,\lambda) = \frac{2\pi h c_0^{\,2}}{n^2 \lambda^5}\left[e^{(hc_0/n\lambda kT)} - 1\right]^{-1} \tag{46}$$

This function represents the energy emission per unit time and per unit area for a specific wavelength from a black-body's surface. The equation includes several constants:

- Planck's constant: $h = 6.62606896 \cdot 10^{-34}\,\mathrm{Js}$
- Speed of light: $c_0 = 299792458\ \mathrm{m/s}$
- Boltzmann's constant: $k = 1.3806504 \cdot 10^{-23}\,\mathrm{J/K}$
- Refractive index: $n \approx 1$ for gases (air) in the beam path

The spectral radiation for a black-body at a temperature of 330 K is shown in Figure 4.4a. The total energy radiated from a black-body's surface unit e_b is the integration of the equation (46) over the wavelength:

$$e_b(T) = \int_0^\infty e_{b\lambda}(T,\lambda)d\lambda \tag{47}$$

The integration leads to Stefan-Boltzmann's law:

$$e_b(T) = n^2\sigma_s T^4 \tag{48}$$

where σ_s is the Stefan-Boltzmann constant:

$$\sigma_s = \frac{2\pi^5 k^4}{15{c_0}^2 h^3} \tag{49}$$

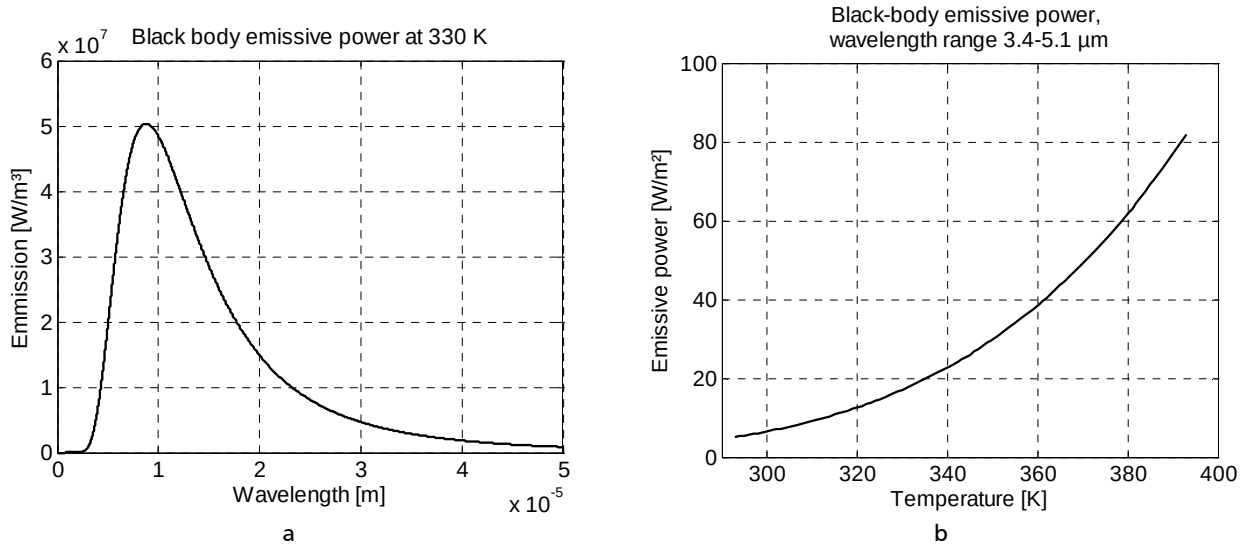

Figure 4.4: Black-body radiation: a) emission at 330K; b) power density at a wavelength range of 3.4 µm to 5.1 µm

The spectral range of the used high speed infrared camera[29] is between $\lambda_1 = 3.4\,\mu\text{m}$ and $\lambda_2 = 5.1\,\mu\text{m}$. This spectral range is often called mid-wavelength infrared (MWIR). Hence, the emissive power that can be detected by the camera can be calculated by integrating equation (46) over the spectral range:

$$e_{b,MWIR}(T) = \int_{\lambda_1}^{\lambda_2} e_{b\lambda}(T,\lambda)d\lambda \tag{50}$$

The resulting curve is presented in Figure 4.4b. It expresses the power radiated by a black body per unit area that can be detected by a MWIR camera in case that all radiation is caught by the lenses and focused on the detector chip. In the real case the power is reduced by the fact that only a portion of the radiation enters the lenses. This reveals an approach to improve the measurement quality by enhancing the portion entering the lenses.

[29] Thermosensorik CMT 256 M HS

A grey-body is defined as a body with an emittance between 0 and 1 that is not dependent on the wavelength. Thus, the spectral curve of a grey-body is the spectral curve of a black-body multiplied by the emittance. The emittance of an actual surface is more or less dependent on the wavelength. However, Figure 4.4b clearly indicates the basic shape of the curve that is a blend of two dependencies resulting from two theoretical extremes. The first extreme would be the case that the camera spectral range is infinite ($\lambda_1 = 0,\ \lambda_2 = \infty$). In that case the emissive power at the camera detector is dependent on $e_{b,cam} \sim T^4$ as it is derived from the Stefan-Boltzmann law. The second extreme is an infinitesimal small spectral range ($\lambda_1 = \lambda_2 = const$). The dependency of the emissive power on the temperature would be $e_{b,cam} \sim (e^{C_1/T} - 1)^{-1}$. This consideration helps to identify a mathematical calibration procedure for the conversion of the camera raw data into temperature. Furthermore, several effects play a role that may influence the dependency. These effects are the spectral emittance of the surface, the response characteristic and non-linearity of the detector chip, the influence of the camera electronics and data conversion algorithm. Nevertheless, during the development of the calibration procedure the dependency of the camera raw data on T^4 was chosen since the best data fittings have been obtained with this relationship.

IR camera operation principle

The core element of the IR camera is a semiconductor matrix of infrared detectors the so called focal plane array (FPA). Several semiconductors can be used in such type of cameras (e.g. indium-antimonite, indium-arsenide, lead-selenide, lead-sulfide, and mercury-cadmium-telluride). Mercury-cadmium-telluride (MCT, HgCdTe) semiconductors are implemented in the FPA of the used camera. An overview of HgCdTe-detectors is provided by Norton [87]. The spectral range of an HgCdTe-detector can be optimized for its application by varying the alloy composition. A typical composition for MWIR is $(Hg_{0.7}Cd_{0.3})Te$. The impact of a photon excites an electron from the valence band into the conduction band. A precondition is a minimum photon energy. The minimum photon energy is equal to the band gap that is adjustable for HgCdTe semiconductors in the range from 0.7 μm to 25 μm. For the proper operation an HgCdTe-IR-detector needs to be cooled down to approximately 77 K. This is accomplished by a built in cryogenic stirling cooler. Most commonly helium is used as working fluid for the stirling cooler.

The used camera has a FPA size of 256 x 256 pixels at a pixel pitch of 40 μm x 40 μm. The maximum full frame rate is 885 Hz at an integration time of 1.1 ms. The integration time is comparable to the shutter time of a normal digital camera. During the integration time the detector accumulates the output generated by photon impact. Hence, a higher integration time means a stronger, less noisy signal as long as the detector is not saturated. For the calculation of the maximum frame rate the operation mode of the camera has to be taken into account. Generally the cameras work in two modes:

- Integrate then read (ITR)
- Integrate while read (IWR)

In the first mode ITR the read out time of the detector has to be added to the integration time reducing significantly the maximum frame rate. In the second mode (IWR) the electronic is already reading out the detector while it is still integrating. This mode is not as robust as ITR but the read out time is not influencing the frame rate. The measurements have been performed in the IWR mode. In order to enable a frame rate of 1000 Hz not the full FPA was used but a sub array with a size of 224 x 224 pixels. The integration time was 0.8515 ms. In conjunction with the sub array size a maximum frame rate of 1105 Hz can be achieved. To set the frame rate on a distinctive value a TTL square wave with a frequency of 1000 Hz was generated by the data acquisition system and

applied at the trigger input of the camera. The IR images were triggered by the rising edge of the signal.
Standard MWIR lenses with a focal length of 50 mm have been used in conjunction with 75 mm of distance tubes between camera and lenses. The resolution was determined by imaging a glass scale. A number of 169 pixels correspond to 5 mm. Hence, the resolution is 29.586 μm/pixel.
During each measurement sequence 4000 images have been recorded. The images were stored as tab-delimited ascii-files containing the raw data of the IR chip. The signal of the single detector in the FPA is converted in this raw data format by the camera electronics. The digital resolution of the AD-converter is 14-bit. The conversation algorithm is company confidential and further information is not available. The raw data is a dimensionless value between 0 and 16383 (2^{14}). The conversion of the raw data to the temperature field is described in Chapter 5.1.
An important specification of the FPA and the whole thermography system is the Noise Equivalent Temperature Difference (NETD) which expresses the noise performance. It is defined as the standard deviation of the single pixel signals (RMS noise) converted into a corresponding temperature difference [89]. While the NETD value of the FPA is provided by the camera manufacturer, for the determination of the NETD of the whole thermography system also the optical path has to be taken into account. This includes for example the transmission through any medium, the reproduction scale and the relative aperture of the lenses (f/#).

4.3. Nucleation Site

The aim of the experiment is to investigate boiling at a steadily working single artificial cavity that is located in the middle of the FOV. Creating an artificial nucleation site in a thick heating wall is an easy task. The creation of a reliable nucleation site in a 20 μm thick stainless steel foil is challenging especially taking into account the requirements:

- Low activation superheat
- Reliable operation
- FC-72/nPFH as working fluid (highly wetting and air solution capability)
- Distinctive location
- Puncturing of the foil has to be avoided
- No pinning of the contact line at the cavity edges
- Small influence area

To determine the order of magnitude for the artificial cavity the approach of Hsu [47] was applied as it is described in [9] (see Chapter 2.1.5, Equation (9)).
The range of the active cavity sizes are illustrated in Figure 4.5. The approach gives an indication about the order of magnitude for the manufacturing of the cavity. For a desired superheat of less than 10 K the mouth radius of the nucleation site should be in the range of 0.7 to 30 μm.
Several manufacturing techniques have been tested. Some of these techniques were quite low sophisticated like the technique used for the 42nd ESA PFC. The foil was punctured manually using a fine needle and sealing the hole afterwards by rapid glue. Although the influencing area was large ($d \sim 0.1\,\mathrm{mm}$) and visible due to a small bump in the thermography image the nucleation sites created with this technique had a comparatively low activation superheat and high reliability. Otherwise, a successful experiment with the TLC thermography system would not have been possible. Not the punctured hole but the fissured structures that can be seen in Figure 4.6a created

by the rapid glue inside the hole were assumed to serve as nucleation sites. Nevertheless, the danger of leakages and the large influence area issue remained.

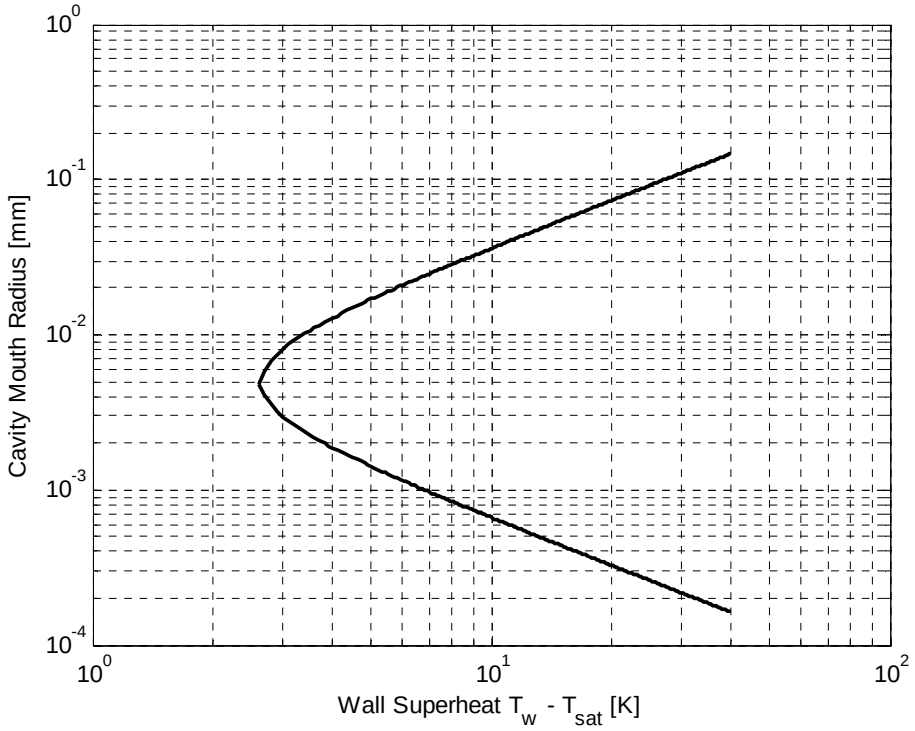

Figure 4.5: Predicted range of active cavity sizes for FC-72/nPFH using Hsu's analysis

Artificial cavities with highly defined geometry could be manufactured by focused ion beam (FIB) sputtering. The surface molecules of the foil are excited by the impact of heavy Gallium ions.
Several cylindrical cavities have been tested. To enhance the probability that at least one of the cavities is functioning several cavities have been created next to each other as it can be seen in Figure 4.6b. Cavities with 20 μm diameter and almost 20 μm depth were the most reliable nucleation sites as also reported by Wagner [128]. However, large initial superheat was required to activate these sites and still approximately 30% of the manufactured cavities failed. Another main drawback of this technique are high manufacturing costs.

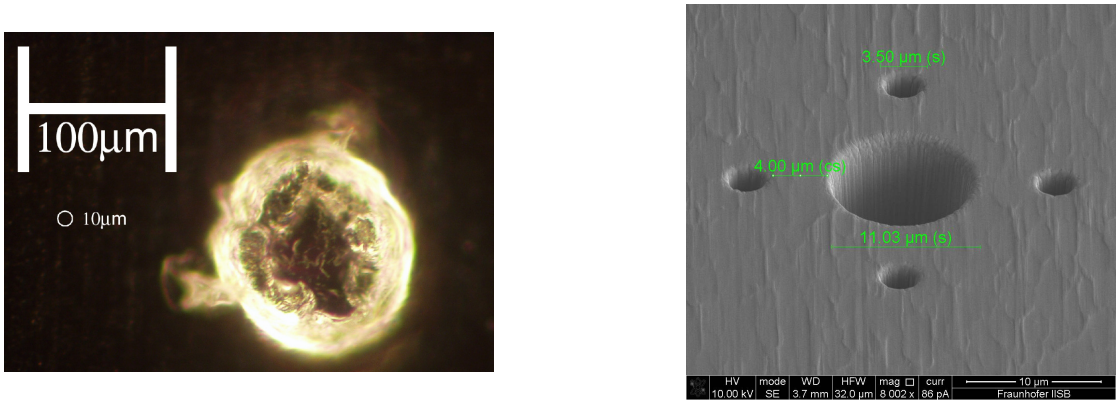

a: Punctured hole

b: FIB manufactured cavities

Figure 4.6: Artificial nucleation sites: a) punctured hole; b) FIB manufactured cavities, large hole D=11.03µm, small holes D=3.5 µm - 4 µm

According to Hsu the theoretical equilibrium superheat for a cavity with a diameter of 20 μm would be 3.3 K. The measured superheat was 30 K to 40 K corresponding to a site diameter of 0.2 μm. This leads to the conclusion that not the cylindrical cavity serves as nucleation site but sub-structures inside this cavity as it was already assumed for the site used in the 42nd ESA PFC. This conclusion is also supported by Wagner.
Smaller cylindrical cavities with a diameter of 1 μm have not successfully been tested. It seems that the approach of Hsu fails in the prediction of the maximum cavity mouth radius for the actual case. The entrapment of nPFH vapour is hindered by its properties like low surface tension and high wettablility. These properties reduce the ability of a cavity to hold a vapour embryo. Additionally, due to the high solubility of air in nPFH (48 ml air/100 ml FC-72/nPFH [4]) gas entrapments may vanish quickly.
For the 50th ESA PFC a new method of creating an artificial nucleation site was developed. The principle is based on what was learned from both the low sophisticated punctured site and the high sophisticated FIB cavity. Instead of manufacturing a defined microstructure a fissured surface should be created in a tiny area in the middle of the foil.
It is very likely that one or more cavities are within that area requiring a low activation superheat. Even if more than one site is active in the area the distance between the sites is small enough that they appear as one.
The treatment of the surface is performed by electrolytic abrasion. The heating surface was masked by transparent tape leaving out a tiny hole in the middle of the foil. Several techniques have been applied to implement the hole in the tape (e.g. laser cutting). The hole for the foil used in the flights was manually created by using a fine needle. However, significant improvement potential exists for the masking technique.
The hole was filled with NaCl-Solution in that way that the solution is only in contact with the foil at the bottom of the hole. The foil was attached to the positive pole of a DC power supply, therefore acting as anode for the electrolytic process. A copper wire serving as cathode was inserted into the droplet of the NaCl-Solution above the hole. By applying a voltage of 27 V for less than 1 s foil material is removed where the foil is in contact with the solution.
At the foil anode negative charged Cl-ions take an electron from the foil and become Cl-molecules. The chlorine immediately reacts with the ferrite of the foil to $FeCl_3$.
The electrolytic abrasion is not acting uniformly at the foil material. The abrasion rate is different among the alloy components. Fissured structures are created whose length scale is in the order of the grain boundaries of the stainless steel alloy. The advantages of the cavities created by electrolytic abrasion are:

- High reliability (~75 %)
- Inexpensive manufacturing
- High improvement potential

The disadvantage is the undefined, not reproducible geometry. Instead of a single nucleation site, the electrolytic abrasion technique creates rather an ensemble of nucleation sites with different sizes. It is not known which parts of the fissured structure in the main dimple act as nucleation sites. So, it is not possible to create a cavitiy with a defined activation superheat using the described technique. However, this has also not yet been achieved with any other technique. The cavity used in the 50th ESA PFC is shown in Figure 4.7. The overall size is approximately 190 μm x 130 μm. The fissured structures at the bottom of the main dimple are clearly visible. Any influence of the nucleation site on the electrical heat flux uniformity was not observed.

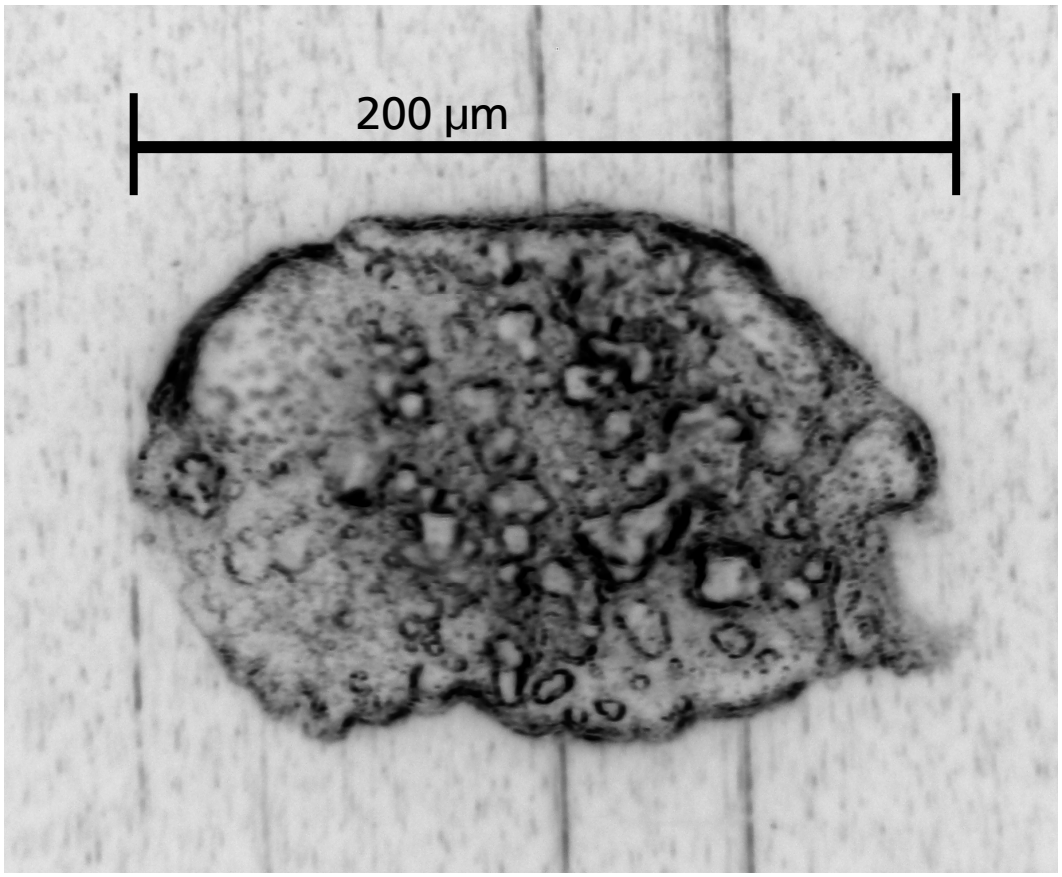

Figure 4.7: Artificial cavity used in the 50th ESA PFC created by electrolytic abrasion.

4.4. Thin Foil Heater

The heating foil has to be considered as part of the thermography system. The temperature of the foil is measured at its back side. The temperature imprint imposed by the boiling process on the foil is attenuated at the back side. The attenuation is dependent on the foil material and thickness. However, the chosen foil thickness of 20 μm is the result of a trade-off between two contrary requirements. On the one hand the foil should be as thin as possible to minimize the blurring of the temperature signal. On the other hand the boiling process is significantly influenced by the foil thickness. The bubbles do not benefit from the heat that is normally stored in a thick heating wall and can be conducted to the bubble foot due to the high thermal conductivity. Heat capacity and lateral conduction in a thin foil are limited. The boiling behaviour may be atypical from a "real" process as expressed by Kenning et al. [58].
The results of the measurements on a 20 μm foil showed the compromise. Kunkelmann and Stephan [67] performed numerical simulations of a boiling process on a 50 μm stainless steel foil. They evaluated the blurring of the temperature signal (see Figure 2.8). A significant attenuation of the sharp temperature drop at the contact line was observed but except from this sharp drop the temperature signal corresponded on both sides. Therefore, the assumption of equal temperatures at both sides could be justified with good agreement.
The emittance of the back side of the heating foil should be very close to $\varepsilon = 1$. For this reason the back side is coated with a thin film of black paint[30].

[30] KONTAKT CHEMIE Graphit 33, CRC Industries Deutschland GmbH

The heating foil is the core of the thin foil heater. A section of the thin foil heater is shown in Figure 4.9. Its main functions are:

- Support of the heating foil
- Easy foil exchange
- Connection to current source
- Providing an undisturbed view over the boiling surface
- Prevention of boiling at undesired places
- Providing optical access to the back side of the foil for the IR camera
- Sealing of the test cell

A piece of stainless steel foil (1.4301, 33 mm x 22 mm) is glued onto its copper support using heat conductive tape[31]. The heat flux generated by the electrical current is conducted through the tape into the copper support. Since the tape covers the entire back side of the foil except the FOV cut out for the optical access, the temperature of the foil is significantly lower in the covered part than in the cut out. This prevents the activation of cavities on all parts of the foil except above the cut out. The foil cutting process generally creates a bumpy border where the foil is not well attached to the heat conductive tape. Thereby created cavities at this border may be activated at lower superheat than the artificial cavity in the middle of the foil. The bubbles created at these cavities would block the view of the high-speed camera and, therefore, have to be prevented. Beside its functions of foil attachment and thermal connection the heat conductive tape seals the foil and the support and isolates the foil electrically from the copper support. The cut out has a diameter of 15 mm where the foil is covered with black paint. The described element including copper support, foil, tape and coating is in the following named as foil carrier and shown in Figure 4.8. Due to a reliability of the nucleation site of less than 100% several of these foil carriers have been manufactured and prepared in advance of the parabolic flight. The foil carrier allows a quick and easy foil exchange.
As shown in Figure 4.9 and Figure 4.10 the foil carrier is mounted on the base plate of the boiling cell. Both parts are sealed by a gasket. The heating foil socket is framed by Plexiglas. The Plexiglas frame holds the electrodes for the heating foil. The electrodes are pressed against the foil by two headless screws each. Electrical connection of the electrodes is conducted through the cell base plate and is sealed and electrically isolated by a gasket. A second Plexiglas frame surrounds the whole assembly to achieve a flat surface at the bottom of the cell.
The base plate is equipped with flow channels for the second cooling water circuit.

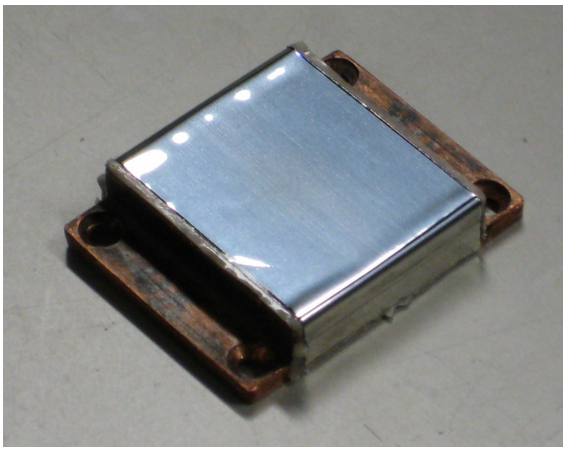

Figure 4.8: Foil carrier

[31] 3M, 8940

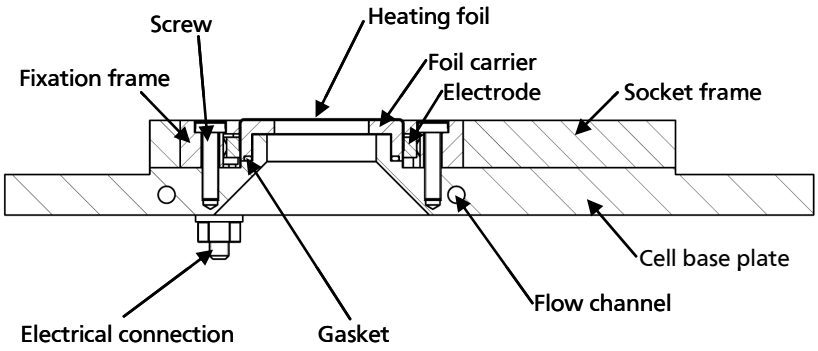

Figure 4.9: Section of the thin foil heater

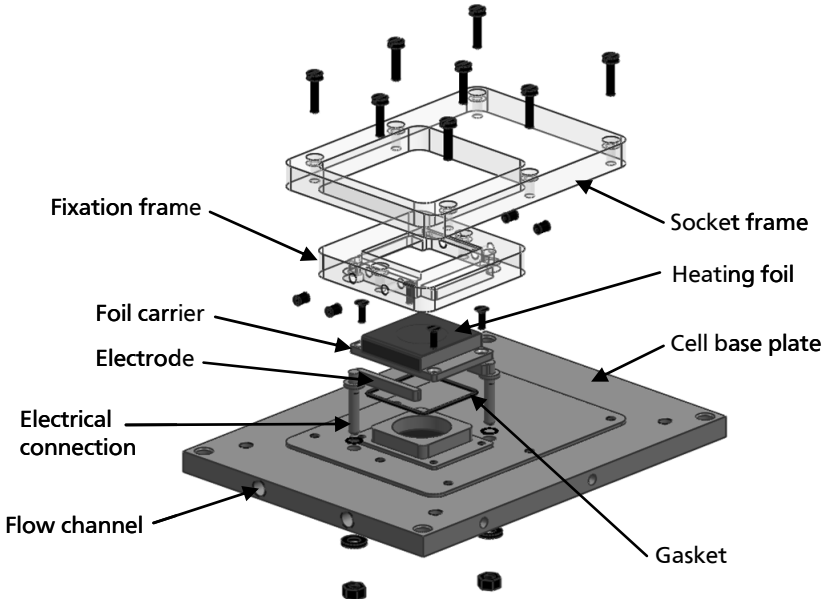

Figure 4.10: Exploded view of the thin foil heater CAD model

4.5. Boiling Cell

A section of the boiling cell is shown in Figure 4.11. The cell is mounted on the thin foil heater. It is box-shaped and has an inner width of 78 mm, an inner depth of 58 mm and a height of 82 mm. The test cell walls and top plate are made of brass and are equipped with flow channels to control the cell temperature. The internal roof of the cell is inclined and a connection at the highest point leads to the accumulation reservoir sitting on top of the test cell. Thus, vapour and non condensable gas enters the reservoir at gravity levels of $g/g_e > 0$ and is re-condensed or could be exhausted at the reservoir's top. The reservoir is made of Plexiglas to allow the observation of the filling state. A second outlet in the bottom of the reservoir is connected to the pressure equalization system. This consists of a Plexiglas cylinder and a Latex membrane. Therefore, the pressure in the cylinder is equal to the pressure in the second containment that includes also the compartment below the heating foil. Hence, the pressure difference at the heating foil is only the hydrostatic pressure due to the height of the membrane above the foil.

The boiling cell features two Plexiglas windows on one optical axis. The window on the front side is for optical access by the high speed bubble camera and the back side window is for bubble illumination. Optional, the heater developed by Tadrist's team at IUSTI in Marseille could be attached at the backside window.

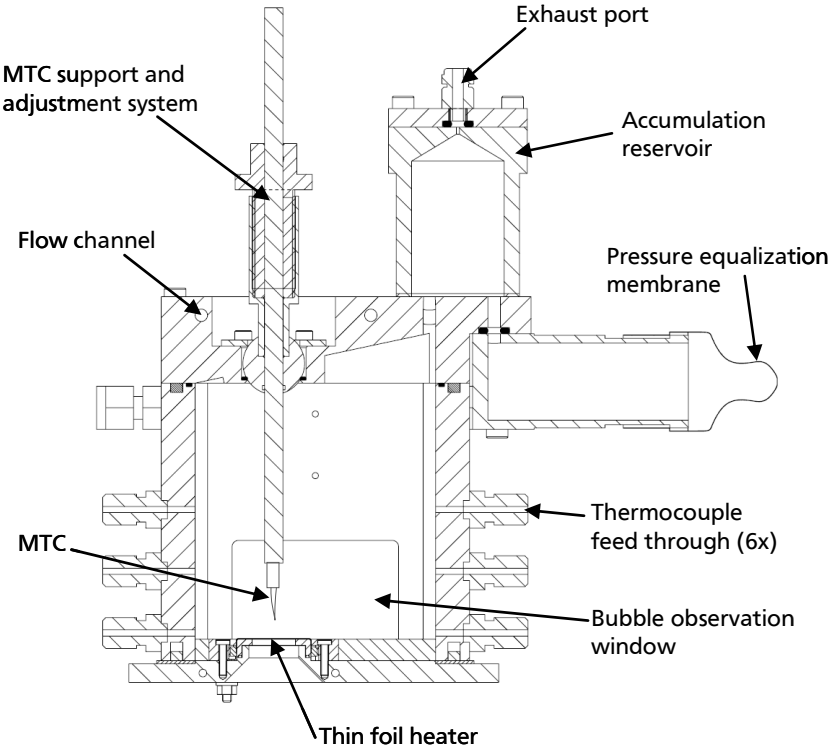

Figure 4.11: Section of the boiling cell

The top plate of the cell features a multi-purpose slot that can be used to insert various stimuli and measurement devices (e.g. MTC, electric field electrode, micro optical fibre, MTC rack). In the 50th ESA PFC a micro thermocouple (MTC) has been introduced in the slot for 62 parabolas and an electric field electrode for 47 parabolas, respectively.
The bulk liquid temperature is measured by 8 K-type thermocouples[32] at various locations inside the cell. The K-type thermocouples were calibrated to a residual uncertainty of 0.1 K. The locations of the thermocouples (TCs) cover the entire boiling cell in order to characterize the uniformity of the temperature distribution.

- 4 TCs covers the central area of the cell
- 1 TC is located in an upper corner in 5 mm distance from the walls
- 1 TC is in the opposite bottom corner
- 1 TC is in contact of the cell wall directly above the front window
- 1 TC is positioned just above the bottom surface, not above the heating foil

The bulk liquid temperatures measured by all 8 TCs over a period of 2300 s during the 3rd flight of the 50th ESA PFC are shown in Figure 4.12. As it can bee seen in the plot the liquid in the boiling cell is well homogenously tempered. The difference between the TCs at a time is less than 0.2 °C. Also, the temperature deviation in time is low. The temperatures stay within a band of 0.5 °C. The sharp peaks that can be observed in the temperature curves indicate the microgravity phases. Fluid

[32] ES Electronic Sensor GmbH, IKL05/50

motion that supports the homogenization is driven by natural convection which is absent in microgravity.

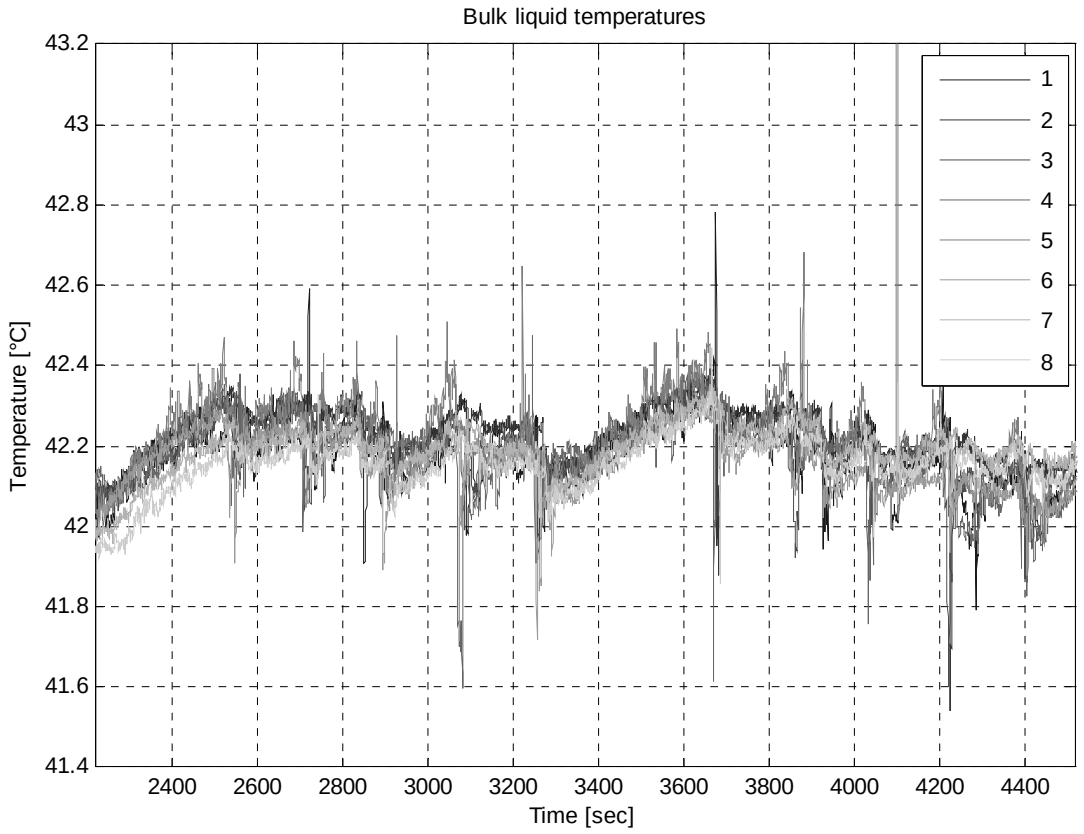

Figure 4.12: Bulk liquid temperatures measured by thermocouples at 8 locations over a period of 2300 s during flight no. 3

4.6. Rack, Subsystems and Devices

The arrangement of the devices and subsystems in the parabolic flight setup is illustrated in Figure 4.13 and Figure 4.14. The photos were taken during the preparation phase of the 50th ESA campaign in June 2009. The setup is shown working in flight configuration. A nominal crew of three persons operates the system during the flight.

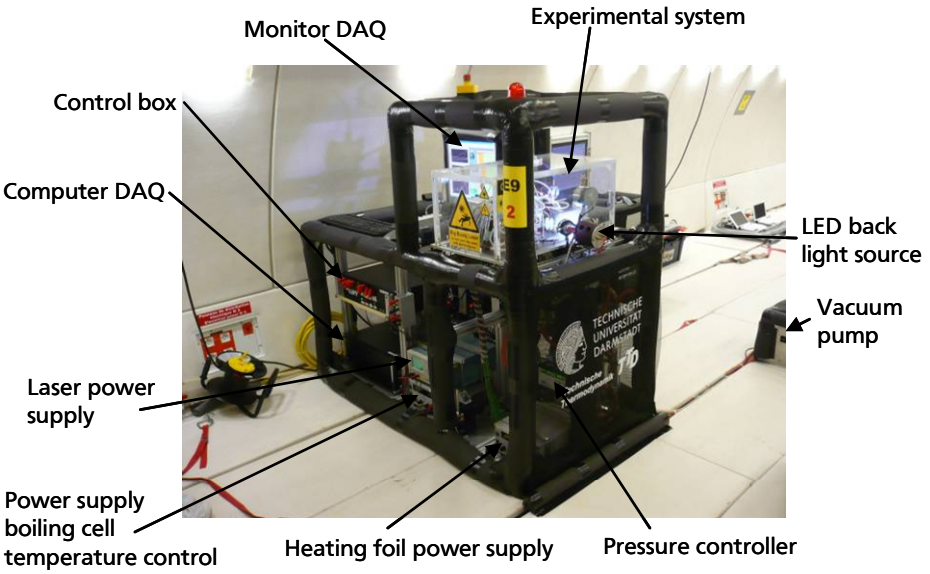

Figure 4.13: Subsystems and devices in the parabolic flight system: front view

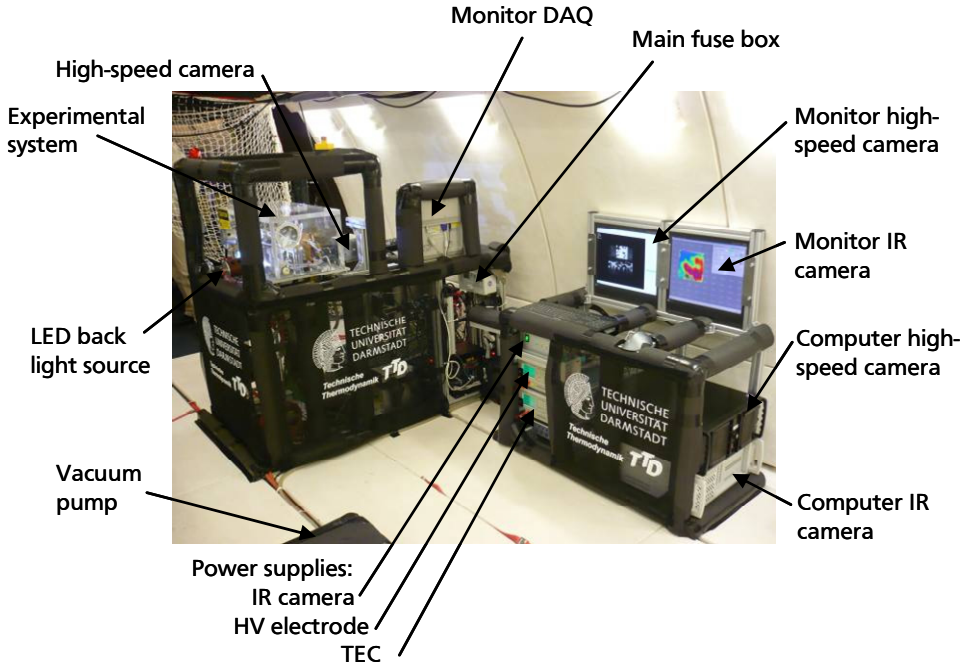

Figure 4.14: Subsystems and devices in the parabolic flight system: back view

4.7. Bubble Initialization Device

In order to provide a local superheat for the initial nucleation site activation a laser is focused at the back side of the heating foil. The laser diode with a wavelength of 632 nm and approximately 200 mW was extracted from a DVD writer. It is collimated and focused using the DVD writer lenses. The beam passes horizontally beneath the heater as it can be seen in Figure 4.15. The beam is redirected by a mirror onto the heating foil. The mirror can be adjusted by a micrometer screw and an inclination lever in order to precisely focus on the nucleation site. The class 3b laser beam path is completely enclosed by heating foil, heater, cell base plate, main base plate and IR camera lenses for safety reasons.

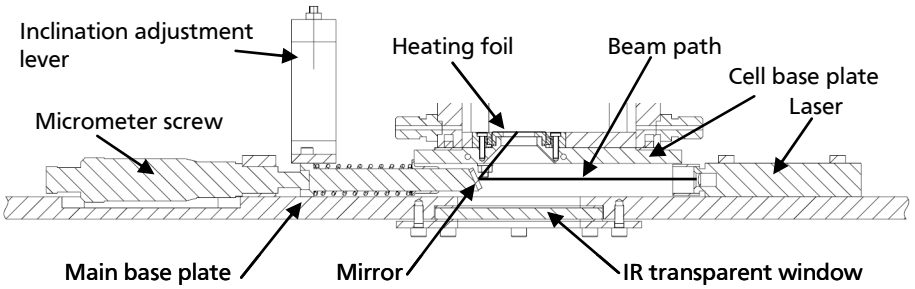

Figure 4.15: Laser beam path and adjustment system

The laser is connected to its power supply via a solid state relay. This allows the precise control of the laser pulse in the automated measurement sequence by the data acquisition system. Alternatively, the laser can be controlled manually to activate the nucleation site during 1g or hyper-g phases. Thereby, continual boiling at the cavity was established and the boiling process could be observed during the hyper-g-micro-g transition without any disturbance of the thermography measurements by the laser.

4.8. Micro Thermocouple

Due to the low heat capacity of the tip of a micro thermocouple (MTC) it reacts rapidly to temperature changes. Therefore, it is possible to meter temperature changes when the MTC penetrates and passes through a rising bubble [128]. The implemented MTC[33] is an unsheathed K-type thermocouple with wire diameters of 13 μm for both materials. The wires are welded at the tip and are secured in a Kapton foil approximately 7 mm behind the tip. The MTC is shown in Figure 4.16. The MTC fixation system allows the positioning of the MTC in all direction in the vicinity of the heating surface.

[33] Omega Engineering, inc: Unsheated Fine-Gage Thermocouple CHAL-0005

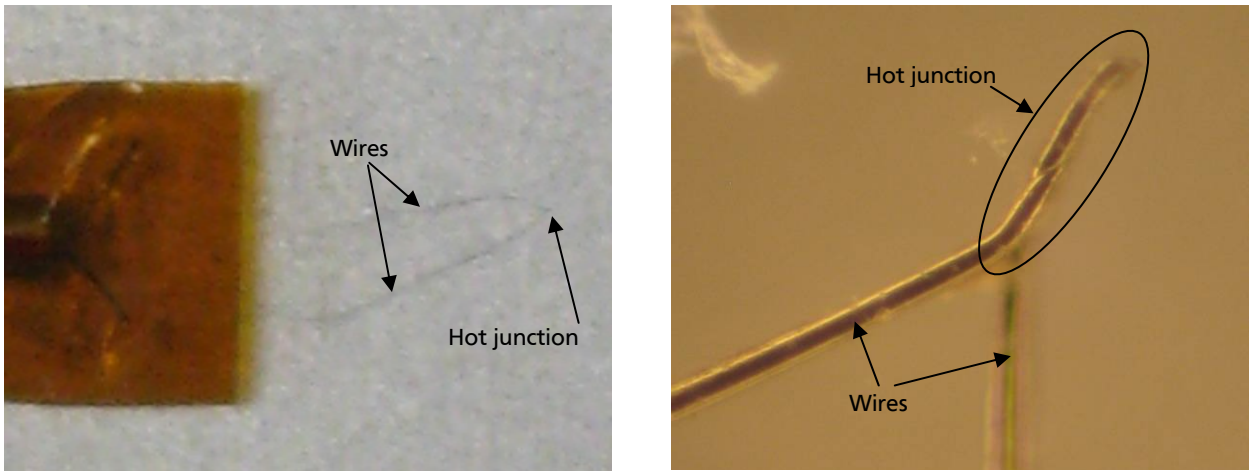

Figure 4.16: Micro thermocouple: a) image with kapton support; b) detailed image of hot junction

4.9. High Voltage Electrode

The shape of the high voltage electrode follows the latest requirements for the RUBI project. The electrode is made of brass and it is disc-shaped with an outer diameter of 15 mm. The hole in the centre of the electrode is 5 mm in diameter. The thickness is 1 mm. All edges are rounded. The electrode is placed 5 mm above the heater. The deviation due to manufacturing tolerances between the electrode centre axis and the nucleation site was 340 μm. The electrode is attached to the end of a Plexiglas tube by rapid glue. The tube is cut out in the direction of the bubble observation axis with a width of 6 mm. This allows also the observation of the bubbles above the electrode. The support of the electrode is a trade-off between reliable fixation and minimum distortion of the field by the support. The electrode is connected to a high voltage power supply[24]. Photos of the electrode are shown in Figure 4.17a and b. An image of the high-speed camera is shown in Figure 4.17c. The image is part of an experimental sequence recorded at an electrode voltage of 10 kV and during microgravity. The elongation of the bubble due to the field forces is clearly visible. Results of the electric field experiments are presented in Chapter 6.7.

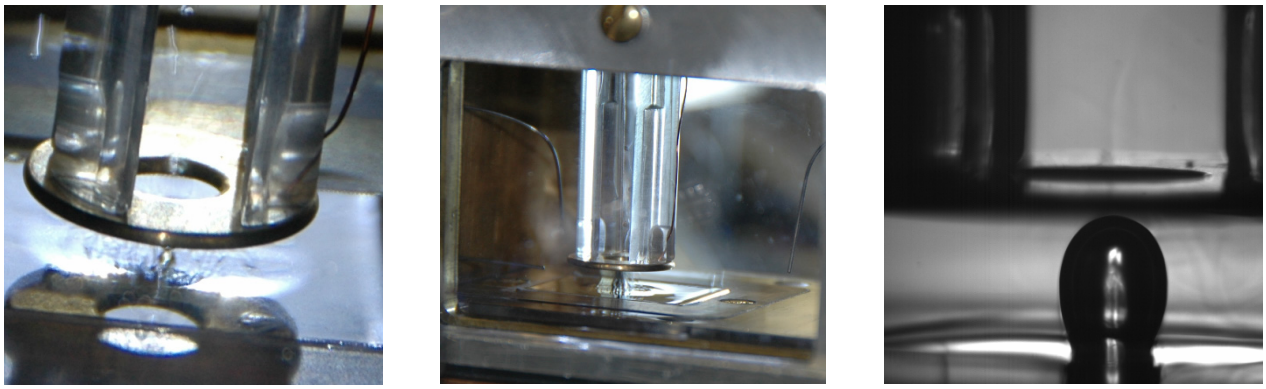

a b c

Figure 4.17: High voltage electrode: a and b) electrode accommodation inside the test cell; c) image of high speed camera taken from measurement sequence

5. Data Evaluation and Reduction

During the 50th ESA PFC approximately 93 measurement sequences have been triggered each with 4000 IR images and the same amount of bubble images. Summarized 744000 images were generated. Extensive and comprehensive image processing is necessary to handle such an amount of data. The functionality of the developed tools and algorithms is presented in this chapter. In the first part of the chapter the evaluation of the IR data is described. This includes the conversion of the IR raw data to temperature fields including a bad pixel correction. Furthermore, the calculation of the local heat flux distribution by applying an unsteady energy balance at single pixel elements is explained. The high heat flux at the contact line, the heat flux in the adsorbed film region and in the bulk liquid are quantified by automatically detecting the characteristic ring-shaped heat flux imprint at the bubble foot. This leads to a further reduction of the data allowing the investigation of the heat flux distribution at different stages of the bubble growth.
In the second part of the chapter the processing procedures of the bubble images are presented. With the developed algorithms it is possible to trace the position of almost every bubble and calculate its volume. From the results of this calculation the bubble frequency and the departure diameter are derived.

5.1. Thermography Data Treatment

The raw data format of the IR cameras is specific to the type and manufacturer. It contains dimensionless scalars that represent the output value of the IR chip. Since the conversion algorithm of the camera electronic is confidential it is not possible to obtain information about the IR radiation having only the raw-data from the chip. To convert the raw data to useful temperature information a calibration procedure was performed. A tempered copper block replaced the fluid cell and was pressed on to the heating foil. The temperature of the block and the heating foil could be assumed as equal and homogenous. For the calibration procedure the camera had to remain in experimental condition, i.e. FOV, framerate, integration time, etc. had to be kept. The copper block temperature was controlled by a bath thermostat from 25 °C to 85 °C in steps of 5 °C. At each step a measurement sequence of 300 IR images was recorded in steady state conditions.
The IR data were stored in multilayered tif-files for the PHOENIX DAS system and in ascii-text-files for the THERMOSENSORIK CMT 256M-HS system. Both formats can be imported in MATLAB. The data of each pixel was temporal averaged over the sequence images in order to reduce the signal noise. The result is a single raw-data matrix with the pixel size of the IR images for each temperature level.
According to the Stefan-Boltzmann law, the heat flux transferred from a hot body to a cold body is proportional to the difference of the forth power of the thermodynamic bodies' temperature [118].
Although the generation of the raw data format is confidential it is assumed to be related to the radiation heat flux when looking at the raw-data-temperature curve. Therefore, a forth order square root function was chosen to fit the calibration data:

$$T = A\sqrt[4]{RawData + B} + C \tag{51}$$

Each pixel of the camera chip has a different response characteristic. That is the reason why a set of fitting coefficients is calculated for each pixel. For the measurements with the Thermosensorik system a bad pixel correction was implemented in the IR-temperature-conversion function of MATLAB. The bad pixel correction is based on a modified Gaussian filter. The filter was modified in such a way that bad pixels in the filter matrix are excluded from weighting.

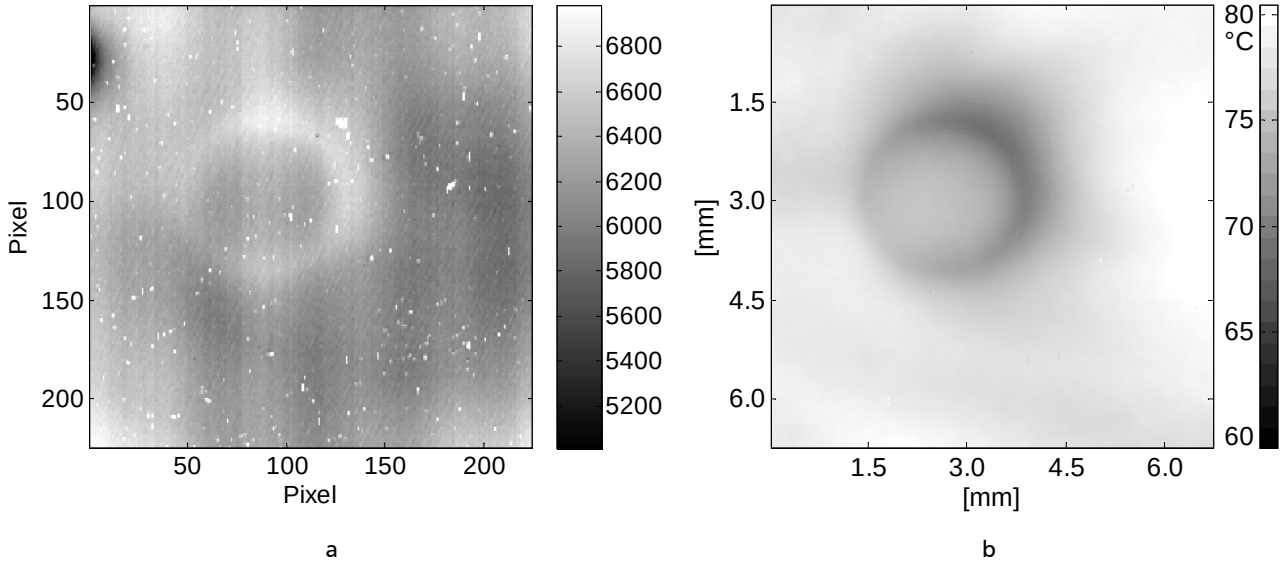

Figure 5.1: IR raw data matrix (a) and computed temperature field (b) showing the imprint of an attached vapour bubble in low gravity

The calibration curves of three pixels are shown in Figure 5.2. A rawdata range from 6500 to 10000 corresponds to a temperature range of approximately 20 °C to 84 °C. The curves demonstrate the different response characteristics of the pixels in the FPA and the justification of the pixel-wise calibration.

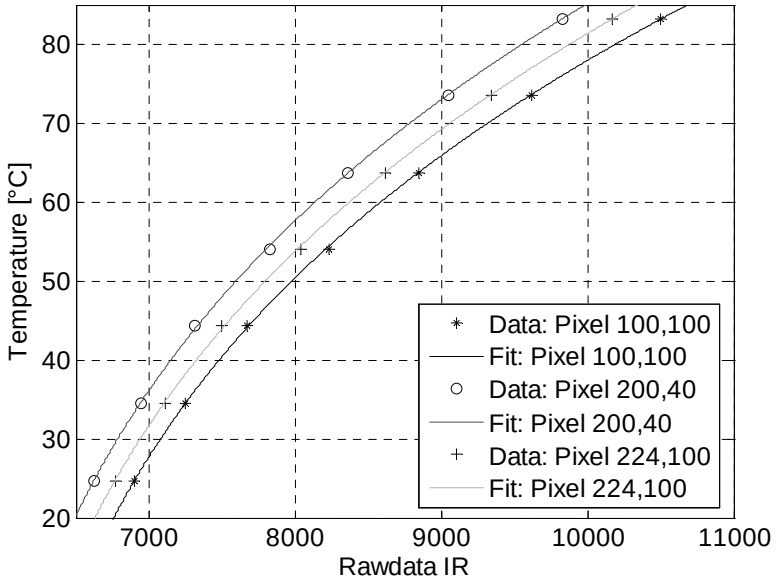

Figure 5.2: Calibration curves for three different pixel

The Noise Equivalent Temperature Difference (NETD) was derived from the calibration sequences. The standard deviation at each pixel was computed from the 300 images of the calibration sequences for the temperature levels. This standard deviation was converted into the NETD using the calibration function with the coefficients for the corresponding pixel. Additionally, the temperature resolution was calculated. The temperature resolution corresponds to the change in temperature when the raw data signal changes by the minimum possible value, which is 1 (digital signal). Both, NETD and temperature resolution depend on the measured temperature and are plotted in Figure 5.3. With the errorbars the standard deviation within the pixel matrix is shown. In the mostly used temperature range of 60 °C to 85 °C for the experiments the NETD was less than 60mK. Nevertheless, the NETD has significant influence on the heat flux calculation by defining the efforts for signal filtering.
The absolute temperature value is subjected to an uncertainty caused by the calibration setup. It is assumed in the range of 1 K. However, the uncertainty in the absolute temperature is not significant for the heat flux computation that is based only on temperature differences (see Chapter 5.1.1). In the evaluation of the experiment the absolute value of the heating foil temperature is mainly used to determine the wall superheat. At a wall superheat of 30 K the uncertainty is less than 4%.

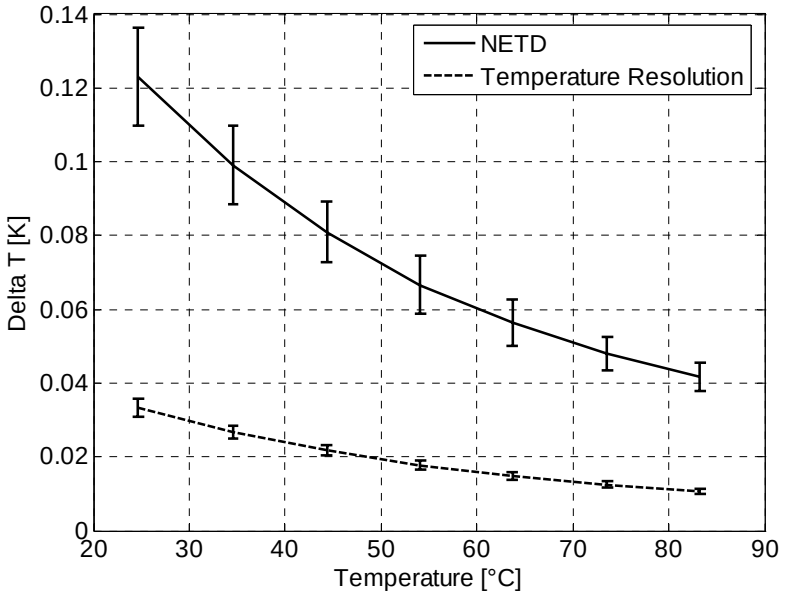

Figure 5.3: NETD and temperature resolution of the thermography system

5.1.1. Heat Flux Calculation

In order to obtain the local heat flux distribution from the foil to the fluid an unsteady energy balance was applied at each pixel element. The pixel element was defined as the portion of the heating foil that is mapped to one pixel in the image of the IR camera with the thickness of the foil. Thus, the pixel element is a cuboid as it is illustrated in Figure 5.4.

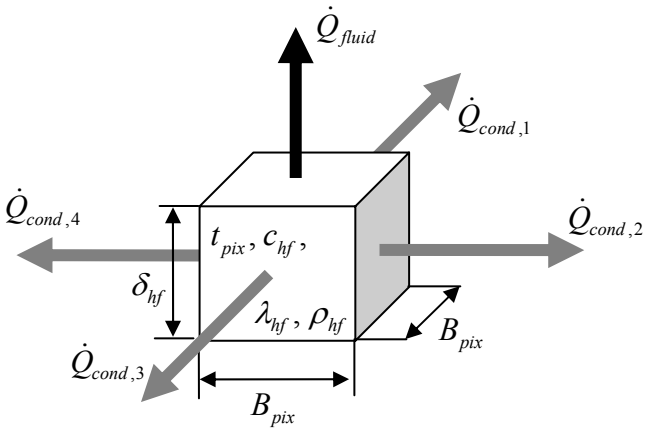

Figure 5.4: Heat flows at a single pixel element

The calculation of the heat flux is based upon several assumptions and simplifications:

- The influence of the black coating on the back side of the foil is negligible.
- The back side of the foil is adiabatic.
- The temperature of the foil is supposed to be constant over the foil thickness δ_{hf} and within the pixel element.
- The electrical heat source is homogenous in the entire heating foil.

Energy conversation of the pixel element is expressed in equation (52).

$$\dot{q}_{fluid} B_{pix}^{\ 2} + \dot{Q}_{cond} + \dot{Q}_{store} + \dot{q}_{el,vol} \delta_{hf} B_{pix}^{\ 2} = 0 \tag{52}$$

Beside the heat flux to the fluid $\dot{q}_{fluid}$ which is the result of the computation the equation contains three different terms which must be treated independently in the evaluation algorithm.

1. Volumetric electrical heating power $\dot{q}_{el,vol}$ of the foil caused by Joule heating.
2. Heat that is stored in the pixel element due to the temperature change in time $\dot{Q}_{store}$.
3. Heat flow due to conduction to/from the four neighbouring pixels $\dot{Q}_{cond} = \sum_i \dot{Q}_{cond,i}$.

1. Volumetric electrical heat source $\dot{q}_{el,vol}$ and electrical heat flux $\dot{q}_{el}$

The stainless (1.4301) steel foil is used as a resistance heater. The volumetric heat source $\dot{q}_{el,vol}$ is caused by Joule heating of the foil via DC current and assumed to be homogeneously distributed in the heating foil. Hence, it can be obtained by dividing the electrical power $\dot{Q}_{el}$ of the foil by the foil volume V_{hf}. The volume of the foil V_{hf} is the foil-fluid surface time A_{hf} times the foil thickness δ_{hf}.

$$\dot{q}_{el,vol} = \frac{\dot{Q}_{el}}{V_{hf}} = \frac{U \cdot I}{A_{hf} \delta_{hf}} \tag{53}$$

The electrical heat flux $\dot{q}_{el}$ (also called heating power) is the electrical power $\dot{Q}_{el}$ divided by the foil-fluid surface A_{hf} assuming an adiabatic back side of the foil.

$$\dot{q}_{el} = \frac{\dot{Q}_{el}}{A_{hf}} = \dot{q}_{el,vol}\delta_{hf} \tag{54}$$

The voltage drop over the heating foil is hardly allocable due to unknown contact resistances at the electrodes which value is assumed to be in the order of magnitude of the foil resistance itself. Therefore, the approach proposed by Wagner [128] is adopted to calculate the power of the heating foil $\dot{Q}_{el}$. The foil resistance was determined using the material properties of the stainless steel (1.4301) and the foil geometry summarized in Table 5.1:

$$R = \rho_{20}\frac{L_{hf}}{A_{cross,hf}}\left[1 + \alpha_t\left(t - 20\,°\mathrm{C}\right)\right] \tag{55}$$

Parameter	Symbol	Value	Uncertainty
Electrical resistivity of stainless steel 1.4301 at 20 °C	ρ_{20}	$0.73\,\Omega\cdot\mathrm{mm^2/m}$	$0.03\,\Omega\cdot\mathrm{mm^2/m}$
Temperature coefficient (stainless steel 1.4301)	α_t	$0.005\,\mathrm{K^{-1}}$	$0.001\,\mathrm{K^{-1}}$
Thermal conductivity (stainless steel 1.4301)	λ_{hf}	$15\,W/(m\cdot K)$	$<10\%$
Density	ρ_{hf}	$7900\,\mathrm{kg/m^3}$	$<10\%$
Heat capacity	c_{hf}	$500\,J/(kg\cdot K)$	$<10\%$
Length of the heating foil between the electrodes	L_{hf}	$34\cdot10^{-3}$ m	$1\cdot10^{-3}$ m
Cross section of the foil	$A_{cross,hf}$	$b_{hf}\cdot\delta_{hf}$	
Foil width	b_{hf}	$20\cdot10^{-3}$ m	$4\cdot10^{-4}$ m
Foil thickness	δ_{hf}	$20\cdot10^{-6}$ m	$2\cdot10^{-6}$ m
Resolution IR camera	B_{pix}	29.59 µm/pixel (2009)	0.5 µm/pixel

Table 5.1: Material properties for stainless steel (1.4301) and geometrical properties of the heating foil used in the 50th ESA campaign 2009.

Wagner evaluated the uncertainty for the electrical heat flux $\dot{q}_{el}$. With the proposed approach he found an uncertainty for $\dot{q}_{el}$ of 18%. However, the evaluation of the local heat flux distribution revealed a characteristic ring-shaped heat flux imprint as described in Chapter 6.1. The measured heat flux in the adsorbed film region in the middle of the bubble foot is approximately zero. This agrees very well with the prediction from theoretical and numerical models. Hence, the actual value of the uncertainity in the electrical heat flux $\dot{q}_{el}$ is an overestimation and assumed to be much lower than 18%.

2. Heat capacity of the pixel element

The heat stored in the pixel element Q_{store} was calculated using the temperature change of the element in time:

$$Q_{store} = M_{pix} \cdot c_{hf} \cdot \Delta t_{pix} \tag{56}$$

$$\dot{Q}_{store} = B_{pix}{}^{2} \cdot \rho_{hf} \cdot \delta_{hf} \cdot c_{hf} \cdot \frac{\left(t_{\tau\_av,x,y,i+1} - t_{\tau\_av,x,y,i}\right)}{\Delta\tau} \tag{57}$$

In order to minimize the signal noise a weighed averaging of the pixel temperature in time (index τ_av) was performed (see Figure 5.5):

$$t_{\tau\_av,x,y,i} = \frac{t_{x,y,i-2} + 2t_{x,y,i-1} + 3t_{x,y,i} + 2t_{x,y,i+1} + t_{x,y,i+2}}{9} \tag{58}$$

The indices x and y refer to the pixel coordinates and the index i to the image number (time step) within the sequence.

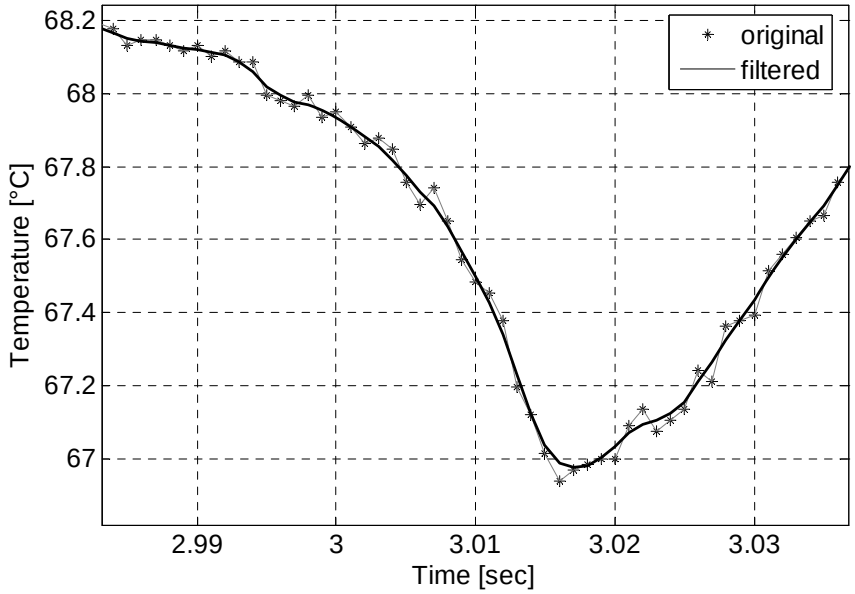

Figure 5.5: Temporal weighted averaging of temperature signal at a single pixel

3. Heat conduction in foil plane

Heat is conducted to the neighbouring pixel element at the four sides of the regarded element. The heat flux through on side can be expressed by Fourier's law:

$$\dot{Q}_{cond,y+} = A_{cross,pix} \frac{\lambda_{hf}}{\delta_{hf}} \left(t_{x,y+1,i} - t_{x,y,i}\right) \tag{59}$$

with

$$A_{cross,pix} = b_{pix} \cdot \delta_{hf} \tag{60}$$

Accounting all four sides the heat conduction terms can be written as:

$$\dot{Q}_{cond,x,y,i} = A_{cross,pix} \cdot \delta_{hf} \cdot \lambda_{hf} \cdot \nabla^2 t_{sp\_av,x,y,i} \tag{61}$$

with

$$\nabla^2 t_{sp\_av,x,y,i} = t_{sp\_av,x+1,y,i} + t_{sp\_av,x-1,y,i} + t_{sp\_av,x,y+1,i} + t_{sp\_av,x,y-1,i} - 4t_{sp\_av,x,y,i} \tag{62}$$

It can be shown that the heat conduction term is extremely sensitive to spatial signal noise of the input temperature field. The spatial signal noise performance is expressed in the NETD value of the thermography system and was determined to be less than 60mK in the used temperature range (see Chapter 5.1. Nevertheless, extensive filtering is necessary. In the first step of the filtering a mean temperature field was calculated from the temporal average temperature fields $t_{\tau\_av,i}$ and $t_{\tau\_av,i+1}$ which were already calculated for the heat storage term:

$$t_{m\_av,i} = \frac{t_{\tau\_av,i} + t_{\tau\_av,i+1}}{2} \tag{63}$$

In the second step a MATLAB-provided Gaussian filter h_g was applied to this field $t_{m\_av,i}$ resulting in the spatial filtered temperature field $t_{sp\_av,i}$.

$$h_g(x,y) = \frac{h'_g(x,y)}{\sum_x \sum_y h_g} \tag{64}$$

with

$$h'_g(x,y) = e^{-(x^2+y^2)/(2\sigma_{std}{}^2)} \tag{65}$$

The used filter had a size of 30 pixel and the standard deviation σ_{std} was set to 4. The Gaussian filter matrix is shown in Figure 5.6.

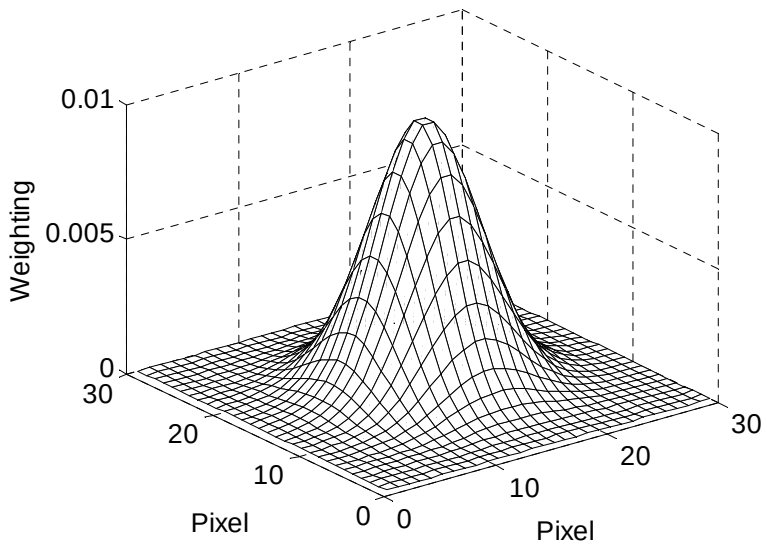

Figure 5.6: Gaussian filter matrix

The settings of the filter were empirically determined and the result of a compromise between noise and peak damping. A comparison between different values of the standard deviation parameter is shown in Figure 5.7. As stated before, the result was a filtered temperature field $t_{sp\_av,i}$ that is used to compute the heat conduction in the foil.
The filtering procedure is a strong enhancement of the algorithm used by Wagner [128]. He used a discrete cosine transformation and did not apply any temporal filtering. A significant improvement also regarding computation time was achieved.

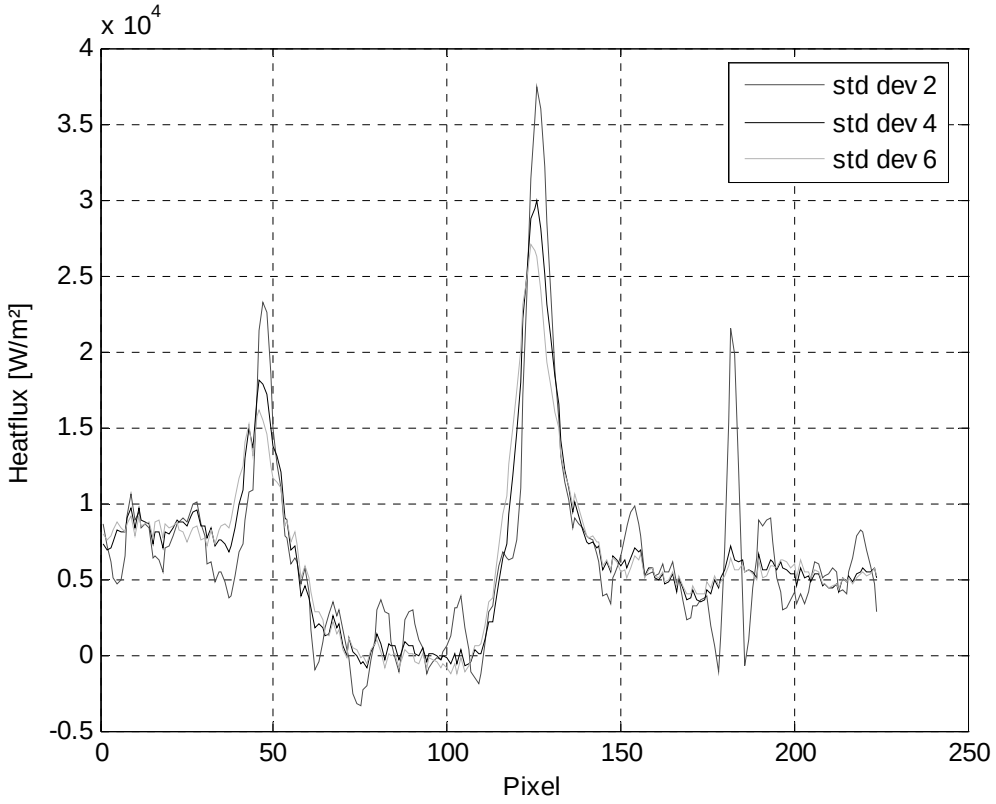

Figure 5.7: Influence of different values for the standard deviation parameter of the Gaussian filter on the local heat flux

The resulting heat flux field is shown in Figure 5.8 for different stages of a bubble ebullition cycle:

a) Bubble nucleation
b) Bubble growth
c) Maximum bubble foot diameter
d) Bubble detachment

Three regions can be separated in the heat flux image:

1. Heat flux to the bulk liquid, not influenced by the bubble growth (approximately equal to $\dot{q}_{el}$).
2. High heat flux near the contact line at the bubble foot, a characteristic circular imprint is formed.
3. Low heat flux ($\dot{q}_{fluid} \sim 0$) in the middle of the bubble foot in the adsorbed film region.

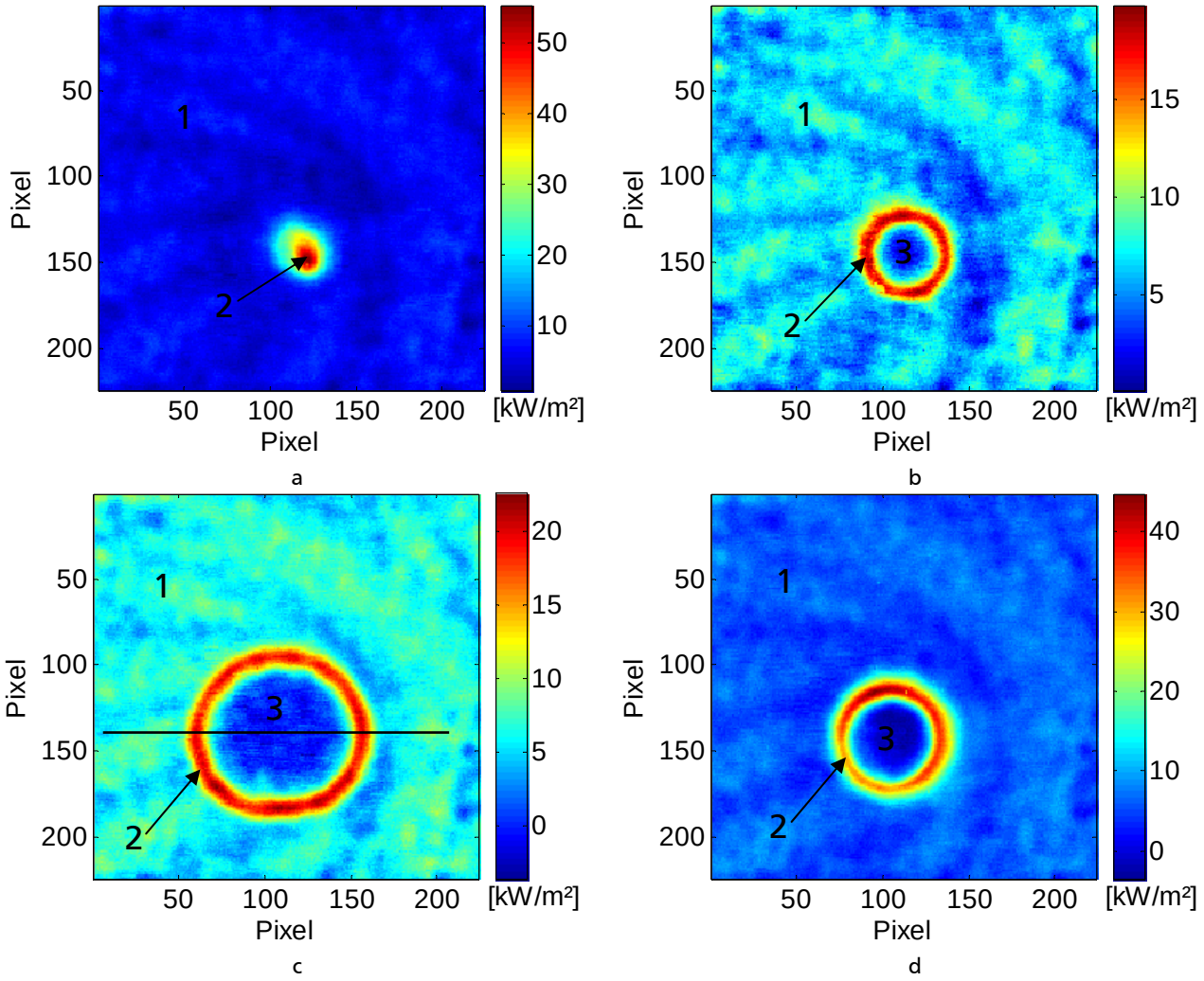

Figure 5.8: Heat flux distributions at different stages of a bubble ebullition cycle, sequence 70: a) bubble nucleation (τ=3.355 s); b) growth period (τ=3.365 s); c) maximum bubble foot diameter (τ=3.4 s); d) detachment process (τ=3.457 s)

The heat flux profile along the black line in Figure 5.8c is shown in Figure 5.9. The location of the contact line is assumed at the peak heat fluxes. The area next to the peak is also of special interest. Since the diameter of the ring-shaped heat flux imprint pulsates with the bubble frequency the location of the peak has to be detected automatically. For this purpose an MATLAB algorithm was developed. It fits an ellipse to the maximum peak values giving back the centre of the bubble foot and the ellipse main axis diameters and angle. It calculates the peak heat flow summarized over the peak pixel and the heat flow within an area defined by offset ellipses.

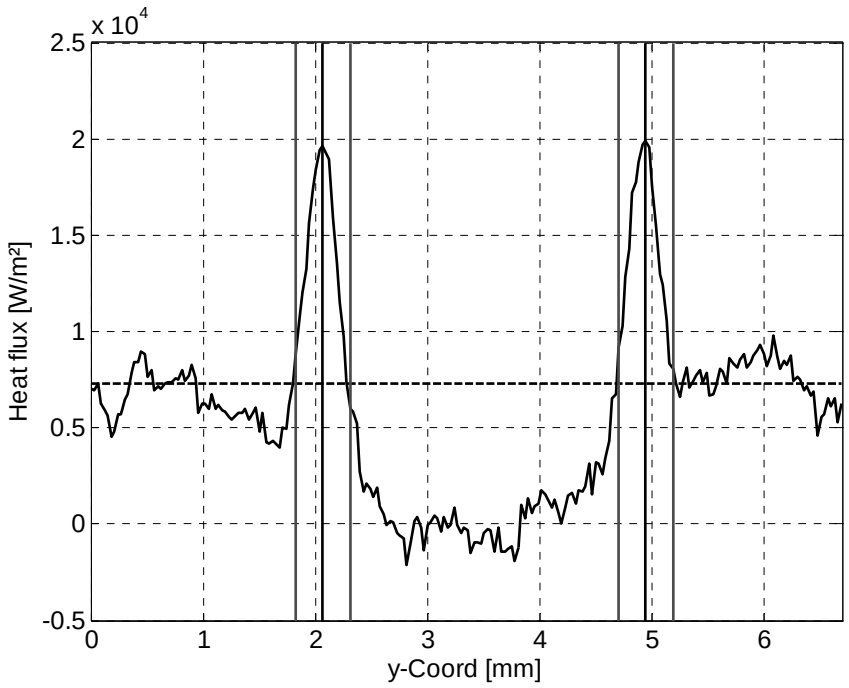

Figure 5.9: Heat flux profile

In the first step, the algorithm automatically defines a threshold between the bulk and the peak heat flux. A histogram of the heat flux image was computed (see Figure 5.10). The histogram has the shape of a norm curve with two extensions on both sides for a characteristic heat flux image containing all three regions mentioned above. The pixels forming the norm curve belong to the bulk liquid area, the extension on the right side is formed by the pixels of the high heat flux near the contact line and the left extension is due to the low heat flux in the adsorbed film region. A norm curve was fitted to the histogram and a straight line was fitted to the right extension. The intersection between the two fits marks the heat flux threshold.

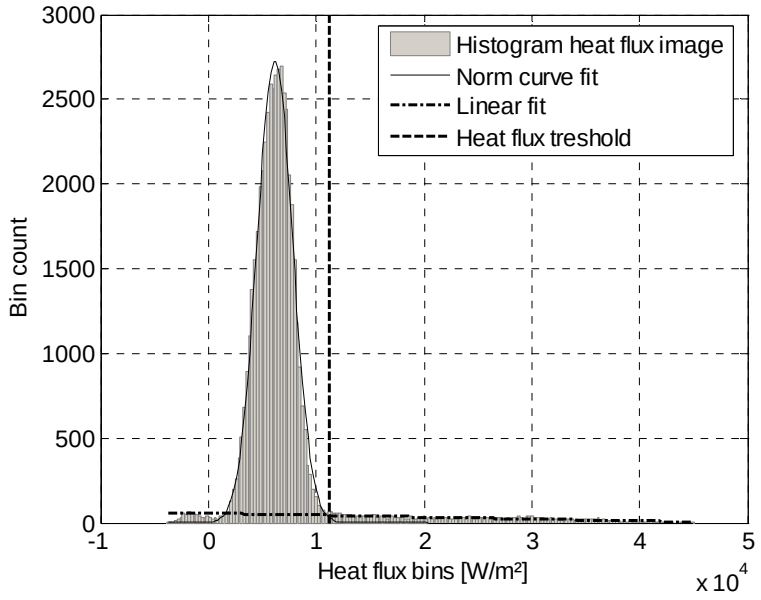

Figure 5.10: Histogram of heat flux image and fitted curves

The coordinates of all pixels whose heat flux is above the threshold are extracted. An ellipse was fitted to these coordinates using the MATLAB function provided by Ohad Gal[34]. This first ellipse does not yet fit the peak values but its centre is already very close to the centre of the bubble foot. In the next step a vector is created containing the heat flux values of the pixels along a line from the ellipse centre to the image border with a certain angle to the x-axis. The maximum heat flux of this vector is extracted as well as the location of the corresponding pixel. This step is repeated for 1000 angles between 0° and 360°. The result is a vector containing value and coordinates of the heat flux peak at the circular area of the high heat flux at the contact line. A second ellipse is fitted to the peak coordinates. This ellipse represents the route of the contact line. In order to evaluate the heat flux at the bubble foot three areas were defined by three offset values. The first area contains all pixel that have a maximum distance of 0.045 mm to the contact line ellipse. This first area is illustrated in Figure 5.11 as the area between the two innermost ellipses. The second area is defined by a maximum distance of 0.12 mm bordered by the second and fifth ellipse and the third area by 0.24 mm (innermost and outermost ellipses). Additionally, the peak values are marked by the erratic black curve.

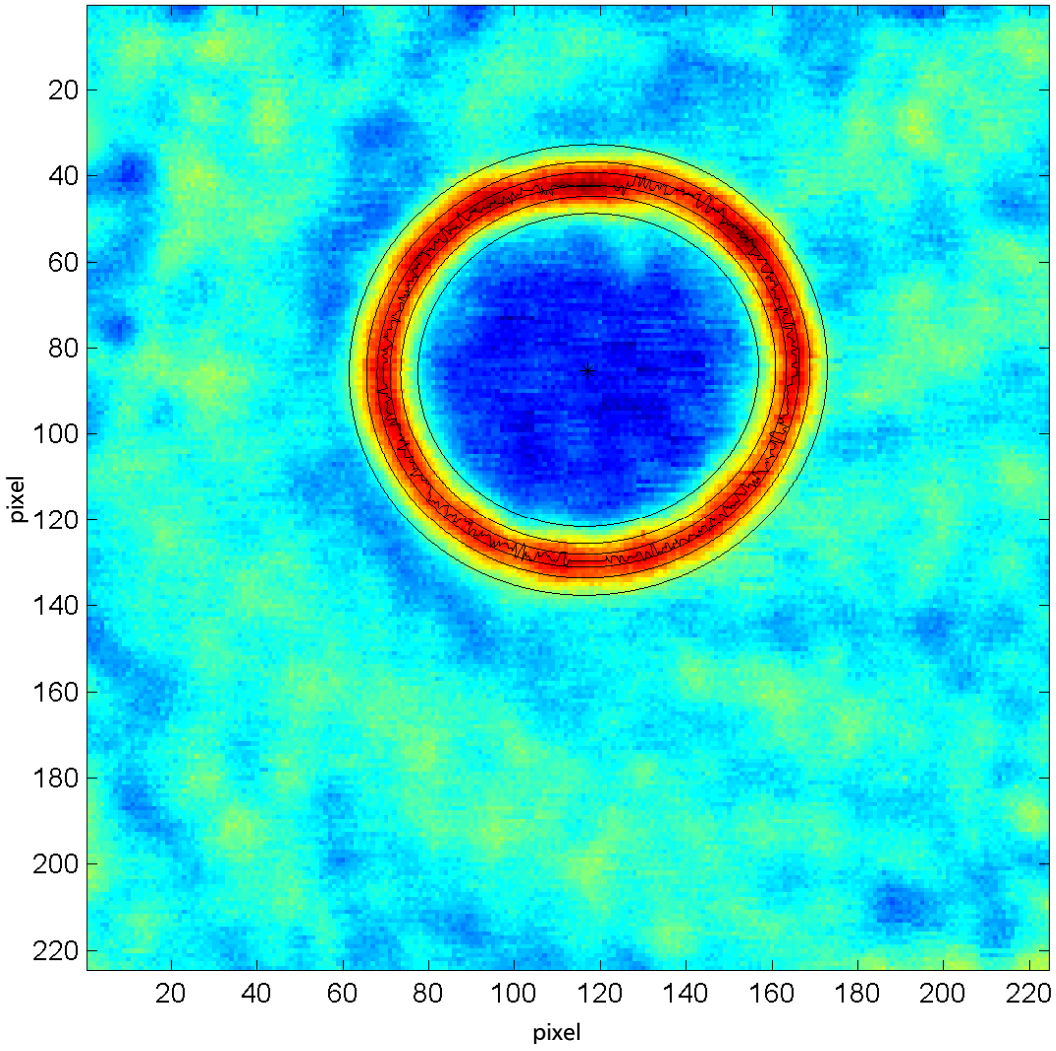

Figure 5.11: Area defined by the offset ellipses

[34] MATLAB function fit_ellipse from www.mathworks.com/matlabcentral/fileexchange/3215

5.2. Bubble Image Processing

During each measurement sequence 4000 images were recorded by the high speed bubble camera at 1000 Hz. With approximately 90 sequences per campaign around 360000 images of vapour bubbles needed to be analyzed. It is obvious that the processing of these images has to be performed automatically by a software tool. MATLAB was chosen as it provides a script language with powerful mathematical algorithms. Especially the algorithms of the image processing toolbox were highly interesting for the evaluation procedure.
In Figure 5.12 the different steps of the processing algorithm that detects position and volume of all bubbles in a picture is illustrated. In Figure 5.12a the original image as it was stored as bmp-file by the camera software is shown. To prevent that reflections of the bubbles in the heating foil are detected as bubbles, the area below the nucleation site at a known position is erased i.e. set to white colour (see Figure 5.12b). Bubbles appear dark in the picture, darker than all other objects, for example than the micro thermocouple. Darker means in this context that the pixel have a lower greyscale value (0 is black, 255 is white). In the next step the greyscale image is converted to a Boolean black and white image. For this purpose, a greyscale threshold was empirically determined. The threshold value is dependent on the contrast and brightness of the images which are defined by illumination aperture and shutter time. Since the setup was not changed the threshold value is valid for the complete data of the campaign. Now, all pixels with a greyscale value below the threshold were converted to logical 1, all other to logical 0. The image matrix consists of a logical 0 background with connected regions of logical 1s representing the bubbles and some small noise regions. MATLAB image processing toolbox was used to label these regions. To get rid of the noise regions all regions whose size is below a certain pixel number were erased. An image of the labelled bubbles is shown in Figure 5.12c. The geometrical centre of each bubble is marked with a white cross. The coordinates of the geometrical centre represent the bubbles trajectory coordinates.

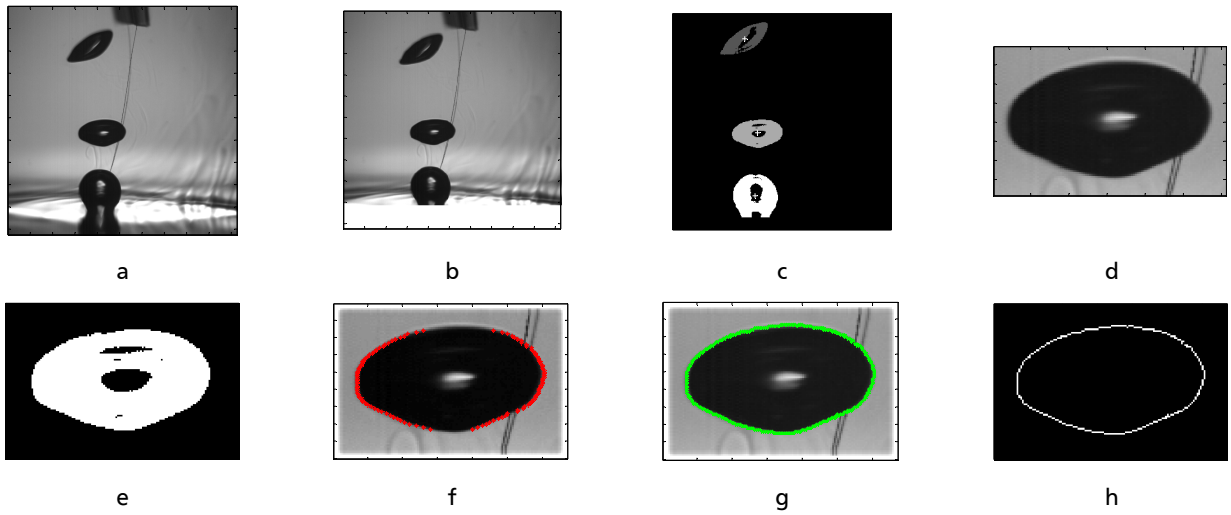

Figure 5.12: Illustration of the steps in the bubble evaluation algorithm: a) – h) steps of image processing as described in the text

To calculate the volume of each bubble in the image sub-pictures are cut out of the original image containing only the regarded bubble (Figure 5.12b). The border of this bubble image was defined using the labelled bubble region and extend it by certain pixel numbers.

The border of the bubble has to be detected with high precision. The determination of the border by using a greyscale threshold would lead to large uncertainties in the volume computation. Moreover, the calculated volume would depend on the threshold value. To avoid this problem, the bubble edge was detected by row-wise and column-wise searching for local maxima in the gradient of the greyscale. To determine if the detected maximum belongs to a bubble edge its position was compared to the border of the threshold image (Figure 5.12e). The result of the row-wise bubble edge detecting is shown in Figure 5.12f. It can be seen that the row-wise searching algorithm is not able to detect the bubble border at top and bottom of the bubble due to less pronounced greyscale gradient in horizontal direction. That is the reason why the algorithm was also applied column-wisely. The result is shown in Figure 5.12g, the border of the bubble is seamlessly detected.
In order to compute the volume of the bubble it was separated in horizontal slices, each with a thickness of one pixel. The diameter d_i of the slice at row i is defined by the bubble edge $x_{b,i}$ of that row:

$$d_i = \max(x_{b,i}) - \min(x_{b,i}) \tag{66}$$

The diameter d_i has the unit "pixel". The volume of each slice is computed assuming the volume of a cylinder and summarized to the bubble volume V_b in pixel³. To convert into SI units the camera resolution $B_{pix,hs} = 20 \cdot 10^{-6}$ m/pixel has to be taken into account.

$$V_b = \frac{\pi}{4} \cdot B_{pix,hs}{}^3 \cdot \sum_i d_i^2 \tag{67}$$

In literature, instead of the bubble volume the bubble diameter is commonly used to express the bubble size. To be able to compare with literature the volume V_b was converted into the equivalent bubble diameter $d_{b,eq}$ assuming a sphere of the same volume as proposed by Qiu et al. [95].

$$d_{b,eq} = d_{b,volume} = \sqrt[3]{\frac{6}{\pi} V_b} \tag{68}$$

To have the opportunity for the comparison of the maximum diameter of the bubble as it appears on the image it was also derived by the algorithm as:

$$d_{b,edge} = \max_i(d_i) \cdot B_{pix,hs} \tag{69}$$

For the evaluation of the detachment diameter it is necessary to detect if a bubble is attached to the heating foil or has already detached. This was accomplished by comparing the coordinates of the lowest border point to the coordinates of the nucleation site.
At the current point location, shape and volume of each bubble in an image are obtained. In order to trace the trajectory of each bubble in successive images the information has to be linked. Therefore, the algorithm searches in the following images for the next higher bubble coordinate that is also in reasonable horizontal distance.
A structure array (see Appendix) has been generated that contains all information about every bubble in a sequence. A second structure array is created containing the trajectory and volume information about the bubbles in a sequence.

6. Results

6.1. Local Temperature and Heat Flux Distribution

The bubble images, temperature fields and heat flux distributions represent the core part of the scientific data. The evaluation of averaged heat flux and temperature, peak values, departure diameter and bubble frequency is based on this data. The purpose of this chapter is to show how this data looks like for different boiling phenomena. A set of three images (bubble shape, temperature and heat flux) is displayed in each figure belonging to the same sequence at the same time step.

6.1.1. Bubble Ebullition Cycle in Low Gravity

The presented bubble cycle (Figure 6.1 - Figure 6.5) was recorded at the beginning of the microgravity phase with a low residual gravity of $g/g_e = 0.07$ still causing the detachment of the regarded bubble. The electrical heating power was $\dot{q}_{el} = 3572\ \mathrm{W/m^2}$ and the saturation temperature $t_{sat} = 42.34\ °\mathrm{C}$. In Figure 6.1 the conditions at $\tau = 1.3\ \mathrm{s}$ before bubble nucleation are shown. Natural convection is already absent, no schlieren are visible in the bubble images (Figure 6.1a). Although the temperature field with a mean temperature of $t_{mean} = 67.23\ °\mathrm{C}$ has a slightly colder region at the left side the local heat flux is uniformly distributed. The mean heat flux to the fluid averaged over the entire image is $\dot{q}_{mean} = 3184\ \mathrm{W/m^2}$. The difference of the electrical heat flux $\dot{q}_{el}$ and the mean heat flux to the fluid $\dot{q}_{mean}$ causes an increase of the heating foil mean temperature. This increase is connected to the diminishing of natural convection as shown in Chapter 6.4. The temperature and heat flux profiles of a single pixel row through the centre of the bubble foot is shown in Figure 6.6 and Figure 6.7 for the time steps presented in Figure 6.1 - Figure 6.5.

Initial bubble nucleation happened without laser initiation. This is remarkable and does generally not often occur. The present study benefits from this behaviour because the IR measurements are not disturbed by the laser spot. At $\tau = 1.323\ \mathrm{s}$ (Figure 6.2) a small cold spot at the nucleation site is visible. The corresponding heat flux imprint shows a thick ring of high heat flux around the nucleation site. The maximum heat flux exceeds 55 kW/m² as shown in Figure 6.7. The average heat flux is $\dot{q}_{mean} = 5333\ \mathrm{W/m^2}$.

The temperature and heat flux imprint at the maximum foot diameter is presented in Figure 6.3. This heat flux imprint is characteristic for the boiling process. A sharp ring of high heat flux (18 kW/m²) is surrounded by heat flux to the bulk liquid which is close to the electrical heat source. The heat flux in the middle of this ring under the adsorbed film region is nearly zero. This justifies the assumption of an adiabatic heating surface underneath the foot of the bubble in some numerical models (e.g. of Fuchs [32]).

The same characteristic shape is observable during the detachment process in Figure 6.4 with an even higher peak heat flux of 25 kW/m². The enlargement of the peak height could be attributed to transient conduction. This phenomena is explicitly described in Chapter 6.6.

The temperature imprint evolutes from a cold spot in Figure 6.2b to a cold ring in Figure 6.3b. The temperature of the foil underneath the adsorbed film is rising quickly. If the bubble is attached long enough the temperature in this region significantly exceeds the temperature underneath the bulk liquid as it can be seen in Figure 6.4b. At the time of detachment a tiny spot of very high heat flux (53 kW/m²) is visible in Figure 6.5c.

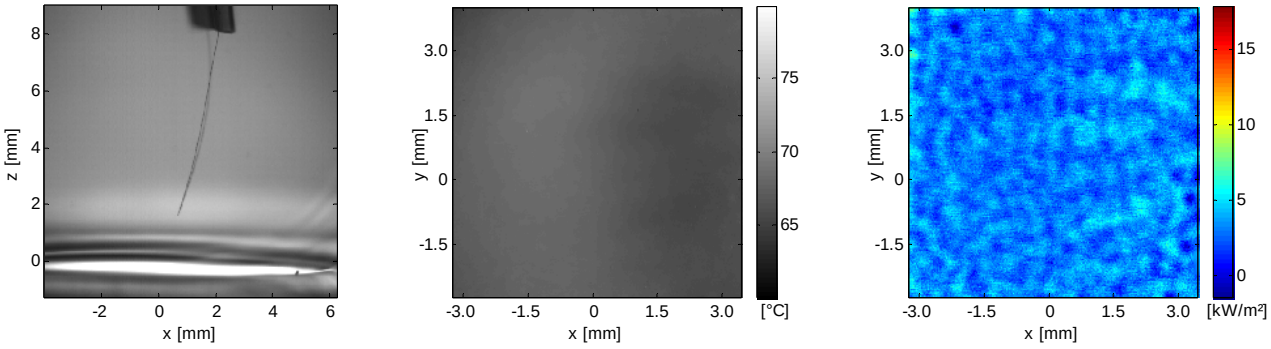

Figure 6.1: Bubble shape (a), temperature (b) and heat flux (c) during growth and detachment of a single bubble in low gravity, sequence 86, τ=1.3 s, q_{mean}=3184 W/m², t_{fluid}=42.12 °C, t_{mean}=67.23 °C

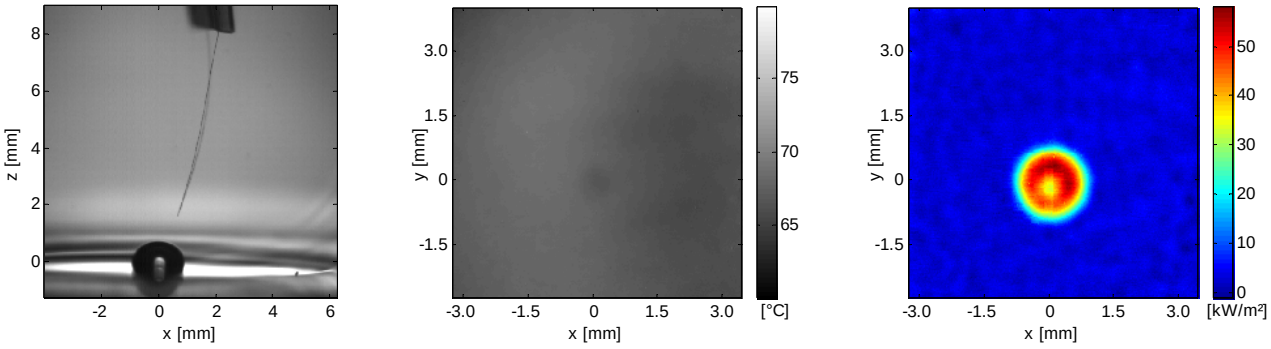

Figure 6.2: Bubble shape (a), temperature (b) and heat flux (c) during growth and detachment of a single bubble in low gravity, sequence 86, τ=1.323 s, q_{mean} =5333 W/m², t_{fluid}=42.12°C, t_{mean}=67.32

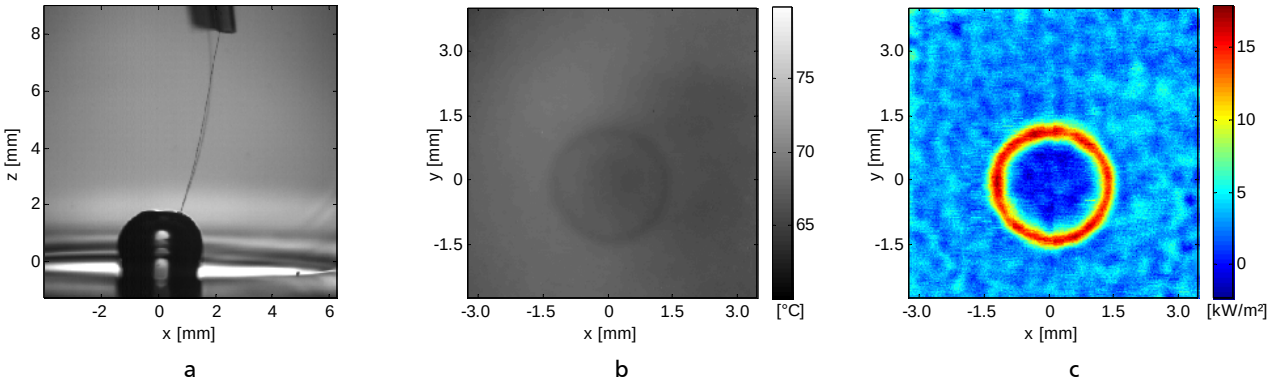

Figure 6.3: Bubble shape (a), temperature (b) and heat flux (c) during growth and detachment of a single bubble in low gravity, sequence 86, τ =1.335 s, q_{mean} =3730 W/m², t_{fluid}=42.12 °C, t_{mean}=67.21 °C

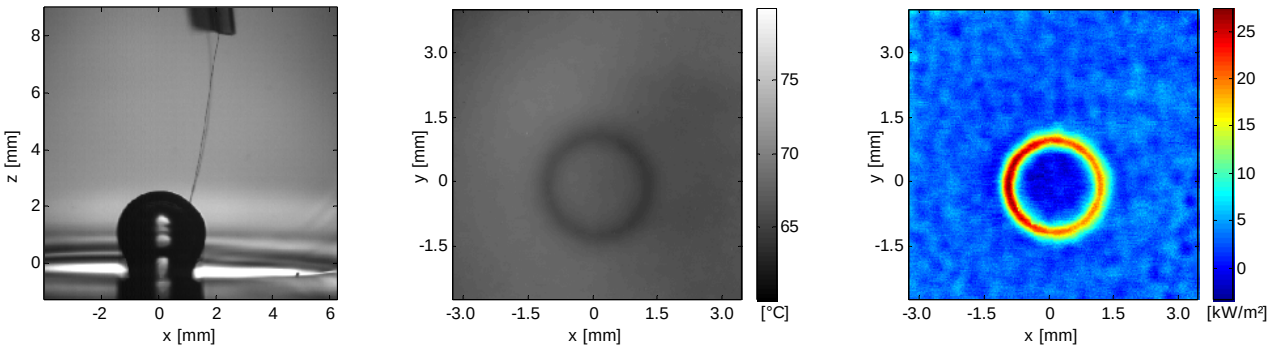

Figure 6.4: Bubble shape (a), temperature (b) and heat flux (c) during growth and detachment of a single bubble in low gravity, sequence 86, τ=1.350 s, q_{mean} =3865 W/m², t_{fluid}=42.12 °C, t_{mean}=67.16 °C

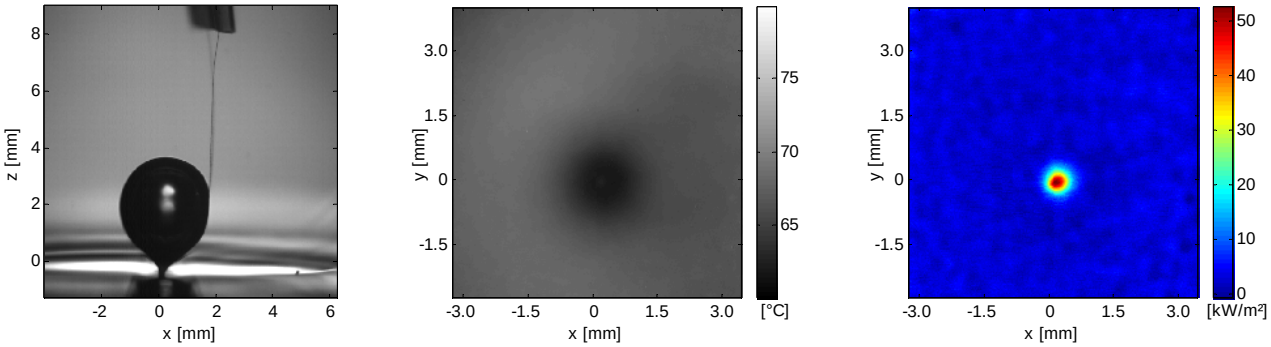

Figure 6.5: Bubble shape (a), temperature (b) and heat flux (c) during growth and detachment of a single bubble in low gravity, sequence 86, τ=1.406 s, q_{mean} =3325 W/m², t_{fluid}=42.12 °C, t_{mean}=67.08 °C

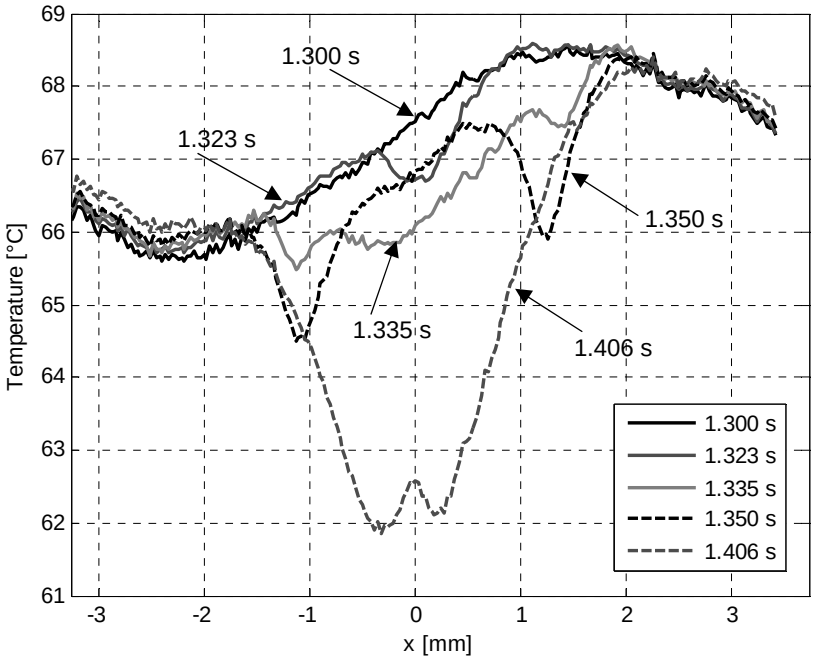

Figure 6.6: Temperature profiles of a single pixel row through the centre of the bubble foot

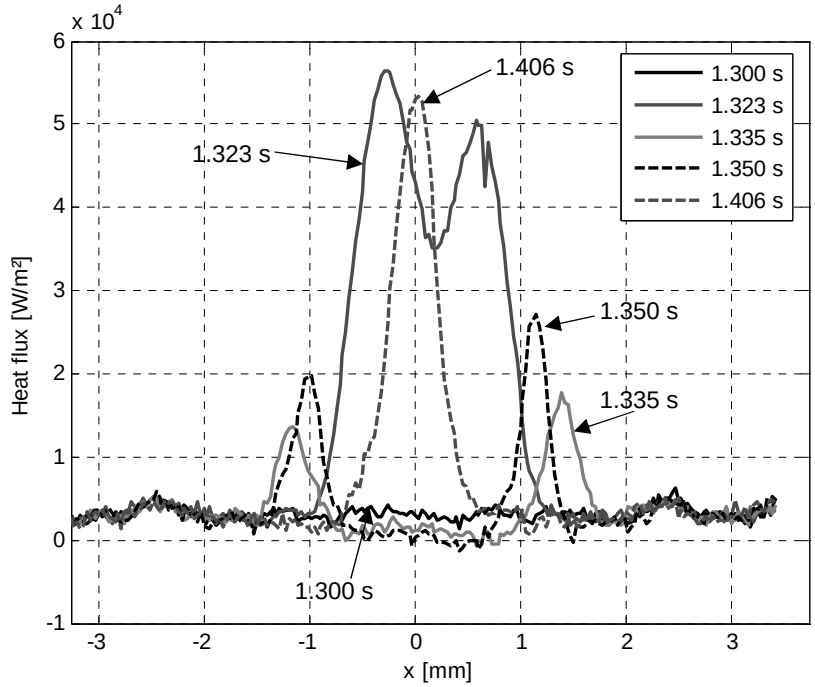

Figure 6.7: Heat flux profiles of a single pixel row through the centre of the bubble foot

6.1.2. Fully Developed Nucleate Boiling

Fully developed pool boiling was established on the heating foil with an electrical heating power of $\dot{q}_{el} = 18.8\,\mathrm{kW/m^2}$. The saturation temperature was $t_{sat} = 42.41\,°\mathrm{C}$ and the bulk liquid temperature $t_{fluid} = 42.0\,°\mathrm{C}$. Numerous cavities were active. The sequence was recorded during the hyper-g-micro-g-transition. The boiling process at a gravity of $g/g_e = 1.3$ is illustrated in Figure 6.8. Many bubbles of different sizes emerge from the surface. The number of active sites seems to be higher in the upper half of the FOV, leading to a lower mean temperature in this area. Aside from spots of high heat fluxes the characteristic ring-shaped imprints are also already visible.
The bubble sizes increase with decreasing gravity as it can be seen in Figure 6.9. Bubble eruptions take place from time to time. During these eruptions large clouds of vapour are formed at the surface. The heat flux imprint of the vapour cloud is visible in the lower half of the image (Figure 6.9c). A region of low heat flux is framed by the contact line peak. The contact line is not circular as it is typical for bubbles but disturbed by the influence of neighbouring bubbles and hydrodynamics. Dots and rings of high heat flux are often visible inside this area indicating the existence of droplets inside the vapour cloud at the heating foil. As the gravity further decreases the contact line imprints become clearly visible. The bubble diameter increases. The foil under the adsorbed film is the hottest part in the FOV (see Figure 6.11b). In Figure 6.11c large adsorbed film areas are surrounded by contact line imprints. The bubbles are very close together which promotes the occurrence of bubble coalescence.

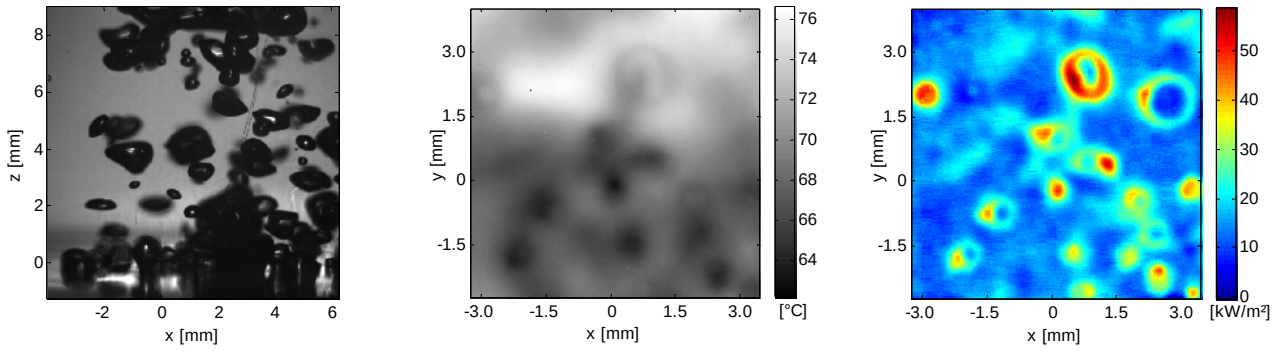

Figure 6.8: Bubble shapes (a), temperature (b) and heat flux (c) during fully developed nucleated boiling, sequence 57, τ=0.54 s, q_{el}=18.8 kW/m², q_{mean}=17.76 kW/m², t_{fluid}=42.0 °C, t_{sat}=42.41 °C, t_{mean}=69.63 °C, g/g_e=1.33

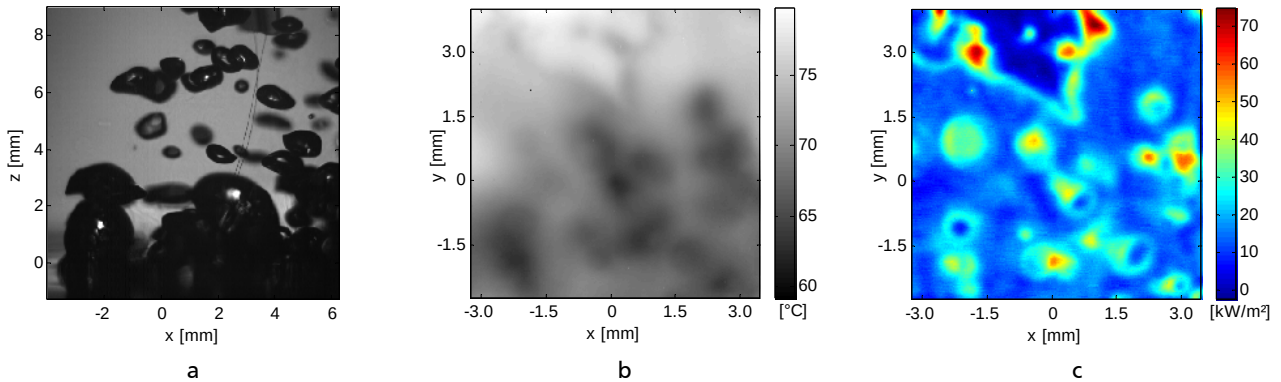

Figure 6.9: Bubble shapes (a), temperature (b) and heat flux (c) during fully developed nucleated boiling, sequence 57, τ=1.2 s, q_{el}=18.8 kW/m², q_{mean}=18.89 kW/m², t_{fluid}=42.0 °C, t_{sat}=42.41 °C, t_{mean}=70.05 °C, g/g_e=1

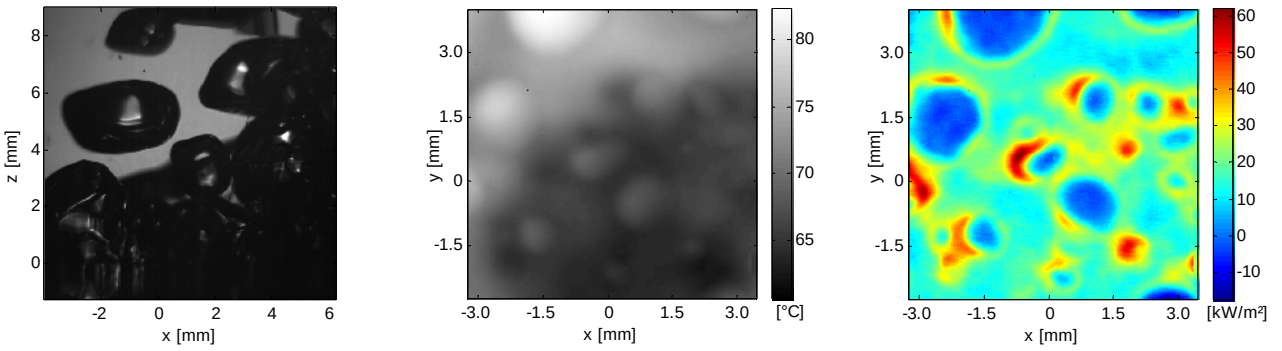

Figure 6.10: Bubble shapes (a), temperature (b) and heat flux (c) during fully developed nucleated boiling, sequence 57, τ=2.36 s, q_{el}=18.8 kW/m², q_{mean}=18.06 kW/m², t_{fluid}=42.0 °C, t_{sat}=42.41 °C, t_{mean}=69.1 °C, g/g_e=0.19

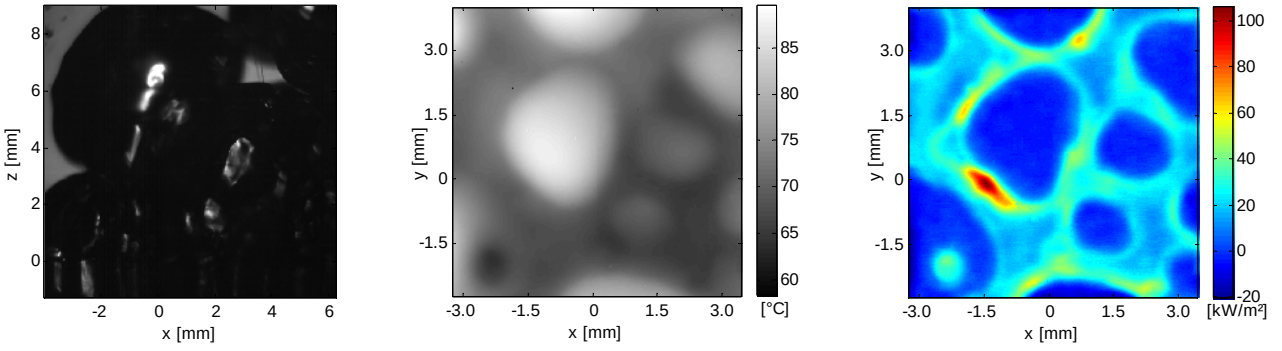

Figure 6.11: Bubble shapes (a), temperature (b) and heat flux (c) during fully developed nucleated boiling, sequence 57, τ=2.92 s, q_{el}=18.8 kW/m², q_{mean}=14.72 kW/m², t_{fluid}=42.0 °C, t_{sat}=42.41 °C, t_{mean}=72.6 °C, g/g_e=0.05

The temperature and heat flux distribution during dry out is presented in Figure 6.12. Vapour is insulating large portions of the foil in the FOV. The temperature is rising quickly in these areas, due to a heat flux to the fluid of around zero, and exceeds 110 °C. However, these values are not in the range of the IR-temperature calibration and therefore subjected to large errors. The grainy area in the lower, middle part of both the temperature and heat flux image is due to the saturation of the IR detector.

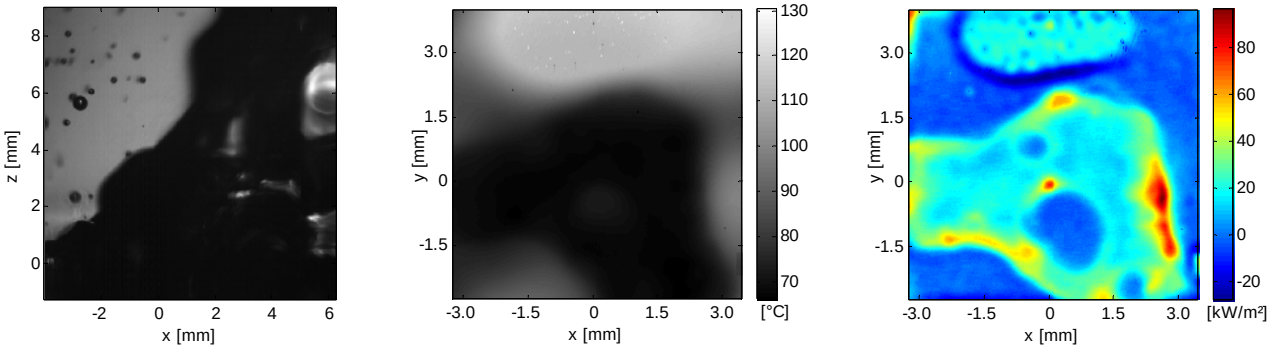

Figure 6.12: Bubble shapes (a), temperature (b) and heat flux (c) during fully developed nucleated boiling, sequence 57, τ=3.2 s, q_{el}=18.8 kW/m², q_{mean}=13.9 kW/m², t_{fluid}=42.0 °C, t_{sat}=42.41 °C, t_{mean}=84 °C, g/g_e=0.002

6.2. Bubble Diameter

In Figure 6.13 the development of the bubble diameters in a section of the sequence is shown for three successive bubbles (see also Appendix 8.10) for the bubble images, temperature and heat flux distributions). The gravity at $\tau = 2.54$ s is $g / g_e = 0.61$. The diameters of the bubbles are calculated using two different methods. The grey curves show the diameter $d_{b,edge}$ derived from the maximum distance of the left and right edge of the bubble as described by equation (69). The black curve represents the equivalent diameter $d_{b,eq} = d_{b,volume}$ calculated from the bubble volume V_b assuming a spherical bubble as described by equation (68) and proposed by Qiu et al. [95]. Figure 6.13 proves that until detachment both methods result in the same diameter. The discrepancy after detachment is due to the flattening of the bubbles after detachment where the bubbles are not spherical but disc-shaped. The maximum in the dashed black curves ($d_{b,volume}$) indicates the point when evaporation and condensation mass flows of the bubble are at equilibrium. The bubble cap has entered a slightly subcooled region ($t_{sat} = 42.4$ °C and $t_{bulk} = 42.2$ °C). After this point the condensation mass flow exceeds the evaporation mass flow and the bubble volume in total shrinks. In subcooled boiling this generally happens already when the bubble is still attached. The increasing volume after detachment in the present case indicates the superheated liquid state. The steep decrease at the end of either the black and grey black curves is due to the bubble leaving the field of view.

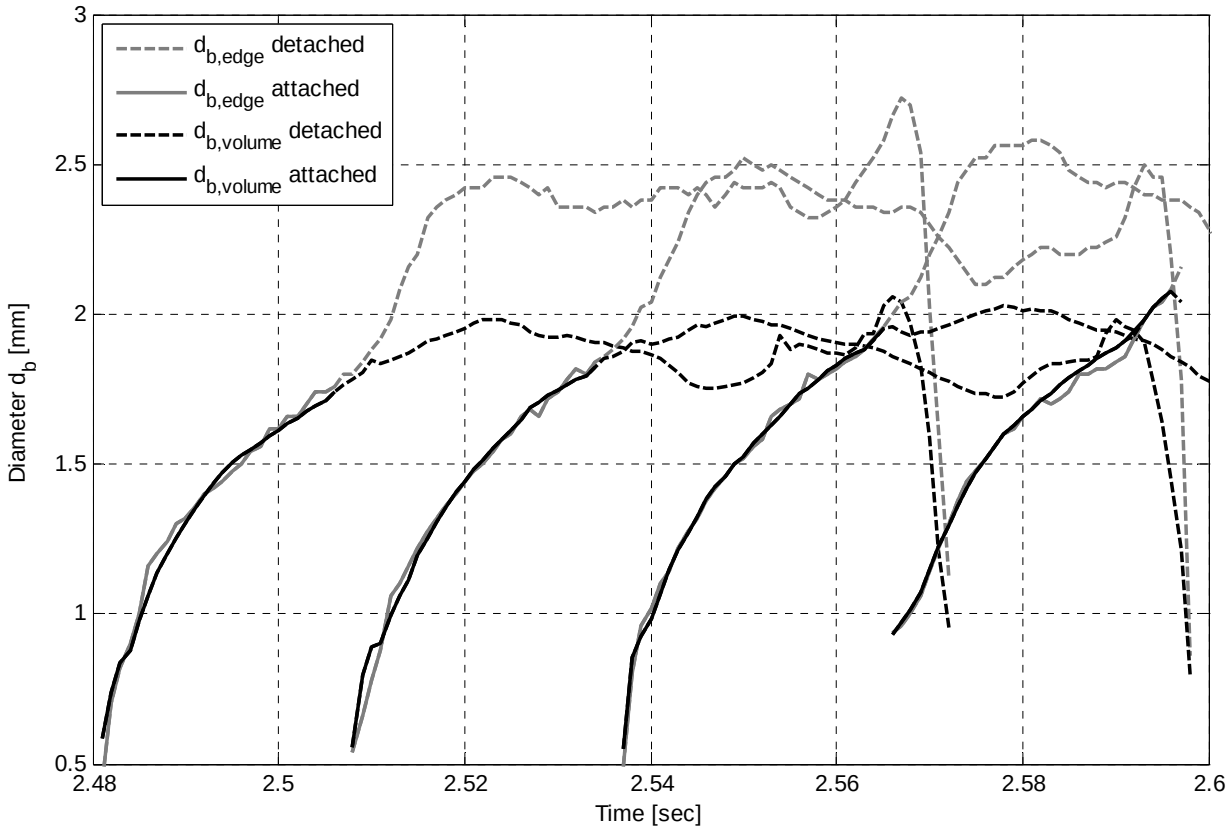

Figure 6.13: Bubble diameter versus time for successive bubbles, g=0.61, sequence no. 70

In the following evaluation only the equivalent bubble diameter $d_{b,volume}$ is considered as the bubble diameter d_b. The development of the bubble diameter d_b versus time for different gravity levels is presented in Figure 6.14. The corresponding bubbles belong to the same measurement sequence

which was recorded during the transition between hypergravity and microgravity. Therefore, the experimental parameters for all bubbles were constant. The electrical heat flux was $\dot{q}_{el} = 7325\ \mathrm{W/m^2}$, the pressure $p = 600\ \mathrm{mbar}$ with a corresponding saturation temperature of $t_{sat} = 42.4\ °\mathrm{C}$. The mean bulk liquid temperature in the boiling cell was $t_{fluid} = 42.2\ °\mathrm{C}$ indicating saturated conditions.

The dependency of the bubble diameter on time is influenced by gravity. The bubble growth rate decreases faster at higher gravity levels. This is in contradiction to the second statement of Siegel (see Chapter 2.3). It is assumed that the reason for the dependency is the thicker thermal boundary layer at lower gravity. The bubble cap leaves the thermal boundary layer at a later time and is longer in contact with superheated liquid. However, the transition of gravity happens relatively fast in a time frame of 1-2 seconds. So, the transient reshape of the thermal layer has still to be taken into account.

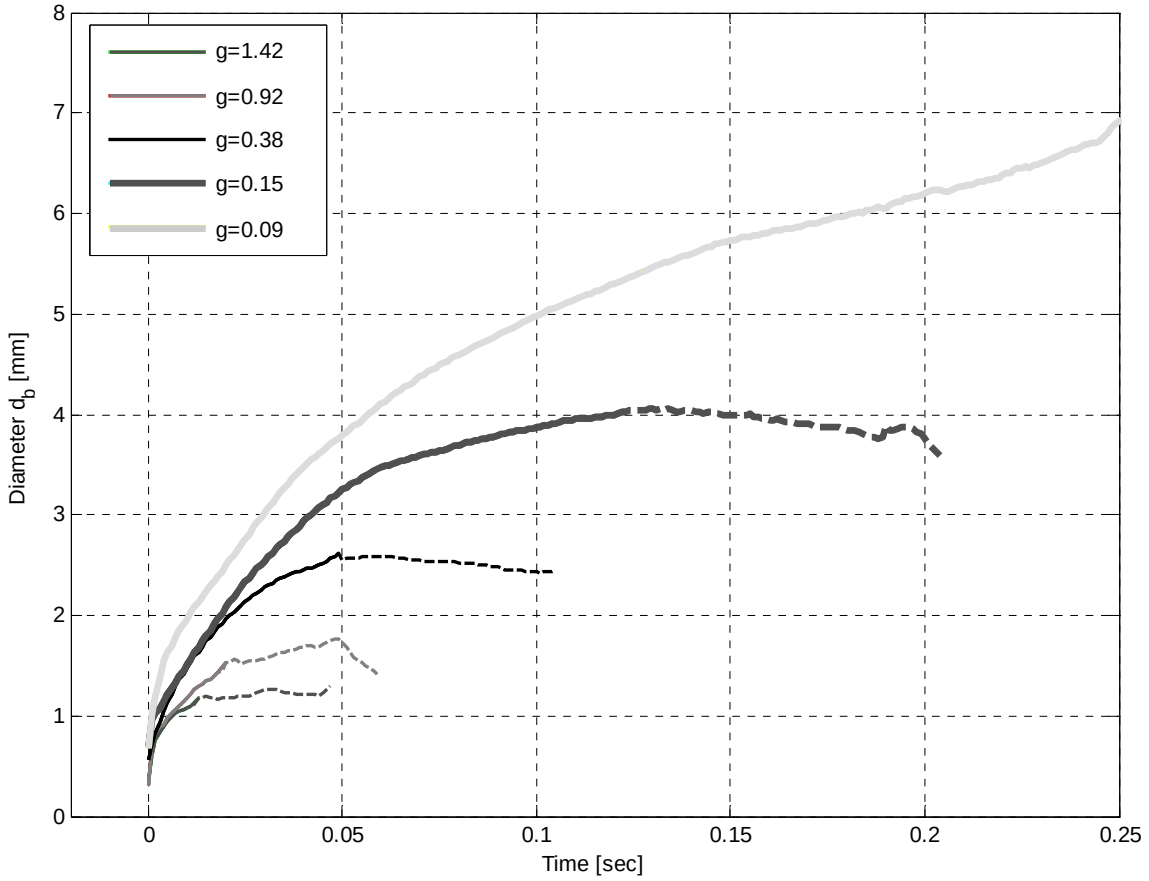

Figure 6.14: Equivalent bubble diameter versus time at different gravity levels

The end of the continuous curve and the beginning of the dashed one indicates the diameter of the bubble at the time of departure. Departure diameter and gravity versus time for two measurement sequences are presented in Figure 6.15. As predicted by theory the departure diameter instantly follows the gravity in an inverse way. From this data the departure diameter was related to the gravity which leads to Figure 6.16.

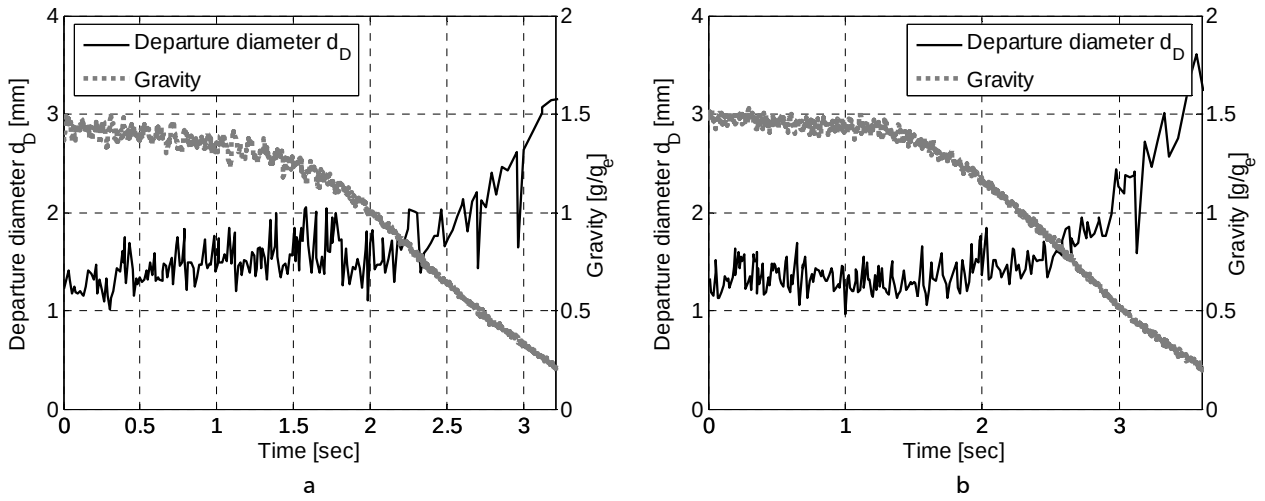

Figure 6.15: Detachment diameter and gravity versus time: a) sequence 70; b) sequence 74

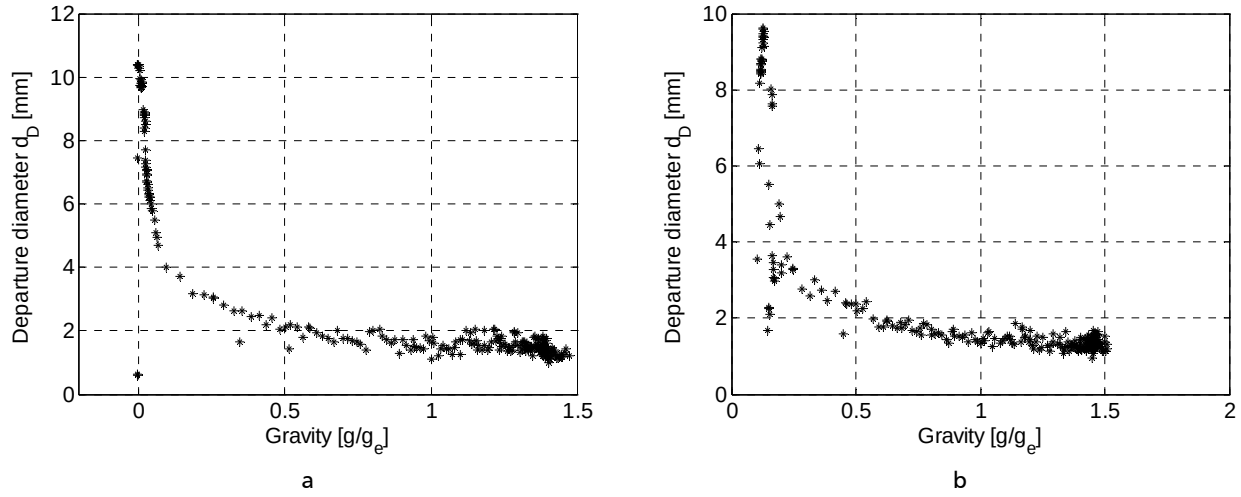

Figure 6.16: Detachment diameter versus gravity: a) sequence 70; b) sequence 74

In Figure 6.17 the data points for gravity levels above $g/g_e = 0.07$ of all evaluated sequences are compared to the most common empirical correlations introduced in Chapter 2.4.1. Obviously, the departure diameter is dependent on $g^{-1/2}$ as firstly proposed by Fritz [30]. The same relation can also be found in the correlations of Cole [13], Cole & Shulman [11] and Cole & Rohsenow [12]. The rest of the regarded correlations under-predict the dependency of gravity on the departure diameter in the given case. This can be explained by looking at the governing detachment forces. The measured boiling process is thermodynamically controlled (see definition by Ivey [48]). That means detachment is governed by buoyancy and surface tension forces. At higher heat fluxes the bubble departure is more and more driven by the bubbles own inertia. The inertial forces are not gravity dependent. That means even at zero gravity these bubbles are detaching. Nevertheless, the correlations that include $g^{-1/2}$ do not fit the measured data in the absolute value.

The correlation of Borishanky & Fokin [6] significantly underpredicts the departure diameter. But also the correlations of Golorin [36], Kutateladze & Gogonin [69], Jensen & Memmel [52], Fritz [30] and Zuber [135] result in a departure diameter that is too small compared to the experimental data. The correlations of Ruckenstein [99], Cole [13] and Cole & Rohsenow [12] overpredict the departure diameter. Only the correlation of Cole & Shulman [11] shows a fairly good agreement to the data.

A very simple correlation was developed by the author that astonishingly fits the data very well without incorporating any empirical fitting parameter. It is based on the force balance between buoyancy and surface tension as already performed by Fritz [30]. Assuming a spherical bubble attached to the heating foil forming a certain contact angle θ at the moment it starts to depart leads to the expression of the surface tension force F_σ:

$$F_\sigma = -\pi \cdot d_D \cdot \sigma \cdot \sin^2 \theta \tag{70}$$

For the calculation of the buoyancy force F_B the bubble volume is calculated. Unlike to the approach of Siegel [106] it is assumed that the whole volume contributes to buoyancy. This assumption accounts for the deformable liquid-vapour interface.

$$F_B = (\rho_l - \rho_v) \cdot V_b \cdot g \tag{71}$$

The bubble volume can be calculated with the geometrical relationship of a sphere sitting on a planar surface.

$$V_b = \frac{\pi}{24} \cdot {d_D}^3 \cdot \left[4 - (1 - \cos\theta)^2 (2 + \cos\theta)\right] \tag{72}$$

Drag, inertia and pressure forces are not included in this approach. These assumptions are justified because the correlation is developed only for the present case of heat-transfer controlled bubble growth in the low heat flux regime. Hence, the force balance is:

$$F_B + F_\sigma = 0 \tag{73}$$

Including the Bond number Bo like it is expressed in most correlations in Chapter 2.4.1 yields to:

$$\mathrm{Bo}^{1/2} = \left[\frac{4 - (1 - \cos\theta)^2 (2 + \cos\theta)}{24 \sin\theta}\right] \tag{74}$$

or

$$\mathrm{d}_D = \sqrt{\frac{\sigma}{g(\rho_l - \rho_v)}} \left[\frac{24 \sin\theta}{4 - (1 - \cos\theta)^2 (2 + \cos\theta)}\right] \tag{75}$$

The contact angle in the correlation is not the contact angle for an isothermal fluid system which can be derived from the surface energies of solid, liquid and vapour phase. Instead, it is the apparent contact angle of the bubble at the time it starts to detach. The apparent contact angle of the bubble is larger than the isothermal one due to evaporation at the contact line.
The contact angle of the bubble at the time the forces are at equilibrium was derived from the diameter of the ring-shaped heat flux peak that indicates the location of the contact line in the local heat flux images and the apparent diameter of the attached bubble in the high speed images. A spherical bubble was assumed.

$$\sin\theta = \frac{d_{b,\,foot}}{d_{b,edge}} \tag{76}$$

The derivation was performed for a number of bubbles and a mean contact angle of $\theta_{measured} = 50°$ was found with a variation of $\pm 10°$.
An alternative way for determining the apparent contact angle at the time the bubble starts to detach is to make use of the microregion model from [120] (Chapter 2.1.4). With the model it is possible to calculate the static contact angle which deviates from the dynamic contact angles during bubble growth and detachment. However, at the time the bubble starts to detach the bubble foot is at its maximum diameter and the contact line is not moving. This justifies the implementation of the static apparent contact angle from the model in the correlation that was $\theta_{calc} = 46.8°$ and, therefore, in very good agreement to the measured contact angle.
This correlation is marked as the Schweizer correlation (74) in Figure 6.17 including the uncertainty of the contact angle of $\pm 10°$. It can be seen that it fits the data above $g/g_e = 0.07$ very well. But it has to be emphasized that it is not valid when inertial forces are non-negligible. Nevertheless the author proposes this correlation for nucleate boiling in the low heat flux regime where the bubble growth is heat transfer controlled and for gravity value above $g/g_e = 0.07$.

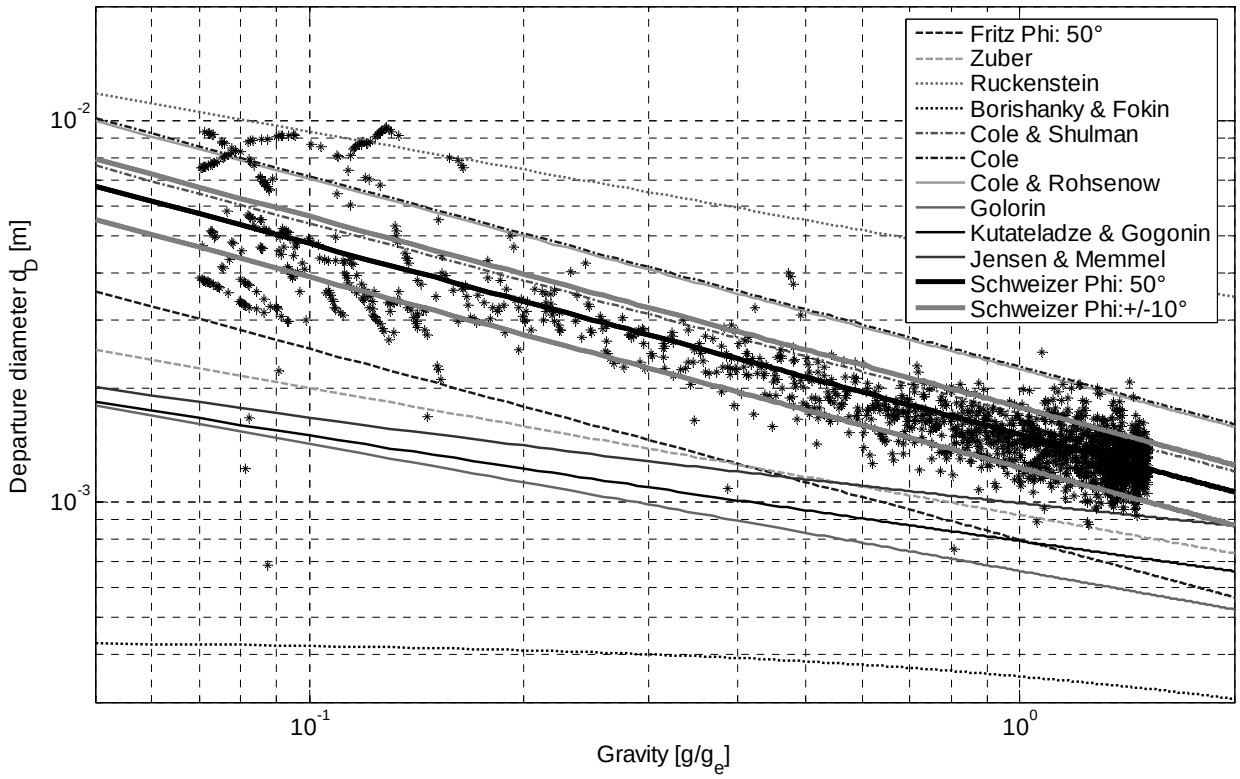

Figure 6.17: Detachment diameter versus gravity, all data points, comparison to empirical correlations

The plot of the bubble volume at departure V_D versus gravity where only the gravity axis is logarithmically scaled (Figure 6.18) indicates a sharp transition from detaching bubbles to not detaching bubbles at a gravity value of around $g/g_e = 0.07$. It seems that at this value the buoyancy force is not sufficient to overcome the attaching surface tension force. Below $g/g_e = 0.07$ the evaluation of the maximum bubble size is not possible since they slide out of the field of view or fill it entirely. The sharp transition between "high-g"-heat transfer and "low-g"-heat transfer was also recently reported by Raj et al. [97] but in their experiments it occurred at $g/g_e = 0.2$. It separates two different boiling behaviours. Although the gravity value of the transition was clearly at $g/g_e = 0.07$ in the present case, some change in the data trend in Figure 6.17 is also visible at a gravity of $g/g_e = 0.2$. Below $g/g_e = 0.2$ the scatter of the data points seems to increase. While

above $g/g_e = 0.07$ the basic behaviour and mechanisms are comparable to boiling in normal earth gravity the regime changes below the threshold. In this regime, phenomena typical for boiling in microgravity like the hovering primary bubble taking in smaller bubbles are observable.

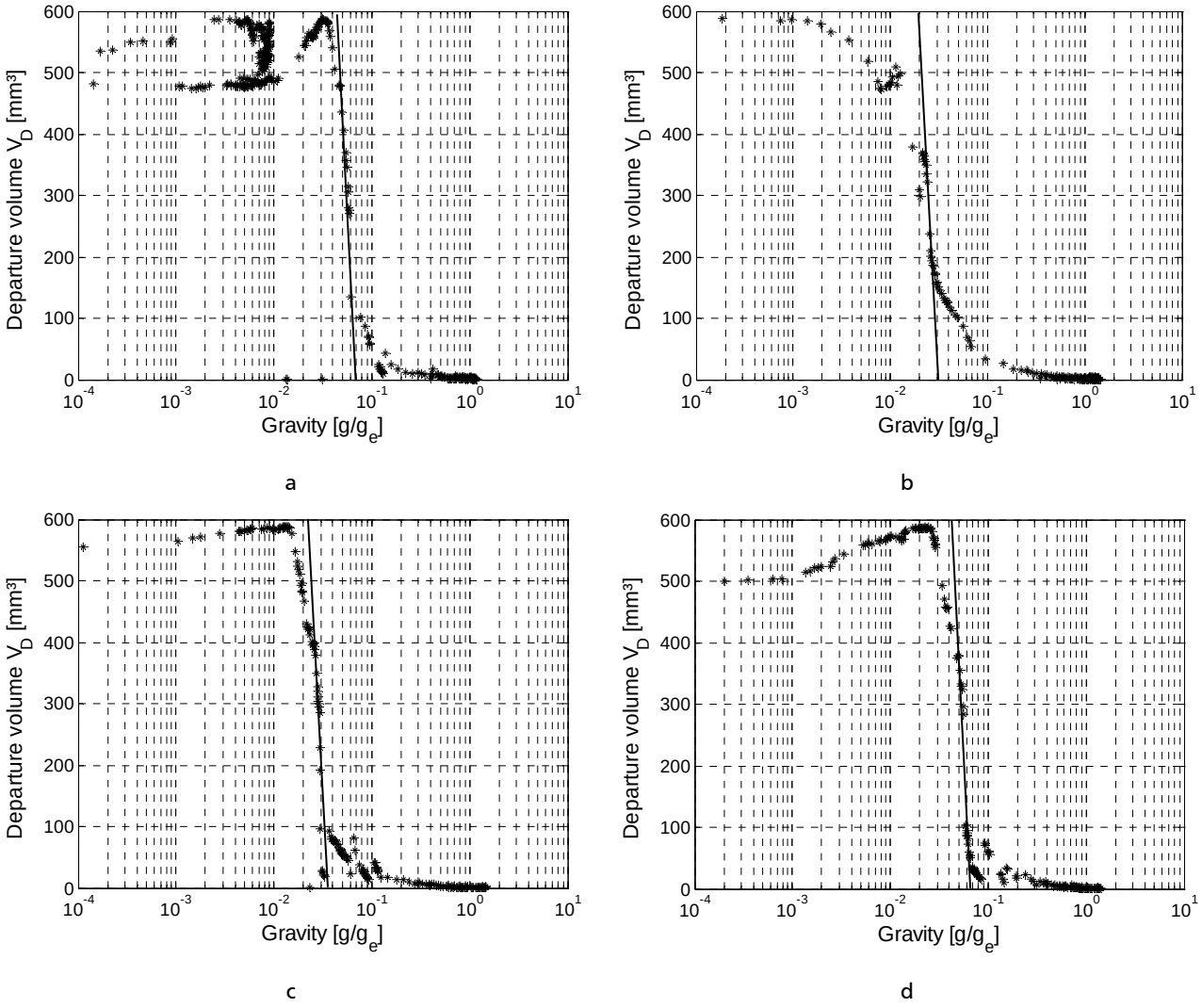

Figure 6.18: Departure volume versus gravity, sequences 77 (a), 70 (b), 67 (c), 64 (d)

6.3. Bubble Frequency

The height of the bubble centre (z-coordinate) versus time is shown in Figure 6.19 for a section of the sequence during the transition between hypergravity and microgravity. The gravity changes from $g/g_e = 0.34$ to $g/g_e = 0.08$ during the $0.56\,\mathrm{s}$ of the section. A black asterisk indicates that the bubble is still attached and a grey asterisk marks detached bubbles; bubble detachment is additionally marked in the figure. While still attached the centre of the bubble accelerates until detachment. As soon as the bubble breaks loose it rises steadily at a constant velocity upwards. The last two bubbles decelerate their upward movement due to the significant decrease in gravity during their rise. For the earlier bubbles this gravity change during the rise period is not pronounced enough to visibly influence the upwards movement of the single bubble.

With the increase of the departure diameter the height of the bubble centre also increases indicated by the position of the last black asterisk of a bubble and the black bar. The first black asterisk of the next bubble follows directly after the departure asterisk of the previous one indicating that there is no waiting time τ_{wait} between two successive bubbles.

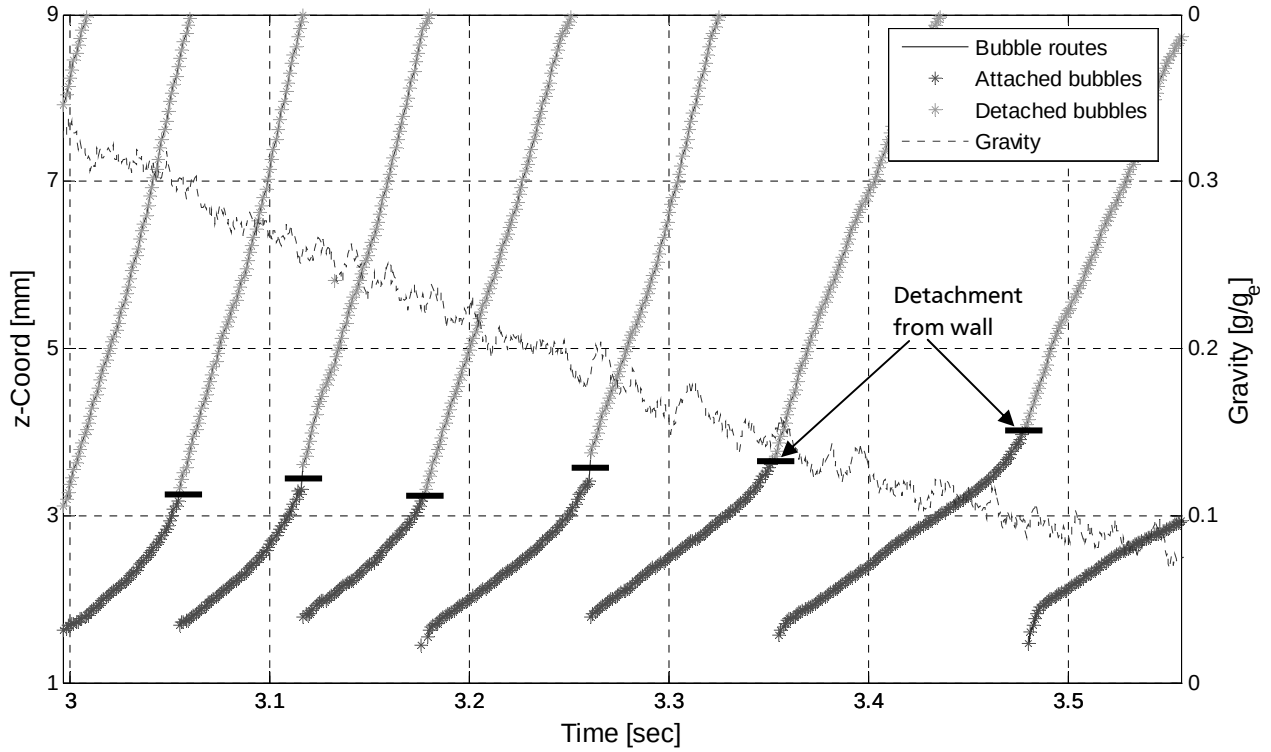

Figure 6.19: Bubble centre rise and gravity versus time during transition between hypergravity and microgravity

The bubble frequency was derived from the time between two bubbles at a certain z-coordinate. The development of the bubble frequency over the entire sequence is shown in Figure 6.20 for four different measurement sequences that were recorded during the transition. The boiling process is not evenly periodic. Sometimes two bubbles emerge from the nucleation site very quickly after each other having a smaller departure diameter, sometimes the bubbles grow larger and the time between two bubbles is longer. Since the bubble frequency is not evaluated by averaging over several bubbles but it is derived directly from the inverse time between two bubbles the natural fluctuation of the boiling process leads to a significant noise in the frequency signal. Nevertheless, it is clearly visible that the average value of the frequency directly follows the gravity.
The electrical heating power was $\dot{q}_{el} = 7325\,\mathrm{W/m^2}$ (sequences 70, 67, 72). The mean temperature measured at several locations inside the test cell was $t_{fluid} = 42.2\,^{\circ}\mathrm{C}$ and the saturation temperature was $t_{sat} = 42.4\,^{\circ}\mathrm{C}$. Since the fluid temperature above the cooled copper block and near the cell walls is slightly colder superheated conditions above the heating foil are assumed.

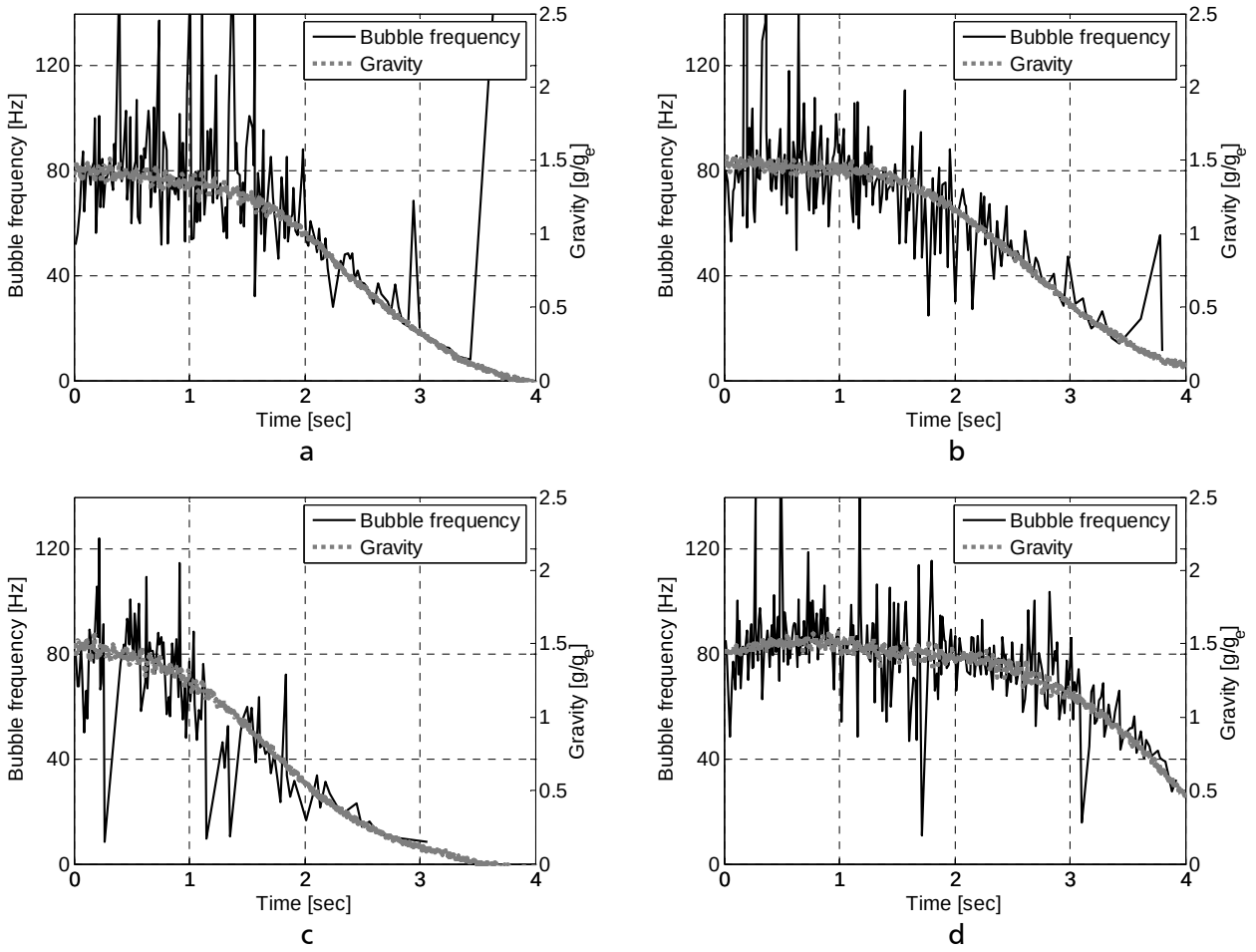

Figure 6.20: Bubble frequency and gravity versus time, sequences 70 (a), 74 (b), 67 (c) and 72 (d)

In order to compare the measured data to empirical correlations the frequency was related to gravity and the data points of all evaluated sequences are plotted in Figure 6.21. The best fit of the data is a linear approach. The dependence of the departure diameter on gravity was already evaluated in Chapter 6.2. The found dependency was $d_D \sim g^{1/2}$. Since the bubble growth is definitely not inertia controlled in the given case the approach of Ivey [48] $f_b^{1/2} d_D = const.$ for heat transfer controlled bubble growth (see Chapter 2.4.2) yields to:

$$f_b \sim g \tag{77}$$

Several empirical correlations include the gravity in this way. However, none of these correlations fit the absolute value of the data. The correlations of Zuber [136] and Malenkov [75] clearly underpredict the bubble frequency and the indicate a non-linear relationship between f_b and g. The best fitting correlations are is the ones of Peebles & Garber [93] and Jakob & Fritz [50] in the range of $0.5 < g/g_e < 1.5$ but both correlations do also not include gravity as $f_b \sim g$.
In the correlations of Mikic & Rohsenow, equations (35) and (36), the approach of Ivey for heat transfer controlled bubble growth was implemented. However, the gradients of the resulting linear relationship between f_b and g do not fit to the measurement data indicating that the empirical constants are not valid for the present boiling case.

At this point it has to be emphasized that none of the correlations have been developed for the given boiling process. Nevertheless, the reliability of bubble frequency correlations is low and, therefore, their usability questionable.
Nevertheless, the approach of Mikic & Rohsenow was used to express a new correlation by adapting the empirical constant for the present case.

$$f_b^{1/2} d_D = C_1 \mathrm{Ja} \sqrt{a_l} \quad \text{with } C_1 = 1 \tag{78}$$

The new correlation is also included in Figure 6.21 as Schweizer correlation. But although it fits the experimental data of the present boiling case very well it has to be emphasized that the development of the correlation was not based on physical phenomena as it is the case for the departure diameter correlation proposed by the author (74). By including the Jakob number Ja in the proposed way the results are very sensitive to the accuracy of the wall superheat. Furthermore, it does not include potential influences for example of the heat flux or the nucleation site behaviour (waiting time) which could be implemented in the empirical constant C_1. These influences could only be investigated by further parameter variation using the introduced experimental setup.

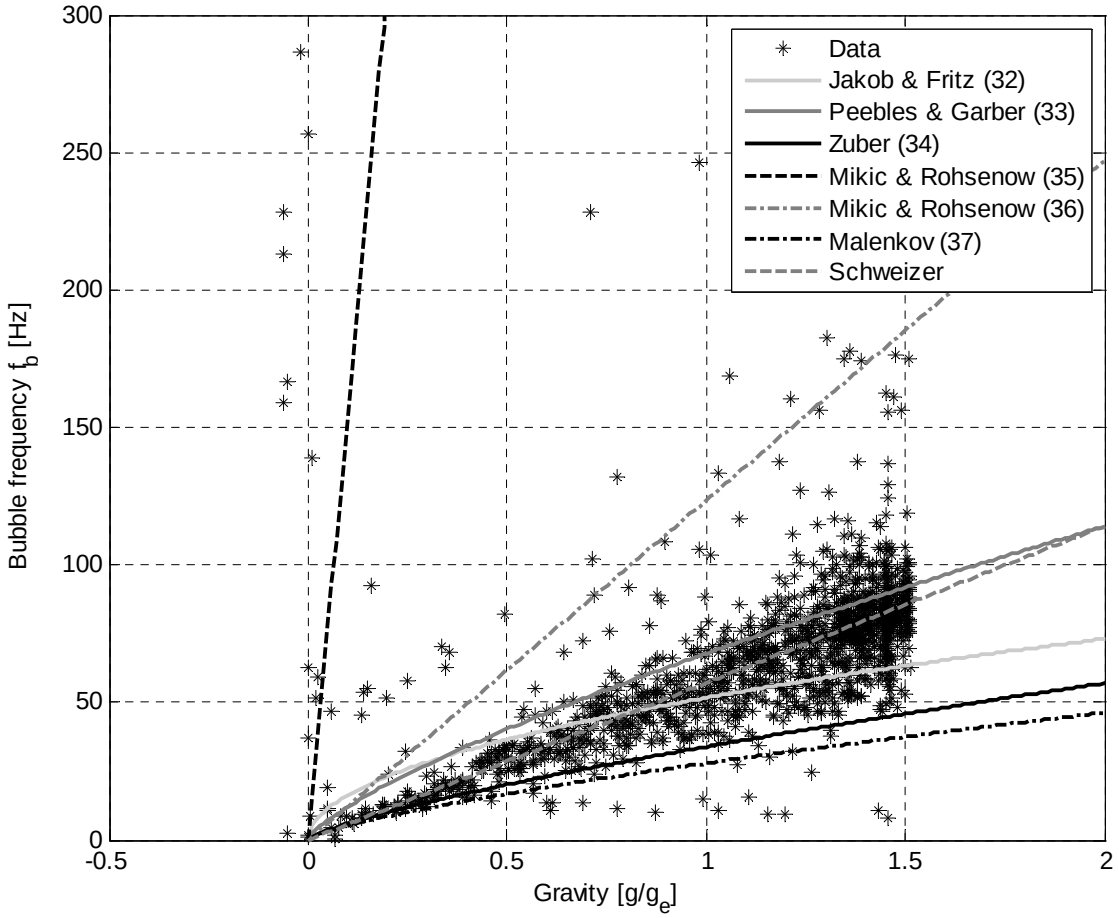

Figure 6.21: Bubble frequency versus gravity, all sequences data points; comparison to empirical correlations

6.4. Mean Heat Flux and Temperature during Transition from Hypergravity to Microgravity

The mean heat flux $\dot{q}_{mean}$ is the averaged heat flux to the fluid over the entire FOV of the IR camera that has a size of 6.6 mm x 6.6 mm. Also, the mean temperature t_{mean} is the result of averaging over the whole FOV. These two values are plotted over the entire sequence time for different measurement sequences in Figure 6.22-Figure 6.25. The sequences were recorded in the transition between hypergravity and microgravity. At the beginning of each of the shown sequences a single bubble column detaches at the artificial nucleation site. No other sites are active. The diameter of the bubbles is less than $2\ \mathrm{mm}$ as long as $g/g_e > 1$. Therefore, the area of the temperature and heat flux imprint imposed by the bubbles is small compared to the FOV. Fluctuations in the mean values are hardly visible. The mean heat flux is equal to the electric heating power $\dot{q}_{el}$ which is 7324 W/m² for sequence 64 and 70 and 7773 W/m² for sequence 75 and 77. The back side of the foil is assumed to be adiabatic. Heat conduction in the foil plane at the borders of the FOV is zero since there is no temperature gradient. The electric heating power is entirely transferred to the fluid by natural convection in the area of the surface that is not influenced by the bubble growth. The natural convection heat transfer coefficient depends strongly on buoyancy and, thus, on gravity. The heat capacity of the foil is small due to its thickness. Hence, the heating power has to be equal to the mean heat flux as the heat storage is negligible and as long as only natural convection is regarded (excluding the boiling process, e.g. in the area not influenced by the process). A decreasing heat transfer coefficient accompanied with constant heating power and bulk liquid temperature leads to the observed increase in the mean wall temperature.

The vertical grey line indicates the time at a gravity level of $g/g_e = 0.07$. On the left side of the line the temperature fluctuations are caused by ebullition cycles of now larger growing but still detaching bubbles. The characteristic transient wall temperature fluctuations occur on a larger portion of the FOV as gravity decreases. Additionally, the natural convection heat transfer decreases with the gravity causing a rising mean temperature. At the right side of the grey line two effects are observable: a) the bubbles do not detach anymore and b) at mean temperature values between 75 °C and 80 °C rapid bubble growth occurs. The rapid bubble growth firstly causes a small decrease of the mean temperature. Due to microgravity, buoyancy does not move the bubbles away from the heating surface. Thus, the vapour is insulating the surface. A steep increase in the wall temperature is the consequence. Re-wetting of the heating surface is caused by fluid inertial motion in the test cell and by g-jitter. A large number of nucleation sites are active after re-wetting. Vapour has obviously been trapped inside these cavities due to the previous dry-out. This, in conjunction with high wall superheat results in high mean heat transfer, a significant temperature decrease and, again, vapour production that insulates the surface. The process repeats but it is not stable. If the fluid motion stops and g-jitter disappears vapour stays at the surface leading to a burn-out. Alternatively, a large bubble may rest above the heating surface collecting smaller bubbles from the surface as it was observed by several authors (see Chapter 2.3). In the present case this could only happen coincidentally since the bubble growth is thermodynamically controlled. The bubbles do not detach by inertial forces.

A large contact line length caused by multiple bubbles growing, sliding and merging on the surface is characteristic for the boiling process after re-wetting. Often, droplets are trapped inside larger bubbles forming also a circular contact line with high evaporation rates (see Chapter 3.3.3).

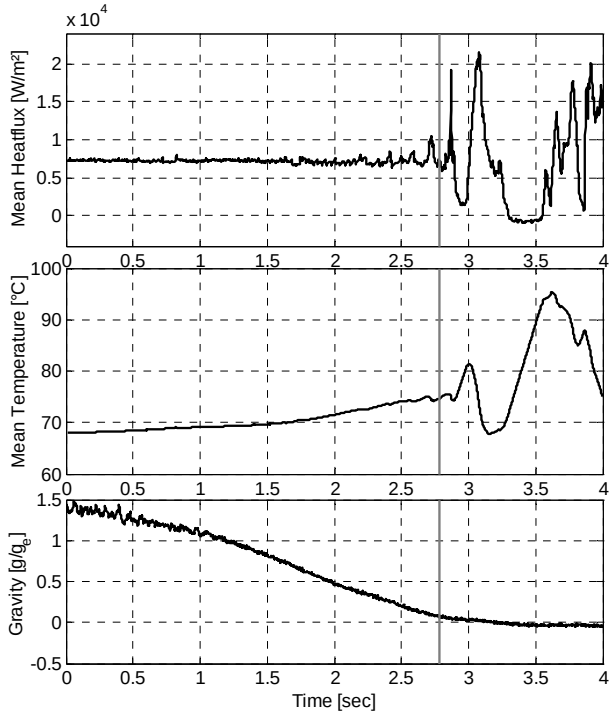

Figure 6.22: Development of mean heat flux, mean temperature and gravity during the transition into microgravity, sequence no. 64

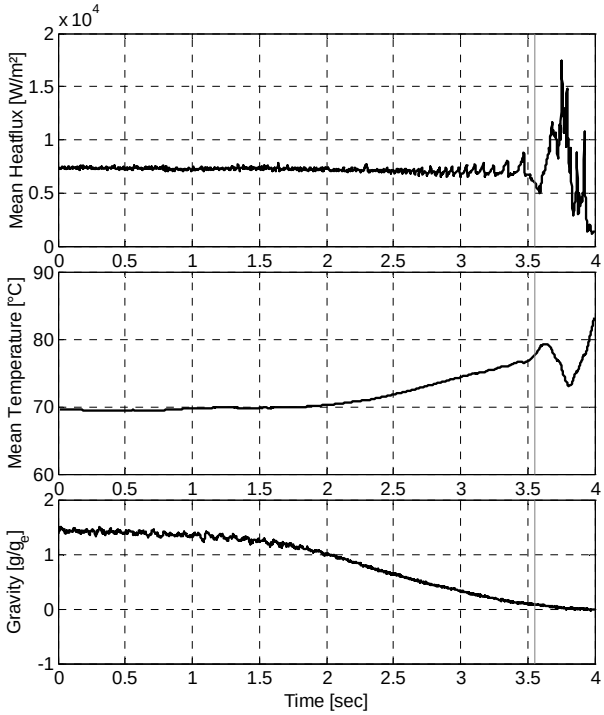

Figure 6.23: Development of mean heat flux, mean temperature and gravity during the transition into microgravity, sequence no. 70

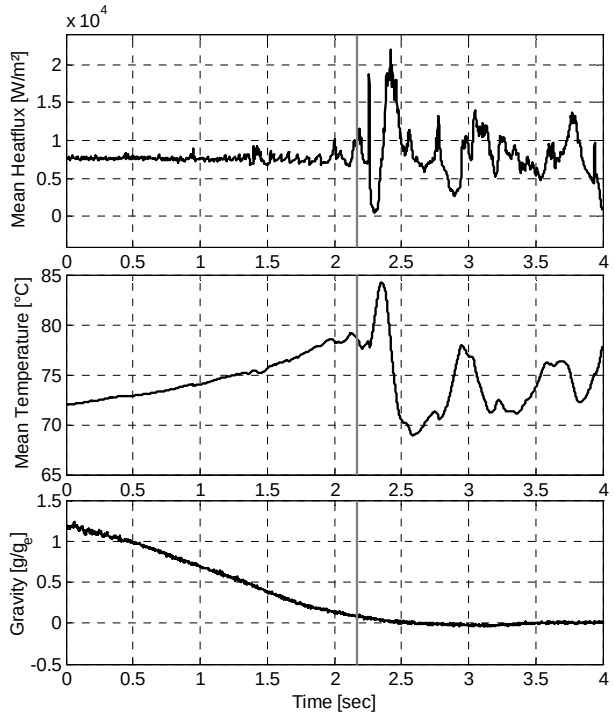

Figure 6.24: Development of mean heat flux, mean temperature and gravity during the transition into microgravity, sequence no. 77

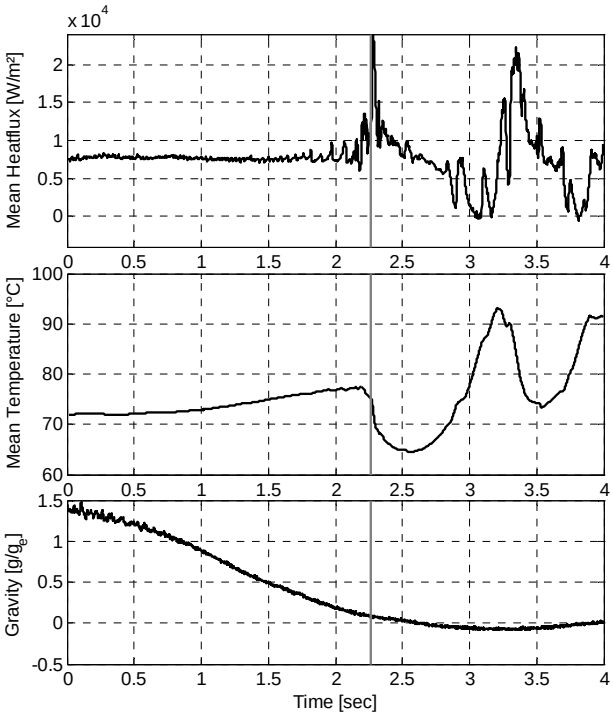

Figure 6.25: Development of mean heat flux, mean temperature and gravity during the transition into microgravity, sequence no. 75

6.5. Mean Heat Flux of Single Bubble Cycles at Varying Gravity Levels

An interesting question is how the heating surface area surrounding the nucleation site contributes to the heat transfer. A similar investigation was recently published by Moghaddam and Kiger [81] (see Chapter 2.2). In this study, circular areas were defined concentric around the nucleation site with an increment in the diameter of 0.6 mm (see Figure 6.26).

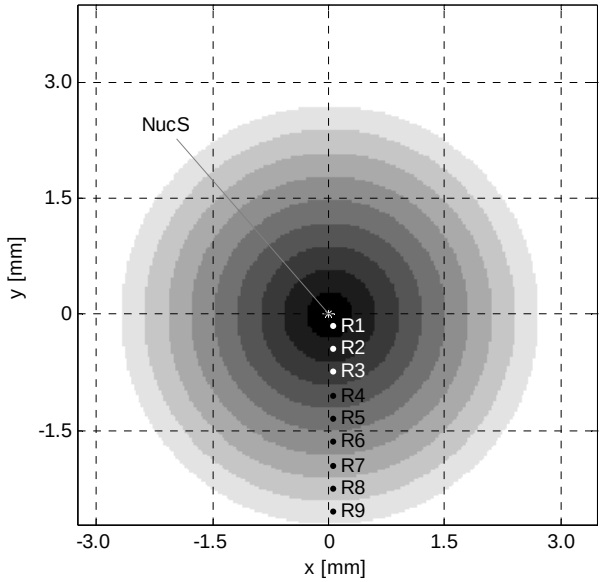

Ring	Inner diameter D_i	Outer diameter D_a
R1	0 mm	0.6 mm
R2	0.6 mm	1.2 mm
R3	1.2 mm	1.8 mm
R4	1.8 mm	2.4 mm
R5	2.4 mm	3.0 mm
R6	3.0 mm	3.6 mm
R7	3.6 mm	4.2 mm
R8	4.2 mm	4.8 mm
R9	4.8 mm	5.4 mm

Figure 6.26: Mask for evaluation of heat flux and temperature around nucleation site (NucS)

The heat flux was averaged over each of these rings and is shown in Figure 6.27 for a section of sequence 70 and in Figure 6.28 for a section of sequence 77. The plotted bubble cycles are the last detaching bubbles at low residual gravity. At $\tau = 1.81\,\mathrm{s}$ of sequence 77 the bubble detaches and the next bubble is nucleated without any waiting time. The heat flux at the nucleation site pixel is highest. The second highest peak is at the circular area R1 around the nucleation site with an outer diameter of D_a=0.6 mm. The heat flux imprint influences additionally the next ring R2. The larger rings are not affected. The mean heat flux in the larger rings is equal to the electrical heating power. At $\tau = 1.817\,\mathrm{s}$ the highest heat flux is at the second ring R2. The heat flux in the first ring R1 and at the nucleation site (NucS) is well below and decreasing. The heat flux of the third ring R3 has a positive gradient indicating that the bubble foot diameter increases. The heating surface underneath the first ring R1 is now entirely covered by the adsorbed film where the heat transferred to the vapour is negligible. The bubble foot diameter further increases until it reaches its maximum diameter at $\tau = 1.848\,\mathrm{s}$. At the maximum foot diameter the fifth ring R5 is the largest affected ring. The heat flux in the next outer rings remains constant.
While the bubble departs the bubble foot diameter decreases and the heat flux peak caused by strong evaporation at the contact line passes through the rings in reverse order. Remarkable is that the heat flux peak of the rings is larger in the departure process with an advancing contact line than in the growing process with a receding contact line. Also, the departure process takes more time than the growing process ($\Delta\tau_{departure} = 50\,\mathrm{ms}$, $\Delta\tau_{growing} = 31\,\mathrm{ms}$).

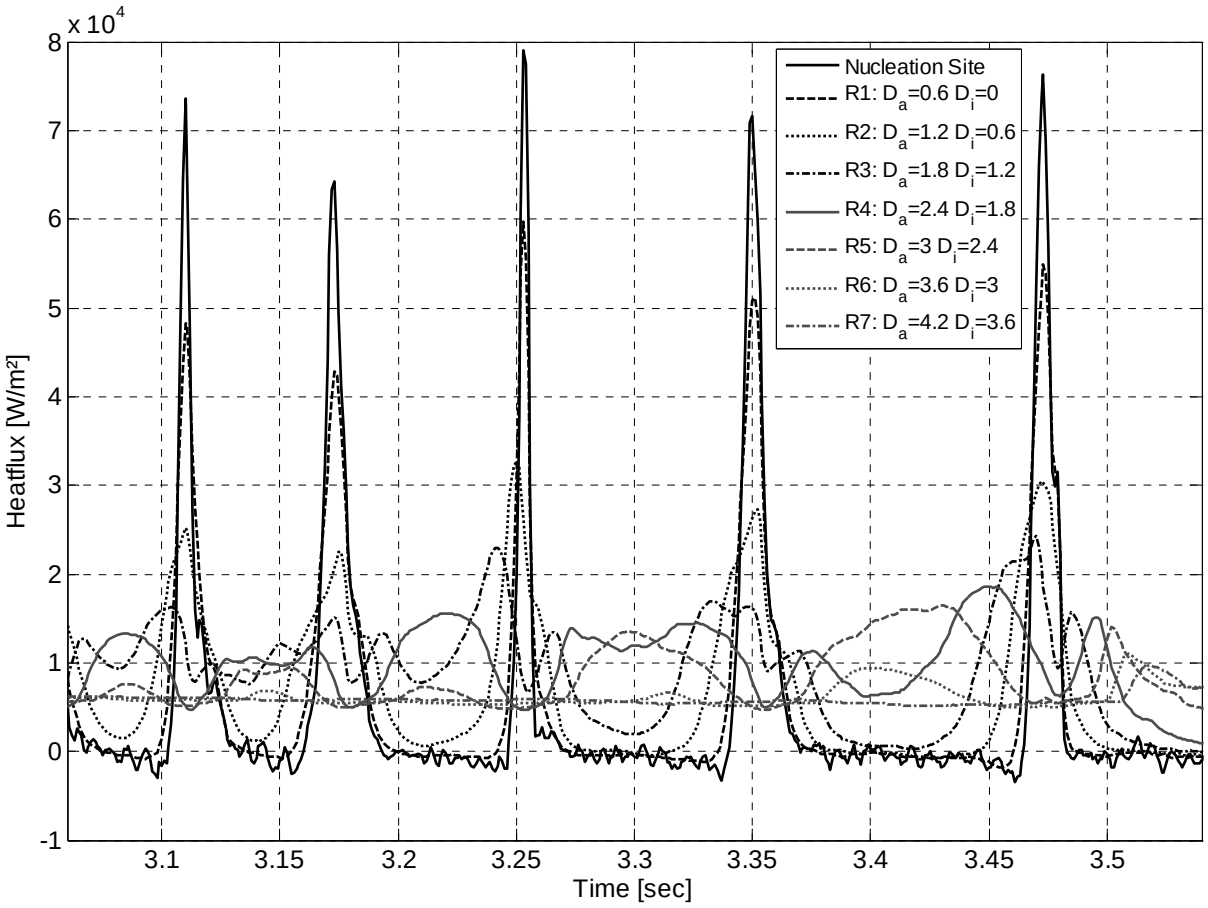

Figure 6.27: Mean heat flux in concentric circular areas around the nucleation site, sequence no. 70

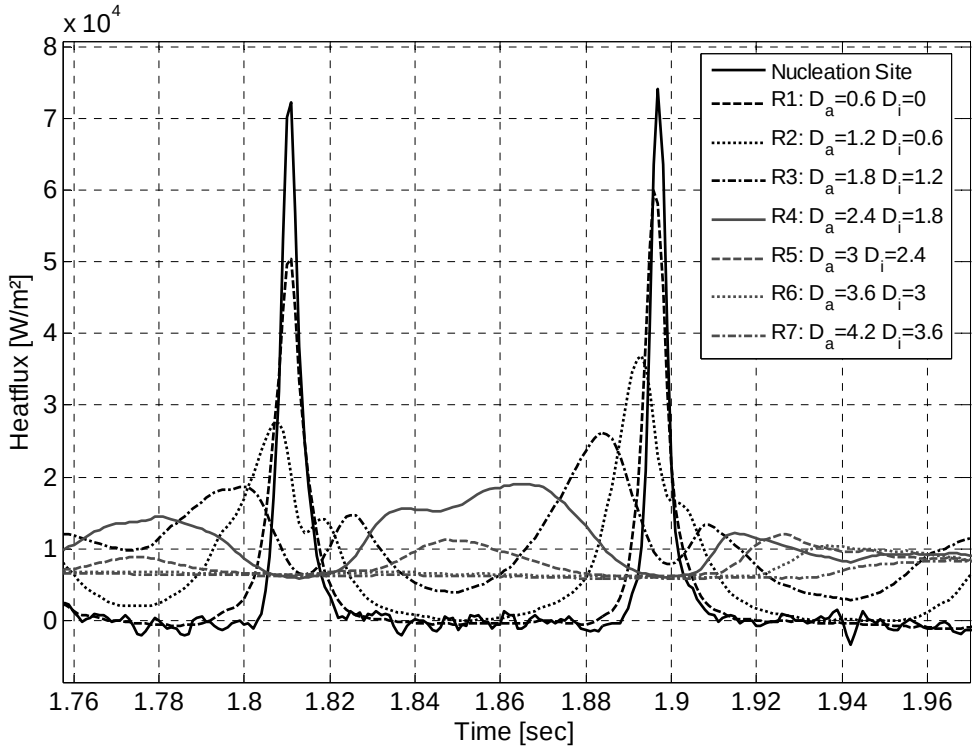

Figure 6.28: Mean heat flux in concentric circular areas around the nucleation site, sequence no. 77

The mean temperature of each ring versus time is shown in Figure 6.29. The temperature in the outer two rings R6 and R7 is not influenced by the bubble ebullition cycle. The temperature in these rings increases during the section by approximately 1.5 °C due to the diminishing natural convection during the transition into microgravity. The temperature at the nucleation site and in the inner ring R1 is ~69 °C at the minimum because of the heat flux peak when the bubble foot diameter is small i.e. during detachment of the previous and nucleation of the next bubble. After this minimum it steeply increases because the heat flux to the fluid is much lower than the electrical heating power in the adsorbed film region.
It could be assumed that the larger peak of the departure process is attributed to a higher wall superheat when the advancing contact line moves over the former adsorbed film area where the temperature was steeply increasing. This assumption was disproved by looking at the local heat transfer coefficient (see Figure 6.30). The local heat transfer coefficient α_{loc} is defined as:

$$\alpha_{loc} = \frac{\dot{q}_{fluid}}{t_w - t_{sat}} \tag{79}$$

If the conditions near the contact line are equal during advancing and receding the heat transfer coefficient near the contact line is also maintained. Therefore, the ratio $\Delta T_{w,advancing} / \Delta T_{w,receding}$ of the wall superheats $\Delta T_w = T_w - T_{sat}$ of the peaks must be equal to the ratio of the heat fluxes $\dot{q}_{fluid,advancing} / \dot{q}_{fluid,receding}$. At the third ring R3 the ratio of the heat fluxes of the peaks at $\tau = 1.825$ s (receding contact line) and at $\tau = 1.885$ s (advancing contact line) is $\dot{q}_{\tau=1.885s} / \dot{q}_{\tau=1.825s} = 1.5$. The superheat at the first peak is $\Delta T_{w,receding} = 30$ K at $t_{w,receding} = 72$ °C. Hence, to verify the assumption the wall temperature at the second peak must be approximately $t_{w,advancing} = 87$ °C which is not the case. The measured wall temperature is $t_{w,advancing} = 72.5$ °C.

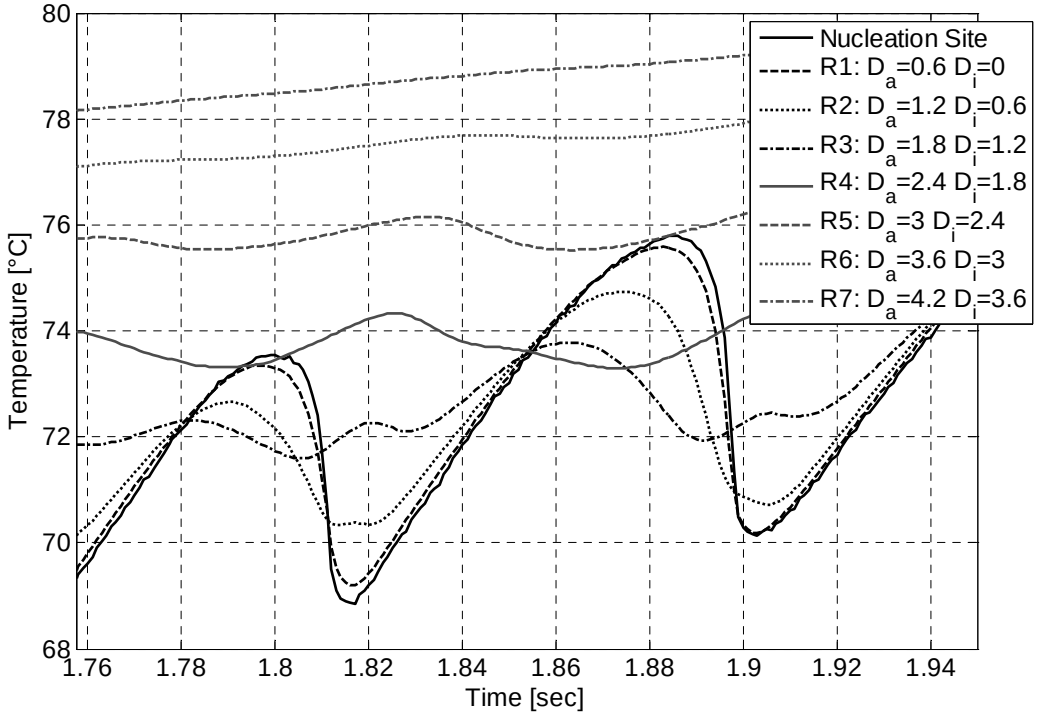

Figure 6.29: Mean temperature in concentric circular areas around the nucleation site, sequence no. 77

The conclusion that can be drawn from this investigation is that other effects enhance the heat transfer during the departure process. Moghaddam and Kiger [81] attributed this to transient conduction. They defined transient conduction as the heating up of colder liquid sucked near the wall by the constricting bubble foot during departure.
However, in the quantification of their data they allocated not only the increase of the peak heat flux to transient conduction but the complete peak during bubble detachment. They neglected contact line evaporation during bubble departure what can not be justified as shown in Chapter 6.6. Nevertheless, the increase of the peak height during bubble detachment is due to periodic heat storage in the liquid boundary layer, in literature often referred as transient conduction (see Chapter 2.1.2).
In order to allow the future comparison of numerical computations to the experimental data of the regarded bubble 88, sequence 77, the diameters of the bubble $d_{b,volume}$, $d_{b,edge}$ and the foot diameter d_{foot} are shown in Figure 6.31. The gravity was $g/g_e = 0.2$ at $\tau = 1.82\,\mathrm{s}$ and the contact angle of the bubble at the maximum foot diameter was $\theta = 58.6°$ using equation (76). Heating power was $\dot{q}_{el} = 7773.5\ \mathrm{W/m^2}$ and saturation temperature $t_{sat} = 42.1\,°\mathrm{C}$.

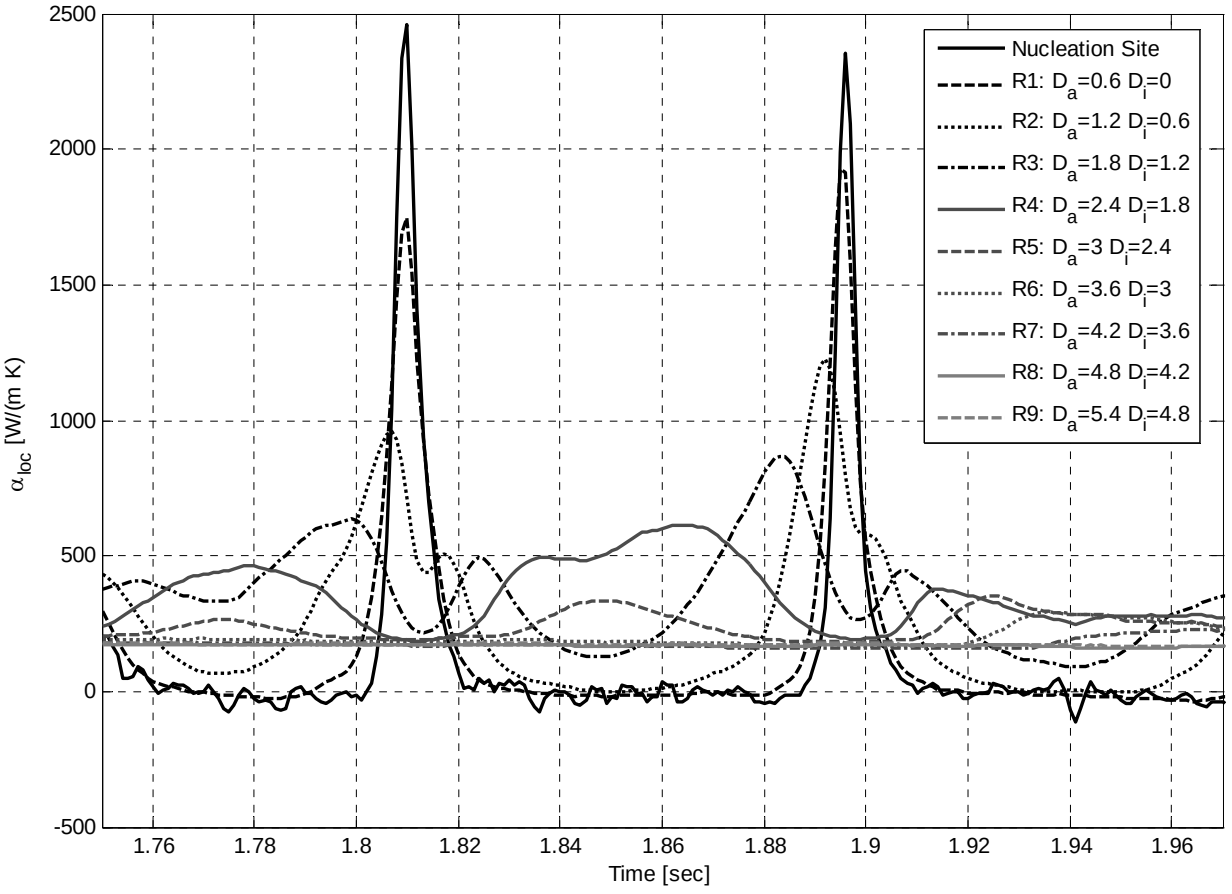

Figure 6.30: Heat transfer coefficient in concentric circular areas around the nucleation site, sequence no. 77

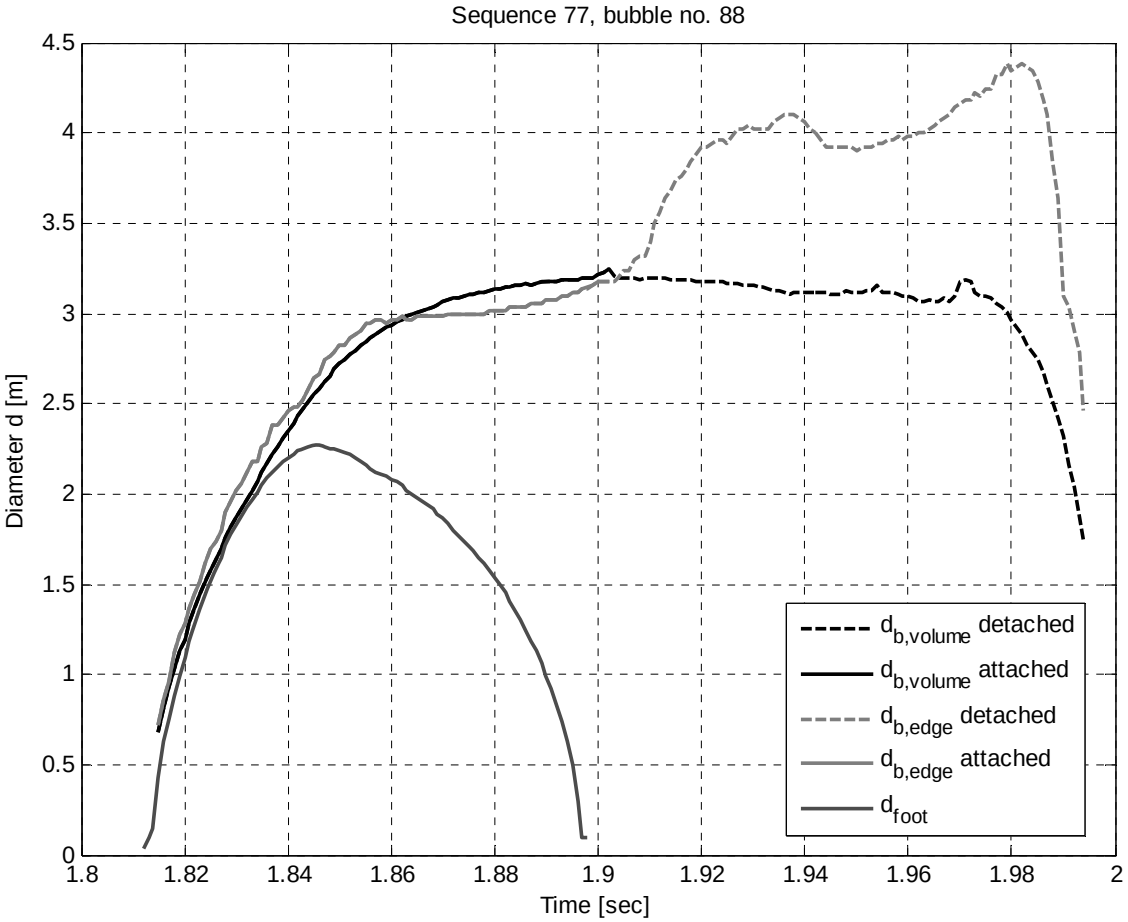

Figure 6.31: Diameters of the bubble, sequence no. 77

6.6. Heat Flow Distribution at Single Vapour Bubbles

In order to properly describe and model a nucleate boiling process it is mandatory to understand all heat transfer mechanisms playing a role in the process and their contribution to the overall heat transfer. Based on the attempt of Stephan et al. [119] to visualize the heat paths the flow chart in Figure 6.32 is proposed. Heat is transferred from the heat source to the heating wall where the boiling process takes place. As firstly stated by Kenning and Yan [58] and also clearly shown in this study constant wall temperature boundary conditions can not be applied and, hence, the wall has to be included in the evaluation. Transient heat conduction and periodic heat storage occurs in the wall material. General agreement exists within the scientific community concerning the heat transfer mechanisms in nucleate boiling but not concerning their contribution to the overall heat transfer.

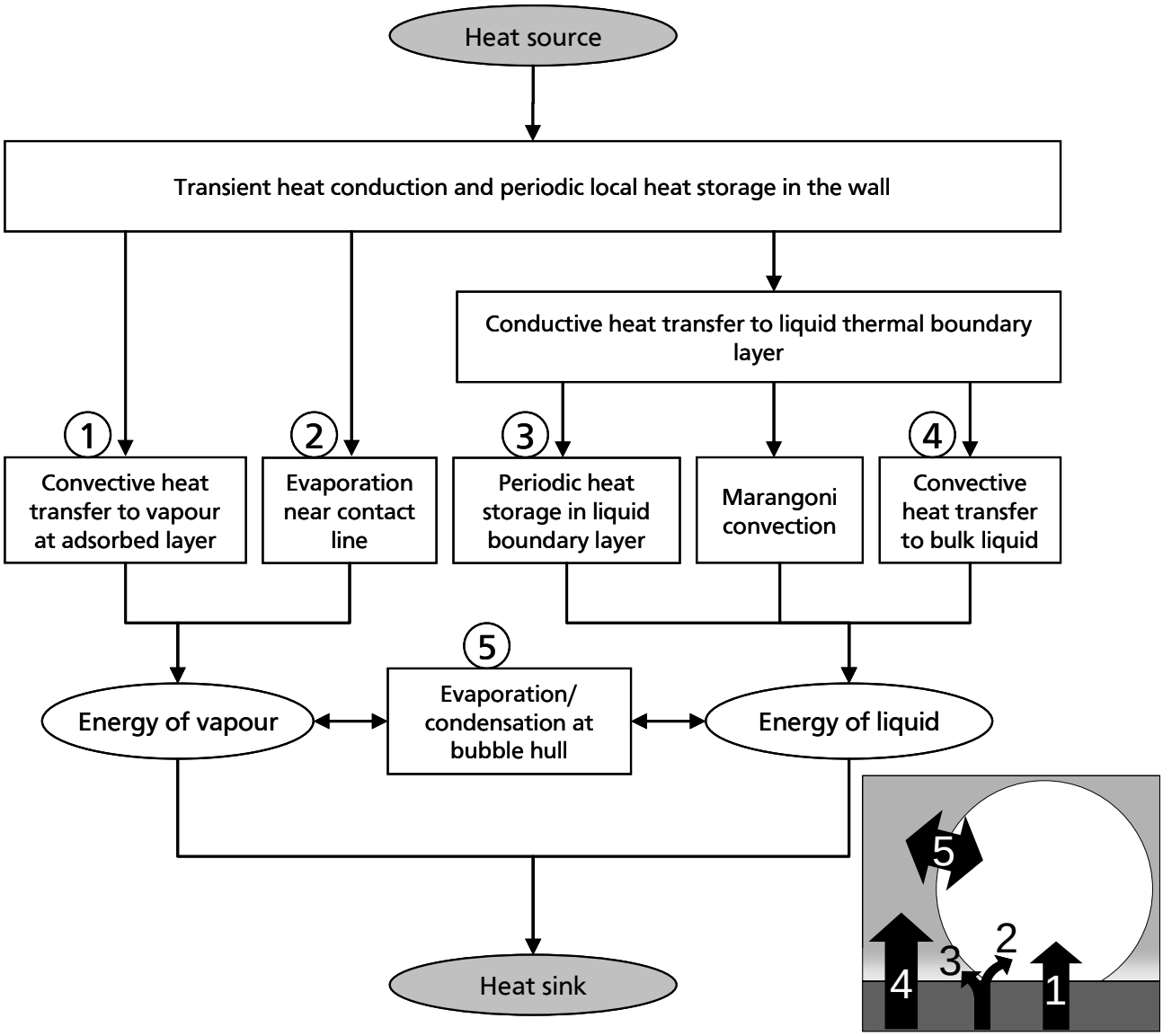

Figure 6.32: Heat paths and transport mechanisms

The heat transfer mechanisms from wall to fluid in nucleate boiling are generally convective heat transfer to the vapour at the dry patch inside an attached bubble, evaporation near the contact line of an attached bubble, periodic heat storage in the liquid boundary layer (also often referred as transient conduction), Marangoni convection and convective heat transfer to the bulk liquid. Beside the heat transfer from wall to liquid and vapour, also heat transfer between vapour and liquid is present. Evaporation and condensation takes place at the bubble hull depending whether the surrounding liquid is sub-cooled or superheated.
An evaluation of the contribution of all heat transfer mechanisms during the whole ebullition cycle of a single bubble is presented in this chapter. In the following the mechanisms and their characterization are described.

6.6.1. Forced Convective Heat Transfer to Vapour

When a bubble grows on the wall the receding contact line leaves a thin, non-evaporating fluid film. The intermolecular (van-der-Waals) forces are too strong to allow the evaporation of the adsorbed layer. Its influence on the heat transfer from the wall to the vapour inside the bubble, however, is negligible. Hence, the heat transfer mechanism in this area is convection. Due to vapour motion

induced by the bubble growth, interface movement and high evaporation rate at the contact line forced convective heat transfer is present at the adsorbed layer. It is already shown in previous chapters of this thesis that the heat flux in this region is very low and, therefore, the contribution to the overall heat transfer is negligible. Nevertheless, the effect on the boiling process should be evaluated. Due to low vapour heat capacity the influence on the vapour temperature can not be neglected. Kunkelmann included the vapour phase in his recently published numerical study [67]. He showed a strong superheat in the lower third of an attached bubble (see Figure 6.33).

6.6.2. Evaporation near Contact Line

Evaporation near the contact line is of tremendous importance for the boiling process [119]. As shown by both numerical and experimental studies a significant portion of the overall heat flows through this relatively small part of the bubble. The ring-shaped region of high heat flux clearly indicates the location of the contact line. However, it is not easy to quantify the evaporation at the contact line in all bubble states because an additional effect which is the periodic heat storage in the liquid boundary layer (transient conduction) is superposed during bubble detachment. Numerical studies of Fuchs [32] and Kunkelmann [67] proved that the heat flow at the contact line is nearly proportional to the contact line length. That implies an approximately constant evaporative heat flow per unit contact line length. Transient conduction is only present during bubble detachment when the contact line is advancing and not during bubble growth. Hence, the integrated peak heat flux is completely allocated to contact line evaporation in the state of an expanding bubble foot. The evaporative heat flux per unit contact line can be calculated for this period and is applied to the detachment period where also transient conduction occurs.

6.6.3. Periodic Heat Storage in Liquid Boundary Layer (Transient Conduction)

During bubble detachment the contracting bubble foot affects the thermal layer that was pushed previously outwards during bubble growth. The thermal layer is reshaped in such a way that the liquid temperature gradient at the wall is significantly enhanced resulting in a strong increase of the heat conduction. The most common image of cold bulk liquid sucked to the wall during bubble foot constriction as published by several authors (see Chapter 2.1.2) is often interpreted in a wrong way. The vapour is not replaced by cold bulk liquid but by adjacent liquid of the thermal boundary layer. Cold bulk liquid could be driven towards the wall by the motion of the bubble wake after detachment. The influence on the thermal layer occurs only in a tiny region near the contact line underneath the bubble hull. A concrete visualization of the spatial influence of transient conduction is shown in Figure 6.33.

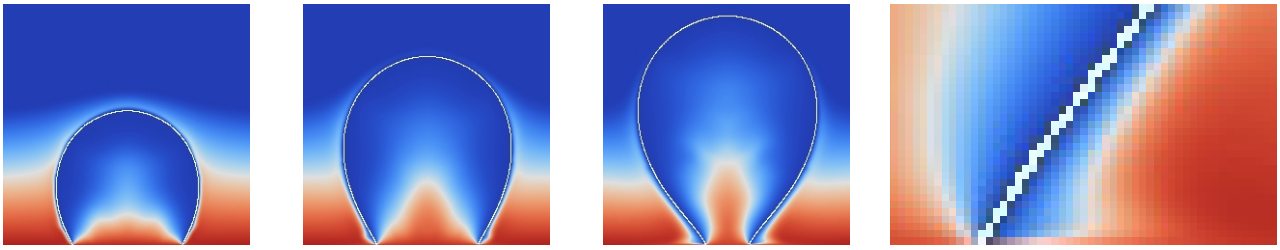

Figure 6.33: Numerical simulation of a growing and detaching vapour bubble (HFE-7100, 5K wall superheat), performed by Kunkelmann [67] at 10, 17 and 24 ms (from left). The right image zooms to the near contact line region at 24 ms.

The presented images are part of the results of a numerical simulation performed by Kunkelmann [67] described in Chapter 2.6. The deformation of the thermal boundary layer is clearly visible. Transient heat conduction is the process to re-establish the initial thermal layer. A significant heat flow is transferred for this purpose. Since the shape of the thermal layer is hardly influenced during bubble growth transient conduction is not present during the growth period but during bubble detachment and waiting time.
Transient conduction heat flow can be calculated by subtracting the contact line heat flow from the integrated heat flux peak.

6.6.4. Marangoni Convection

Marangoni or thermocapillary convection is induced by a surface tension gradient. Generally, this gradient is due to the temperature dependency of the surface tension, non-condensable gases or mixture effects. In the present study degassed, pure n-Perfluorohexane was used. Hence, only the temperature dependency of the surface tension can cause Marangoni convection. The Marangoni number in the present case is in the range of $Ma = 10^5 \ldots 10^7$ indicating the presence of the thermocapillary convection. However, its contribution to the overall heat transfer is assumed to be negligible in saturated boiling conditions according to the findings of Ammerann et al. [1], Jabardo [49] and Tong et al. [125]. Tong et al. estimated the heat transfer due to Marangoni convection to be less than 2.5% of the overall heat transfer. In the present study no evidence of thermocapillary convection was observed in convection patterns in the high speed images. Hence, the contribution of Marangoni convection was neglected.

6.6.5. Convective Heat Transfer to Bulk Liquid

Whereas in fully developed nucleate boiling the rising bubbles may induce strong liquid motion which results in strong forced convective heat transfer at the heated wall. In the present case of boiling at a single nucleation site natural convection takes place outside the bubble influenced area. Here, the characterization of natural convection is an easy task since wall and liquid temperature as well as heat flux to the fluid is known. Remarkable is that the diameter of the bubble influenced area is nearly always smaller than the bubble diameter. That means, in the present case, the bubbles have no influence on the heat transfer to the bulk liquid outside a circular area which has a diameter equivalent to the bubble diameter. Natural convection diminishes in microgravity as shown in Chapter 6.4.

6.6.6. Evaporation / Condensation at Bubble Hull

The liquid vapour interface of a bubble is divided in two parts: the contact line area where high heat fluxes occur due to thin film evaporation and the rest of the interface that is referred to as bubble hull. Heat and mass transfer is not uniformly distributed over the bubble hull. It is dependent on the temperature of the liquid at the portion of the hull. When a bubble grows out of the superheated liquid layer into sub-cooled bulk liquid condensation occurs at the bubble cap while evaporation still takes place at the lower parts of the hull. An evaluation on this topic introducing the heat flux ratio is also described in Chapter 3.3.3 and further described in [102].
In the present study only the net mass flow (net latent heat flow) at the bubble hull was calculated. The development of the bubble volume in time leads to the overall latent heat flow to the bubble that is composed of the evaporation at the contact line and the mass flow at the bubble hull.

6.6.7. Evaluation Procedure of the Distinctive Heat Flows from Experimental Data

In order to calculate the overall heat flow at a bubble the evaluation of the bubble images described in Chapter 5.2 and the heat flux evaluation involving the ellipse fitting algorithm described in Chapter 5.1.1 have been taken into account.
One output of the bubble image evaluation is the volume of every bubble. The overall latent heat flow can be calculated:

$$\dot{Q}_b = \rho_v \cdot \Delta h_v \frac{V_{i+1} - V_i}{\Delta \tau} \tag{80}$$

The evaluation of the other heat flows is based on the heat flux distribution of the foil and involves the ellipse fitting algorithm.
For the quantification of the heat flow to the vapour in the adsorbed film region all pixels within the innermost ellipse are allocated to this region. The heat flow of this region is calculated by integrating the heat flow of all pixels within the ellipse.
The radial heat flux profiles of an evaluated bubble (sequence 77, bubble 88) are presented in Figure 6.34. These profiles are the results of averaging in circumferential direction around the centre of the fitted ellipse, i.e. the mean value of all pixels at a specific radial distance from the bubble foot centre versus this radial distance coordinate. From an initial wide peak at $\tau = 1815$ ms a smaller peak with constant height and shape moves in positive radial direction as the bubble foot diameter expands ($\tau = 1820 - 1840$ ms). This is remarkable because it supports the assumption of a constant latent heat flux per unit contact line length since the integrated area underneath the peak is constant. As soon as the bubble starts to detach and the foot is constricting the height of the peak increases with decreasing foot diameter. This increase is attributed to transient conduction/periodic heat storage in liquid boundary layer.
The calculation of the heat flow per unit contact line length was performed by accumulating all peak pixel located in between the innermost and outermost ellipses (see Chapter 5.1.1) and dividing by the contact line length.

$$\dot{Q}_{CL} = \frac{B_{pix}^{\ 2}}{L_{CL}} \sum_{peak} \dot{q}_i \tag{81}$$

The contact line course corresponds in good agreement to the fitted ellipse. Therefore, the contact line length is the circumference of the ellipse.

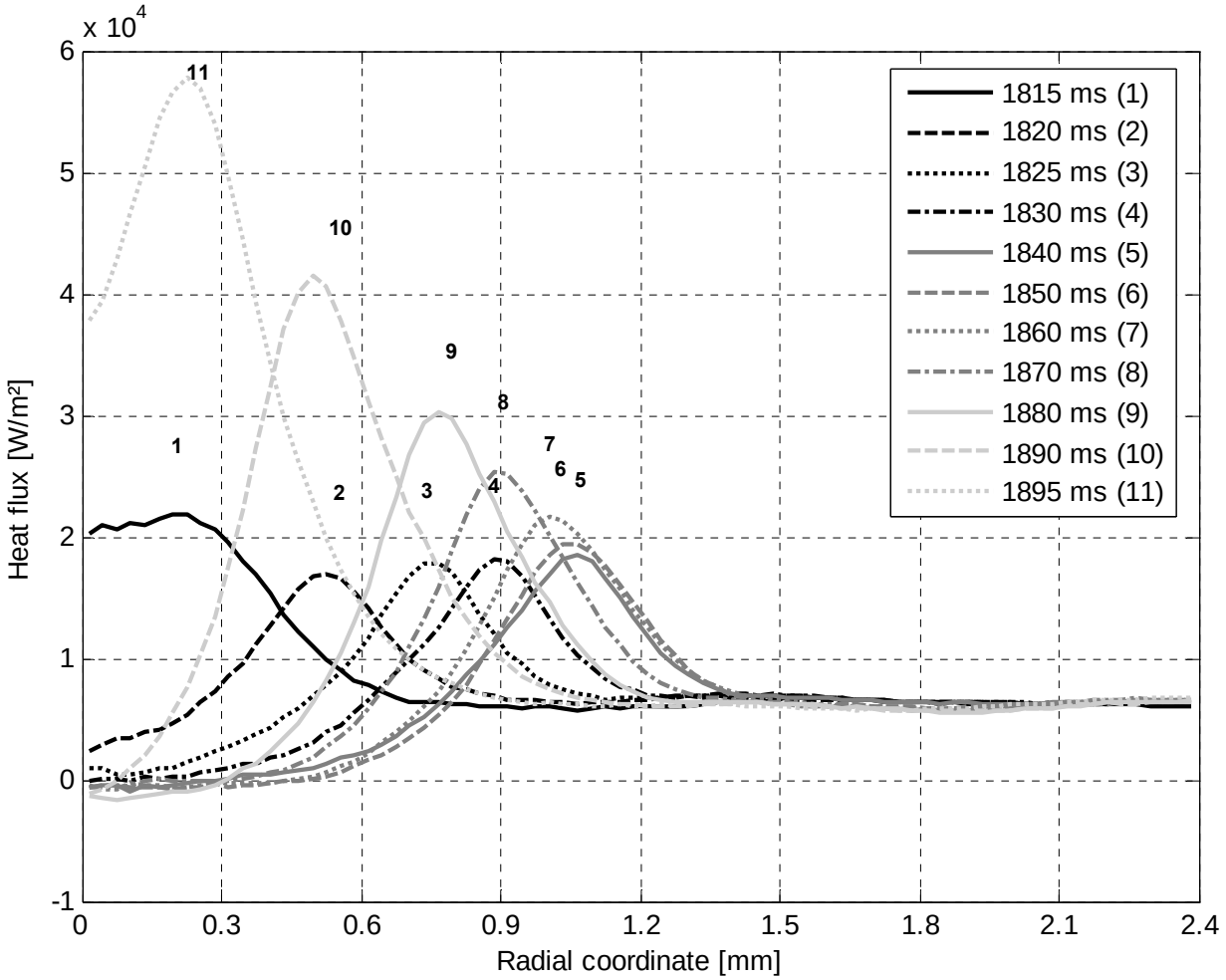

Figure 6.34: Heat flux profiles averaged in circumferential direction during the ebullition cycle of bubble 88, sequence 77

This heat flow per unit contact line length is shown in Figure 6.35 for the ebullition cycle of two bubbles. It still includes both contact line evaporation and transient conduction. In the first period of the bubble growth until a foot diameter of 0.7 mm the heat flow is influenced by the previous bubble. From that point an almost constant (slightly enhancing) contact line heat flow is observable until the bubble reaches its maximum foot diameter. During the constriction the heat flow per unit contact line length is increasing. As stated before, the difference between the heat flows is attributed to transient conduction.

A similar numerical evaluation was performed by Kunkelmann on the bubble presented in [67] and is shown in Figure 6.36. Experimental and numerical results are in very good qualitative and surprisingly also reasonably good quantitative agreement although the simulated boiling process has completely different boundary conditions. The numerical simulation was performed with working fluid HFE-7100 and a wall superheat of 5K in earth gravity conditions. Additional to the integrated peak heat flux the heat flow in the microregion is plotted. This heat flow was computed using the microregion model, parameterized and applied to the first liquid cell at the contact line (see Chapter 2.6.2). It can be seen that through this single cell already a large portion of the evaporative heat flow at the contact line is transferred. Also, high heat fluxes occur in the adjacent cells where the liquid film is still very thin.

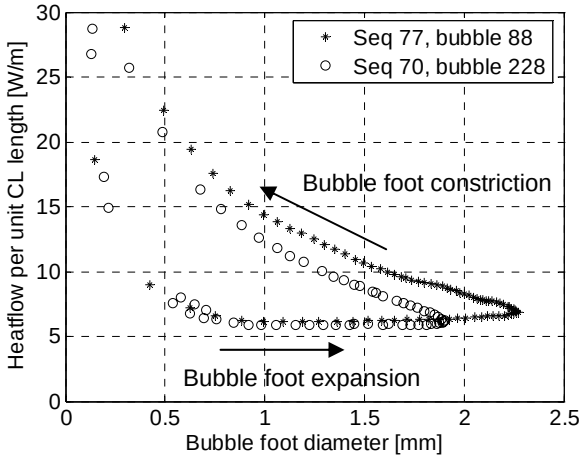

Figure 6.35: Heat flow per unit contact line (CL) length for two bubbles of two different sequences

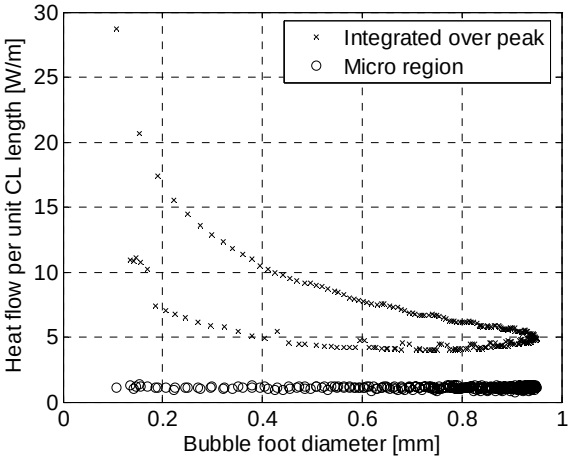

Figure 6.36: Heat flow per unit contact line length and micro region heat flow per unit contact line length of the simulated bubble (Kunkelmann)

The evaluation of the heat flow per unit contact line length was performed for all attached bubbles of a sequence. The results are plotted in Figure 6.37. It can be seen that the heat flow is very slightly, linearly increasing during expansion of the bubble foot for all bubbles in the same way. The assumption of a constant heat flow per unit contact line length is justified. The sequence was recorded during the hyper-g-micro-g-transition. The results of a large number of bubbles with a foot diameter not exceeding 1 mm create the black asterisk cloud. The foot diameter of the last bubble exceeded 4 mm. It did not detach, hence, the heat flow data of the constricting bubble foot is missing.

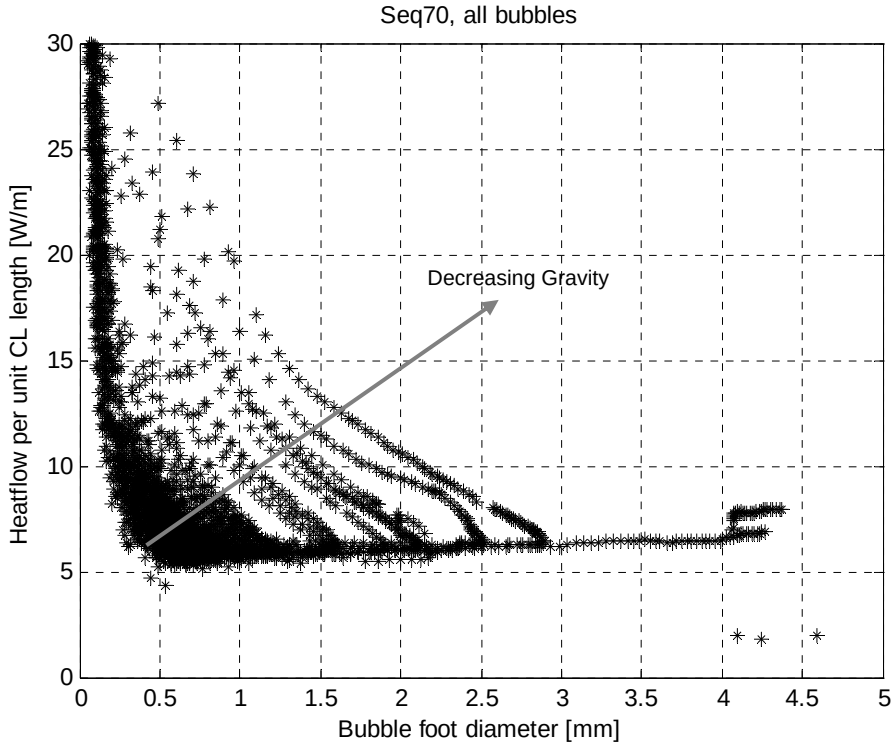

Figure 6.37: Heat flow per unit contact line for all bubbles of sequence 70

A characteristic behaviour of the heat transfer at the contact line is shown in Figure 6.38 where the heat flow per unit contact line length is plotted versus the contact line velocity. The contact line velocity was extracted from the experimental data by evaluating the change of the fitted ellipse. A negative velocity indicates a receding contact line (bubble growth) and a positive value an advancing contact line (bubble detachment). The shown data points belong to seven bubbles of sequence 77 recorded between τ=1.53 s and τ=2.00 s. During this period the gravity changed from 0.37g to 0.14g. When the contact line is receding the heat flow per unit contact line is nearly independent of the velocity. This constant value is attributed to the evaporative heat flow at the contact line as stated before. A linear dependency of the heat flow on the contact line velocity is indicated for positive velocities. The linear fit starts at the value of constant heat flow that is attributed to the contact line evaporation. Hence, the heat transfer due to transient conduction seems to be proportional to the contact line velocity.

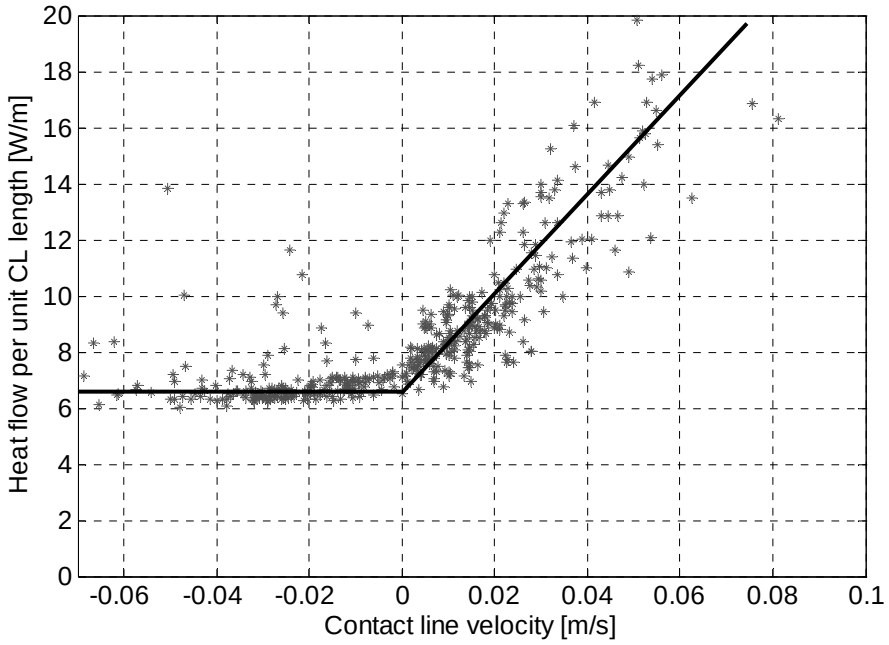

Figure 6.38: Heat flow per unit contact line versus contact line velocity, sequence 77, all data points between τ=1.53 s and τ=2.00 s

6.6.8. Results of the Evaluation

The development of the various heat flows during growth and detachment of two bubbles are presented in Figure 6.39 and Figure 6.40. Both bubbles were recorded during the transition phase in low residual gravity. The parameters of the bubbles are shown in Table 6.1. The bubbles are nucleated immediately after the previous bubble without any noticeable waiting time. Also subsequent bubbles had no waiting time. As it was expected the heat flow in the adsorbed film region is nearly zero during the whole ebullition cycle. At the beginning of the cycle the heat flow at the bubble hull is small due to the small interfacial area of the hull. The hull heat flow steeply increases as the hull

Sequence #	70	77
Bubble #	228	88
Electrical Heat Flux	7325 W/m²	7773 W/m²
Mean Foil Temperature	75.3 °C	79 °C
Bulk Liquid Temperature	42.2 °C	42.1 °C
Saturation Temperature	42.4 °C	42.2 °C
Gravity	0.3g	0.2g

Table 6.1: Parameters of the presented bubbles.

surface becomes larger and is still in contact with superheated liquid. The gradient decreases as the bubble grows into sub-cooled liquid. Even though the hull surface area still increases (indicated by a positive latent heat flow) the evaporation at the bubble hull decreases as the bubble proceeds to rise into sub-cooled regions. Bubble 88 seems to get in touch with higher sub-cooled liquid because the decrease is steeper. Remarkable is that more vapour is generated at the contact line than at the entire bubble hull in the last stage of bubble detachment.

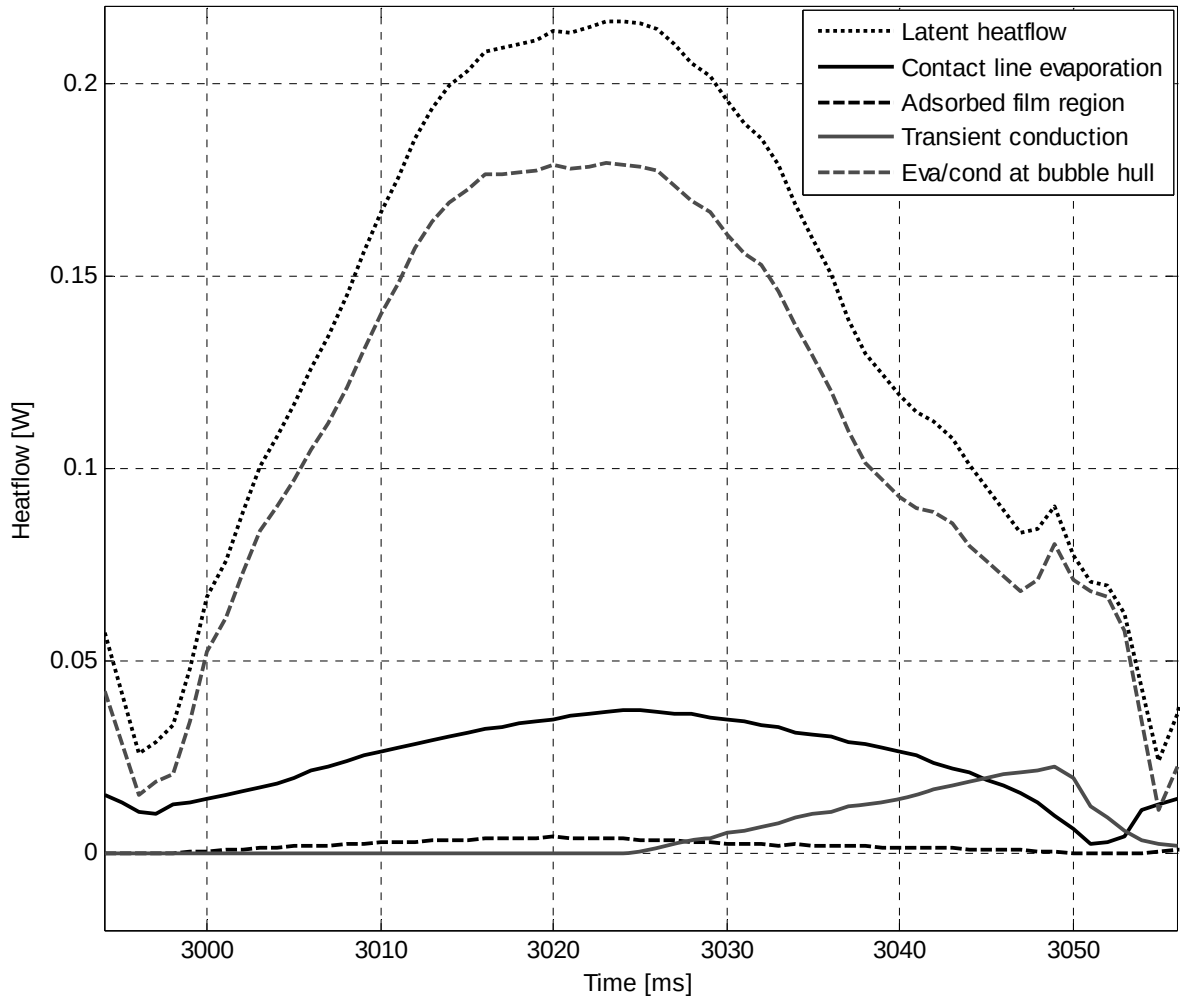

Figure 6.39: Heat flows distribution at a single vapour bubble (sequence 70, bubble 228)

The contact line evaporation is nearly proportional to the foot diameter and gives an indication about the ebullition state of the bubble. Growth and departure time are almost identical for bubble 228. Bubble 88 needs longer to detach than to grow. Transient conduction heat flow seems to increase linearly during the detachment time. At its maximum it is in the same order of magnitude as the latent heat flow at the contact line. However, the integrated contact line heat flow is much higher than the integrated transient conduction heat flow. That leads to a conclusion which contradicts the statements of Moghaddam and Kiger [80],[81]. In the studied case transient conduction is much less contributing to the overall heat flow than contact line evaporation.

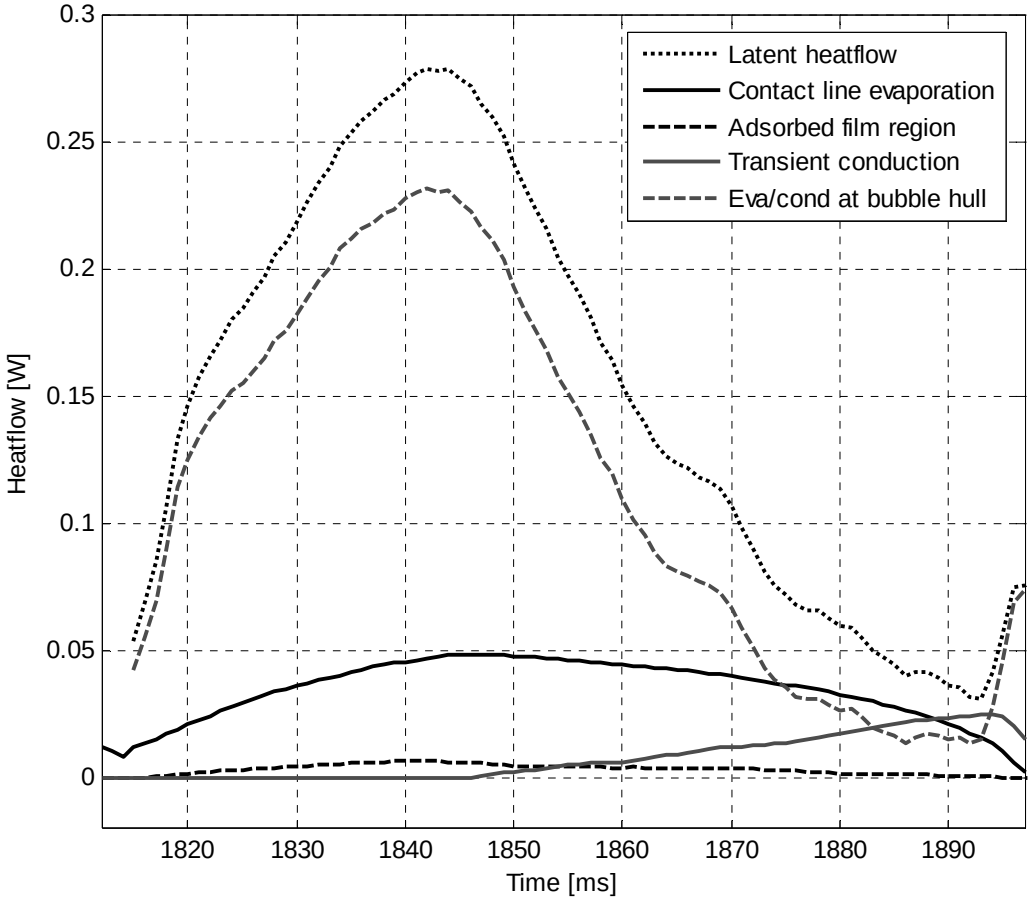

Figure 6.40: Heat flows distribution at a single vapour bubble (sequence 77, bubble 88)

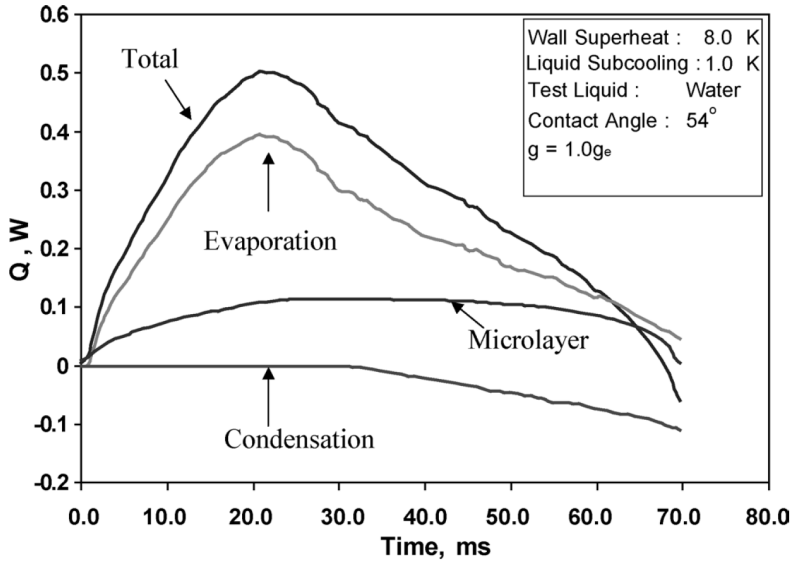

Figure 6.41: Evolution of various latent heat flows at a bubble, results of a simulation performed by Dhir et al. [18]

The heat flows at the simulated bubble using the VOF model of Kunkelmann is shown in Figure 2.7. Qualitative agreement exists concerning the development of the heat flows. In the simulation the transient conduction heat flow is included in the heat flow to the liquid. The enhancement of the heat flow to the liquid during bubble detachment visible in Figure 2.7 is comparable to the development of the transient conduction heat flow in Figure 6.39 and Figure 6.40. The heat flow at

the contact line is considerably smaller because only the microregion heat flow of the single cell is plotted and not the integrated heat flux peak.
The results of a numerical simulation performed by Dhir et al. [18] are shown in Figure 6.41. Even though the boundary conditions are completely different the development of the latent heat flows of bubble 88 are qualitatively in extremely good agreement to the numerical results.
The portion of the contact line evaporation on the overall latent heat flow to the bubble is plotted in Figure 6.42 for both bubbles over the ebullition cycle time. During the growth period the percentage of contact line evaporation is around 18% for both bubbles. This agrees well with previous findings of an initial heat flux ratio of 0.2 as part of the results of the 42nd ESA campaign (Chapter 3.3.3). The portion of the contact line evaporation to the latent heat flow is equal to the defined heat flux ratio in the period of bubble growth. During bubble detachment the heat flux ratio also include transient conduction in the contact line heat flux. The later development of the portion is strongly dependent on the sub-cooling state. The increases of the contribution of contact line evaporation to over 60% is not caused by an increase of contact line evaporation but by a decrease of evaporation at the bubble hull that comes in contact with subcooled liquid. Nevertheless, the significance of contact line evaporation becomes evident and is even more pronounced in sub-cooled boiling processes that are often used in industry. The measured contribution agrees well with the findings of other researchers who quantified the contribution in the range of 16% to 33% (see Chapter 2.1.2)

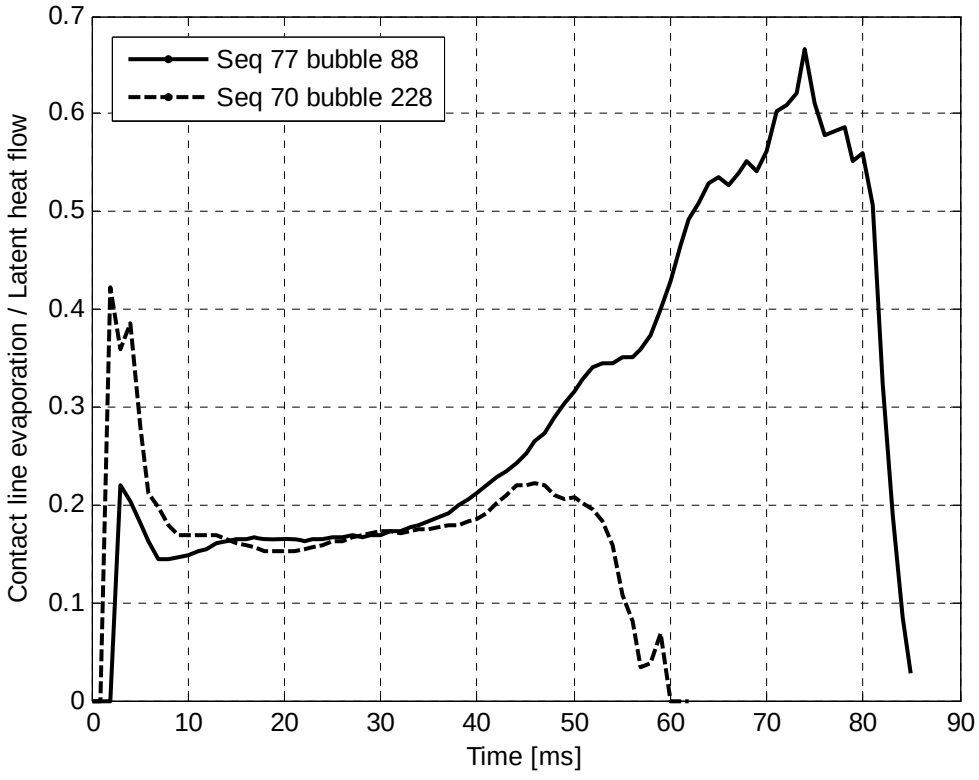

Figure 6.42: Portion of contact line evaporation to the overall latent heat flow of the evaluated bubbles

6.7. Electric Field

As already mentioned in Chapter 4.9 the electrode is washer-shaped according to the requirements of the RUBI project. The design was proposed by Paolo Di Marco who already investigated the electric field effect on boiling processes and two-phase systems (see Chapter 2.5.2). According to Snyder and Chung [108] the electric permittivity is 1.76 for FC-72/nPFH in liquid state and 1.01 for FC-72/nPFH vapour. Hence, the bubble has a lower permittivity and will be driven towards the zone of weaker electric field.

The electric field in the actual configuration was calculated using COMSOL Multiphysics. The electrode ($D_a = 15$ mm ; $D_i = 5$ mm ; $\delta = 1$ mm) is placed 5 mm above the heating surface that is at ground potential. The electrode is charged to 10 kV. The calculation is performed in an axis symmetric domain with the centre axis intersecting the location of the nucleation site (in the actual configuration the centre axis deviates 340 μm from the nucleation site). The electric field [V/m] is indicated as the colour in the plot. Additionally, contours of equal electric potential [V] are shown as well as the streamlines of the field. Below the electrode ring the field is almost homogeneous. It weakens towards the outer diameter. The electric field along the symmetry axis z is shown in Figure 6.44. The zone of weak electric field near the axis of symmetry at the height of the electrode is of special interest because bubbles formed at the nucleation site will be driven towards this region. At the axis the electric field decreases with height until z~5mm. Then it increases slightly again until a maximum at z~8 mm. Above z~8 mm the field decreases with height.

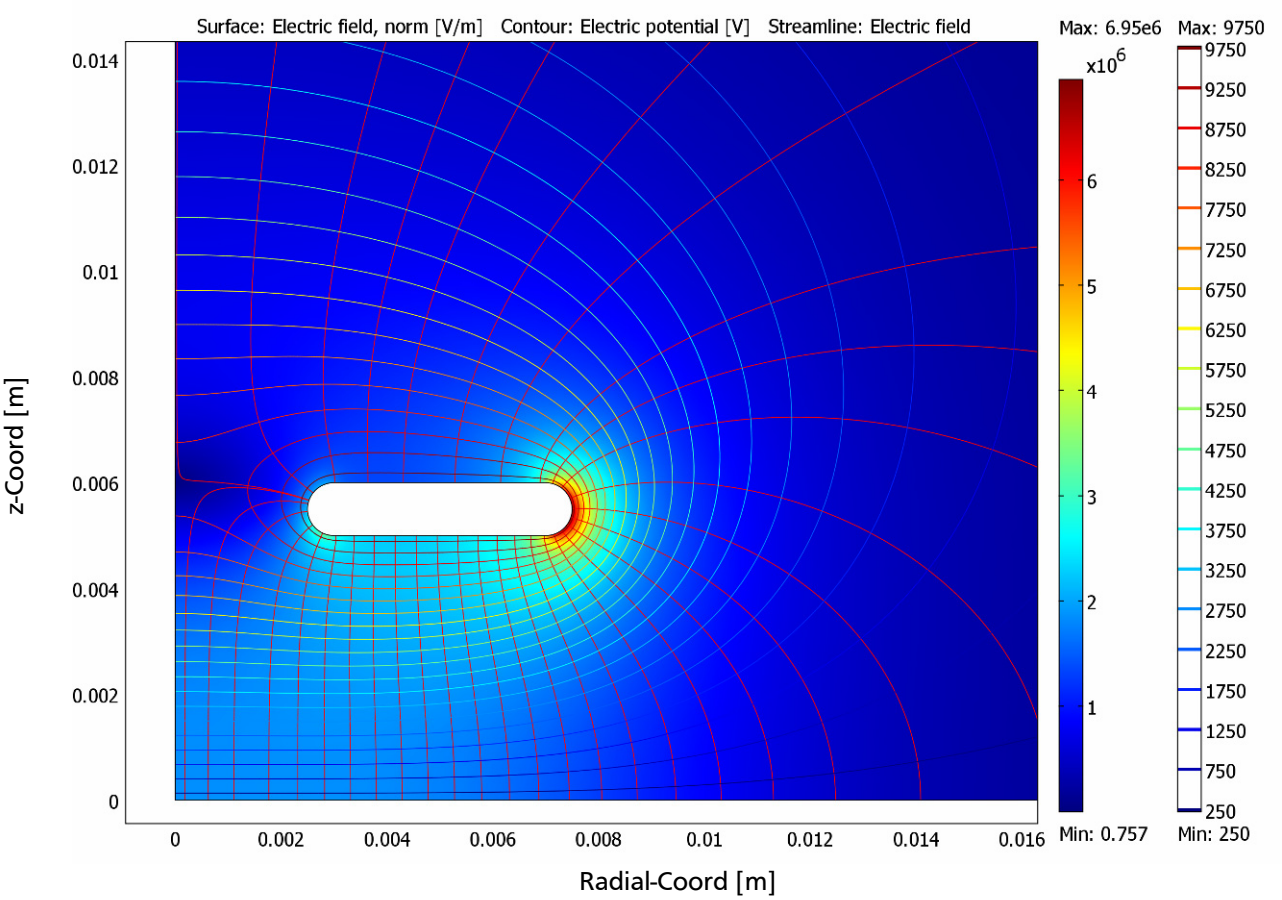

Figure 6.43: Calculation of the electric field

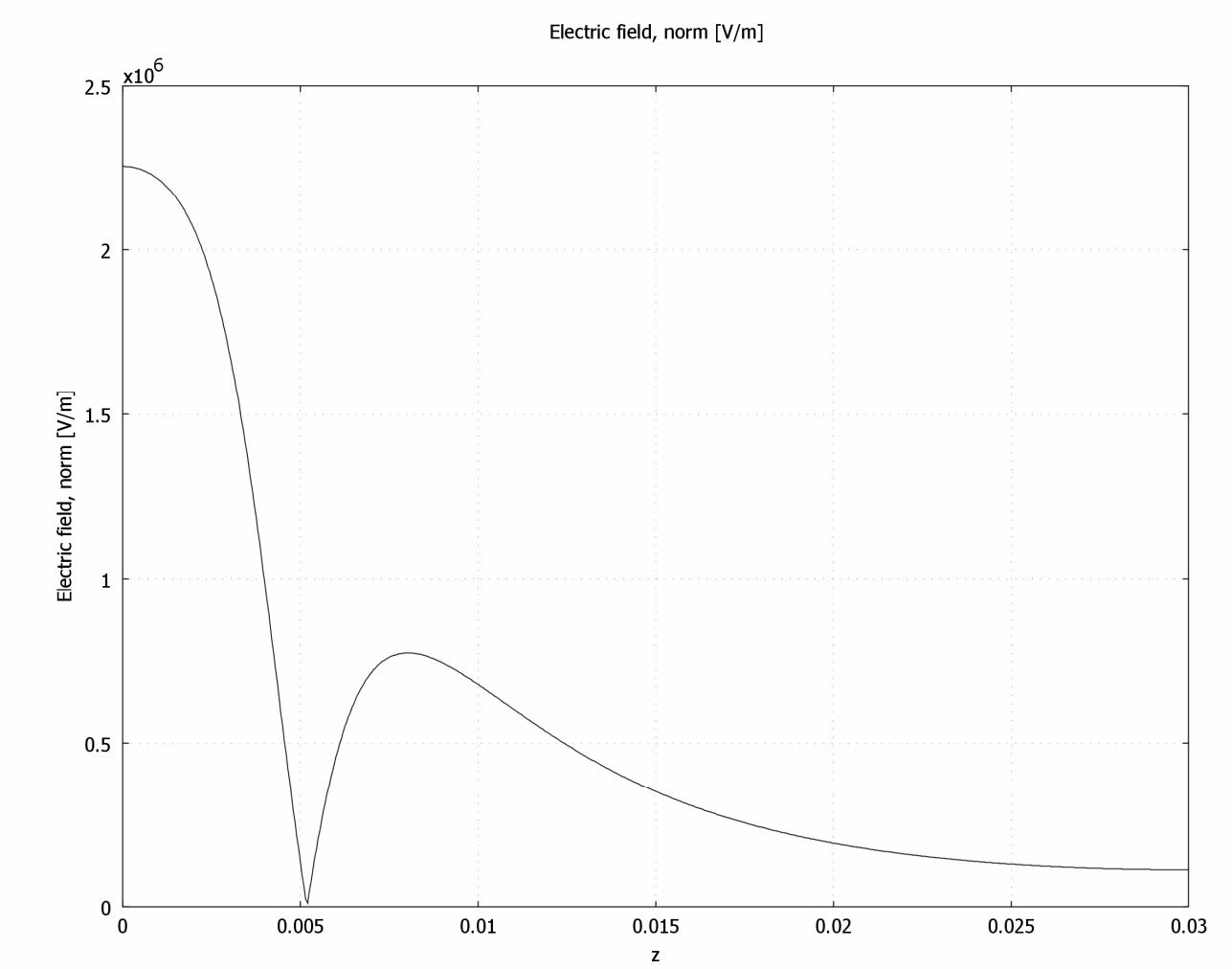

Figure 6.44: Electric field along the symmetry axis z

The effect of the electric field on the vapour bubbles can be shown in sequence 20. The heating power was $\dot{q}_{el} = 3572$ W/m², the fluid temperature $t_{fluid} = 41.56$ °C and the saturation temperature $t_{sat} = 42.36$ °C. The development of gravity, electrode voltage, mean temperature and mean heat flux versus the entire sequence time is presented in Figure 6.45. The electrode was charged at $\tau = 1.427$ s after reaching the microgravity phase. Small peaks in the heat flux curve indicate the eruption of bubbles at the nucleation site. Some of these bubbles are shown in Figure 6.46, Figure 6.47 and Figure 6.48. The bubbles at $\tau = 0.374$ s and $\tau = 0.654$ s have been nucleated during the first eruption. The bubble shapes are spherical. During the second eruption only a single bubble is nucleated. The shape of this bubble is shown at $\tau = 1.200$ s and $\tau = 1.427$ s. It is attached to the heating foil and sliding slightly. A small decrease in the mean heat flux is visible due to the bubble insulating a part of the heating foil. The electric field is activated at $\tau = 1.430$ s. The vapour is immediately sucked into the centre of the electrode, thereby detaching the bubble as it can be seen in Figure 6.47. Several bubbles are nucleated at the re-wetted surface where vapour embryos have been trapped in surface cavities due to the covering of the initial big bubble. These bubbles are detaching and significantly improving the heat transfer. A peak in the mean value of 20 kW/m² occurs and the mean wall temperature rapidly decreases from 70 °C to 63 °C. Due to their inertia the bubbles overcome the second maximum of the electric field at z~8 mm and exit the FOV at the top. At $\tau = 1.7$ s no vapour is visible and no bubbles are nucleated until the time of the next peak in the heat flux.

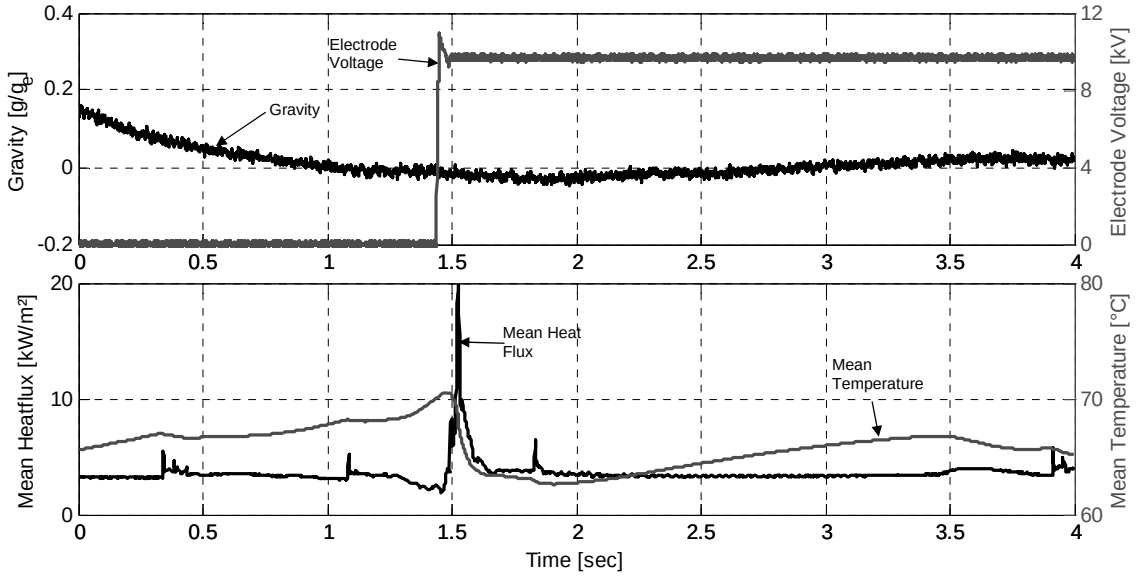

Figure 6.45: Mean heat flux, mean temperature, gravity and electrode voltage development (Sequence 20)

A bubble of the eruption at $\tau = 1.8\,\mathrm{s}$ is presented in Figure 6.48. Initially it has the same spherical shape as it would have without electric field. This is due to the high grow rate in the early stage of the growth and due to the small field gradient near the wall. As the bubble grows larger its shape becomes elongated and it is driven towards the centre of the electrode. The elongation is not entirely vertical but has a horizontal component. This is caused by the deviation between the bubble's nucleation site and the electrode centre axis. The elongation is directed directly to the middle of the centre hole where the electric field minimum is located. Remarkable is the detachment of the bubble even though negative gravitational acceleration ($g/g_e = -0.03$) is present at this time. The difference between this bubble and the bubble without electric field is clearly visible.

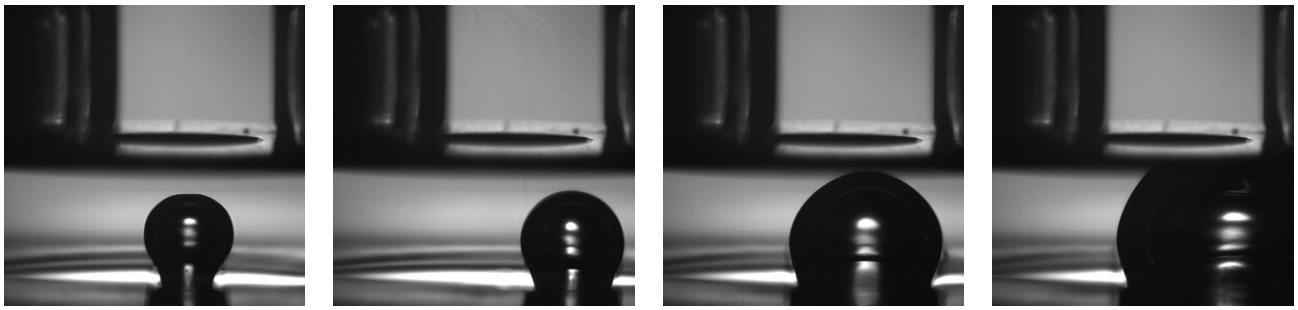

Figure 6.46: Bubbles of sequence 20 during microgravity prior to the electrode charging

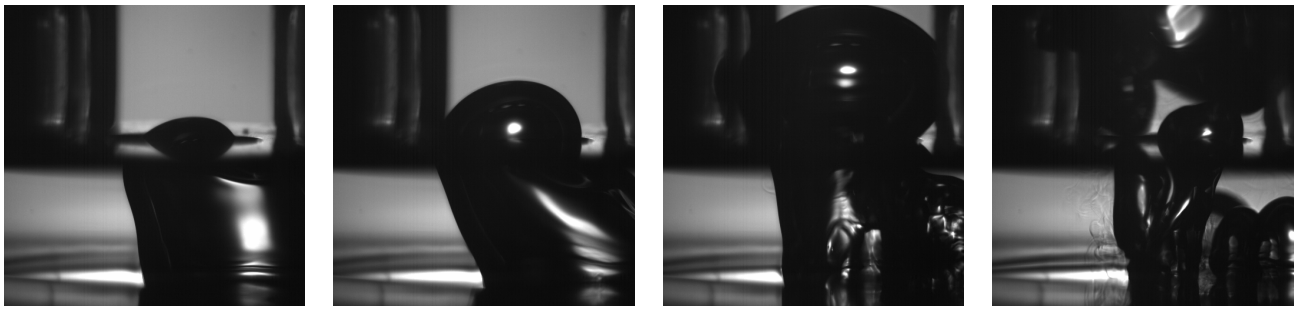

Figure 6.47: Bubble just after the charging of the electrode to 10 kV (sequence 20)

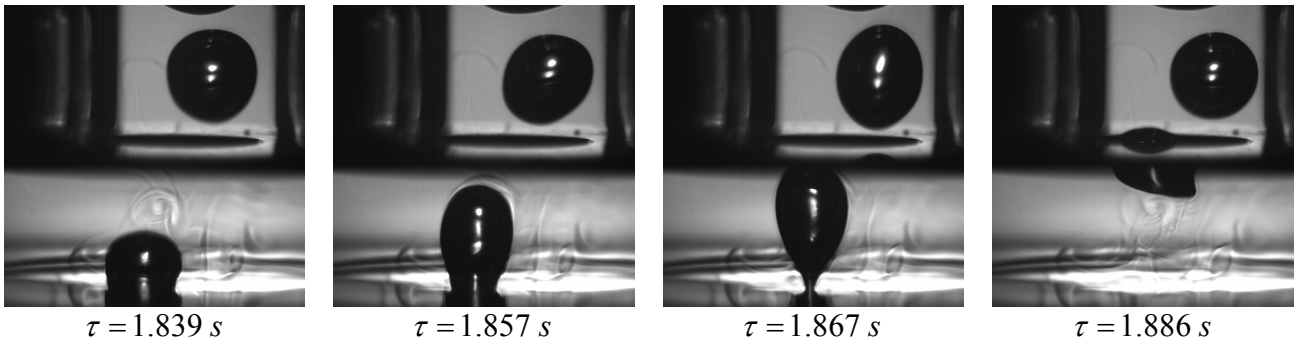

Figure 6.48: Bubble detachment by electric field (10 kV) force in microgravity (sequence 20)

Sequence 23 (Figure 6.49) was recorded at a heating power of 10 kW/m² during the first part of the microgravity phase including the last section of the transition. Several nucleation sites were active in the FOV. In the first part of the sequence until $\tau = 0.6\,\mathrm{s}$ the bubbles are detaching due to buoyancy. Then, the buoyancy forces are not sufficient anymore and the bubbles stay beneath the electrode. Instead of detachment a sliding on the surface is observable. The cooling of the heating surface is due to a randomly movement of contact lines on the surface. Bubbles grow large and insulate the foil. This leads to large peaks in the mean wall temperature like the one at $\tau = 1.5\,\mathrm{s}$. Immediately after the charging of the electrode the bubbles are sucked into its centre hole. The mean temperature is now limited to 71 °C. The described behaviour of the boiling process was observed in all sequences that incorporated an activation of the electrode in the microgravity phase. In Figure 6.50 the behaviour is shown for sequence 24. The heating power was 7325 W/m². The mean temperature peak at $\tau = 1\,\mathrm{s}$ was caused by a large vapour bubble stuck under the electrode. The temperature decrease after the maximum was due to the bubble sliding slowly out of the FOV leaving a re-wetted surface behind. After activation of the electrode none of these temperature peaks were observed.

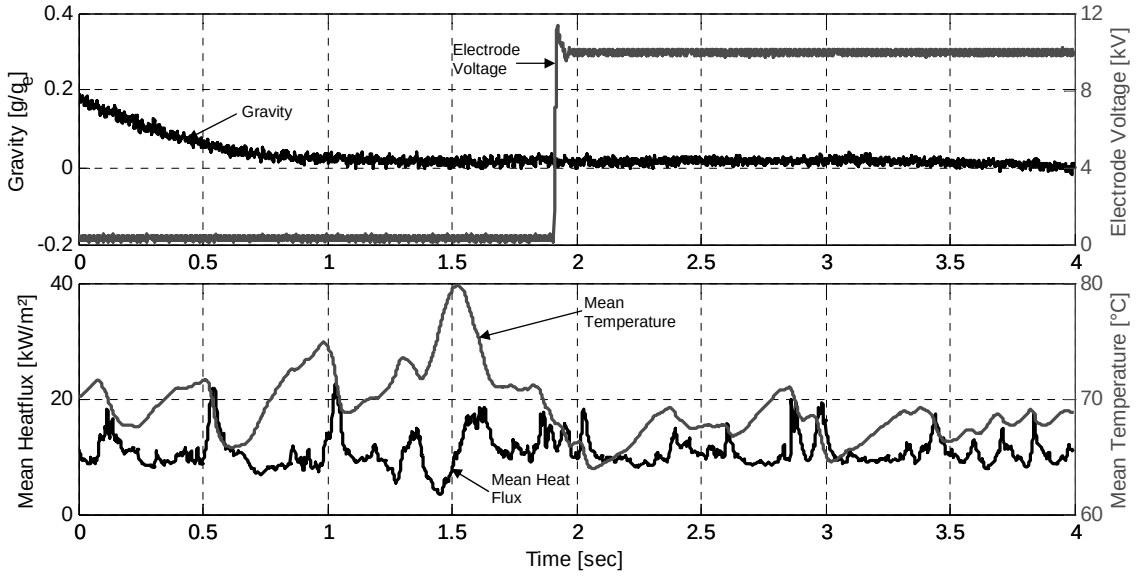

Figure 6.49: Mean heat flux, mean temperature, gravity and electrode voltage development (sequence 23)

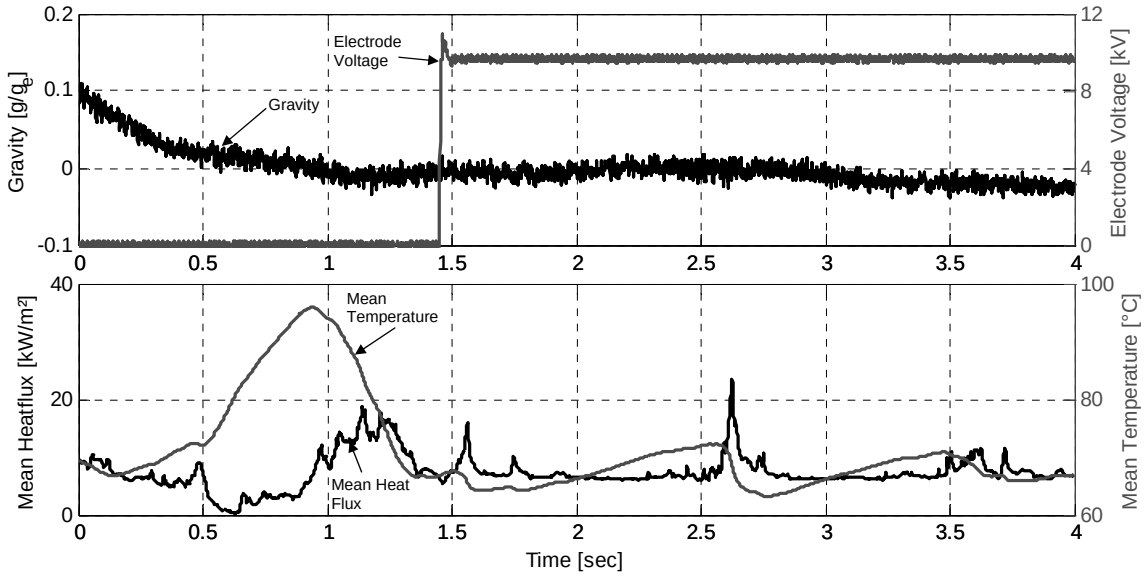

Figure 6.50: Mean heat flux, mean temperature, gravity and electrode voltage development (sequence 24)

The heat flux with and without electric field can be compared by looking at Figure 6.51 (without electric field) and Figure 6.52 (with electric field). Both sequences were recorded during the microgravity phase and both with a heating power of 16 kW/m². The mean fluid temperature in sequence 28 was 42.1 °C and in sequence 29 41.76 °C. The saturation temperature was 41.35 °C for both sequences. The temperature curve of sequence 28 shows that a mean temperature of 73 °C was never exceeded. The mean heat flux fluctuated between 12 kW/m² and 25 kW/m². Mean temperature and mean heatflux were changing rapidly. During the rapid temperature increase most of the surface in the FOV is covered by vapour. In the periods of high mean heat flux numerous imprints of bubble foots are visible in the heat flux and temperature images as shown in Figure 6.53. The vapour bubbles accumulate near the bottom surface of the electrode and are sucked

through the hole. The boiling process is stable. Even at negative gravitational acceleration that occurs at $\tau = 1\,\mathrm{s}$ the dielectrophoretic force is sufficient to drive the vapour away from the surface.

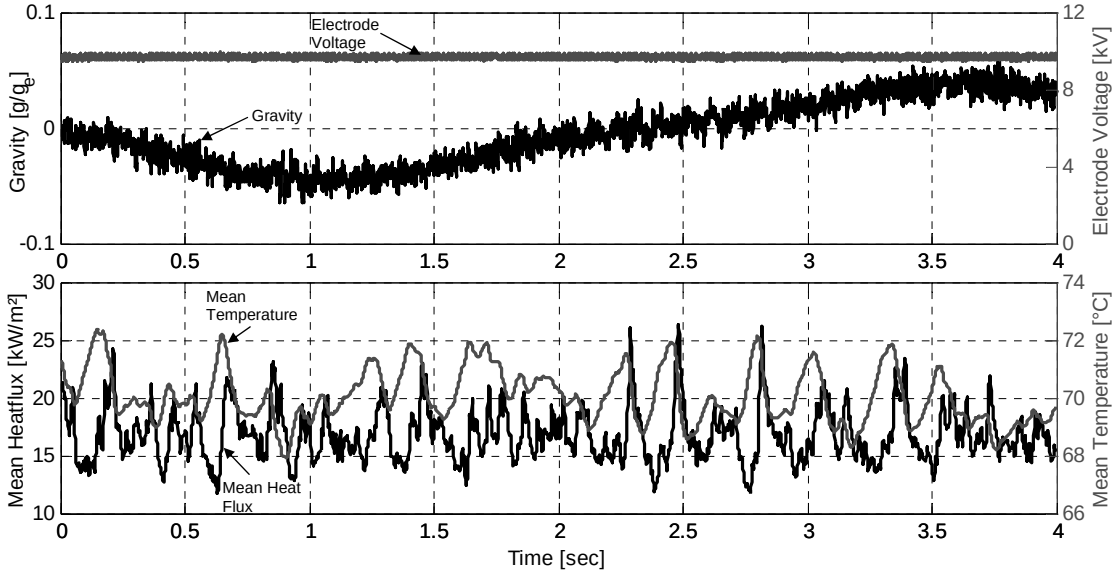

Figure 6.51: Mean heat flux, mean temperature, gravity and electrode voltage development (sequence 28)

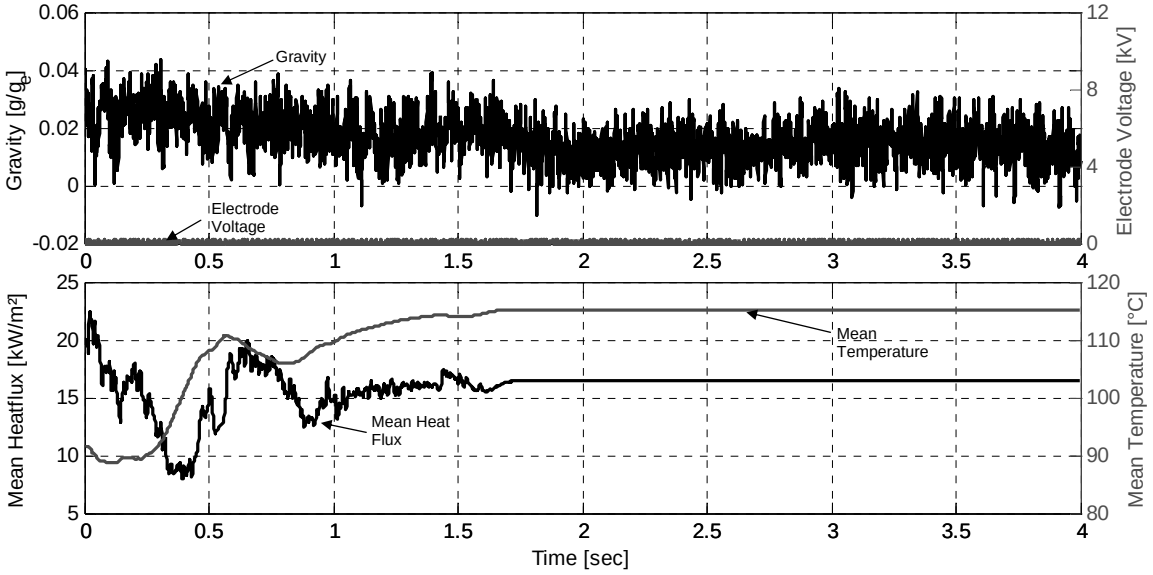

Figure 6.52: Mean heat flux, mean temperature, gravity and electrode voltage development (sequence 29)

Sequence 29 was recorded in order to directly compare the boiling processes with and without electric field. A large bubble was formed at the heating surface. Until $\tau = 1.5\,\mathrm{s}$ a part of the contact line imprint of this bubble is visible in the FOV cooling the portion of the heating foil as it can be seen in Figure 6.54. After $\tau = 1.5\,\mathrm{s}$ the surface in the FOV is entirely covered by vapour. The thermography image indicates a mean temperature of above 110 °C. This temperature exceeds the range of the thermography system in the used configuration. With an integration time of 0.8515 s the IR detectors are saturated. Therefore, no exact temperature information is obtained.

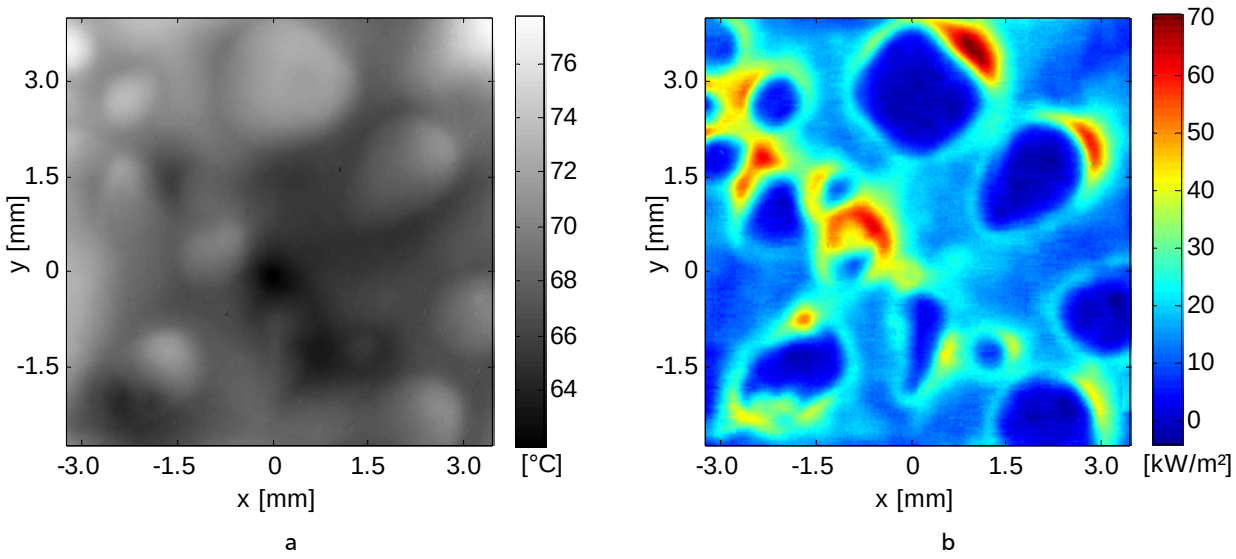

Figure 6.53: Temperature (a) and heat flux (b) distributions of stable and fully developed boiling in microgravity at 16535 W/m² under the presence of an electric field (sequence 28, 10 kV, 3.747 s)

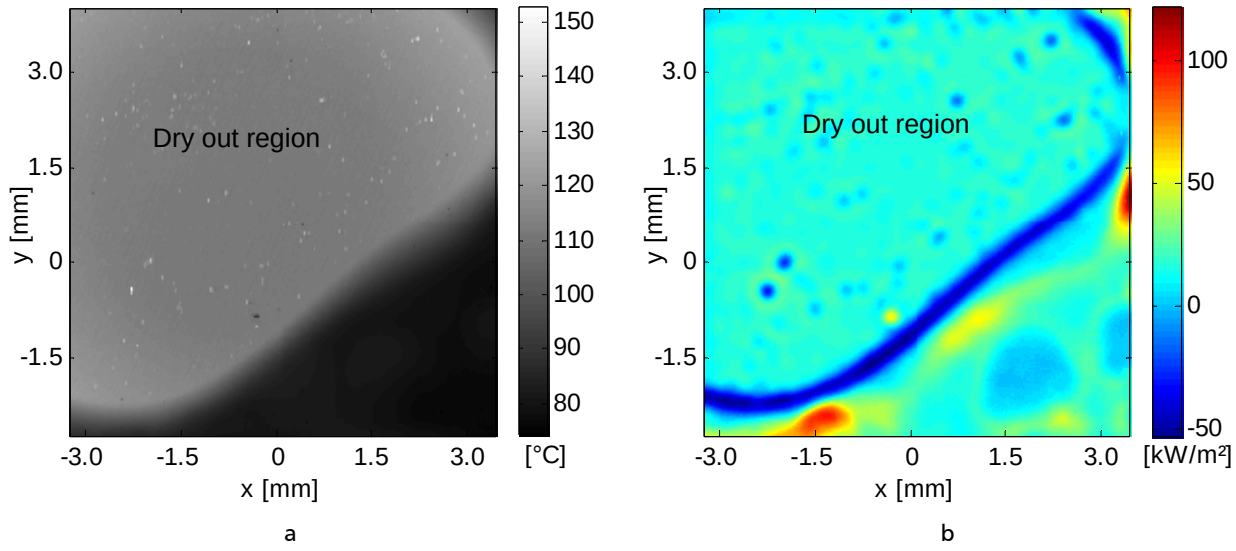

Figure 6.54: Temperature (a) and heat flux (b) distributions during dry out due to vapour insulating the heating foil, no electric field (sequence 29, 0.835 s)

7. Summary and Conclusions

Nucleate boiling is of tremendous significance in industry and applied in numerous industrial processes like power generation, air conditioning and chemical and food industry. Although the history of boiling research is long and significant results have been achieved the fundamental understanding of nucleate boiling is not yet accomplished. Due to the highly transient and unsteady nature of the process and the numerous physical phenomena involved and interacting, a closed theoretical description does not yet exist.
The purpose of this work is to contribute to the basic research by experimentally investigating the process locally with sophisticated **high resolution measurement techniques**. The scale of the experimental investigations is focused on an elementary level of the boiling process which is the **ebullition cycle** of vapour bubbles at a single nucleation site. Furthermore, one of the most influencing forces which is buoyancy was varied in the experiments by conducting them during **parabolic flights**. The experiments have been performed from 2004 to 2009 during six parabolic flight campaigns (PFC) on board the Airbus A300 zero-g that is sited in Bordeaux. Although the high resolution measurement techniques were strongly enhanced over theses years the basic measurement principle was preserved for all campaigns.

The **common experiment principle** was the measurement of the **heating wall temperature distribution** with very high spatial resolution accompanied by a **synchronized observation of the bubble shapes**. A thin metallic foil was used as a resistance heater for the boiling of the working fluid FC-72/nPFH and the temperature was measured at the back side of the foil by thermochromic liquid crystals and IR thermography, respectively. In the latest version of the experimental setup for the PFC in 2009 the temperature distribution was measured with a spatial resolution of $\sim$30 μm/pixel, a FOV of 224 x 224 pixels and a frame rate of 1000 Hz. The synchronized high speed imaging system for bubble observation had a resolution of 20 μm/pixel, a FOV of 512 x 512 pixels and also a frame rate of 1000 Hz. The objectives of the experiments were measurements at a **single stationary vapour bubble** (2004), during the **ebullition cycle** of a single bubble under highly predefined conditions (2007, 2008, 2009) and **continual boiling at a single artificial cavity** under the various gravity levels of parabolic flights (2005, 2006, 2009). The focus of this thesis is on the results of the 50th ESA campaign in 2009 involving the furthest development of the setup.
The core of the setup in 2009 is the 20 μm thick stainless steel heating foil featuring a single artificial cavity created by electrolytic abrasion in the centre of the foil. The foil is located in the bottom of a box-shaped test cell filled with degassed **n-Perfluorohexane** at a pressure of 600 mbar. A **disc-shaped electric field electrode** and a micro thermocouple could be inserted into the cell, respectively. The electric field electrode allowed the investigation of the **dielectrophoretic force** as the replacement of buoyancy. The objective of the micro thermocouple was the measurement of the liquid temperature near the liquid-vapour interface of a bubble or, furthermore, the vapour temperature when it is puncturing the interface. The implemented micro thermocouple was a technological test for the RUBI project and, unfortunately, did not fulfil the expectations due to insufficient stiffness for bubble interface penetration. Furthermore, the cell is equipped with a **laser**

that is focused on the back side of the heating foil in order to activate the artificial nucleation site on demand by locally superheating.
Due to the high amount of data generated during the experiments algorithms for the automated data evaluation and reduction were developed. With these algorithms it is possible to obtain **trajectory and volume of almost every bubble** in the high speed images. The calculation of the **local heat flux** to the fluid was performed by applying an **unsteady energy balance** to every pixel element of the temperature image. The **characteristic ring-shaped heat flux imprints** allowed a further evaluation of the heat flows at the bubbles by applying an ellipse fitting algorithm.

The **characteristic ring-shaped heat flux imprint** is presented for a bubble in low residual gravity with the corresponding bubble images and temperature fields. Due to the low gravity the bubble ebullition cycle duration was significantly enlarged which enhanced the clear pronunciation of the temperature and heat flux field. In normal or high gravity conditions the temperature and heat flux field is blurred due to the high bubble frequency in conjunction with the heat capacity of the foil.
The heat flux in the area of the foil that is not influenced by the bubble is nearly equal to the electrical heat flux as it can be trivially predicted. As natural convection diminishes in microgravity this bulk liquid heat flux is reduced, governed now by heat conduction in the liquid. The reduction leads to a temperature rising of the heating foil. The area of the heat flux distribution that is influenced by the bubble can be further divided into two regions: A region with almost **no heat flux underneath the adsorbed layer** of the attached bubble that is surrounded by a **peak ring of very high heat flux at the contact line**.

The **heat flow distribution** over the various **heat flow paths** was quantitatively evaluated for the ebullition cycle of a single bubble. From an initial single peak of high heat flux that is observable when the bubble nucleates this peak ring expands with constant height and width until the bubble foot diameter reaches its maximum. The integrated heat flow of the ring is attributed to evaporation at the contact line. The evaporative heat flow per unit contact line length is nearly constant. As the bubble detaches and the bubble foot constricts the peak ring significantly increases in height. This increase is allocated to the effect referred to as **transient conduction**. When the contact line advances during bubble detachment it deforms the thermal layer at the heated wall in such a way that the temperature gradient increases strongly. Transient conduction is the re-shaping of the thermal layer and is accompanied with high heat fluxes in the affected area. The affected area is small and in close vicinity to the contact line. During bubble foot constriction the vapour is replaced by liquid from the adjacent thermal layer and not by cold bulk liquid. Hence, the common image of cold bulk liquid sucked near the wall during bubble foot constriction is often interpreted in a wrong way. Only after bubble detachment cold bulk liquid is driven near the wall due to the bubble wake. The mathematical distinction between transient conduction and contact line evaporation heat flows allowed a detailed evaluation of the heat flows during the whole ebullition cycle. This evaluation was performed in close cooperation with Kunkelmann incorporating his highly promising numerical VOF approach.
Heat is supplied from a heat source to the heated wall where also transient conduction and periodic heat storage in the wall material occur. Therefore, the heating wall has to be included in the description of boiling processes and the assumption of constant temperature or heat flux boundary conditions can not be justified.
From the wall the heat is transferred to the fluid by five mechanisms:

- Forced convective heat transfer to the vapour in the adsorbed film region
- Evaporation near the contact line

- Periodic heat storage in the liquid boundary layer (often referred as transient conduction)
- Marangoni convection
- Convective heat transfer to bulk liquid

The first two mechanisms contribute directly to the **energy of the vapour phase** while the other three mechanisms are increasing the **thermal energy of the liquid**. Furthermore, heat and mass is transferred via the liquid-vapour interface of the bubble hull. The distribution of the evaporation or condensation heat flux is dependent on the local liquid superheat or sub-cooling at the interface. Whereas the contribution of forced convective heat transfer to the vapour and Marangoni convection to the overall heat transfer was assumed as negligible in the present case the other four heat flows could be quantified. It was found that in saturated conditions **approximately 18% of the overall latent heat is transferred at the contact line**. This value is significantly enlarged in sub-cooled conditions. The comparison of this evaluation to the results of numerical simulations performed by Dhir [18] and by Kunkelmann [67] revealed very good qualitative and surprisingly also reasonably good quantitative agreement between numerical and experimental results.

The dependency of the **bubble frequency and departure diameter** on gravity was also studied. In the studied case of thermodynamically controlled bubble growth where inertial forces do not play a role the relation $d_D \sim g^{-1/2}$ as already included in the famous Fritz' correlation is valid. The experimental data was compared to some of the most common empirical correlations of the departure diameter. None of them showed a good agreement. A **new departure diameter correlation** for the thermodynamically controlled regime was developed based on a force balance of surface tension as the attaching and buoyancy as the detaching force. The correlation fits the experimental data very well without incorporating any empirical parameter.
A sharp transition of detaching bubbles to not detaching bubbles was observed at a gravity threshold of $g/g_e = 0.07$.
From the evaluation of the bubble frequency a proportional dependency on gravity was found for the studied boiling case. The measured frequencies were also compared to most common empirical correlations. The result was that the correlations of Peebles & Garber [93] and Jakob & Fritz [50] showed the best quantitative agreement but a wrong trend in the gravity-dependency while the correlations of Mikic & Rohsenow [79] that include the gravity in the appropriate way for the present boiling case had large deviations to the experimental results. The correlation of Mikic & Rohsenow [79] was adapted to fit the experimental data resulting in a **new bubble frequency correlation.**

Beside the local investigations the evaluation of the **global parameters** during the transition between hypergravity and microgravity was studied. The global parameters were the mean temperature and the mean heat flux to the fluid averaged over the entire FOV of the IR camera. The increase of the mean temperature as a result of the diminishing natural convection heat transfer in the transition was observed. The increasing departure diameter and decreasing bubble frequency lead to a more and more pronounced fluctuation in the mean heat flux. When the gravity level fell below $g/g_e = 0.07$ the activation of numerous nucleation sites caused a peak in the mean heat flux and a steep decrease in the mean temperature. The subsequent boiling process is governed by chaotic dry-out and re-wetting phases induced by residual fluid motion and g-jitter. Quasi-stable phases of a stationary vapour cloud hovering above the heating foil collecting small satellite bubbles that emerge from the foil were also observed.

On a smaller scale, the evaluation of the mean heat flux in distinctive rings around the nucleation site was performed. This simulated punctuated heat flux sensors at these distinctive distances from the nucleation site as published by other authors and reduced the data amount.

The effect of an **electric field** on the boiling process in microgravity has been studied in close cooperation with Professor P. Di Marco from the University of Pisa. Beside the scientific objectives the implementation of an electric field electrode was part of the preparation for the RUBI boiling experiment for the Fluid Science Laboratory on board the ISS. **Elongated bubbles** have been observed that were sucked from the heating foil into the centre hole of the charged electrode. The effect of charging the electrode during the microgravity phase on the boiling process was investigated. Before charging the process was unsteady and chaotic. Dry-out periods accompanied with high mean wall temperatures alternated with a complete re-wetting of the surface. The charging of the electrode immediately stabilized the process. Large temperature fluctuations vanished and a steady re-wetting of the surface was ensured as the vapour is removed from the heating foil through the centre hole. A fully developed boiling process could be maintained during the microgravity phase in the presence of the electric field.

Various interesting **boiling phenomena** have been presented in this work revealing the high potential of the comprehensive measurement techniques. The presented evaluations address fundamental aspects of nucleate boiling. These aspects are the influence of gravity on the boiling process, the various heat paths, temperature and heat flux distributions at growing and detaching vapour bubbles and dielectrophoretic forces on the liquid-vapour interface.
The author hopes that this thesis contributes a little bit to the basic research and helps in the fundamental understanding of nucleate boiling.

An **outlook** to ongoing and future research activities strongly related to this work is presented in the Appendix. Currently, the comprehensive boiling experiment **RUBI** (Reference mUltiscale Boiling Investigation) for the Fluid Science Laboratory on board the Columbus module of the ISS is under development. The basic measurement principle as described in Chapter 3.2 will also be implemented in the RUBI experiment but it addresses even more fundamental aspects and includes additional stimuli and diagnostics. Beside the high speed camera and the thermography system a micro-thermocouple rack will be integrated in order to measure the temperature field in the vicinity of the bubble interface and the vapour temperature by penetrating the interface. As an additional stimulus a shear flow can be created over the heated surface to address also flow boiling aspects. A brief overview on the RUBI experiment is provided in Chapter 8.1.
Boiling in mini/micro-channels is currently in the focus of world-wide research activities. In order to identify and quantify the involved mechanisms the knowledge of the local temperature and heat flux distribution and fluctuation along the channel walls is mandatory. The basic measurement principle was implemented in a mini-channel test cell and first experiments were conducted. In Chapter 8.2 the mini-channel experiment is introduced and preliminary results are presented.

8. Appendix

8.1. RUBI: A Reference Boiling Experiment for the ISS

Beside the scientific objectives, the parabolic flight experiments served also as preparation for the RUBI experiment. The abbreviation RUBI stands for Reference mUltiscale Boiling Investigation. It is a comprehensive nucleate pool and flow boiling experiment to be conducted in microgravity on board the International Space Station (ISS). The experimental container (EC) of RUBI is currently developed by an engineering team of Astrium Space Transportation GmbH in Friedrichshafen to which the author belongs since January 2010. RUBI will use resources provided by the Fluid Science Laboratory (FSL) of the Columbus module (see Figure 8.1). It is part of the second batch of experiments that consists additionally of the experiments SAFIR and EMERALD. Experiments of the first batch are GEOFLOW, FASES, FOAM and CIMEX. GEOFLOW was already operated in orbit, FASES is almost ready for launch and FOAM and CIMEX are still in development.

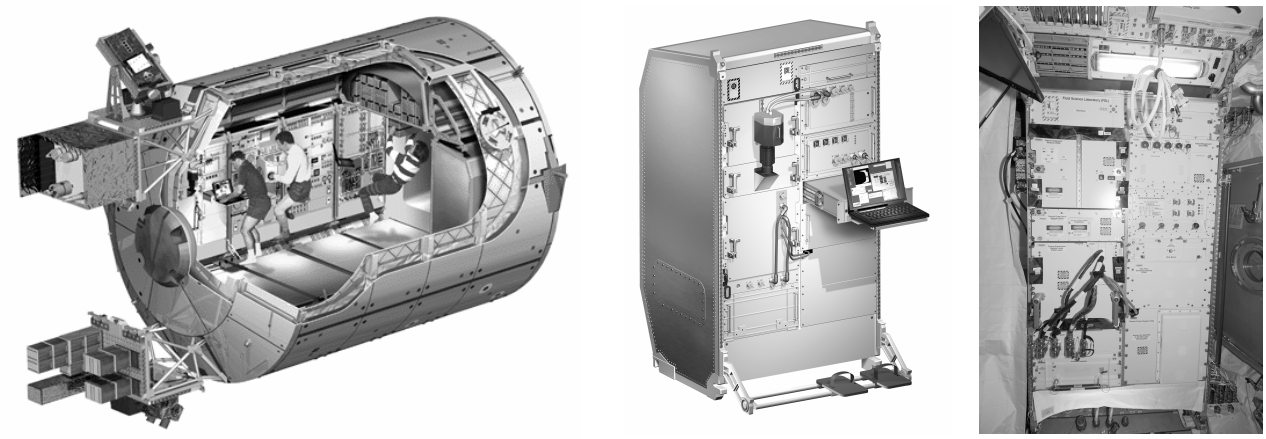

Figure 8.1: From right: Columbus module of the ISS, Fluid Science Laboratory, FSL front panel in the ISS (images: ESA)

Generally, the experiment containers for FSL are rectangular boxes as shown in Figure 8.2 with a size of 400 mm x 270 mm x 280 mm containing the complete experiment including measurement techniques that are not provided by FSL and electronics.

Figure 8.2: EC GEOFLOW as an example for FSL experiment containers (images: ASTRIUM)

The scientific objectives of RUBI have been defined by the members of the ESA topical team “Boiling and Multiphase Flow”. The baseline is a multi-scale approach to study boiling phenomena on various length scales. The basic measurement principle of this thesis that is the high resolution measurement of heating wall temperature distribution in conjunction with high speed bubble imaging is the core of the RUBI experiment. Additional diagnostics and stimuli covering the research interests of the team members will be implemented:

- Electric field electrode similar to the setup used in the parabolic flight
- Micro thermocouple rack consisting of four micro thermocouples to study temperatures of vapour and liquid in the vicinity of the bubble interface
- Forced convection loop for the investigation of shear flow influence
- Second liquid to create a binary mixture

The involved team members are researchers from several European universities and institutes:

Prof. Lounès Tadrist – Scientific coordinator	
Laboratoire IUSTI	Marseille / FRANCE
Prof. Dr.-Ing. Peter Stephan – Deputy Scientific Coordinator	
Institute of Technical Thermodynamics	Darmstadt / GERMANY
Prof. Walter Grassi and Prof. Paolo Di Marco – Studies on electric field influence	
University of Pisa	Pisa / ITALY
Prof. Catherine Colin – Studies on shear flow influence	
Institute de Mécanique des Fluides de Toulouse (IMFT)	Toulouse / FRANCE
Prof. Gian Piero Celata – Studies on shear flow influence	
Institute of Thermal-Fluid Dynamics, ENEA	Rome / ITALY
Prof. John Thome – Studies on mixtures	
Ecole Polytechnique Fédérale de Lausanne	Lausanne / SWITZERLAND
Prof. Oleg Kabov – Condensation/separation and loop	
Microgravity Research Center, Université Libre de Bruxelles	Bruxelles / BELGIUM

RUBI is addressed to fundamental boiling research. With the high microgravity quality provided by the ISS in conjunction with the various stimuli and measurement techniques effects and phenomena can be investigated that are generally masked by gravity. Without natural convection highly predefined conditions may be established prior to bubble nucleation. The data obtained under these conditions can be used to verify the implementation of fluid physics in theoretical and numerical models and, therefore, contributes in the long term goal of boiling research that is the development of precise nucleate boiling calculation tools for the practical application in industry.

8.2. Investigation of Forced Convective Boiling in a Single Mini Channel

8.2.1. Introduction

Boiling in micro- and mini-channels has recently attracted big interest in electronic industry. The requirements for cooling systems of electronic devices have increased significantly. The high performance of flow boiling in mini/micro channels and the possibility to integrate the evaporator directly into the electronic part make the process very interesting for the application in electronic cooling. Many investigations on convective boiling in small channels have already been conducted.
Kandlikar [54] summarized investigations related to this subject and enunciated three fundamental questions for researchers:

1. How does the small passage dimension affect the bubble dynamics and the two-phase flow?
2. How is the heat transfer and pressure drop affected in these channels?
3. What is the difference in performance between single and multiple parallel channels?

Furthermore, he investigated the heat transfer mechanisms during flow boiling in micro channels [55]. After nucleation, the accumulated superheat in the wall leads to rapid bubble growth. The channel is quickly filled by the bubble. The main heat transfer mechanism is then defined by the moving three phase contact line at both ends of the bubble and/or by an evaporating thin liquid film which remains at the channel wall as the elongated bubble passes through which was observed by Hardt et al. [43]. The scientific community still does not agree in this point.
Nevertheless, Kandlikar states that the heat transfer mechanism is similar to that of nucleate boiling because of the dry out and rewetting processes of the wall. This statement contradicts the conclusion of Qu and Mudawar [96] who predict that annular flow is the dominant flow pattern and forced convection boiling is the dominant heat transfer mechanism for water micro-channel heat sinks.
However, all experimental investigations up to date were focused on either flow pattern observation and/or on the evaluation of the heat transfer on a macro scale. Global heat transfer measurements were typically performed with discrete temperature sensors like thermocouples. By measuring the channel wall temperature distribution using thermochromic liquid crystals (Piasecka et al. [94], Muwanga and Hassan [85]) or infrared thermography (Diaz et al. [26]) the heat transfer coefficient was evaluated. Although the resolution of these thermography techniques is far higher than with a thermocouple measurement system the investigations were still performed on a macro scale. Because the wall thickness is in the order of hundreds of microns the temperature field is smeared due to thermal inertia and heat conduction in the wall. High frequency temperature fluctuations on a micro scale are not observable with these systems. That means local heat transfer investigations on a micro scale to identify the heat transfer mechanism inside the channels have not been conducted yet.
In order to fundamentally investigate the heat transfer mechanism during flow boiling in micro/mini channels the thermography/high speed imaging techniques used for the parabolic flight experiment and described in this thesis should be deployed. By applying the technique on flow boiling in a micro/mini channel the role of moving contact lines and thin liquid film evaporation at the channel wall can be clarified. It would lead to a deeper knowledge of what is happening in the vicinity of a vapour slug passing through the channel.
The objectives of the proposed experiment are:

- High spatial and temporal resolution measurement of wall temperature distribution during flow boiling in micro/mini channels using infrared thermography

- Evaluation of the local heat flux and the relation to the global heat transfer coefficient
- Identification of heat transfer mechanisms
- Investigation of the influence of global parameters such as mass flow rate, heat load and system pressure on the heat transfer mechanism
- Clarification of the role of contact line evaporation versus the role of thin film evaporation

8.2.2. Experimental setup

The comprehensive IR thermography technique that was used in the microgravity pool boiling experiments has been adapted for the mini channel investigations. The design of the test cell (shown in Figure 8.3) is based on the parabolic flight test cell. A single, rectangular mini channel with a width of 2 mm and a height of 0.5 mm is manufactured into a copper block.
The temperature of the copper block is controlled by a constant temperature circuit. One side of the channel is covered by a thin (25 μm) stainless steel foil. This channel wall is heated by electrical current. The temperature of the outer side of the foil is measured by IR thermography. The spatial resolution is 30 μm and the frame rate 1000 Hz. The channel wall opposite to the heating foil is a transparent Plexiglas window. This allows synchronized observations of local heat transfer and flow patterns. The working fluid nPFH enters the channel in liquid state with an exactly predefined temperature. Convective boiling takes place inside the channel. Two-phase flow exits the channel and the vapour is re-condensed inside the condenser. A reservoir provides enough working fluid. The fluid circulation is maintained by a micro annular gear pump. The flow rate is precisely adjustable and will be measured by a flow meter. Absolute pressure inside the loop and the pressure difference over the micro channel will be measured as well.

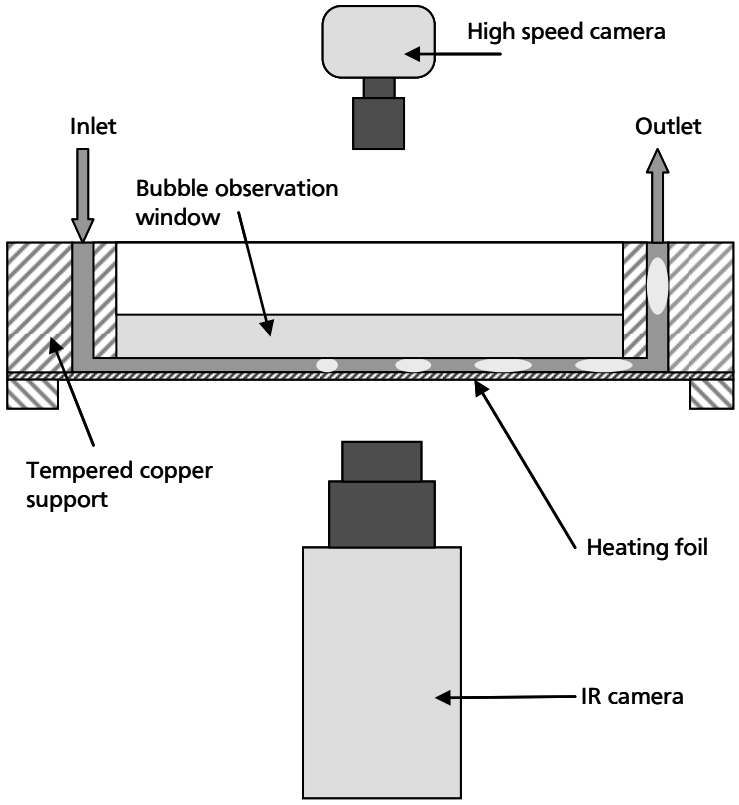

Figure 8.3: Principle of the mini-channel experiment

8.2.3. Preliminary results

The data evaluation procedure for the parabolic flight experiment (see Chapter 5) was applied for the minichannel data. In the first set of experiments the channel was oriented in the way that the heating foil closes the bottom side of the channel. The orientation will be varied in further experiments since the Bond number is above 1.2 for experiments with nPFH at atmospheric pressure. Hence, the process can not be regarded as gravity independent. In the planned experiments with water the Bond number is one order of magnitude smaller, well below 1. So, the surface tension dominates and gravity can be neglected. In the preliminary experiments three flow patterns have been observed: bubbly flow, slug flow and partial dry out. Images of the high speed camera, the thermography image and the calculated heat flux distribution are presented in Figure 8.4-Figure 8.7 for the different flow patterns. Bubbly flow was observed at a flow rate of 14.4 ml/min and a heating power of 15.02 kW/m². Comparatively large areas of very high heat flux are visible. The characterized contact line peak observed in the pool boiling experiments was not observed. This could be attributed to the gravity dependence. The bubbles were attached at the upper Plexiglas wall and not at the heating foil. Different behaviour is expected with a flipped orientation of the channel. Nucleation of bubbles occurred at the corner of the channel where the heating foil is attached to the copper enclosure.

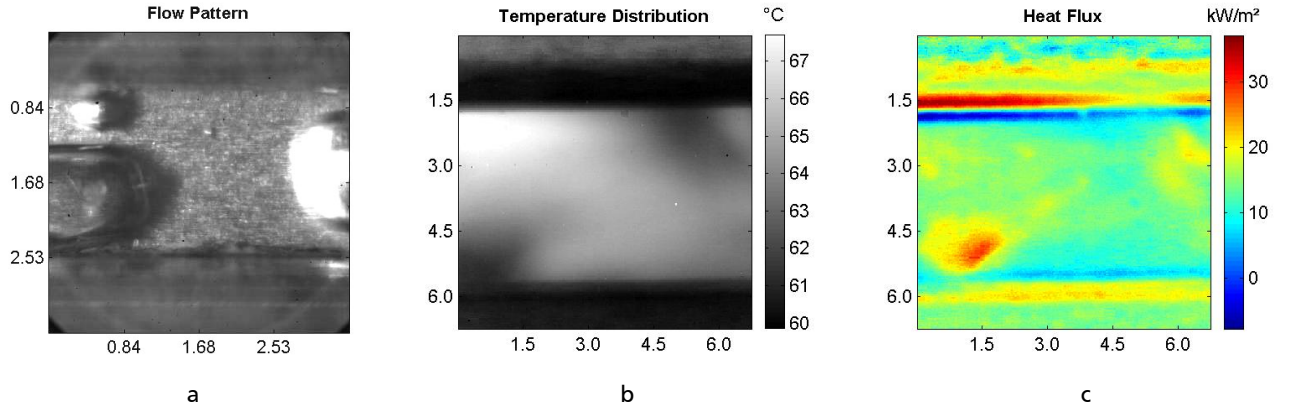

Figure 8.4: Flow pattern image (a), wall temperature distribution (b) and local heat flux (c) during bubbly flow

At a flow rate of 14.4 ml/min and 17.43 kW/m² slug flow patterns could be observed. Characteristically, two parallel lines of high heat fluxes in channel direction were visible. This is maybe an indication for contact line evaporation. Remarkable is that the lines are not closing at the beginning and the end of the slug. However, further experiments are needed to gain a deeper understanding of this phenomenon. The pressure difference across the channel is pulsating periodically. Partial dry-out of the heating foil occurred at a flow rate of 9 ml/min and 22.78 kW heating power. The characteristic contact line peaks are visible.

The application of the comprehensive high resolution thermography technique developed at TTD that was already successfully applied in pool boiling experiments into a mini-channel flow boiling experiment clears the way for a fundamental understanding of the underlying heat transfer mechanisms. For the first time, temperature and heat flux imprint imposed by the force convective boiling process on a thin heated wall can be studied with high spatial and temporal resolution. Thereby, it is possible to investigate the local phenomena that lead to the high performance heat transfer of such a process. The assumption and prediction of several theoretical models could also be justified.

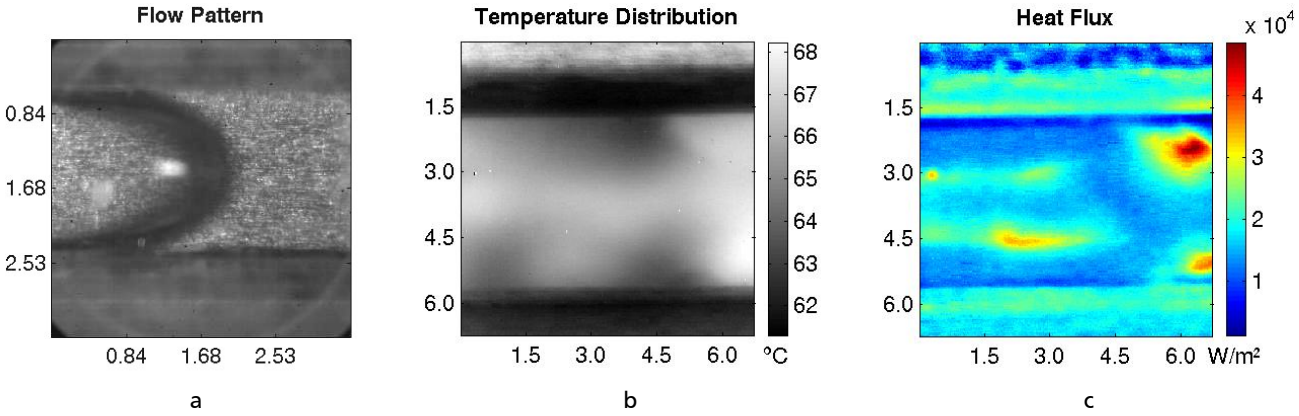

Figure 8.5: Flow pattern image (a), wall temperature distribution (b) and local heat flux (c) during slug flow

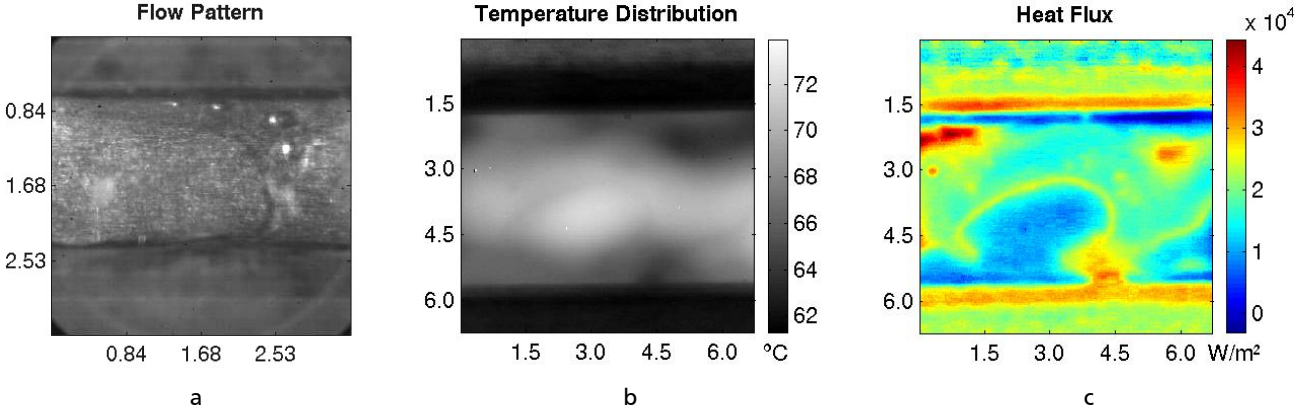

Figure 8.6: Flow pattern image (a), wall temperature distribution (b) and local heat flux (c) during partial dry-out in the mini channel, image set 1

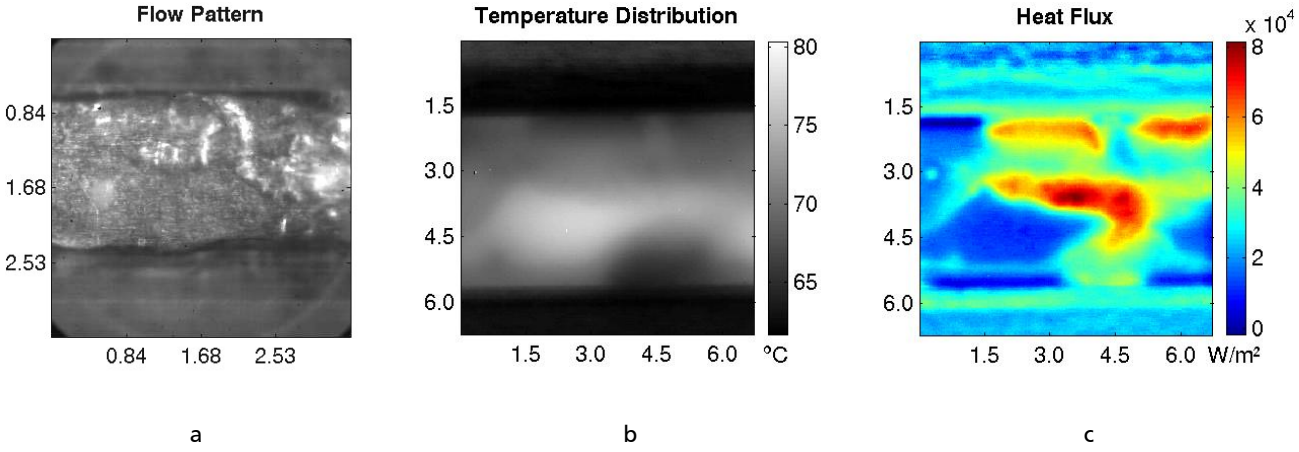

Figure 8.7: Flow pattern image (a), wall temperature distribution (b) and local heat flux (c) during partial dry-out in the mini channel, image set 2

8.3. Overview on measurement sequences of 50th ESA PFC

Flight	Date	Bubbledir	IR Dir
1	12.05.2009	2009_05_12_Flug1	2009_05_12\Flug1

Nr	Par	Time	Seqdata	Bubblepics	IR Data	Heating Power [W/m²]	Mean Fluid Temp [°C]	Pressure [mbar]	Saturation Temp [°C]	Gravity	E-Field
1	NP	10:00	seqdata_09-05-12_1000_005.lvm	Seq_S0002	pretest2.ser	6746.10	41.72	599.65	42.38	1g	off
2	0	10:12	seqdata_09-05-12_1011_006.lvm	Seq_S0003	Par01	6746.70	41.96	598.56	42.34	0g	off
3	1	10:14	seqdata_09-05-12_1013_007.lvm	Seq_S0004	Par01__asci	5535.10	41.87	598.92	42.35	1g	off
4	2	10:17	seqdata_09-05-12_1016_008.lvm	Seq_S0005	Par02	6466.20	41.85	598.42	42.33	1g	off
5	3	10:21	seqdata_09-05-12_1020_009.lvm	Seq_S0006	Par03	6193.40	41.79	598.25	42.32	0g	off
6	4	10:24	seqdata_09-05-12_1023_010.lvm	Seq_S0007	Par04	6746.60	41.74	598.60	42.34	Transition	off
7	5	10:27	seqdata_09-05-12_1026_011.lvm	Seq_S0008	Par05	6747.00	41.61	598.53	42.34	Transition	10kV
8	6	10:33	seqdata_09-05-12_1032_012.lvm	Seq_S0009	Par06	6746.70	41.84	598.06	42.31	Transition	off
9	7	10:36	seqdata_09-05-12_1035_013.lvm	Seq_S0010	Par07	5924.80	41.84	598.51	42.33	Transition	10kV
10	8	10:39	seqdata_09-05-12_1038_014.lvm	Seq_S0011	Par08	5281.40	41.74	598.41	42.33	Transition	10kV
11	9	10:42	seqdata_09-05-12_1041_015.lvm	Seq_S0012	Par09	5281.60	41.88	598.81	42.35	Transition	10kV
12	10	10:45	seqdata_09-05-12_1044_016.lvm	Seq_S0013	Par10	6059.50	41.93	598.32	42.33	Transition	5kV
13	11	10:52	seqdata_09-05-12_1051_017.lvm	Seq_S0015	Par11	4793.40	41.74	598.59	42.34	Transition	10kV
14	12	10:54	seqdata_09-05-12_1054_018.lvm	Seq_S0016	Par12	6606.90	41.73	598.25	42.32	0g	10kV
15	13	10:58	seqdata_09-05-12_1057_019.lvm	Seq_S0017	XXXXX	7031.50	41.57	598.40	42.33	0g	1kV
16	15	11:04	seqdata_09-05-12_1103_020.lvm	Seq_S0018	Par15	7031.50	41.17	598.86	42.35	Transition	1kV
17	16	11:14	seqdata_09-05-12_1113_021.lvm	Seq_S0019	Par16	6466.40	41.10	598.10	42.32	Transition	off
18	17	11:17	seqdata_09-05-12_1116_022.lvm	Seq_S0020	Par17	3572.30	41.44	598.97	42.36	0g	10kV
19	18	11:20	seqdata_09-05-12_1119_023.lvm	Seq_S0021	Par18	3572.10	41.60	598.60	42.34	0g	10kV
20	19	11:23	seqdata_09-05-12_1122_024.lvm	Seq_S0022	Par19	3572.10	41.56	599.00	42.36	Transition	switched on
21	20	11:28	seqdata_09-05-12_1133_026.mat	XXXXXXXXXX	XXXXX	10564.00	41.67	597.88	42.31	0g	10kV
22	21	11:33	seqdata_09-05-12_1133_026.mat	Seq_S0023	XXXXX	10564.00	41.67	597.88	42.31	0g	10kV
23	22	11:35	seqdata_09-05-12_1136_029.lvm	Seq_S0024	Par22_asci	10564.00	42.06	597.72	42.30	Transition	switched on
24	23	11:38	seqdata_09-05-12_1139_030.lvm	Seq_S0025	Par23_asci	7324.00	42.11	599.19	42.36	0g	switched on
25	24	11:43	seqdata_09-05-12_1142_031.lvm	Seq_S0026	Par24_asci	7324.20	42.03	598.48	42.33	Transition	switched on
26	25	11:46	seqdata_09-05-12_1145_AAA.lvm	Seq_S0027	Par25_asci	1811.50	42.18	598.72	42.34	0g	10kV
27	26	11:52	seqdata_09-05-12_1152_034.lvm	Seq_S0028	Par26_asci	4675.50	42.21	598.24	42.32	0g	10kV
28	27	11:56	seqdata_09-05-12_1155_035.lvm	Seq_S0029	Par27_asci	16535.00	42.10	598.74	42.35	0g	10kV
29	28	11:59	seqdata_09-05-12_1158_036.lvm	Seq_S0030	Par28_asci	16535.00	41.76	598.71	42.34	0g	off
30	29	12:02	seqdata_09-05-12_1201_037.lvm	Seq_S0031	Par29_asci	16536.00	41.75	599.10	42.36	0g	5kV
31	30	12:05	seqdata_09-05-12_1204_038.lvm	Seq_S0032	Par30_asci	16535.00	41.52	598.77	42.35	0g	off

Flight	Date	Bubbledir	IR Dir
2	13.05.2009	2009_05_13_Flug2	2009_05_13\Flug2

Nr	Par	Time	Seqdata	Bubblepics	IR Data	Heating Power [W/m²]	Mean Fluid Temp [°C]	Pressure [mbar]	Saturation Temp [°C]	Gravity
32	0	10:02	seqdata_09-05-13_1001_004.lvm	Seq_S0003	Par00	7619.50	41.53	598.99	42.36	Transition
33	1	10:05	seqdata_09-05-13_1004_005.lvm	Seq_S0005	Par01	4674.70	41.68	599.98	42.40	Transition
34	2	10:08	seqdata_09-05-13_1007_006.lvm	Seq_S0006	Par02	4675.10	42.07	599.25	42.37	0g
35	3	10:11	seqdata_09-05-13_1010_007.lvm	Seq_S0007	Par03	5924.00	42.12	599.00	42.36	Transition
36	4	10:14	seqdata_09-05-13_1013_008.lvm	Seq_S0008	Par04	5924.40	42.00	598.66	42.34	Transition
37	5	10:17	seqdata_09-05-13_1016_010.lvm	Seq_S0009	Par05	5922.70	41.80	599.89	42.40	InvTransition
38	6	10:22	seqdata_09-05-13_1022_011.lvm	Seq_S0010	Par06	5924.20	42.03	599.67	42.39	Transition
39	7	10:27	seqdata_09-05-13_1025_012.mat	Seq_S0011	Par07	8868.40	42.32	598.97	42.36	Transition
40	8	10:28	seqdata_09-05-13_1028_014.lvm	Seq_S0012	Par08	18821.00	42.37	599.56	42.38	Transition
41	9	10:31	seqdata_09-05-13_1031_015.lvm	Seq_S0013	Par09	6465.80	42.19	599.56	42.38	Transition
42	10	10:34	seqdata_09-05-13_1034_016.lvm	Seq_S0014	Par10	6465.90	42.10	598.99	42.36	Transition
43	11	10:41	seqdata_09-05-13_1041_017.lvm	Seq_S0015	Par11	6465.80	42.51	599.88	42.40	Transition
44	12	10:45	seqdata_09-05-13_1044_018.lvm	Seq_S0016	Par12	4105.50	42.41	599.57	42.38	Transition
45	13	10:48	seqdata_09-05-13_1047_019.lvm	Seq_S0017	Par13	4675.20	42.40	598.98	42.36	Transition
46	14	10:51	seqdata_09-05-13_1050_020.lvm	Seq_S0018	Par14	6465.70	42.30	598.90	42.35	Transition
47	15	10:53	seqdata_09-05-13_1053_021.lvm	Seq_S0019	Par15	5924.60	42.54	598.42	42.33	0g
48	16	11:05	seqdata_09-05-13_1105_022.lvm	Seq_S0020	Par16	7323.30	42.68	598.65	42.34	0g
49	17	11:09	seqdata_09-05-13_1108_023.lvm	Seq_S0021	Par17	4674.60	42.26	598.95	42.35	0g
50	18	11:12	seqdata_09-05-13_1111_024.lvm	Seq_S0022	Par18	10563.00	41.45	599.43	42.38	InvTransition
51	19	11:15	seqdata_09-05-13_1114_025.lvm	Seq_S0023	Par19	10564.00	38.79	599.03	42.36	0g
52	20	11:20	seqdata_09-05-13_1119_026.lvm	Seq_S0024	Par20	10564.00	41.44	599.20	42.37	0g
53	21	11:27	seqdata_09-05-13_1126_027.lvm	Seq_S0025	Par21	7323.50	42.03	599.51	42.38	0g
54	22	11:32	seqdata_09-05-13_1131_AAA.lvm	Seq_S0026	Par22	10564.00	41.76	599.27	42.37	0g
55	23	11:36	seqdata_09-05-13_1135_030.lvm	Seq_S0027	Par23	8868.40	41.99	599.08	42.36	0g
56	24	11:39	seqdata_09-05-13_1138_031.lvm	Seq_S0028	Par24	4674.90	41.89	599.28	42.37	0g
57	25	11:42	seqdata_09-05-13_1141_032.lvm	Seq_S0029	Par25	18821.00	42.01	600.18	42.41	Transition
58	26	11:49	seqdata_09-05-13_1148_033.lvm	Seq_S0030	Par26	4912.60	41.63	599.84	42.39	Transition
59	27	11:52	seqdata_09-05-13_1151_034.lvm	Seq_S0031	Par27	4912.60	41.56	599.57	42.38	Transition
60	28	11:55	seqdata_09-05-13_1154_035.lvm	Seq_S0032	Par28	4912.50	41.46	599.81	42.39	Transition
61	29	11:58	seqdata_09-05-13_1157_036.lvm	Seq_S0033	Par29	5281.30	41.53	600.05	42.40	Transition
62	30	12:01	seqdata_09-05-13_1200_037.lvm	Seq_S0034	Par30	5924.70	41.48	599.56	42.38	Transition

Flight	Date	Bubbledir	IR Dir
3	14.05.2009	2009_05_14_Flug3	2009_05_14\Flug3

Nr	Par	Time	Seqdata	Bubblepics	IR Data	Heating Power [W/m²]	Mean Fluid Temp [°C]	Pressure [mbar]	Saturation Temp [°C]	Gravity
63	0	09:58	seqdata_09-05-14_0958_003.lvm	Seq_S0002	Par00	7323.80	42.08	599.41	42.37	Transition
64	1	10:01	seqdata_09-05-14_1001_004.lvm	Seq_S0003	Par01	7323.60	42.03	599.04	42.36	Transition
65	2	10:05	seqdata_09-05-14_1004_005.lvm	Seq_S0004	Par02	7324.00	41.98	598.94	42.35	Transition
66	3	10:07	seqdata_09-05-14_1007_008.lvm	Seq_S0005	Par03	6607.00	41.95	599.34	42.37	Transition
67	4	10:10	seqdata_09-05-14_1010_009.lvm	Seq_S0006	Par04	7324.50	41.93	598.94	42.35	Transition
68	5	10:13	seqdata_09-05-14_1013_010.lvm	Seq_S0007	Par05	7324.20	42.00	599.05	42.36	Transition
69	6	10:19	seqdata_09-05-14_1019_012.lvm	Seq_S0008	Par06	7324.20	42.16	599.68	42.39	Transition
70	7	10:22	seqdata_09-05-14_1022_013.lvm	Seq_S0009	Par07	7324.70	42.17	599.94	42.40	Transition
71	8	10:26	seqdata_09-05-14_1025_014.lvm	Seq_S0010	Par08	7324.30	42.14	599.27	42.37	0g
72	9	10:29	seqdata_09-05-14_1028_017.lvm	Seq_S0011	Par09	7324.30	42.16	599.61	42.38	Transition
73	10	10:31	seqdata_09-05-14_1031_022.lvm	Seq_S0013	Par10	7324.70	42.10	599.34	42.37	Transition
74	11	10:38	seqdata_09-05-14_1038_023.lvm	Seq_S0014	Par11	7773.40	42.23	599.48	42.38	Transition
75	12	10:41	seqdata_09-05-14_1041_024.lvm	Seq_S0015	Par12	7773.10	42.16	599.27	42.37	Transition
76	13	10:44	seqdata_09-05-14_1044_025.lvm	Seq_S0016	Par13	7773.60	42.14	599.10	42.36	Transition
77	14	10:47	seqdata_09-05-14_1047_026.lvm	Seq_S0017	Par14	7773.50	42.11	600.01	42.40	Transition
78	15	10:50	seqdata_09-05-14_1050_AAA.lvm	Seq_S0018	Par15	7773.40	42.01	599.47	42.38	Transition
79	16	11:02	seqdata_09-05-14_1102_029.lvm	Seq_S0019	Par16	7773.00	40.46	599.12	42.36	Transition
80	17	11:05	seqdata_09-05-14_1105_030.lvm	Seq_S0020	Par17	4675.40	39.97	599.02	42.36	0g
81	18	11:08	seqdata_09-05-14_1108_031.lvm	Seq_S0021	Par18	4675.50	39.68	599.56	42.38	0g
82	19	11:11	seqdata_09-05-14_1111_032.lvm	Seq_S0022	Par19	3572.10	39.45	599.18	42.36	0g
83	20	11:14	seqdata_09-05-14_1114_033.lvm	Seq_S0023	Par20	3572.50	39.41	599.34	42.37	Transition
84	21	11:22	seqdata_09-05-14_1122_034.lvm	Seq_S0024	Par21	2618.50	42.28	599.00	42.36	0g
85	22	11:25	seqdata_09-05-14_1125_035.lvm	Seq_S0025	Par22	3572.20	42.24	598.51	42.33	Transition
86	23	11:28	seqdata_09-05-14_1128_036.lvm	Seq_S0026	Par23	3572.30	42.12	598.70	42.34	Transition
87	24	11:31	seqdata_09-05-14_1131_037.lvm	Seq_S0027	Par24	4674.40	42.14	599.07	42.36	0g
88	25	11:34	seqdata_09-05-14_1134_038.lvm	Seq_S0028	Par25	4675.30	41.98	599.83	42.39	Transition
89	26	11:40	seqdata_09-05-14_1140_039.lvm	Seq_S0029	Par26	3572.40	42.11	598.88	42.35	0g
90	27	11:43	seqdata_09-05-14_1143_040.lvm	Seq_S0030	Par27	18823.00	42.01	599.33	42.37	0g
91	28	11:46	seqdata_09-05-14_1146_041.lvm	Seq_S0031	Par28	3076.90	41.88	598.68	42.34	0g
92	29	11:49	seqdata_09-05-14_1149_042.lvm	Seq_S0032	Par29	2618.60	41.76	598.67	42.34	0g
93	30	11:52	seqdata_09-05-14_1152_043.lvm	Seq_S0033	Par30					
94	NP	09:46	seqdata_09-05-14_0946_002.lvm	Seq_S0001	test1					

Pages 127 – 179 can be found in separate appendix files

Appendix 1 (pp. 127 – 147):	Data sets of sequences 20, 23, 24, 28, 29, 57
Appendix 2 (pp. 148 – 163):	Data sets of sequence 70
Appendix 3 (pp. 164 – 179):	Data sets of sequences 77 and 86 Arry description of bubble image evaluation

8.14. Parabolic Flight Team for the 50th ESA Campaign

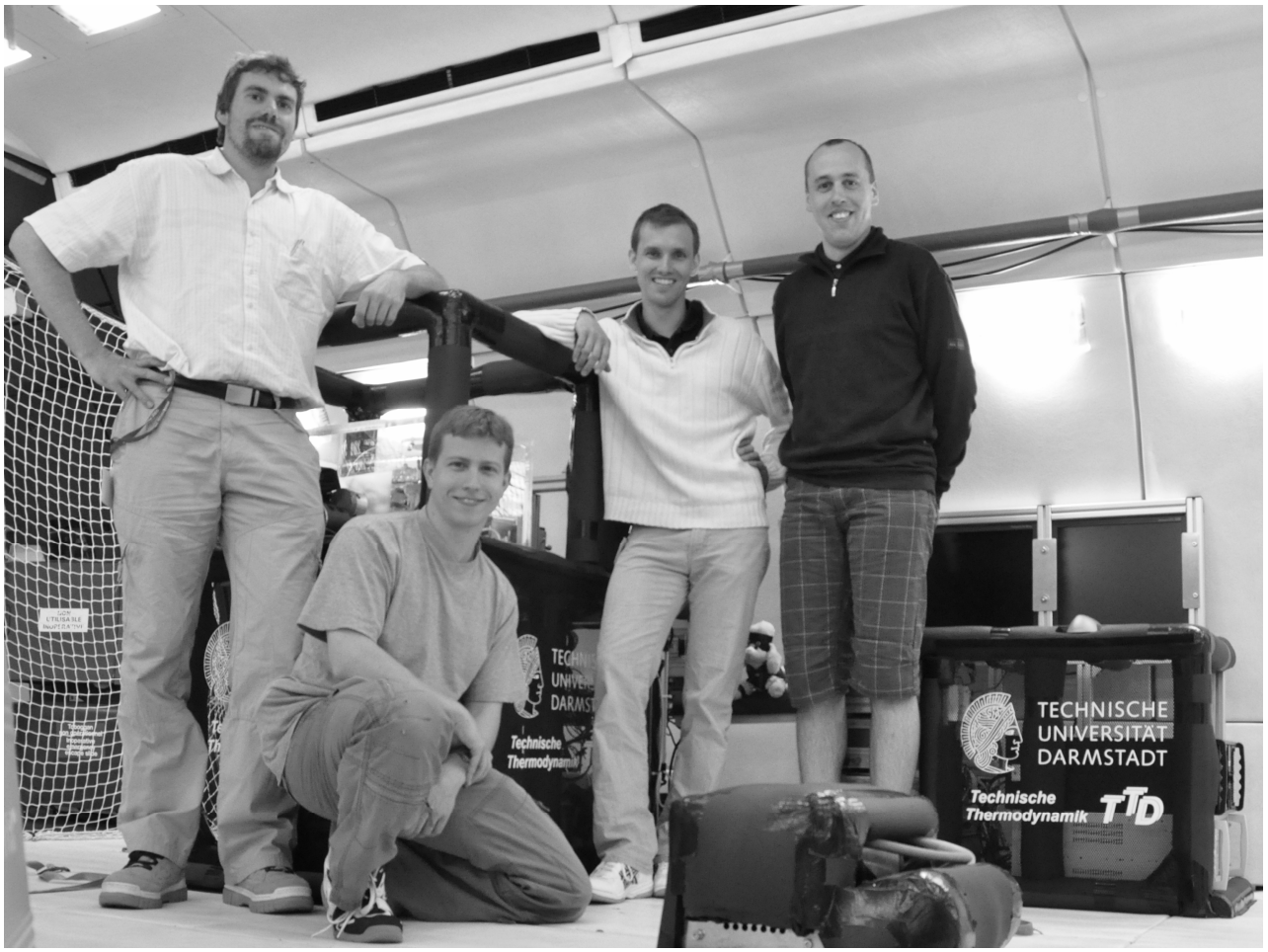

Figure 8.8: Parabolic flight team with experimental setup on board the Airbus A300 ZERO-G (June 2009): Nils Schweizer[1], Sebastian Fischer[1], Felix Brinckmann[1] and Balazs Toth[2] (from left to right)

[1] Institute of Technical Thermodynamics (TTD), Technische Universität Darmstadt, Germany

[2] European Space Research and Technology Centre (ESTEC), European Space Agency (ESA), Noordwijk, The Netherlands

Literature

[1] AMMERMAN, C.N., S.M. YOU and Y.S. HONG: *Identification of Pool Boiling Heat Transfer Mechanisms From a Wire Immersed in Saturated FC-72 Using a Single-Photo/ LDA Method.* Journal of Heat Transfer, 118:117-123, 1996.

[2] BAEHR, H.D. and K. STEPHAN: *Wärme- und Stoffübertragung.* Springer Verlag, Berlin, Heidelberg, New York, 4. Auflage, 2004.

[3] BANKOFF, S.G.: *Entrapment of gas in the spreading of a liquid over a rough surface.* AIChE Journal, 4:24-26, 1958.

[4] BARTHES M., C. REYNARD, R. SANTINI and L. TADRIST: *Non-condensable gas influence on Marangoni convection during a single vapour bubble growth in a subcooled liquid*. Europhysics Letters, 77:14001, 2007

[5] BONJOUR, J., M. CLAUSSE and M. LALLEMAND: *Experimental study of the coalescence phenomenon during nucleate pool boiling.* Experimental Thermal and Fluid Science, 20:180-187, 2000.

[6] BORISHANSKY, V.M. and F.S. FOKIN: *Heat transfer and hydrodynamics in steam generators.* Trudy TsKTI, 62:1, 1963.

[7] BRANDT, C.: *Wärme- und Flüssigkeitstransport in Verdampfern von Wärmerohren mit Hochleistungskapillarstrukturen.* Dissertation, Fortschritt-Berichte VDI, Reihe 19, Nr. 147, VDI-Verlag, Düsseldorf, 2003.

[8] BUFFONE, C. and K. SEFIANE: *Temperature measurement near the triple line during phase change using thermochromic liquid crystal thermography.* Experiments in Fluids, 39:99-110, 2005.

[9] CAREY, V.P.: *Liquid-Vapor Phase-Change Phenomena: An Introduction to the Thermophysics of Vaporization and Condensation Processes in Heat Transfer Equipment*. Taylor & Francis, 1. Auflage, 1992.

[10] CHEN, T. and J.N. CHUNG: *Coalescence of bubbles in nucleate boiling on microheaters.* International Journal of Heat and Mass Transfer, 45:2329-2341, 2002.

[11] COLE, R. and H.L. SHULMAN: *Bubble departure diameters at subatmospheric pressures.* Chemical Engineering Progresses Symposium Series, 62:6-16, 1966.

[12] COLE, R. and W.M. ROHSENOW: *Correlation of bubble departure diameters for boiling saturated liquids.* Chemical Engineering Progresses Symposium Series, 65:211-213, 1968.

[13] COLE, R.: *Bubble frequencies and departure volumes at subatmospheric pressures.* AIChE Journal, 13:779-783, 1967.

[14] CROUCHER M.D.: *A simple expression for the Hamaker constant of liquid-like materials.* Colloid and Polymer Sciences, 259:462-466, 1981.

[15] DASGUPTA, S., J.A. SCHONBERG, I.Y. KIM, P.C. WAYNER, JR: *Use of the augmented Young-Laplace equation to model equilibrium and evaporating extended menisci.* Journal of Colloid and Interface Science, 157:332-342, 1993.

[16] DEMIRAY F. and J. Kim: *Microscale heat transfer measurements during pool boiling of FC-72: effect of subcooling*, International Journal of Heat and Mass Transfer, 47:3257-3268, 2004.

[17] DHAVALESWARAPU, H.K., S.V. GARIMELLA and J.Y. MURTHY: *Microscale Temperature Measurements Near the Triple Line of an Evaporation Thin Liquid Film.* Journal of Heat Transfer, 131:061501, 2009.

[18] DHIR, V.K., H.S. ABARAJITH and D. LI: *Bubble Dynamics and Heat Transfer during Pool and Flow Boiling.* Heat Transfer Engineering, 28:608-624, 2007.

[19] DI MARCO, P. and W. GRASSI: *Combined effect of electric field, subcooling and microgravity on critical heat flux on a wire in pool boiling.* Proceedings of the Convective and Flow Boiling Conference, Irsee, Germany, pp. 395-402, 1997.

[20] DI MARCO, P. and W. GRASSI: *Effect of external electric field on pool boiling: Comparison of terrestrial and microgravity data in the ARIEL experiment.* Proceedings of the ECI International Conference on Boiling Heat Transfer, Florianopolis, Brazil, 2009.

[21] DI MARCO, P. and W. GRASSI: *Effect of force fields on pool boiling flow patterns in normal and reduced gravity.* Journal of Heat and Mass Transfer, 45:959-966, 2009.

[22] DI MARCO, P. and W. GRASSI: *EHD Effects on Pool Boiling in Reduced Gravity.* Proceedings of the 5th ASME/JSME Joint Thermal Engineering Conference, San Diego, 1999.

[23] DI MARCO, P. and W. GRASSI: *Pool Boiling in Microgravity: Assessed Results and Open Issues.* Paper presented at the 3rd European Thermal Sciences Conference, Heidelberg, Germany, September 2000.

[24] DI MARCO, P., W. GRASSI, G. MEMOLI, T. TAKAMASA, A. TOMIYAMA and S. HOSOKAWA: *Influence of electric field on single gas-bubble growth and detachment in microgravity.* International Journal of Multiphase Flow, 29:559-578, 2003.

[25] DI MARCO, P.: *Review of Reduced Gravity Boiling Heat Transfer: European Research*. Journal of the Japan Society of Microgravity Application, 20:252-263, 2003.

[26] DIAZ, M.C., BOYE, H., HAPKE, I., SCHMIDT, J., STAATE, Y., ZHEKOV, Z.: *Investigation of flow boiling in narrow channels by thermographic measurement of local wall temperatures*. Microfluidics and Nanofluidics 2:1-11, 2005.

[27] ERVIN J.S., H. MERTE JR., R.B. KELLER and K. KIRK: *Transient pool boiling in microgravity*, International Journal of Heat and Mass Transfer, 35:659-674, 1992.

[28] FORSTER, H.K. and GREIF, R.: *Heat transfer to a boiling liquid – Mechanism and correlations,* Journal of Heat Transfer 81:43-54,1959.

[29] FORSTER, H.K. and N. ZUBER: *Growth of a Vapor Bubble in a Superheated Liquid*. Journal of Applied Physics, 25:474-478, 1954.

[30] FRITZ, W.: *Berechnung des Maximalvolumens von Dampfblasen.* Physikalische Zeitschrift, 36:379-388, 1935.

[31] FUCHS, T., J. KERN and P. STEPHAN: *A Transient Nucleate Boiling Model Including Microscale Effects and Wall Heat Transfer.* Journal of Heat Transfer, 128:1257-1265, 2006.

[32] FUCHS, T.: *Numerische Analyse transienter Wärmetransport- und Wärmespeicherungsmechanismen in Heizwand und Fluid beim Blasensieden eines binären Gemischs.* Dissertation, Fortschritt-Berichte VDI, Reihe 3, Nr. 902, VDI-Verlag, Düsseldorf, 2009.

[33] GNIELINSKI, V., S. KABELAC, M. KIND, H. MARTIN, D. MEWES and K. SCHABER: *VDI-Wärmeatlas.* Verein Deutscher Ingenieure, Springer Verlag, Berlin, Heidelberg, New York, 9. Auflage, 2002.

[34] GOLOBIC, I., J. PETKOVSEK, M. BASELJ, A. PAPEZ and D.B.R. KENNING: *Experimental determination of transient wall temperature distributions close to growing vapor bubbles.* Heat and Mass Transfer, 45:857-866, 2009.

[35] GOLOBIC, I., J. PETKOVSEK, M. BASELJ, A. PAPEZ and D.B.R. KENNING: *Experimental determination of transient wall temperature distributions close to growing vapor bubbles.* Paper presented at the ECI International Conference on Boiling Heat Transfer, Spoleto, Italy, May 2006.

[36] GOLORIN, V.S., B.A. KOLCHUGIN and E.A. ZAKHAROVA: *Investigation of the mechanism of nucleate boiling of ethyl alcohol and benzene by means of high-speed motion-picture photography.* Heat Transfer – Sov. Res., 10:79-98, 1978.

[37] GUNTHER, F.C. and F. KREITH: *Photographic Study of Bubble Formation in Heat Transfer to Subcooled Water*. Progress Report 4-120, Jet Propulsion Laboratory, California Institute of Technology, 1950.

[38] HAIDER, S.I., and WEBB R.I.: *A transient micro-convection model of nucleate pool boiling*, International Journal of Heat and Mass Transfer, 40:3675-3688, 1997.

[39] HAMMER, J. and P. STEPHAN: *Results of the micro-region model for nucleate boiling heat transfer.* IMechE, C510/112, p. 283-287, 1995.

[40] HAMMER, J.: *Einfluss der Mikrozone auf den Wärmeübergang beim Blasensieden*. Dissertation, Universität Stuttgart, 1996.

[41] HAN, C. and P. GRIFFITH: *The mechanisms of heat transfer in nucleate pool boiling.* International Journal of Heat and Mass Transfer, 8:887-913, 1965.

[42] HARDT, S. and F. WONDRA: *Evaporation model for interfacial flows based on a continuum-field representation of source terms.* Journal of Computational Physics, 227:5871-5895, 2008.

[43] HARDT, S., SCHILDER, B., TIEMANN, D., KOLB, G., HESSEL, V., STEPHAN, P.: *Analysis of flow patterns emerging during evaporation in parallel microchannels*. International Journal of Heat and Mass Transfer, 50:226-239, 2007.

[44] HENRY, C.D and J. KIM: *A study of the effects of heater size, subcooling and gravity level on pool boiling heat transfer.* International Journal of Heat and Fluid Flow, 25:262-273, 2004.

[45] HÖHMANN, C. and P. STEPHAN: *Microscale temperature at an evaporating liquid meniscus.* Experimental Thermal and Fluid Science, 26:157-162, 2002.

[46] HÖHMANN, C.: *Temperaturmessverfahren zur räumlich hochauflösenden Untersuchung des Wärmetransports an einem verdampfenden Flüssigkeitsmeniskus.* Dissertation, Shaker Verlag, Aachen, 2004.

[47] HSU, Y.Y.: *On the size range of active nucleation cavities on a heating surface.* Journal of Heat Transfer, 84:207-213, 1962.

[48] IVEY, H.J.: *Relationships between bubble frequency, departure diameter and rise velocity in nucleate boiling.* International Journal of Heat and Mass Transfer, 10:1023-1040, 1967.

[49] JABARDO, J.M.S.: *Investigation of thermocapillary flows around hemispherical bubbles.* PhD Thesis, University of Illinois at Urbana-Champaign, 1981.

[50] JAKOB, M and W. FRITZ: *Versuche über den Verdampfungsvorgang*. Forschung im Ingenieurwesen, 2:435-447, 1931.

[51] JAKOB, M and W. LINKE: *Der Wärmeübergang beim Verdampfen von Flüssigkeiten an senkrechten oder waagrechten Flächen*. Physikalische Zeitschrift, 36:267-280, 1935

[52] JENSEN, M.K. and G.J. MEMMEL: *Evaluation of bubble departure diameter correlations*. Proceedings of the 8th International Heat Transfer Conference, San Francisco, USA, pp 1907– 1912, 1986.

[53] JUDD, R.L. and K.S. HWANG: *A Comprehensive Model for Nucleate Pool Boiling Heat Transfer Including Microlayer Evaporation.* Journal of Heat Transfer, 98:623-629, 1976.

[54] KANDLIKAR, S.G.: *Fundamental issues related to flow boiling in minichannels and microchannels*. Experimental Thermal and Fluid Science, 26:387-407, 2002.

[55] KANDLIKAR, S.G.: *Heat Transfer Mechanisms During Flow Boiling in Microchannels*. Journal of Heat Transfer, 126:8-16, 2004.

[56] KANDLIKAR, S.G., M. SHOJI and V.K. DHIR: *Handbook of Phase Change: Boiling and Condensation.* Taylor & Francis, Philadelphia, 1999.

[57] KARAYIANNIS T.G. and Y. Xu: *Electric Field Effect in Boiling Heat Transfer. Part A: Simulation of the Electric Field and Electric Forces.* Enhanced Heat Transfer, 5:217-229, 1998.

[58] KENNING, D.B.R. and Y. YAN: *Pool boiling heat transfer on a thin plate: features revealed by liquid crystal thermography*. International Journal of Heat and Mass Transfer, 39:3117-3137, 1996.

[59] KENNING, D.B.R., T. KONO and M. WIENECKE: *Investigation of boiling heat transfer by liquid crystal thermography*. Experimental Thermal and Fluid Science, 25:219-229, 2001.

[60] KENNING, D.B.R.: *Wall temperature patterns in nucleate boiling.* Journal of Heat Transfer, 35:73-86, 1991.

[61] KERN, J. and P. STEPHAN: *Theoretical model for nucleate boiling heat and mass transfer of binary mixtures.* Journal of Heat Transfer, 125:1106-1115, 2003.

[62] KERN, J., C. SODTKE, N. SCHWEIZER and P. STEPHAN: *Microgravity Measurements of Microscale Wall Temperature Distribution Underneath a Single Vapour Bubble.* Paper presented at the 6th World Conference on Experimental Heat Transfer, Fluid Mechanics and Thermodynamics, Matsushima (Miyagi), Japan, April 2005.

[63] KIM, J. and J.F. BENTON: *Highly subcooled pool boiling heat transfer at various gravity levels.* International Journal of Heat and Fluid Flow, 23:497-508, 2002.

[64] KERN, J.: *Modellierung und Berechnung des Wärmeübergangs beim Blasensieden binärer Gemische.* Dissertation, Fortschritt-Berichte VDI, Reihe 3, Nr. 727, VDI-Verlag, Düsseldorf, 2002.

[65] KIM, J., J.F. BENTON and D. WISNIEWSKI: *Pool boiling heat transfer on small heaters: effect of gravity and subcooling.* International Journal of Heat and Mass Transfer, 45:3919-3932, 2002.

[66] KIM, J.: *Review of Reduced Gravity Boiling Heat Transfer: US Research*. Journal of the Japan Society of Microgravity Application, 20:264-271, 2003.

[67] KUNKELMANN, C. and P. STEPHAN: *CFD Simulation of Boiling Flows using the Volume-Of-Fluid Method within OpenFOAM.* Numerical Heat Transfer A, 56:631-646, 2009.

[68] KUNKELMANN, C.: *Modellierung und numerische Berechnung des Wärmetransports bei der Verdampfung aus Kapillarstrukturen in Wärmerohren.* Diplomarbeit, Technische Universität Darmstadt, Fachgebiet Technische Thermodynamik, Darmstadt, 2007.

[69] KUTATELADZE, S.S. and I.I. GOGONIN: *Growth rate* and *detachment diameter* of a *vapor bubble in free convection boiling of a saturated liquid.* High Temperature, 17:667-671, 1980.

[70] LANDAU L.D. and E.M. Lifshitz: *Electrodynamics of Continuous Media.* Pergamon, New York, 1963.

[71] LEE, H.S. and H. MERTE JR.: *Pool Boiling Mechanisms in Microgravity*. Proceedings of the Engineering Foundation Conference on Microgravity Fluid Physics and Heat Transfer, Hawai, 1999

[72] LEE, H.S. and H. MERTE JR.: *The Pool Boiling Curve in Microgravity*. Journal of Thermophysics and Heat Transfer, 12:216-222, 1997.

[73] LEVY, S.: *Generalized Correlation of Boiling Heat Transfer.* Journal of Heat Transfer, 81-2:37-42, 1959.

[74] LUKE, A.: *Pool boiling heat transfer from horizontal tubes with different surface roughness.* International Journal of Refrigeration, 20:8:561-574,1997.

[75] MALENKOV I.G.: *The frequency of vapor bubble separation as function of bubble size*, Fluid Mechanics Soviet Research, v.1, p. 36, 1971.

[76] MANN, M., and K. STEPHAN: *Influence of convection on nucleate boiling heat transfer around horizontal tubes.* Multiphase Science and Technology, Vol 12, Issue 3, 15 p, 2000.

[77] MELCHER, J.R. and G.I. TAYLOR: *Electrohydrodynamics: A review of the role of interfacial shear stresses*, Annual Review of Fluid Mechanics, 1:111-146, 1969.

[78] MIKIC, B.B. and W.M. ROHSENOW: *A new correlation of pool boiling data including the effect of heating surface characteristics,* International Journal of Heat and Mass Transfer 91:245-250, 1969.

[79] MIKIC, B.B. and W.M. ROHSENOW: *Bubble growth rates in non-uniform temperature field.* Progress in Heat and Mass Transfer, 2:283-292, 1969.

[80] MOGHADDAM, S.: *Microscale study of nucleation process in boiling of low-surface-tension liquids,* PhD thesis, University of Maryland, College Park, MD, USA, 2006

[81] MOGHADDAM, S. and K. KIGER: *Physical mechanisms of heat transfer during single bubble nucleate boiling of FC-72 under saturation conditions – I. Experimental investigation.* International Journal of Heat and Mass Transfer, 52:1284-1294, 2009.

[82] MOGHADDAM, S. and K. KIGER: *Physical mechanisms of heat transfer during single bubble nucleate boiling of FC-72 under saturation conditions – II. Theoretical analysis.* International Journal of Heat and Mass Transfer, 52:1295-1303, 2009.

[83] MOORE, F.D. and R.B. MESLER: *The Measurement of Rapid Surface Temperature Fluctuations During Nucleate Boiling of Water.* AIChE Journal, 7:620-624, 1961.

[84] MUKHERJEE, A. and V.K. DHIR: *Study of Lateral Merger of Vapor Bubbles During Nucleate Pool Boiling.* Journal of Heat Transfer, 126:1023-1039, 2004.

[85] MUWANGA, R., HASSAN, I.: *A Flow Boiling Heat Transfer Investigation of FC-72 in a Microtube Using Liquid Crystal Thermography*. Journal of Heat Transfer, 129:977-987, 2007.

[86] MYERS, J.G., V.K. YERRAMILLI, S.W. HUSSEY, G.F. YEE and J. KIM: *Time and space resolved wall temperature and heat flux measurements during nucleate boiling with constant heat flux boundary conditions.* International Journal of Heat and Mass Transfer, 58:2429-2442, 2005.

[87] NORTON P.: *HgCdTe infrared detectors*. Opto-Electronics Review 10:159-174, 2002.

[88] NUKIYAMA, S.: *The maximum and minimum values of the heat q transmitted from metal to boiling water under atmospheric pressure.* International Journal of Heat and Mass Transfer, 9:1419-1433, 1935.

[89] Oehmann, C.: *Measurement in Thermography*. FLIR Pub. No. 1 557 498 Rev. A, 2001.

[90] OHTA, H.: *Review of Reduced Gravity Boiling Heat Transfer: Japanese Research*. Journal of the Japan Society of Microgravity Application, 20:272-285, 2003.

[91] OKA, T., Y. ABE, K. TANAKA, Y.H. MORI und A. NAGASHIMA: *Observational Study of Pool Boiling under Microgravity.* JSME International Journal – Series II, 35:280-286, 1992.

[92] PANCHAMGAM, S.S., J.L PLAWSKY, P.C. WAYNER JR.: *Microscale heat transfer in an evaporating moving extended meniscus.* Experimental Thermal and Fluid Science, 30:745-754, 2006.

[93] PEEBLES, F.N. and H.J. GARBER: *Studies on motion of gas bubbles in liquids*. Chemical Engineering Progress, 49:88-97, 1953.

[94] PIASECKA, M., HOZEJOWSKA, S., PONIEWSKI, M. E.: *Experimental Evaluation of Flow Boiling Incipience of Subcooled Liquid in a Narrow Channel*. International Journal of Heat and Fluid Flow, 25:159-172, 2004.

[95] QIU, D.M., V.K. DHIR, D. CHAO, M.M. HASAN, E. NEUMANN, G. YEE and A. BIRCHENOUGH: *Single-Bubble Dynamics During Pool Boiling Under Low Gravity Conditions.* Journal of Thermophysics and Heat Transfer, 16:336-345, 2002.

[96] QU, W. and MUDAWAR, I.: *Flow boiling heat transfer in two-phase micro-channel heat sinks – I. Experimental investigation and assessment of correlation methods.* International Journal of Heat and Mass Transfer, 46:2755-2771, 2003.

[97] RAJ, R., J. KIM and J. MCQUILLEN: *Subcooled Pool Boiling in Variable Gravity Environments.* Journal of Heat Transfer, 131:091502, 2009.

[98] ROHSENOW, W.H.: *A Method for Correlation Heat-Transfer Data for Surface Boiling Liquids.* Journal of Heat Transfer, 74:969-976, 1952.

[99] RUCKENSTEIN, E.: *A physical model for nucleate boiling heat transfer from a horizontal surface*. Buletinul Institutului Politehnic Bucuresti, 33:79-88, 1961.

[100] RUYTERS, G. and P. PREU: *Vom Bremer Fallturm zur Internationalen Raumstation – Faszinierende Forschung in der Schwerelosigkeit*. Spektrum der Wissenschaft Extra, 7/2010:14-19, 2010

[101] SCHULZE, T., C. SODTKE, P. STEPHAN, T. GAMBARYAN-ROISMAN and C. BRANDT: *Performance of heat pipe evaporators for space applications with combined re-entrant and micro grooves.* Paper presented at the 14th International Heat Pipe Conference, Florianópolis, Brazil, April 2007.

[102] SCHWEIZER, N. and P. STEPHAN: *Experimental study of bubble behavior and local heat flux in pool boiling under variable gravitational conditions*. Multiphase Science and Technology, 21:329-350, 2009.

[103] SHATTO, D.P. and G.P. PETERSON: *Pool Boiling Critical Heat Flux in Reduced Gravity.* Journal of Heat Transfer, 121:865-873, 1999.

[104] SIEDEL S., S. CIOULACHTJIAN and J. BONJOUR: *ELectric field effect on the rise of single bubbles during pool boiling.* Proceedings of the ECI International Conference on Boiling Heat Transfer, Florianopolis, Brazil, 2009.

[105] SIEGEL, R. and E.G. KESHOCK: *Effects of Reduced Gravity on Nucleate Boiling Dynamics in Saturated Water.* AIChE Journal, 10:509-517, 1964.

[106] SIEGEL, R.: *Effects of Reduced Gravity on Heat Transfer.* In: *Advances in Heat Transfer* (J.P. Hartnett/ T.F. Irvine Jr., Ed.), Vol. 4, S. 143-228, Academic Press, New York, 1967.

[107] SINGH S., V.K. DHIR: *Effect of gravity, wall superheat and liquid subcooling on bubble dynamics during nucleate boiling*, Microgravity Fluid Physics and Heat Transfer, Kahuko, Hawai, 1999.

[108] SNYDER, T.J. and J.N. CHUNG: *Terrestrial and microgravity boiling heat transfer in a dielectrophoretic force field.* International Journal of Heat and Mass Transfer, 43:1547-1562, 2000.

[109] SNYDER, T.J., J.N. CHUNG and J.B. SCHNEIDER: *Competing Effects of Dielectrophoresis and Buoyancy on Nucleate Boiling and an Analogy With Variable Gravity Boiling Results.* Journal of Heat Transfer, 120:371-379, 1998.

[110] SODTKE, C. and P. STEPHAN: *Spray cooling on micro structured surfaces.* International Journal of Heat and Mass Transfer, 50:4089-4097, 2007.

[111] SODTKE, C., J. KERN, N. SCHWEIZER and P. STEPHAN: *High resolution measurements of wall temperature distribution underneath a single vapour bubble under low gravity conditions.* International Journal of Heat and Mass Transfer, 49:1100-1106, 2006.

[112] SODTKE, C., N. SCHWEIZER, E. WAGNER and P. STEPHAN: *Experimental study of nucleate boiling heat transfer under low gravity conditions using TLCs for high resolution temperature measurements.* Heat and Mass Transfer, 42:875-883, 2006.

[113] SODTKE, C., N. SCHWEIZER, E. WAGNER and P. STEPHAN: *Experimental study of nucleate boiling heat transfer under low gravity conditions using TLCs for high resolution temperature measurements.* Paper presented at the ECI International Conference on Boiling Heat Transfer, Spoleto, Italy, May 2006.

[114] SODTKE, C.: *Untersuchung zur Sprühkühlung an mikrostrukturierten Oberflächen.* Dissertation, Fortschritt-Berichte VDI, Reihe 19, Nr. 156, VDI-Verlag, Düsseldorf, 2007.

[115] SPARROW, E.M. and R.D. CESS: *Radiation Heat Transfer.* Brooks/Cole Publishing Company, Belmont, California, 1970.

[116] STEPHAN, P. and J. HAMMER: *A new model for nucleate boiling heat transfer.* Wärme- und Stoffübertragung, 30:119-125, 1994.

[117] STEPHAN, P. and J. KERN: *Evaluation of heat and mass transfer phenomena in nucleate boiling.* International Journal of Heat and Fluid Flow, 25:140-148, 2004.

[118] STEPHAN, P., K. SCHABER, K. STEPHAN and F. MAYINGER: *Thermodynamik – Band 1: Einstoffsysteme*. Springer Verlag, Berlin, 16. Auflage, 2005.

[119] STEPHAN, P., T. FUCHS, E. WAGNER, N. SCHWEIZER: *Transient Local Heat Fluxes During The Entire Vapor Bubble Life Time.* Proceedings of the ECI International Conference on Boiling Heat Transfer, Florianopolis, Brazil, 2009.

[120] STEPHAN, P.: *Wärmedurchgang bei der Verdampfung aus Kapillarrillen in Wärmerohren*. Dissertation, Fortschritt-Berichte VDI, Reihe 19, Nr. 59, VDI-Verlag, Düsseldorf, 1992.

[121] STRAUB, J., M. ZELL and B. VOGEL: *Pool boiling in a reduced gravity field*, Proceedings of the 9th International Heat Transfer Conference, Jerusalem, Israel, pp 91-112, 1990.

[122] STRAUB, J.: *Boiling Heat Transfer and Bubble Dynamics in Microgravity.* In: *Advances in Heat Transfer* (J.P. Hartnett/ T.F. Irvine Jr., Ed.), Vol. 35, S. 57-172, Academic Press, New York, 2001.

[123] THEOFANOUS T.G., J.P. TU, A.T. DINH and T.N. DINH: *The boiling crisis phenomenon – Part I: nucleation and nucleate boiling heat transfer.* Experimental Thermal and Fluid Science, 26:775-792, 2002.

[124] THEOFANOUS T.G., J.P. TU, A.T. DINH and T.N. DINH: *The boiling crisis phenomenon – Part II: dryout dynamics and burnout.* Experimental Thermal and Fluid Science, 26:793-810, 2002.

[125] TONG, W. A. BAR-COHEN and T.W. SIMON: *Thermal Transport Mechanisms in Nucleate Boiling of Highly-Wetting Fluids.* Proceedings of the 9th International Heat Transfer Conference, Jerusalem, 1990.

[126] VAN STRALEN, S. and R. COLE: *Boiling Phenomena: Physicochemical and Engineering Fundamentals and Applications, Volume 1*. Hemisphere Publishing Corporation, 1979.

[127] WAGNER, E., C. SODTKE, N. SCHWEIZER and P. STEPHAN: *Experimental study of nucleate boiling heat transfer under low gravity conditions using TLCs for high resolution temperature measurements.* Heat and Mass Transfer, 42:875-883, 2006.

[128] WAGNER, E.: *Hochauflösende Messung beim Blasensieden von Reinstoffen und binären Gemischen.* Dissertation, Berichte aus der Thermodynamik, Shaker Verlag, Aachen, ISBN 978-3-8322-7881-6, 2009.

[129] WAGNER, E. and P. STEPHAN: *Frequency response of a surface thermometer based on unencapsulated thermochromic liquid crystals.* Journal of Experimental Thermal and Fluid Science, 31:7:687-699, 2007.

[130] WAYNER JR., P.C.: *The effect of the London-Van Der Waals dispersion forces on interline heat transfer.* Journal of Heat Transfer, 100:155-159, 1978.

[131] WAYNER, P., Y.K. KAO and L.V. LA CROIX: *The interline heat transfer coefficient on an evaporation wetting film.* International Journal of Heat and Mass Transfer, 19:487:792, 1976.

[132] WONDRA, F. and P. STEPHAN: *Pool boiling heat transfer from tubular microstructured surfaces in saturated FC-72.* Paper presented at the ECI International Conference on Boiling Heat Transfer, Spoleto, Italy, May 2006.

[133] YADDANAPUDI, N., and KIM, J.: *Single Bubble Heat Transfer in Saturated Pool Boiling of FC-72.* Multiphase Science and Technology, 12:3-4:47-63, 2001.

[134] ZELL, M.: *Untersuchung des Siedevorgangs unter reduzierter Schwerkraft*. Dissertation, Technische Universität München, 1991.

[135] ZUBER, N.: *Hydrodynamic aspects of boiling heat transfer (thesis)*. Unites States Atomic Energy Commission, report AECU 4439, 1959.

[136] ZUBER, N.: *Nucleate boiling. The region of isolated bubbles and the similarity with natural convection*. International Journal of Heat and Mass Transfer, 6:53-60, 1963.

Curriculum Vitae

Persönliche Daten:

Name:	Nils Schweizer
Geburtsdatum:	20. Oktober 1977
Geburtsort:	Erbach/Odw

Schulbildung:

1984 – 1988	Grundschule Michelstadt
1988 – 1990	Förderstufe der Theodor-Litt-Schule in Michelstadt
1990 - 1997	Gymnasium Michelstadt, Abschluss: Abitur

Zivildienst:

1997 - 1998	Deutsches Rotes Kreuz, Fahrdienst

Studium:

10/1998 – 12/2005	Maschinenbau an der Technischen Universität Darmstadt, Abschluss als Diplom-Ingenieur im Dezember 2005

Berufliche Tätigkeiten:

02/2006 – 12/2009	Wissenschaftlicher Mitarbeiter am Fachgebiet Technische Thermodynamik der TU Darmstadt.
Seit 10/2009	Anstellung als System-Ingenieur bei EADS Astrium Space Transportation, Friedrichshafen, in der Abteilung für fluidphysikalische Nutzlasten.